

**Heterotriangulene Based Hemicyanine and Squaraine  
Dyes for Dye-Sensitized Solar Cells and Field Effect  
Transistors**

**Thesis Submitted to AcSIR**  
For the Award of the Degree of  
**DOCTOR OF PHILOSOPHY**  
In  
**CHEMICAL SCIENCES**



BY

**Ms. Neeta Macchindra Karjule**  
(Registration Number: 10CC13J26002)

Under the guidance of  
**Dr. Jayaraj Nithyanandhan**

Physical and Materials Chemistry Division  
CSIR-National Chemical Laboratory  
Pune- 411008, India.

**March 2018**

*Dedicated to My Beloved Father*



## सीएसआयआर-राष्ट्रीय रासायनिक प्रयोगशाला

(वैज्ञानिक तथा औद्योगिक अनुसंधान परिषद)

डॉ. होमी भाभा मार्ग, पुणे - 411 008. भारत

**CSIR-NATIONAL CHEMICAL LABORATORY**

(Council of Scientific & Industrial Research)

Dr. Homi Bhabha Road, Pune - 411 008. India.



**Dr. J. Nithyanandhan**  
Senior Scientist  
[j.nithyanandhan@ncl.res.in](mailto:j.nithyanandhan@ncl.res.in)  
Physical and Materials Chemistry Division

+91 20 2590 3050

### Thesis Certificate

This is to certify that the work incorporated in this Ph.D. thesis entitled **“Heterotriangulene Based Hemicyanine and Squaraine Dyes for Dye-Sensitized Solar Cells and Field Effect Transistors”** submitted by **Ms. Neeta Macchindra Karjule** to Academy of Scientific and Innovative Research (AcSIR) in fulfilment of the requirements for the award of the Degree of **Doctor of Philosophy in Chemical Sciences**, embodies original research work under my supervision. I further certify that this work has not been submitted to any other University or Institution in part or full for the award of any degree or diploma. Research material obtained from other sources has been duly acknowledged in the thesis. Any text, illustration, table etc., used in the thesis from other sources, have been duly cited and acknowledged.

**Ms. Neeta M. Karjule**  
**(Research Student)**

**Dr. J. Nithyanandhan**  
**(Research Supervisor)**

Communication  
Channels

NCL Level DID : 2590  
NCL Board No. : +91-20-25902000  
EPABX : +91-20-25893300  
+91-20-25893400

FAX

Director's Office : +91-20-25902601  
COA's Office : +91-20-25902660  
COS&P's Office : +91-20-25902664

WEBSITE

[www.ncl-india.org](http://www.ncl-india.org)

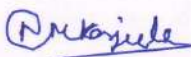


## CSIR-NATIONAL CHEMICAL LABORATORY

### Declaration by the Candidate

I hereby declare that the original research work embodied in this thesis entitled, **“Heterotriangulene Based Hemicyanine and Squaraine Dyes for Dye-Sensitized Solar Cells and Field Effect Transistors”** submitted to Academy of Scientific and Innovative Research for the award of degree of **Doctor of Philosophy (Ph.D.) in Chemical Sciences** is the outcome of experimental investigations carried out by me under the supervision of **Dr. J. Nithyanandhan**, Senior Scientist, Physical and Materials Chemistry Division, CSIR-National Chemical Laboratory, Pune. I affirm that the work incorporated is original and has not been submitted to any other academy, university or institute for the award of any degree or diploma.

**March 2018**  
**CSIR-National Chemical Laboratory**  
**Pune-411 008**

  
**Ms. Neeta M. Karjule**  
**(Research Student)**



---

# CONTENTS

---

	Page No.
Acknowledgement	i
Abbreviations	iii
General Remarks	v
Abstract	vi
<b>Chapter I Introduction</b>	
Section A: Dye-Sensitized Solar Cells	1
Section B: Organic Field Effect Transistors	28
Outline of Thesis	41
References	42
<b>Chapter II Heterotriangulene Based Unsymmetrical Squaraine Dyes for Dye-Sensitized Solar Cells</b>	
2.1 Introduction	45
2.2 Experimental Section	49
2.3 Results and Discussion	60
2.4 Conclusion	76
2.5 Selected NMR Spectra	77
2.6 References	93
<b>Chapter III Heterotriangulene Based Unsymmetrical Hemicyanine Dyes for Dye-Sensitized Solar Cells</b>	
3.1 Introduction	95
3.2 Experimental Section	99
3.3 Results and Discussion	105
3.4 Conclusion	127
3.5 Selected NMR Spectra	128
3.6 References	133
<b>Chapter IV Effect of <math>\pi</math>-spacer and Alkyl Chains on Molecular Orientation, Photophysical and Photovoltaic Properties of Heterotriangulene Based Squaraine Dyes for Dye-Sensitized Solar Cells</b>	
4.1 Introduction	136
4.2 Experimental Section	139
4.4 Results and Discussion	147
4.5 Conclusion	165
4.6 Selected NMR Spectra	166
4.7 References	169

---

# CONTENTS

---

<b>Chapter V</b>	<b>Molecular Engineering of Heterotriagulene Based Small Molecules for Organic Field Effect Transistors</b>	
5.1	Introduction	172
5.2A.1	Section A: Introduction	172
5.2A.2	Experimental Section	175
5.2A.3	Results and Discussion	179
5.2A.4	Conclusion	185
5.2B.1	Section B: Introduction	186
5.2B.2	Experimental Section	189
5.2B.3	Results and Discussion	194
5.2B.4	Conclusion	203
5.3	Selected NMR Spectra	204
5.4	References	210
	List of Publications	212
	Erratum	213

---

*Research is a never ending process involving a team of persons striving to attain newer horizons in the field of sciences. This thesis would not have been completed without the encouragement and co-operation of my teachers, parents, friends, well-wishers and relatives. I take this opportunity to express my deep gratitude to one and all.*

*Firstly, I would like to express my sincere gratitude to my research advisor Dr. J. Nithyanandhan for the support of my Ph.D study and related research. I am very much grateful to him for his valuable guidance and encouragement throughout my course.*

*I would like to thank our Head, Division of Physical and Materials Chemistry and Director NCL for providing infrastructure facilities. UGC New Delhi is acknowledged for financial assistance. I also thank all divisional students and staff members for their timely help throughout. Help rendered by the members of NMR group, mass spectroscopy and library staff members is also acknowledged.*

*I sincerely thank to my AcSIR-DAC members Dr. T. Ajithkumar, Dr. K. Sreekumar, Dr. E. Balaraman and Dr. A. T. Biju for invaluable suggestions, encouragement.*

*I sincerely thank Dr. P. A. Joy, Dr. Anil Kumar, Dr. U. K. Kharul, Dr. Amol Kulkarni, Dr. S. K. Asha and Dr. P. Wadgaonkar for their help and encouragement.*

*I sincerely thanks to Dr. Kothandam Krishnamoorthy for his support, help with device fabrication and characterization.*

*I enjoyed the cheerful co-operation and accompany of my labmates Kubandiran, Munavvar, Rajesh, Manik, Punitharasu and Ananthan who made me feel a member of this family right from the day one in the lab. The warm memories of my days in Lab-B2 will haunt me forever. My thanks to Labmates Ambarish, Amrita, Indrajit, Rengith, Supriya, Swapnali, Rincy, Dhanasari, Sharanya, Neel, Ashwath, Bavisha and Jenny for their co-operation and maintaining amazing atmosphere with humour in the lab. My special thanks to my friend and Labmate Rajesh for his helpful discussion, co-operation and support. I am also thankful to Dr. Krishnamoorthy's group members Dr. Rajashree, Dr. Satej, Dr. Manik, Dr. Arul, Dr. Mrinmoy, Dr. Saumya, Dr. Chayaniqa, Dr. Bhanu, Anup, Gunwant, Kumar, Sudhakar, Chithiravel, Jagdish and Geetanjali.*

*I would like to extend my thanks to NCL friends Dr. Dhanraj, Dr. Sreekuttan, Dr. Pradip, Dr. Beena, Dr. Bihag, Dr. Jijil, Dr. Sagar, Dr. Nagesh, Dr. Chinmay, Dr. Shekhar, Dr. Vishal, Siddheshwar, Veer, Manoj, Shivaji, Kailas, Dr. Ramesh, Dr. Pravat, Dr. Ravi, Prabhajam, Santosh, Mrityunjay, Nivedita, Ekta, Ashwini and my all other friends, Dr. Manjushree, Dr. Sachin, Dr. Sunil for making me very happy every time.*

*My time at NCL was enjoyable and memorable largely because of my GJ-hostel friends Dnyaneshwar, Mahendra, Vinita, Taufeeq, Rohit, Rohini, Dr. Satish, Dr. Atul, Dr. Sanjeev, Brijesh, Suman and Priyanka.*

*I specially acknowledge to Dr. Ravindra Phaktake and thank you so much for your love, friendship, support, care, advice and constructive criticism.*

*No word would suffice to express my gratitude and love to my father, Aai (mother), Sarika, Sonali (Sisters), Amol (Brother) and Ketan jiju for their continuous showering of boundless affection on me and supporting me in whatever I chose or did. It is my fathers and mother's prayer, constant struggle and relentless hard work to overcome the odds of life, which has inspired me to pursue life with a greater optimism. The warmth and moral value of my parents have stood me in good stead throughout my life and I would always look up to them for strength no matter what I have to go through. This Ph.D thesis is a result of the extraordinary will power, efforts and sacrifices of my parents. My successes are dedicated to them now and always.*

*...Neeta M. Karjule*



## ABBREVIATIONS

Abbreviation	Expansion
DSSCs	Dye-sensitized solar cells
HT	Heterotriangulene
FET	Field effect transistor
DFT	Density functional theory
TD-DFT	Time dependent density functional theory
HOMO	Highest occupied molecular orbital
LUMO	Lowest unoccupied molecular orbital
$E_g$	Energy band gap
UV-Vis	Ultraviolet-visible
NMR	Nuclear magnetic resonance
HR-MS	High resolution mass spectrometry
MALDI-TOF	Matrix-assisted laser desorption ionization-time of flight
PXRD	Powder X-ray diffraction
DSC	Differential scanning calorimetry
TGA	Thermogravimetric analysis
CV	Cyclic voltammetry
DPV	Differential pulse voltammetry
IR	Infra-red
IPCE	Incident photon-to-current conversion efficiency
EIS	Electrochemical Impedance Spectroscopy
DCM	Dichloromethane
DMF	N,N-Dimethylformamide
THF	Tetrahydrofuran
CH <sub>3</sub> CN	Acetonitrile
TBP	Tert-butyl pyridine
AcOH	Acetic acid
PCC	Pyridiniumchlorochromate
BuOH	Butanol
PhCH <sub>3</sub>	Toluene
CDCl <sub>3</sub>	Chloroform- <i>d</i>
DMSO- <i>d</i> <sub>6</sub>	Dimethyl sulfoxide- <i>d</i> <sub>6</sub>
MeOH- <i>d</i> <sub>4</sub>	Methanol- <i>d</i> <sub>4</sub>
g	Grams
h	Hours
M <sup>+</sup>	Molecular ion
min	Minute
mg	Miligram
mL	Milliliter
I <sup>-</sup> /I <sub>3</sub> <sup>-</sup>	Iodide/triiodide
FTO	F-doped SnO <sub>2</sub>
TiO <sub>2</sub>	Titanium dioxide
CDCA	3 $\alpha$ ,7 $\alpha$ -dihydroxy-5 $\beta$ -cholic acid
V <sub>oc</sub>	Open-circuit voltage
J <sub>sc</sub>	Short-circuit photocurrent density

$\eta$	Solar cell efficiency
PCE	Power conversion efficiency
$E_{CB}$	Conduction band edge
$\tau$	Electron lifetime
$R_{ct}$	Charge transfer resistance
$C_{\mu}$	Capacitance
$\mu$	Charge carrier mobility
HMDS	Hexamethyldisilazane
OTS	Octadecyltrichlorosilane
MHz	Megahertz
ppm	Parts per million
Å	Angstrom
$\lambda$	Wavelength
eV	Electron volt
°C	Degree Celsius
min	Minute(s)
h	Hour (s)
br	Broad
CuPc	Copper phthalocyanine

---

## GENERAL REMARKS

1. All solvents were distilled and dried before use.
2. Organic layers after every extraction were dried over anhydrous sodium sulfate.
3. Column Chromatography was performed over silica gel (60-120 & 230-400 mesh).
4.  $^1\text{H}$  and  $^{13}\text{C}$ NMR spectra were recorded on AV 200 MHz, AV 400 MHz and AV 500 MHz Bruker NMR spectrometers. All chemical shifts are reported in  $\delta$  ppm downfield to TMS and peak multiplicities are referred as singlet (s), doublet (d), triplet (t), quartet (q), pentet (p), and multiplet (m).
5. HRMS data were recorded on a Thermo Scientific Q-Exactive, Accela 1250 pump.
6. MALDI-TOF mass spectra were obtained from ABSCIEX TOF/TOF<sup>TM</sup> 5800 mass spectrometer using 2,5-Dihydroxybenzoic acid and  $\alpha$ -Cyano-4-hydroxycinnamic acid; as matrix.
7. UV-Vis absorption spectra were recorded at room temperature in quartz cuvette using Analytik Jena UV-Visible spectrophotometer.
8. Cyclic voltammetry experiments were performed on BioLogic potentiostat (model no: SP300).
9. *J-V* characteristics of the cells were measured using Keithley digital source meter (2420, Keithley, USA) controlled by a computer and standard AM 1.5 solar simulator (PET, CT200AAA, USA). To measure the photocurrent and voltage, an external bias of AM 1.5G light was applied using a xenon lamp (450 W, USHIO INC, Philippines).
10. IPCE measurements were carried out with a Newport QE measurement kit by focusing a monochromatic beam of light from 300 W Xe lamp onto the devices.
11. Electrochemical impedance spectroscopy (EIS) measurements of the DSSCs were recorded with a Bio-Logic potentiostat (model no: SP300), equipped with an FRA2 module.
12. OCVD profile was measured with a Bio-Logic potentiostat (model no: SP300), equipped with an FRA2 module,
13. TGA analysis was done using PerkinElmer STA 6000 simultaneous thermal analyzer at a heating rate of  $10\text{ }^\circ\text{C min}^{-1}$ .
14. Differential scanning calorimetry (DSC) was conducted on a TA Instruments Q10 DSC, under nitrogen at a heating/cooling rate of  $5\text{ }^\circ\text{C/min}$ .
15. Powder X-ray diffraction (PXRD) patterns were recorded on a PANalytical X'PERT PRO instrument using iron-filtered Cu  $K\alpha$  radiation ( $\lambda = 1.5418\text{ \AA}$ ).
16. Bottom-gate bottom-contact field-effect transistors substrates were purchased from Fraunhofer IPMS (interdigitated S/D electrodes), with channel lengths (L) 2.5, 5, 10 and 20  $\mu\text{m}$  and channel width (W) of 10 mm. OFET measurements were performed on Agilent 4156C semiconductor probe analyzer and semi probe station.

## ABSTRACT

This thesis entitled “**Heterotriangulene Based Hemicyanine and Squaraine Dyes for Dye-Sensitized Solar Cells and Field Effect Transistors**” consists of five chapters.

### Chapter I: Introduction

**A) Dye-sensitized solar cells (DSSCs):** DSSCs have received considerable attention as a new generation of photovoltaic devices because of their high incident-solar-light-to-electricity conversion efficiency, low cost of production with environmentally friendly characteristics, and it has shown great potential as alternatives to traditional silicon solar cells. There are different types of dyes have been developed and utilized as sensitizers, such as metal-organic complexes, metal-free organic dyes, Zn-porphyrin, and Zn-phthalocyanine dyes. Some basic structural features are required for the application in highly efficient DSSCs, such as the suitable position of HOMO-LUMO energy levels, reduced dye aggregation, efficient injection of the generated electrons into TiO<sub>2</sub> electrode and efficient regeneration of oxidized dyes. Herein, the main focus is to synthesize organic dyes with different types of molecular design and characterize the DSSCs device performance.

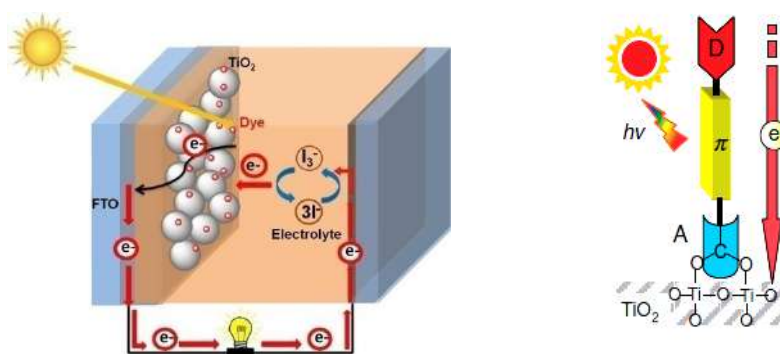


**Figure 1.** a) Schematic working principle of a DSSCs and b) Schematic drawing of D- $\pi$ -A type organic dye.

Hemicyanine and squaraine dyes have attracted special interest because of their intense absorption in the far-red and near-infrared (NIR) regions, and high molar extinction coefficient ( $10^4$  - $10^5$  M<sup>-1</sup> cm<sup>-1</sup>) compared to zinc-porphyrin dyes. Still this dye gives poor efficiency because of aggregation on the metal oxide surface that reduces the excited state lifetime, and leads to inefficient power conversion.

The planarity of an organic dye is one of the most important factors for obtaining high molar extinction coefficient ( $\epsilon$ ), and intramolecular charge transfer (ICT). Among so many aspects, focus on planarity and the donating ability of donors is highly preferable. A donor group



affects the absorption spectra, adjusts the energy levels of the sensitizer and suppresses the charge recombination. A planar heterotriangulene (HT) donor system was incorporated into donor- $\pi$ -acceptor DSSCs to achieve better electron injection. It also increases the electronic coupling between donor and acceptor moieties of the dye, and localizes the positive charge resulting after electron injection. After introduction of a planar rigid moiety, dyes tend to assemble via  $\pi$ - $\pi$  stacking while anchoring on  $\text{TiO}_2$ . In order to avoid the dye-dye interaction, suitably functionalized indolium moiety with in-plane and out-of-plane alkyl groups has been integrated with the hemicyanine and squaraine dyes.

**B) Organic Field Effect Transistors (OFETs):** OFETs have attracted interest due to their advantages such as light weight, low-cost, flexibility and easy fabrication make them highly promising for electronic paper, sensors, RFID and organic displays. Mostly, small organic molecules or conjugated polymers are suitable organic semiconductors for OFET applications. In the bottom-contact configuration, the gate electrode is situated on the substrate; a silicon wafer functions as both substrate and gate. The thermally grown silicon dioxide is used as dielectric which is situated on top of gate electrode. The organic semiconductor deposited on a dielectric is contacted with two metal contacts, namely, the source and drain (**Figure 2**).

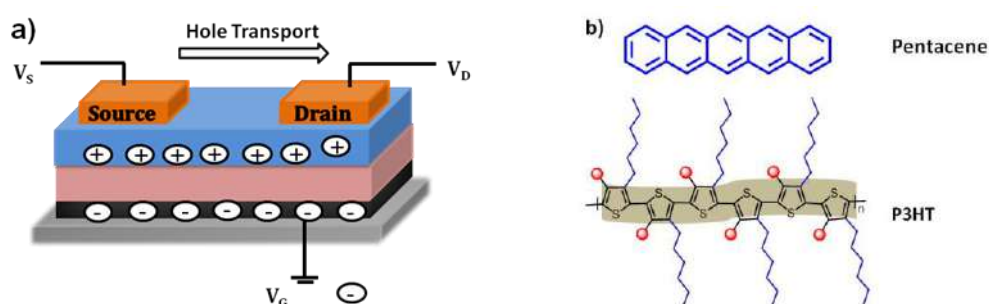


**Figure 2.** a) Schematics of bottom contact OFET configuration and b) Pentacene small molecule and P3HT polymer is a representative compound for organic semiconductors.

Small molecules have the advantage that they order themselves very well due to their crystallinity in the solid state. This generally leads to high charge-carrier mobility, as the mobility depends on the intermolecular interactions and the relative position of the  $\pi$ - $\pi$  orbital. The packing mode of the organic semiconductors becomes very important for the charge transport between molecules. For this reason, HT-squaraine based and HT-hexacyano based small molecules synthesized to investigate the effect of structural variations on the material properties as well as the performance.

## Chapter II: Heterotriangulene Based Unsymmetrical Squaraine Dyes for Dye-Sensitized Solar Cells

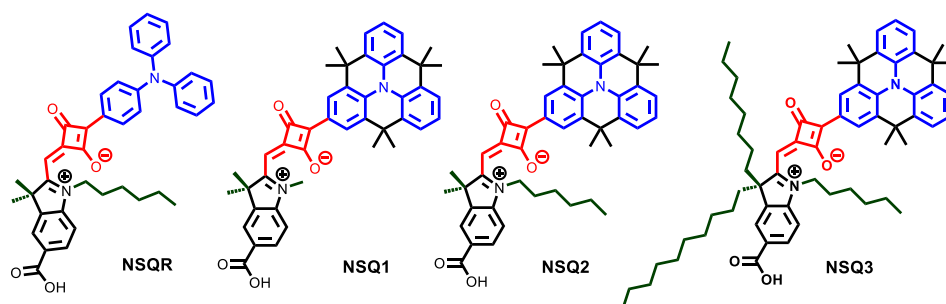


**Figure 3.** Molecular structures of HT-based **NSQR** and **NSQ1-3**.

Triphenylamine (**NSQR**) and heterotriangulene (**NSQ1-3**) based unsymmetrical squaraine sensitizers, for dye-sensitized solar cells (DSSCs) have been designed and synthesized (**Figure 3**). The synergistic effect of HT moieties on extending the conjugation and avoiding the dye aggregations by in-plane and out-of-plane alkyl groups played constructive roles in achieving high PCE efficiency. Heterotriangulene based **NSQ1-3** sensitizers have shown significant improvement in PCE compared to **NSQR**; the **NSQ3** sensitized device achieved an efficiency of 6.73% without a co-adsorbent, and in the presence of CDCA, **NSQ2** and **NSQ3** exhibited 7.4% and 7.17% PCE, respectively. **NSQ1-3** showed higher and broader IPCE due to extended conjugation and strong donor-acceptor coupling shows the better NIR light harvesting efficiency of these metal free dyes than **NSQR**. Electrochemical impedance spectroscopy (EIS) and open-circuit voltage decay measurement (OCVD) studies proved that an alkyl-functionalized indolium unit attached to carboxylic acid suppresses the undesirable charge recombination and prolongs the electron lifetime.

## Chapter III: Heterotriangulene Based Unsymmetrical Hemicyanine Dyes for Dye-Sensitized Solar Cells

The molecular structure of donor part and alkyl functionalities plays an important role to enhance the  $J_{sc}$  and  $V_{oc}$  of D-A hemicyanine ionic dyes, respectively. By connecting a strong HT donor the photo response of sensitizers can extent towards NIR and also increases the injection efficiency, which in turn improves  $J_{sc}$ . The electronic levels, corresponding photophysical properties, and conversion efficiencies of D-A type hemicyanine dyes were systematically investigated. These dyes are designed by adopting two different donors and varying the alkyl functionalities on acceptor unit for controlling the dye aggregation on  $TiO_2$  surface (**Figure 4**).

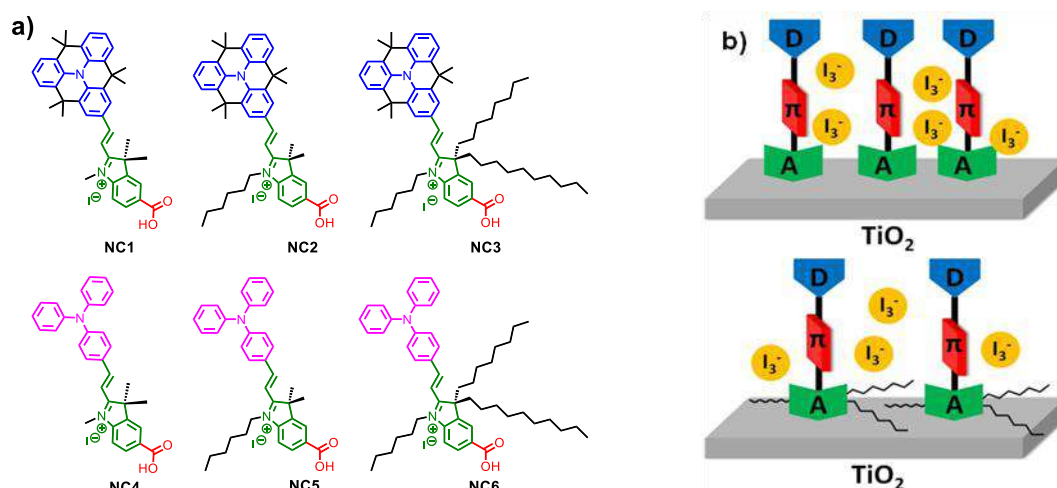


**Figure 4.** a) Molecular structures of HT-based **NC1-3** and TPA-based **NC4-6** hemicyanine dyes and b) Pictorial presentation of dye configuration with and without alkyl chain.

The planar and more conjugated structure of HT is beneficial to the harvest longer wavelength photons, which reflects the higher IPCE response in **NC1-3** than **NC4-6**. The **NC3** sensitized cells showed photovoltaic efficiency of 4.57% without co-adsorbents. Predominantly in hemicyanine dyes, the dipole moments point from dyes to  $\text{TiO}_2$  (vertical) upon dye adsorption which influences a conduction band shift and affects the  $V_{OC}$ . The molecular engineering of D-A dye using strong donor and out-of-plane alkyl functionalities brings an upward shift in  $E_{CB}$  of  $\text{TiO}_2$  which is clearly explained by large charge transfer resistance and a longer injected electron lifetime for HT-NC sensitized cells.

#### Chapter IV: Effect of $\pi$ -spacer and Alkyl Chains on Molecular Orientation, Photophysical and Photovoltaic Properties of Heterotriangulene Based Squaraine Dyes for Dye-Sensitized Solar Cells

A new type of squaraine dyes having HT donor followed by  $\pi$ -spacer (dihydroxybenzene) and the alkyl functionalities on acceptor unit have been designed and synthesized (**Figure 5**). The electronic levels, photo-physical properties and other properties of **HBSQ1-3** dyes have modulated by addition of  $\pi$ -spacer. Here the dihydroxy group is to stabilize the SQ unit and to modulate the injection and regeneration over-potential. Furthermore, benzene group extends conjugation and hence beneficial to the harvest longer wavelength photons. **HBSQ1** dye ( $\eta = 5.4\%$ ) showed better photovoltaic performance than **HBSQ3** ( $\eta = 3\%$ ). **HBSQ3** dye showed different type of orientations on  $\text{TiO}_2$  surface favoring the charge recombination that can affect the PCE. Further EIS studies have been carried out to understand the charge

transfer dynamics at TiO<sub>2</sub>-dye-electrolyte interface. Emission studies on TiO<sub>2</sub> and Al<sub>2</sub>O<sub>3</sub> have been carried out to understand the charge injection efficiency in TiO<sub>2</sub> film.

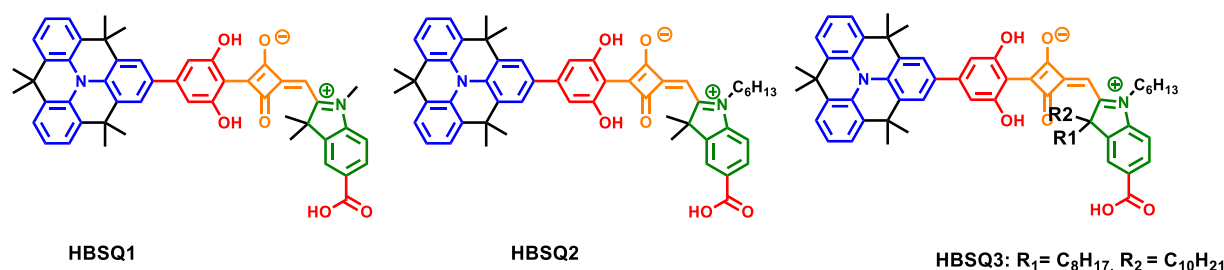


**Figure 5.** Molecular structures of HT-based **HBSQ1-3**.

## Chapter V: Molecular Engineering of Heterotriangulene Based Small Molecules for Organic Field Effect Transistors

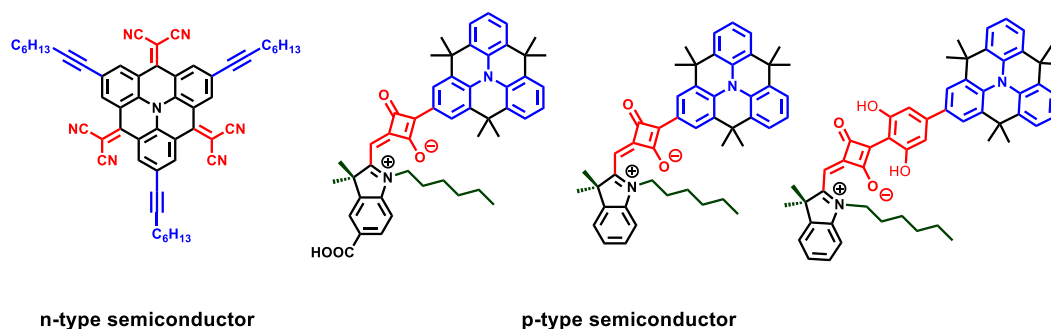


**Figure 6.** Molecular structures of HT-based small organic semiconductors.

As HT moiety offers a planar structure, a series of HT-squaraine based and HT-hexacyano based small molecules have been synthesized for the application of OFETs (**Figure 6**). Planar HT moiety was suitably functionalized with electron deficient –CN groups and systematically incorporated the low-band gap squaraine molecules to understand the structure and charge carrier mobility relationship. The mobility depends on the intermolecular interactions and on the processability of the compounds from solution. The planar HT structure and alkyl chain increases intermolecular interactions, the solubility and also the higher order of the molecules in solid-state structure gives optimal film formation. All of these molecules were investigated for their charge-carrier mobility in FET configuration. HT-squaraine based molecules showed hole transfer mobility in the range of  $10^{-5} \text{ cm}^2 \text{ V}^{-1} \text{ s}^{-1}$  and HT-hexacyano based molecules showed electron transfer mobility of  $10^{-2} \text{ cm}^2 \text{ V}^{-1} \text{ s}^{-1}$ . The substituent's (–OH or –CN or squaraine units) have a surprising effect on the polarity of the charge carried through the molecule for the application of a OFETs.



# CHAPTER I

---

**Introduction A) Dye-Sensitized Solar Cells**

**B) Organic Field Effect Transistors**

## Section A: Dye-Sensitized Solar Cells

### 1.1 Global energy demand

Energy is a vital requirement for humankind; it is available from different sources such as oil, coal, wind, the sun, water, natural gases and biomass. These sources mainly used to generate the electricity for homes, schools, businesses and industries.<sup>1</sup> As per continues development of world in technology and economy, there is constant increasing the demand for additional energy.<sup>2</sup> At the same time growing population (world's population is projected to increase by around 1.5 billion people to reach nearly 8.8 billion people by 2035) is going to demand for considerable amount of energy over the period.<sup>3</sup> Many developing countries will cause strong growth in energy demand with increasing standards of living and population growth. Over 70% of the increased energy demand is from developing countries, led by China and India.<sup>4,5</sup>

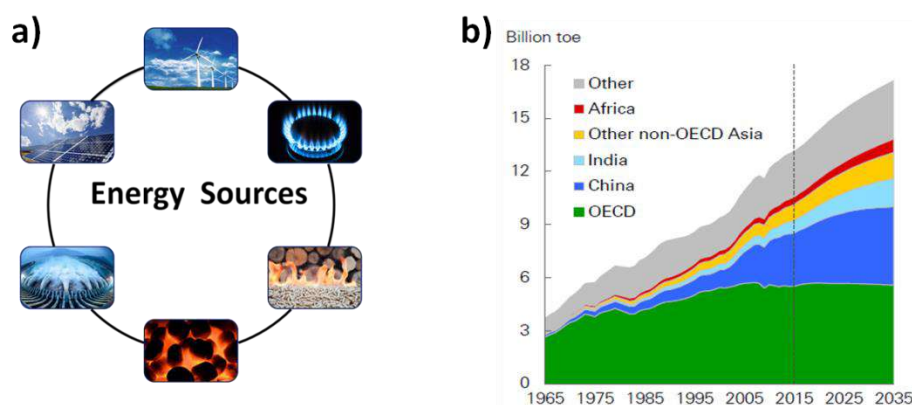


**Figure 1.** a) Different forms of energy sources and b) Energy consumption by region [BP Statistical Review of World Energy 2017].

Primary energy sources are transformed in energy conversion processes to more convenient forms of energy that can directly be used by society, such as electrical energy, refined fuels, or synthetic fuels such as hydrogen fuel.<sup>6</sup> In World Energy Outlook 2013, from 2000 to 2010 total world primary energy demand grew by 26%, and electricity growth is about double this. In the past electricity demand almost doubled from 1990 to 2011, and is projected to grow 81% from 2011 to 2035 (from 19,004 TWh to 34,454 TWh) in the Current Policies scenario, and 69% (to 32,150 TWh) in the central new policies scenario. Electricity demand is very high in Asia, projected to average 4.0% or 3.6% per year. So the energy demands become high priority to address as currently some two billion people have no access to electricity.<sup>3</sup>

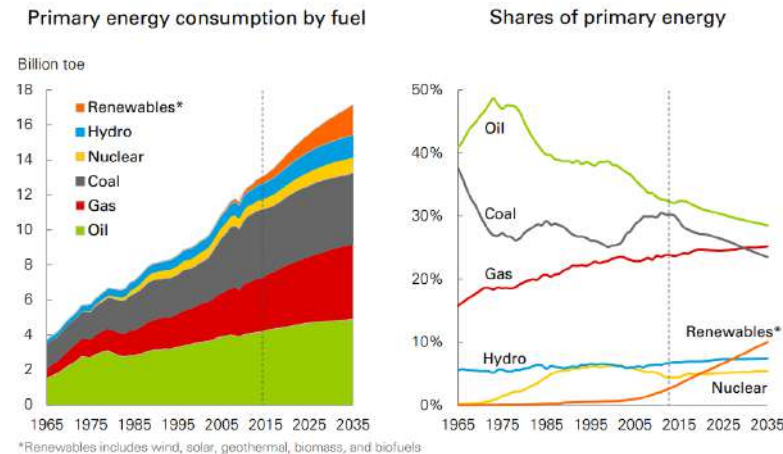


**Figure 2.** Primary energy consumption by fuel-past and future prediction (Source: BP Statistical Review of World Energy 2017).

The energy economy is always dependent on three forms: fossil fuels-oil, natural gases and coal, this covers more than 85% of the total energy production. Non-renewable energy sources are remain the central to powering the world economy, accounting for more than three-quarters of total energy supplies in 2035 (down from 85% in 2015). Now days, renewable energy sources are growing faster (7.1% p.a.), with its share in primary energy increasing to 10% by 2035, up from 3% in 2015.<sup>7</sup>

## 1.2 Renewable energy



**Figure 3.** Renewable energy sources: hydropower, wind energy, geothermal energy and solar energy.

Renewable energy is generated from natural sources. There are five main types of renewable resources that we use for energy. Wind is harnessed from Earth's natural weather.

Hydropower generally comes from flowing rivers and from dams. Solar energy comes from the Sun's light and radiation. Biomass comes from burning plants, plant waste or fuel made from plants. Geothermal energy is collected from the heat produced by the hot dry rocks, and magma. This energy can be generated again and again as and when needed. They are available in plenty and by far most the cleanest sources of energy available on this planet. The sun, wind, geothermal, ocean energy are existing in the abundant quantity and free to use.<sup>8,9</sup>

### **1.2.1 Hydroelectric power**

Hydro energy is a very clean and green technology which produces no pollution. Hydro energy is energy captured from the energy of falling water or fast running water. It is sometimes called hydroelectric power because the water is used to turn turbines that create electricity. When in use, electricity produced by dam systems does not produce green house gases. They do not pollute the atmosphere. The main drawback of hydropower is the construction of dams is extremely expensive and must be constructed to a very high standard.

### **1.2.2 Wind energy**

This is generated by using air flow through wind turbines. A wind turbine basically converts the kinetic energy in the wind into mechanical power. For specific tasks such as pumping water or grinding grain this mechanical power is used and it can convert this mechanical power into electricity to power homes, businesses, schools etc. Wind is a clean source of power, but it requires large, sometimes noisy blades to operate. The wind strength varies from zero to storm force and it is not constant every time. It means wind turbines do not produce the same amount of electricity all the time. There will be times when they produce no electricity at all.

### **1.2.3 Geothermal energy**

This energy comes from the Earth in the form of water or steam. The water is replenished by rainfall and the heat is continuously produced inside the earth. The Earth's interior is extremely hot enough to melt the rock that comes out of a volcano in the form of lava. This heat creates hot water and steam below the Earth's surface, which can be harnessed by digging a well. As the steam or water rises, it can be used to run a turbine and create electricity. Geothermal energy, although sounding feasible and compatible, involves huge investments to assess the feasibility of setting up a geothermal plant. Also, it has issues such as poisonous gas escape into the atmosphere, earthquakes and landslides.

### 1.2.4 Biomass energy

This energy comes from organic material after the plant material and animal waste burned as fuel. Wood is one of the major sources of biomass energy, when biomass is burned; the chemical energy in biomass is released as heat. It can be grown and burned for fuel. Another large source is waste, which can come from garbage or the waste from manufacturing. Some cars now run on a biofuel called ethanol, which is created from crops. And this ethanol can be mixed with gasoline and used in cars. Biomass energy suffers from the same major problem as fossil fuels: it must be burned and can be harmful to the environment. But it is considered as less polluting than fossil fuels. It can help to reduce the use of other non-renewable energy sources.

The idea of drawing energy from the above mentioned renewable sources is beneficial. These sources can never be exhausted, and do not emit greenhouse gases. But capturing these resources is expensive, and many are intermittent, which complicates using them on a large scale.<sup>10</sup> Considering all the above mentioned facts and figures, solar energy is the best alternative clean renewable energy source.

**1.2.5 Solar energy** is an energy that comes from the sun. Everyday sun sends out tremendous amount of energy in the form of heat and radiations called solar energy. The radiation of the sun is captured in solar panels that are exposed to sunlight. The sunlight converts into electrical energy to power all the appliances in a home. It can also be used to heat a house and to create hot water. Solar energy is a limitless source of energy which is available at no cost.<sup>11</sup>

### 1.3 Why solar energy?

The Sun continuously irradiates the Earth, with an energy intensity of  $1.2 \times 10^5$  TW, whereas the current worldwide energy consumption is just 12 TW, which is only 0.001% of the energy that we receive from the Sun. The Sun provides the Earth in one hour with as much energy as all mankind uses in one year. The solar energy has major benefit over other conventional power generators in which sunlight can be directly harvested into solar energy with the use of small and tiny photovoltaic (PV) solar cells.<sup>12</sup> The annual average solar energy density lies in a range from 100-250 W m<sup>-2</sup> for most locations around the globe, so there is sufficient solar energy available to meet all our demands.<sup>13</sup> Electricity generation from solar energy basically can be done by two methods, which are photovoltaics and concentrated solar power system. Photovoltaics (PV) refer to the production of a voltage or electricity from the photons of sunlight. It is a direct method, in which a semiconductor

substrate generates the electrons, upon excitation with photons of sufficient energy.<sup>14</sup> A concentrated solar power system is an indirect method, in which a large portion of sunlight is focused into a small beam, to generate large amounts of concentrated heat. This concentrated heat is used to heat the working fluid in a conventional power plant.<sup>15</sup>

### 1.3.1 The solar radiation

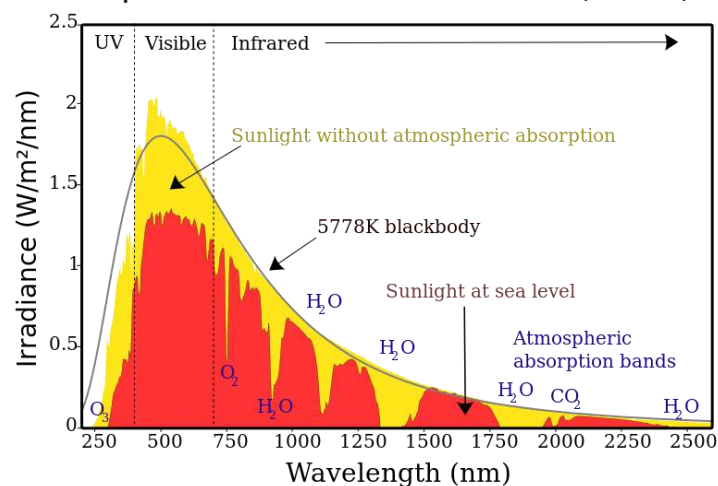


**Figure 4.** Solar irradiance spectrum above atmosphere and at surface.

Sunlight is a portion of the electromagnetic radiation released by the Sun. The energy in solar irradiation comes in the form of electromagnetic waves of a wide spectrum. The spectrum can be depicted in a graph, the spectral distribution, which shows the relative weights of individual wavelengths plotted over all wavelengths, measured in  $W / m$  (wavelength). The Sun emission wavelength range covers the ultraviolet (UV), visible and infrared (IR) regions of electromagnetic spectrum, with a maximum peak at around 500 nm. Its spectrum is similar to that of a blackbody at 5778 K and it is influenced by the absorption of some molecules present in the atmosphere, such as  $O_3$ ,  $CO_2$  and  $H_2O$ . The peak of the spectrum is within the visible spectrum, but still significant amounts of shorter and longer wavelengths are present.<sup>16</sup> The solar spectrum at the Earth's surface depends on a large number of factors, including latitude, altitude, time of year and also weather. As the sunlight travels through the atmosphere, chemicals interact with the sunlight and absorb certain wavelengths changing the amount of short-wavelength light reaching to the Earth's surface. The solar spectrum is characterized by air mass coefficient, after solar radiation has travelled through the atmosphere. The air mass coefficient tells the direct optical path length through the Earth's atmosphere, expressed as a ratio relative to the path length vertically upwards, i.e. at the zenith (solar zenith angle of  $z = 48.2^\circ$ ). At AM 1.5 G condition, 1 sun is defined as equal to  $100 \text{ mW/cm}^2$  of irradiance.<sup>17</sup> The most commonly used spectrum is the Air Mass 1.5

Global (AM 1.5G), which according to ASTM G-173-03 (standard reference spectra) represents the sun at its zenith on a clear day.<sup>18</sup>

#### 1.4 Photovoltaic electricity production using solar energy- History and present scenario

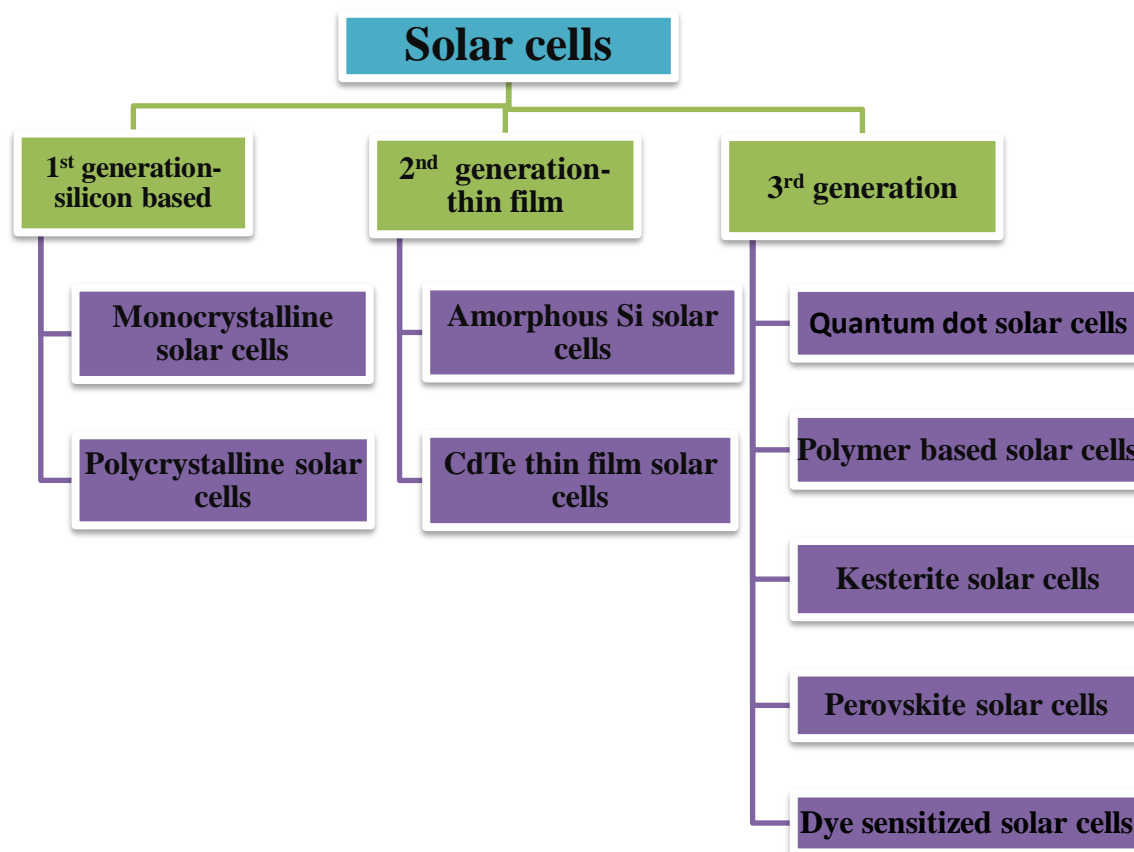


**Figure 5.** Classification of solar cells.

The present trend of using photovoltaics for electricity generation is increasing steadily all over the world. The photovoltaic effect was discovered as early as 1839 by Becquerel; this is the basic principle for the working of a solar cell.<sup>19</sup> In 1954, the first practical photovoltaic cell was developed at Bell Laboratories.<sup>20</sup> Over the years, solar cells have seen many improvements by developing newer technologies. Broadly, solar cells can be classified into three generations.

##### 1.4.1 First generation solar cells

The first silicon solar cells were developed by Chaplin, Fuller and Pearson in which they have used p-n junction silicon strips to convert solar light to electricity and achieved an efficiency of 4%. Si semiconductor as the substrate material is the most widely used solar cells mainly due to the high efficiency, long life time and availability in the market. The band gap of silicon is 1.1 eV, which makes it good semiconductor for solar cell applications. Monocrystalline Si solar cells showed highest efficiency of 24% whereas polycrystalline Si



showed a lower efficiency, of around 19.5%. The main reason for the lower efficiency in polycrystalline solar cells as compared to monocrystalline solar cells is attributed to the crystal defects. Furthermore, the Shockley-Queisser limits the maximum efficiency of Si solar cell that can be reached to 33.7% under AM 1.5G.<sup>21</sup> For this reason, a further increase in the efficiency with the first generation technology is not possible. Si solar cell requires huge amounts of Si for the large scale application, so there is increasing chemical hazards to the environment during Si processing. Hence, the second generation solar cells were designed and developed mainly with the goal of replacing silicon and finding cost-effective materials for solar cells.

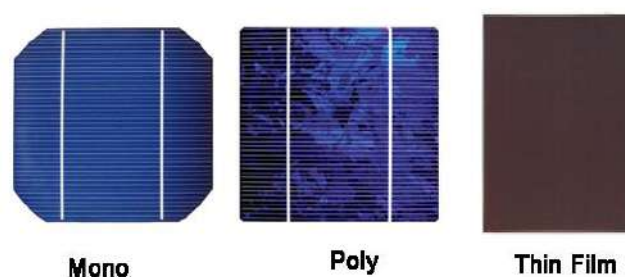


**Figure 6.** First generation solar cells (monocrystalline and polycrystalline Si solar cell) and Second generation solar cells (thin film Si solar cells).

#### 1.4.2 Second generation solar cells

The second generation solar cells were fabricated by Carlson and Wronski of RCA Laboratories, USA in 1976. They are credited with the fabrication of the first amorphous Si solar cell. The second generation solar cells are also known as thin film technology. Amorphous Si has a band-gap of 1.7 eV so they can deliver more voltage than a crystalline Si solar cell. There are other promising semiconductor materials for thin film technologies include cadmium telluride, (CdTe) gallium arsenide (GaAs) or copper indium (gallium) selenide (CIS/CIGS), etc. The band-gap of the CdTe is 1.44 eV, CIS and GaAs are 1 eV and 1.43 eV, respectively.<sup>22</sup> In thin film technologies, materials can be deposited sequentially on cheap substrates, like glass/plastics with very small amounts of material (generally 1-2 mm thick). Hence, this second generation solar cells uses film with a thickness range varies between nanometers to a few micrometers opens a way for multi-junction devices. Several p-n junctions can be formed, with varying substrate materials, harvesting light in a wider range of energies, thus increasing the cell efficiency. However, the cost of second generation solar cells is lower than that based on crystalline Si. However, a solar cell with CdTe has serious disposal problems.<sup>23</sup> It is highly poisonous and hence it is an environmental hazard. CIGS

contains indium, which is a rare earth metal, whose reserves are very limited in the Earth's crust. Hence, the third generation solar cells were designed to replace second generation solar cells of CdTe and CIGS, with cheaper wide band-gap metal oxide semiconductors, like  $\text{TiO}_2$ ,  $\text{SnO}_2$ ,  $\text{ZnO}$ ,  $\text{Nb}_2\text{O}_5$ , etc.

### 1.4.3 Third generation solar cells

Silicon has several physical barriers which limit their efficiency and also use of traditional solar cells. There is current research is going on for developing newer solar cells that are less expensive, flexible, compact, light weight, and efficient. There is need to find alternative materials that can be able to harness solar energy. Third generation solar cells uses organic materials such as small molecules or polymers, they offer very high possibilities for improving charge generation, separation, molecular mass, band gap, molecular energy levels, rigidity, and molecule-to-molecule interactions. Solar cells made up of organic or polymer materials are extremely light weight and flexible making them easy to work with and combine with other molecules. Third generation solar cells are the new promising technologies which is also powered by nanomaterials.<sup>24</sup> Third generation solar cell are classified into this different types of solar cells a) Quantum dot based solar cells b) Polymer based solar cells c) Kesterite solar cells d) Perovskite solar cells e) Dye-sensitized solar cells.

#### 1.4.3a Quantum dots (QD) solar cells

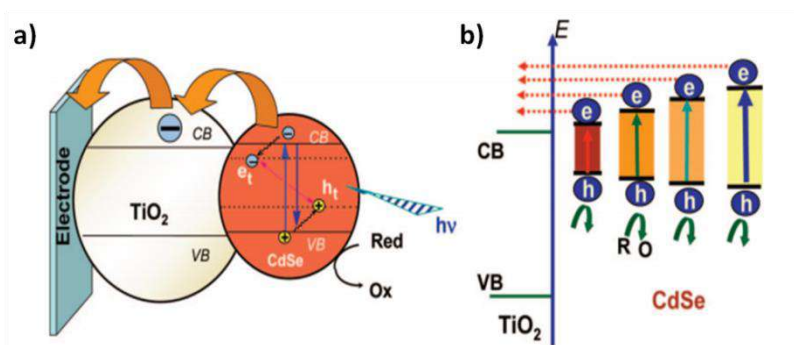


**Figure 7.** a) Charge injection mechanism of excited CdSe quantum dot into  $\text{TiO}_2$  nanoparticle and b) Scheme shows the modulation of energy levels by size control.<sup>25</sup>

Quantum dot based solar cells have drawn so much of interest due to the possibility of boosting the solar cell efficiency beyond the Shockley and Queisser limit of 33.7% for Si based solar cells.<sup>25</sup> QD solar cells use transition metal groups as semiconductors which are in the size of nanocrystal range. Quantum dots is having crystal size ranging typically within a few nanometers in size, for example, porous  $\text{TiO}_2$ , which are frequently used in QD. These nanocrystals of semiconducting material are designed to replace the semiconducting material

in bulk state such as Si, CdTe or CIGS with the advance of nanotechnology.<sup>26</sup> The nanocrystals are mixed into a bath and coated onto the Si substrate; due to their centrifugal force generally crystals rotate very fast and flow away. Generally in conventional silicon semiconductor solar cells a photon will excite an electron there by creating one electron-hole pair.

### 1.4.3b Polymer Solar Cells

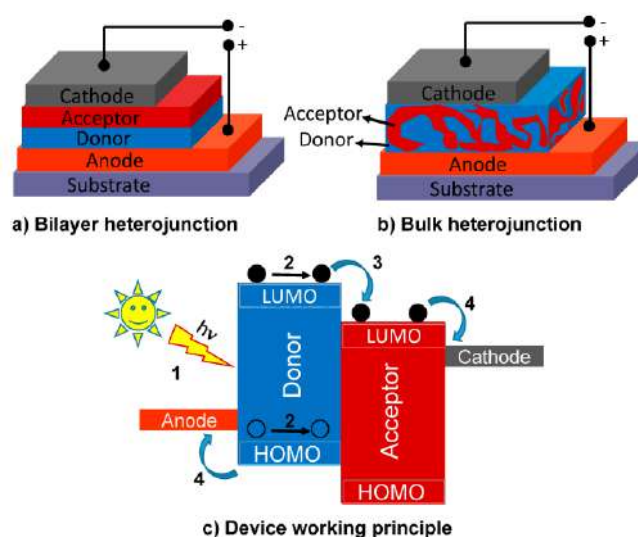


**Figure 8.** Schematic of polymer solar cells (DA-type).<sup>29</sup>

Polymer solar cells composed of a serially connected thin functional layer coated on a polymer foil or ribbon. It works usually as a combination of donor (polymer) and an acceptor (fullerene). Polymer solar cells and other organic solar cells operate on same principle known as the photovoltaic effect. Photovoltaic conversion processes in polymer solar cells follows this sequential processes:<sup>27</sup> (1) absorption of an incident photon leading to the formation of polymer singlet excitons; (2) diffusion of the excitons to a donor/acceptor interface; (3) charge transfer at the interface determined by either the LUMO-LUMO or HOMO-HOMO energy offsets of the donor and acceptor polymers, followed by dissociation of the interfacial charge transfer; and (4) then charge transport to the anode and cathode through bicontinuous networks of donor (hole-transporting) and acceptor (electron-transporting) polymers. It involves the transformation of the energy occurs in the form of electromagnetic radiations into electrical current. It is flexible solar cells due to the polymer substrate. As a result, polymer solar cells open a gateway for new applications in the formation of stretchable solar devices including textiles and fabrics.<sup>28</sup>

### 1.4.3c Perovskite Based Solar Cell

Perovskite Based Solar Cells use a hybrid organic-inorganic lead or tin halide-based material. These materials have the generic form  $ABX_3$  and the same crystallographic structure as perovskite (the mineral) where X represents a halogen such as  $I^-$ ,  $Br^-$ ,  $Cl^-$  and A and B are cations of different size.<sup>30</sup> In perovskite solar cells, the band gaps of these materials are easily tunable and can be optimized by altering the halide content in the film for the solar spectrum. Perovskite solar cells are a recent discovery among the solar cell research community and their efficiencies have increased from 3.8% in 2009 to 22.7% in late 2017.<sup>31</sup> It possesses several advantages over conventional silicon and thin film based solar cells. Perovskite materials such as methylammonium lead halides are very cheap to produce and simple to manufacture. Conventional Si based solar cells are more expensive, they require multiple processing steps and high temperatures ( $> 1000\text{ }^\circ\text{C}$ ). Still perovskite solar cells are suffering due to their stability and durability issues. The perovskite material degrades over time, and hence a drop in overall efficiency.

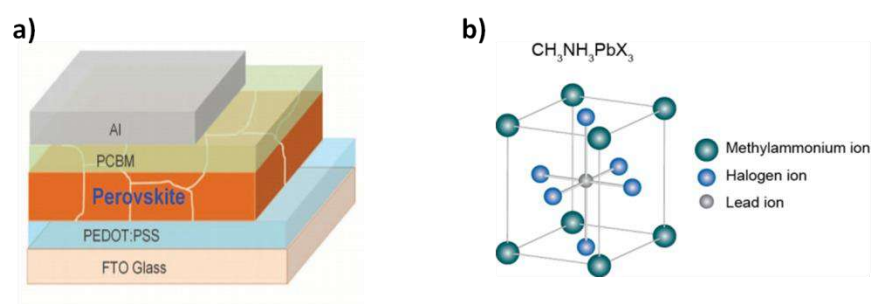


**Figure 9.** a) Planar device configuration of perovskite solar cells and b) Perovskite crystal structure (right).<sup>30</sup>

### 1.4.3d Kesterite-based solar cells

Kesterite-based solar cells have created a centre of attention in recent years, on account of their reduced toxicity and larger availability of their constituent elements.<sup>32</sup> These solar cells are based on the kesterite mineral structure, including  $Cu_2ZnSnS_4$  (CZTS),  $Cu_2ZnSnSe_4$  (CZTSe), and their alloys  $Cu_2ZnSn(S_xSe_{1-x})_4$  (CZTSSe). The first vacuum-deposited CZTS solar cell was reported by Katagiri et al. with a power conversion efficiency of 0.66% in 1997.<sup>33</sup> The current record CZTSSe cell efficiency of 12.6% was reported in 2013.<sup>34</sup> The most successful procedure to prepare CZTS(e) thin films in terms of solar cell efficiency is a liquid-based process where all constituents are dissolved in a hydrazine solution which is spin coated onto a molybdenum-coated glass substrate followed by a short annealing to  $540\text{ }^\circ\text{C}$  on a hot plate.<sup>35</sup> The comparatively low efficiency of kesterite-based solar cells is ascribed to a

large discrepancy in the open-circuit voltage ( $V_{OC}$ ) relative to the band gap of the absorber layer.

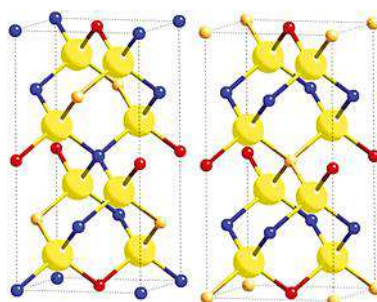


**Figure 10.** Kesterite (left) and stannite (right) structure; large yellow spheres: S and Se; small spheres: blue, Cu; yellow, Zn; red, Sn.<sup>36</sup>

### 1.4.3e Dye-sensitized solar cells (DSSCs)

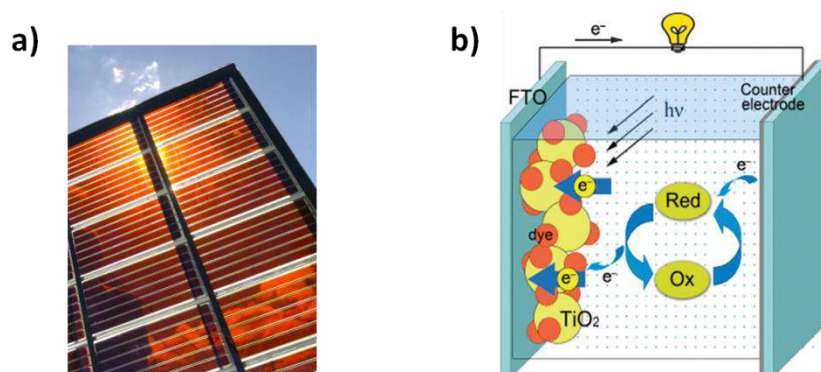


**Figure 11.** a) Dye-sensitized solar panel and b) Schematic working principle of DSSCs.<sup>39</sup>

Dye-sensitized solar cells (DSSCs) are recently developed technology which belongs to the third generation of photovoltaics. These solar cells are more beneficial because of their easy fabrication, high efficiency and low cost. DSSCs is a promising photovoltaic technology for solar energy-to-electricity conversion.<sup>37</sup> They can offer high flexibility and environmental friendly character. The solar-to-electrical energy conversion efficiencies recorded for DSSCs are still lower than those measured for Si-based solar cells. There is potential for the improvement of their efficiency, with the implications of nanotechnology. DSSCs technology is mimicking natural photosynthesis in a low-cost and easily manufacturable way. For DSSCs, the construction and working principle is quite different to the conventional first and second generation solar cells.<sup>38</sup>

For solar power system, the initial installation cost is high. Last 20 years, the price per kW h of electricity produced by photovoltaics has reduced from around \$500 to \$5. Electricity produced by solar power required cost per kW h is still higher than conventional sources, like

coal and nuclear.<sup>40</sup> Photovoltaics and concentrated solar power system are main two technology used for electricity generation from solar energy. These both systems need great attention for the widespread commercialization of solar cell technologies. Their working principle and manufacturing technologies vary greatly from Si solar cells. Even though third generation solar cells have not reached the practical efficiency levels of Si solar cells, but still they possess great potential with the use of nanotechnology.

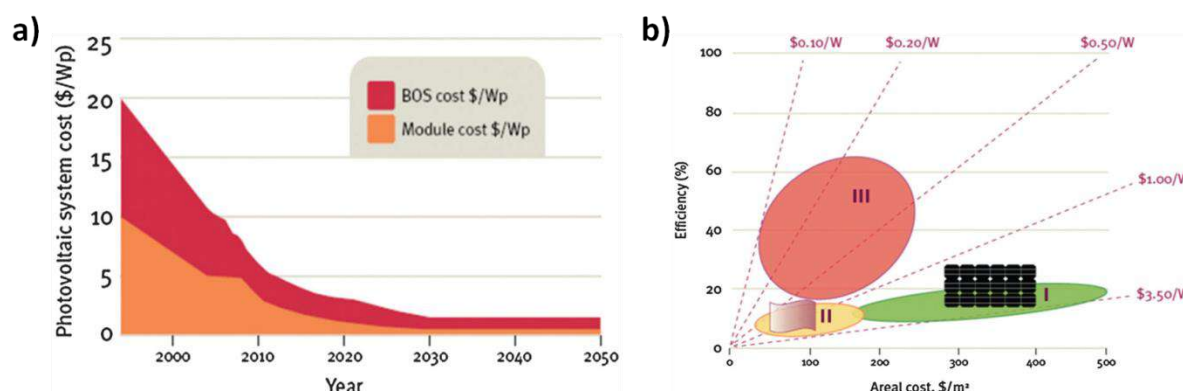


**Figure 12.** a) Price Vs Efficiency among the different generation's solar cells and b) Reduction in the costs of photovoltaic devices. The balance of system (BOS) includes all the components of a solar PV system, except the module.<sup>41</sup>

In current scenario, advanced research is being carried out all over the world, with the aim of the effective commercialisation of these solar cells. For this reason, third generation solar cells aim for a further reduction in the cost and a higher efficiency in comparison to the first and second generation solar cells. It is known that for first generation devices the state-of-the-art efficiency was reached almost ten years ago, while research on second and third generations is presently in progress, thus demonstrating the interest in finding some possible low cost competitors to Si-based solar cells.<sup>41</sup>

### 1.5 Dye-sensitized solar cells (DSSCs)

DSSCs are a new type of photovoltaic technology, it is considered to be a credible alternative to conventional inorganic silicon-based solar cells. Since the pioneering report by O'Regan and Grätzel in 1991, DSSCs has attracted considerable and sustained attention as it offers the possibility of low-cost conversion of the photo energy with a dramatic increase in the light-harvesting efficiency.<sup>42</sup> To date, a DSSCs with ruthenium complex dyes gives efficiency ( $\eta$ ) record of  $> 11\%$ . Enormous effort is also being dedicated to develop efficient dyes, for their reduction in cost, ease of synthesis, large molar extinction coefficient and long-term stability. Metal-free dyes or organic dyes meet all these criteria. Therefore, there has been remarkable



development in organic dyes for DSSCs in recent years and efficiencies exceeding 12% have been achieved using dyes which have broad, red-shifted, and intense spectral absorption in the visible light region (400-800 nm).<sup>43</sup>

The device structure of DSSCs is shown in **Figure 13**. DSSCs devices are composed of a transparent conducting oxide (TCO) substrate, a mesoporous semiconductor ( $\text{TiO}_2$ ) film adsorbed with photosensitizer dyes, an electrolyte layer containing a redox couple, and a counter electrode. After absorption of a photon of a particular energy, a sensitizer molecule which is adsorbed on the  $\text{TiO}_2$  semiconductor surface becomes oxidized. The electron from the highest occupied molecular orbital (HOMO) of dye is excited to the lowest unoccupied molecular orbital (LUMO), from where it is transferred to the CB of the semiconductor. The injected electrons after flowing through the thin mesoscopic semiconductor film are collected by the conducting substrate and flow into the external circuit. Simultaneously, the ground state of the dye is regenerated by the electrolyte ( $\text{I}^-/\text{I}_3^-$  redox couple) to give efficient charge separation. The oxidized species in the electrolyte is regenerated by the reduction of triiodide at the counter electrode after receiving the external circuit electrons to complete the whole circuit. These a cycles are keep on repeating without any material being consumed but energy being transformed from light to electricity.<sup>38</sup>

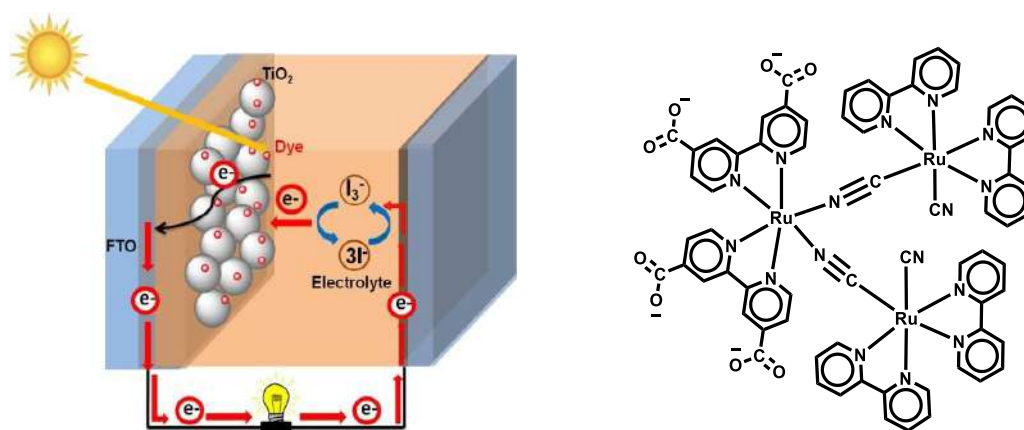


**Figure 13.** a) Basic structure of DSSCs and b) Ruthenium-based dye with first highest efficiency in 1991.

The photo-electrochemical processes in DSSCs occur in a particular sequence, which can be expressed as in the following sections.



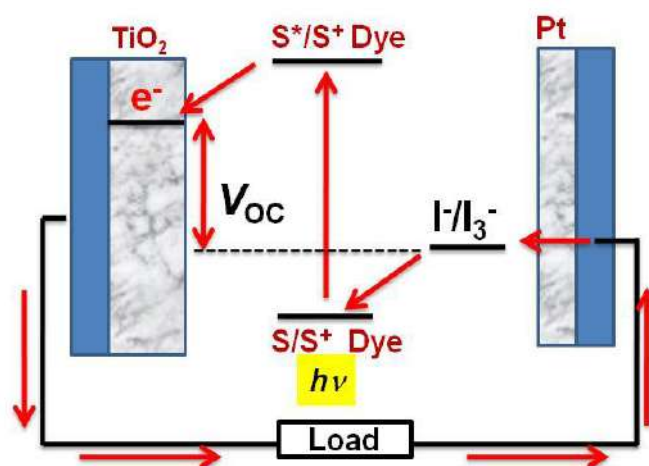


**Figure 14.** Main processes in dye-sensitized solar cells.

### 1.5.1 Working of DSSCs

#### i) Sunlight absorption and electron excitation in dye molecule

The Photons of energy equal to or more than the energy gap of the dye molecule produce an effective excitation of an electron in the dye molecule. This energy in the form of light promotes an electron from the HOMO to the LUMO. The electrons in the LUMO state are less bound to the dye molecule. Thus, the photon absorption by the dye molecule depends on the energy difference between these two energy levels i.e. band gap (**Figure 14**).

#### ii) Electron injection to TiO<sub>2</sub> and the charge separation

The interfacial electron transfer occurs between LUMO state of the dye and conduction band (CB) of TiO<sub>2</sub> through the interfacial bonds between the dye and the TiO<sub>2</sub>. The electrons is collected in the CB of each TiO<sub>2</sub> and then transported all along the semiconductor film effectively, without recombination to the electrolyte or other dye molecules. Also, for the electrons injection into the CB of TiO<sub>2</sub> required the higher LUMO energy level of the dye molecule than the CB. The charge separation is managed by kinetic competition of the electron transfer. After transportation in CB of each TiO<sub>2</sub>, the electrons are finally collected by the transparent conductive film on the electrode.

#### iii) Redox reaction by the electrolyte and at the counter Electrode

The oxidized dye molecules bonded to the TiO<sub>2</sub> nanoparticles are immediately reduced by the electrolyte, in the order of nanoseconds. The typically used electrolytes are I<sup>-</sup>/I<sub>3</sub><sup>-</sup> redox couple in organic solvent. The reduction of the oxidized dye by iodide produces triiodide and the triiodide diffuses to the counter electrode and accepts electrons from the external load by regenerating iodide. The electrons flowing from the transparent conductive film on the anode

to the external load are collected back at the counter electrode. The potential difference across the cell ideally depends on the Fermi level and electrolyte redox potential. The open circuit voltage,  $V_{OC}$  is theoretically determined by the difference between the fermi-level of  $TiO_2$  and the electrolyte anion energy level, typically it is around 0.5-0.7 V.

#### iv) Charge recombination

The recombination reactions are determined by the probability of photoelectrons recombining back with the electrolyte or dye molecule. These reactions reduce the solar cell efficiency of DSSCs. These reactions usually occur at adjacent  $TiO_2$  in the semiconductor layer during the transport of electrons in the CB of  $TiO_2$ . The recombination process occurs to dye molecules is in the range of micro to milliseconds, whereas the recombination to the electrolyte is in the order of millisecond to seconds.<sup>44</sup>

### 1.5.2 Components of DSSCs

DSSCs are composed of five major components (**Figure 15**), namely a transparent conductive substrate, a nanostructured n-type semiconductor, a dye-sensitizer to absorb light, an electrolyte, which creates the interface with the semiconductor and a counter electrode, facilitating the transfer of electrons between them and a counter electrode carrying an electrocatalyst to facilitate the electron transfer from the external load to the counter electrode.<sup>45</sup>

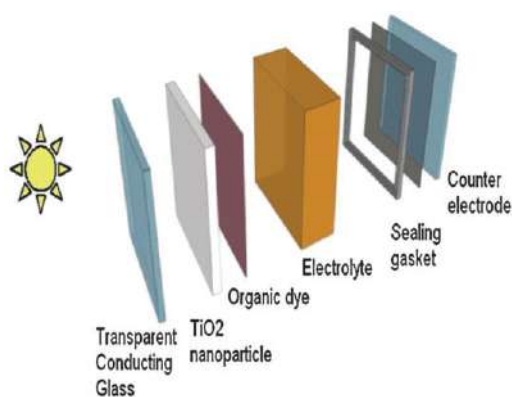


**Figure 15.** Schematic diagram showing the main components of DSSCs (from Y. Jiao, F. Zhang and S. Meng, *Dye Sensitized Solar Cells Principles and New Design*, Solar Cells – Dye-Sensitized Devices, Prof. Leonid A. Kosyachenko (ed.), InTech, 2011, ISBN: 978-953-307-735-2)

#### 1.5.2.1 Transparent conducting substrate

For DSSCs, clear and transparent conducting glass substrates are commonly used as the base substrate. The ideal substrate should be highly transparent in the visible, infrared and far-

infrared regions, stability even at high temperatures around 500 °C and also should be chemically inert so that it should not react with the chemicals and electrolyte system of the DSSCs. The bottom side glass substrate which is facing away from the Sun is coated with a transparent conductive layer usually indium-doped tin oxide (ITO) or fluorine-doped tin oxide (FTO). For flexible substrates, plastic has been widely studied as an alternative.<sup>46</sup> These flexible DSSCs are widely used in many applications, like windows, laptop bags, etc.

### 1.5.2.2 Semiconductor material

As semiconductor material, a variety of metal oxides, such as TiO<sub>2</sub>, ZnO, SnO<sub>2</sub>, Nb<sub>2</sub>O<sub>5</sub>, etc. can be used for DSSCs. These materials are wide band-gap semiconductors. To excite an electron to the conduction band in these semiconductors required photon energy is more than that for Si. In DSSCs, the most commonly used semiconductor material is TiO<sub>2</sub> due to their advantages over other materials, mainly an excellent thermal stability. It is resistant to the chemicals or an electrolyte used in DSSCs and non-toxic. TiO<sub>2</sub> is having more benefit which includes its cost-effectiveness and abundance. The most common crystalline form used in application to solar cells is the TiO<sub>2</sub> anatase form (**Figure 16**). The anatase form has higher electron conductivity compared to the rutile form.<sup>47</sup> Compared to the LUMO of the dye molecule, the CB of TiO<sub>2</sub> is lower in energy. The chemical bonding between them facilitates the injection of an electron from the dye LUMO level into the CB of the TiO<sub>2</sub>. The band-gap of anatase TiO<sub>2</sub> is 3.2 eV this means that only a small fraction of the entire solar spectrum is utilized for the electron excitation. It is required to the dye molecules to sensitize the semiconductor material in the visible and infrared regions.

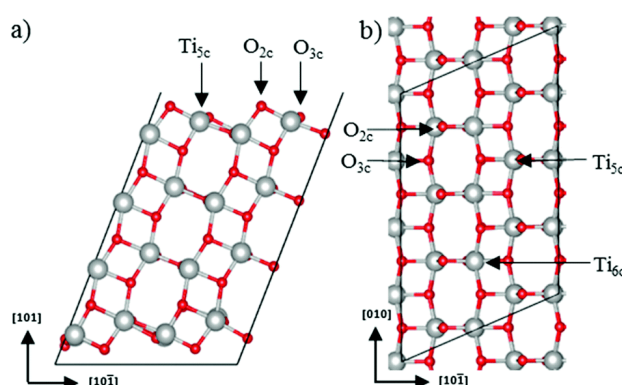


**Figure 16.** a) Side and (b) Top views of the anatase TiO<sub>2</sub> (101) supercell.

### 1.5.2.3 Dye-sensitizer

In DSSCs, the dye plays the most important role for sensitizing the semiconductor to allow absorption in the visible and infrared regions of the solar spectrum. The dyes act as the light

harvesting antennae which are essential for efficient light harvesting and electron generation/transfer. Several requirements have to be met for the efficient dye, such as broad absorption spectrum from visible to NIR regions, good stability, good matching of the HOMO and LUMO levels of the dye with the semiconductor's CB, and the chemical potential of the redox system of the electrolyte. Additionally, an ideal sensitizer has to absorb all the light below a threshold wavelength. Also dye should have a strong bonding with the TiO<sub>2</sub> nanoparticles for an effective electron injection into the CB of TiO<sub>2</sub>, with a quantum yield close to unity.<sup>48</sup>

#### 1.5.2.4 Electrolyte

The electrolyte is one of the key components for facilitating the electron transfer mechanism and kinetics in DSSCs. After flowing through the thin mesoscopic semiconductor film, the electrons flows to the external circuit are collected at the counter electrode. The excited dye molecules come to the ground state by the electrolyte by accepting these electrons. The extent of the recombination losses occurring in DSSCs decides the kinetics of the charge transfer. The electrolyte can be broadly classified into three types; liquid electrolyte, solid electrolyte and quasi-solid electrolyte. Mostly studied liquid electrolyte is I<sup>-</sup>/I<sub>3</sub><sup>-</sup> redox couple in a volatile organic solvent, like acetonitrile, propionitrile, methoxyacetonitrile, and methoxypropionitrile, which offer a high ion conductivity and high dielectric constant. By using the liquid electrolyte of I<sup>-</sup>/I<sub>3</sub><sup>-</sup> in a volatile organic solvent the efficiency obtained is higher. The cationic size plays an important role in the improving efficiency of the solar cell, however small cations, such as Li, show a better performance.<sup>49</sup>

#### 1.5.2.5 Counter electrode

The main role of the counter electrode is to collect the electrons from the external load and efficient reduction of the redox electrolyte in addition to finishing the cell fabrication. This electrode is coated with a conductive film, which acts as the electrocatalyst for enhancing the transport of the electrons into the cell. Platinum (Pt) is mostly used as the conducting film as counter electrode. However, other conductive materials are also used due to high cost of Pt for example graphite, graphene, activated carbon, poly(3,4-ethylenedioxythiophene) (PEDOT), polypyrrole, and polyaniline used as good alternatives, though with a little decrease in the efficiency.<sup>50</sup>

### 1.6 Organometallic and Metal-Free Organic Dyes

Up to now, there are several dye designs have been developed and applied as sensitizers, such as metal-organic complexes, metal-free organic dyes, Zn-porphyrins, and Zn-

phthalocyanines. The most successful organometallic dyes in DSSCs are Ru polypyridyl dyes which exhibit superior performances owing to the broad light absorption capability expanding to the NIR region. They are well known for their appropriate HOMO and LUMO energy levels applying to the TiO<sub>2</sub>-iodide system, a long-lived photo-excited state, high molecular stability, and rich structural variation. In Ru polypyridyl complexes, the HOMO is localized on the Ru and electron donating ligands, and the LUMO is distributed over the polypyridyl ligand. The distribution of HOMO and LUMO is favourable for efficient electron injection into TiO<sub>2</sub> via chemical bonding and the regeneration of oxidized dyes.<sup>38</sup>

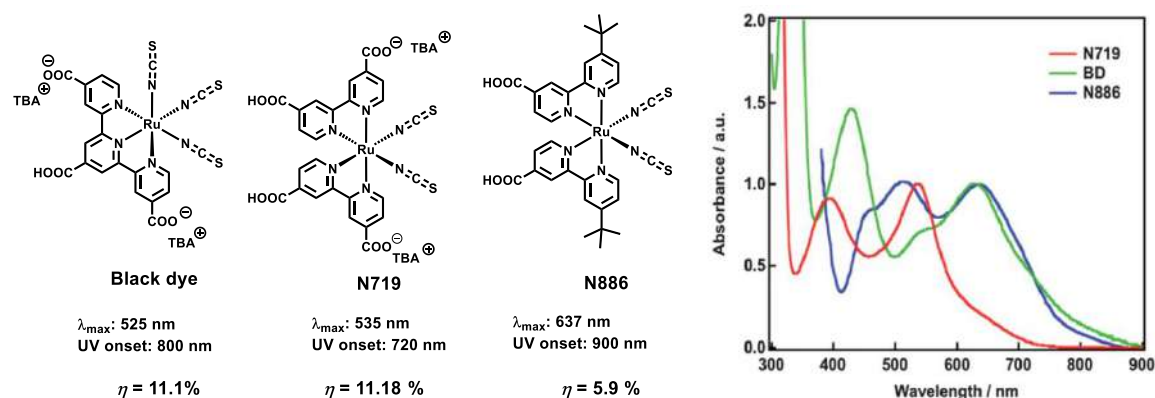


**Figure 17.** Molecular structures and Normalized absorption spectra (by <sup>1</sup>MLCT bands) of Ru–NCS<sub>x</sub>–polypyridyl (red: N719 dye, green: black dye, and blue: N886).

The absorption peak showed in the visible-NIR region is related to singlet to singlet metal-to-ligand charge transfer (<sup>1</sup>MLCT) from Ru to the polypyridyl ligand. Ru-based sensitizers (N719) have strong visible absorption, long excitation lifetime and efficient metal-to-ligand charge transfer with the current maximum cell level efficiency of 11.2%.<sup>51</sup> For the Ru polypyridyl dyes, the molar extinction coefficient of the MLCT band in visible-NIR spectral region is generally lower compared with those of organic dyes.<sup>52</sup> Even though, Ru-based dyes show good efficiencies but limited for commercial use in DSSCs. Ru is a rare earth metal and also toxic. Hence, investigations for the use of cheaper, eco-friendly and metal-free organic dyes have been made.

### 1.6.1 Metal-Free Organic Dyes

In DSSCs, the most of these organic dyes have been designed with an electron donor- $\pi$ -electron acceptor (D- $\pi$ -A) configuration for facilitating photo-induced charge separation (**Figure 18**). Along with this configuration, different design and other configuration of organic sensitizers have been proposed in the last decade. In recent years, the development of

DSSCs based on organic dyes has been varied rapidly and the conversion efficiency of these cells became comparable to the cells based on polypyridyl ruthenium dyes.<sup>43</sup>

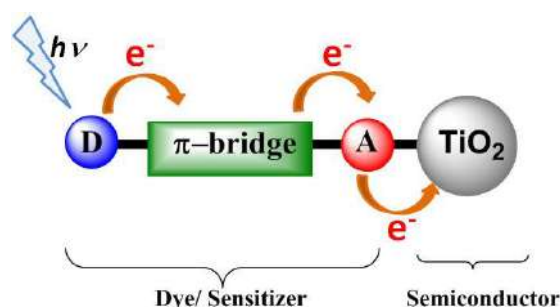


**Figure 18.** Schematic of the D- $\pi$ -A structure of an organic dye.

Metal-free organic dyes include the hemicyanine dye, squaraine dyes, thienylfluorine dye, phenothiazine dye, thienothiophene-thiophene-derived dye, phenyl-conjugated polyene dye, N,N-dimethylaniline-cyanoacetic acid, oligothiophene dye, coumarin dye, indoline dye, etc. Metal-free organic sensitizers are formed by D- $\pi$ -A character. This gives push-pull structure which can create the intramolecular charge transfer (ICT) from subunit A to D through the  $\pi$ -bridge when a dye absorbs light, it is highly important for light harvesting. It is easy to tune the absorption spectra, their HOMO and LUMO levels of the dyes by variation of the D,  $\pi$  and A moieties (**Figure 19**). A hundreds of metal-free organic dyes are designed through this variation with different photophysical, electrochemical, and other properties to act as sensitizers for DSSCs over the past ten years.<sup>39</sup>

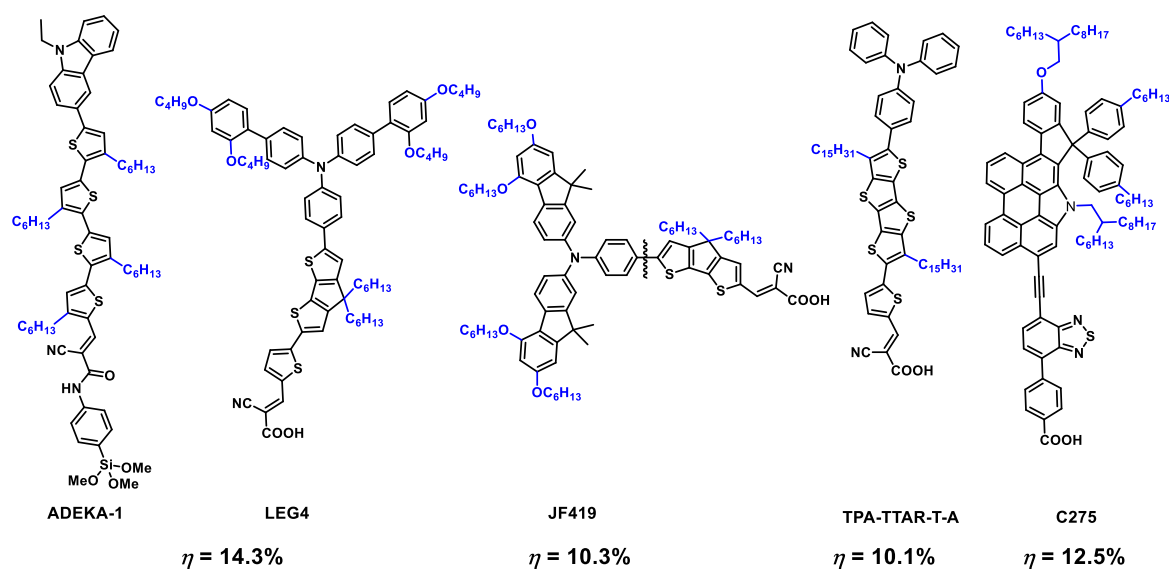


**Figure 19.** Examples of Metal-free organic dyes.

Like metal complexes, porphyrin dyes are also used in DSSCs with significant efficiencies. It is found that the NIR sensitizers such as Zinc (II)-porphyrins (ZnPor) and Zinc (II)-phthalocyanines (ZnPc) are very promising candidates (**Figure 20**).<sup>53,54</sup> The ZnPor and ZnPc dyes in their absorption spectra shows a Soret-band and Q-band at around 400–500 nm and at around 500–700 nm, respectively. They exhibit excellent molecular stability, suitable HOMO-LUMO energy levels for efficient electron injection into the conduction band of TiO<sub>2</sub> film and oxidized dye regenerations and structural flexibility. Zinc-porphyrin dyes (SM315) were reported to show a highest conversion efficiency of 13%.<sup>55</sup> However, due to the wide and planar  $\pi$ -conjugated molecular structure, they strongly aggregate even in the solution which can leads to unfavorable charge recombination.

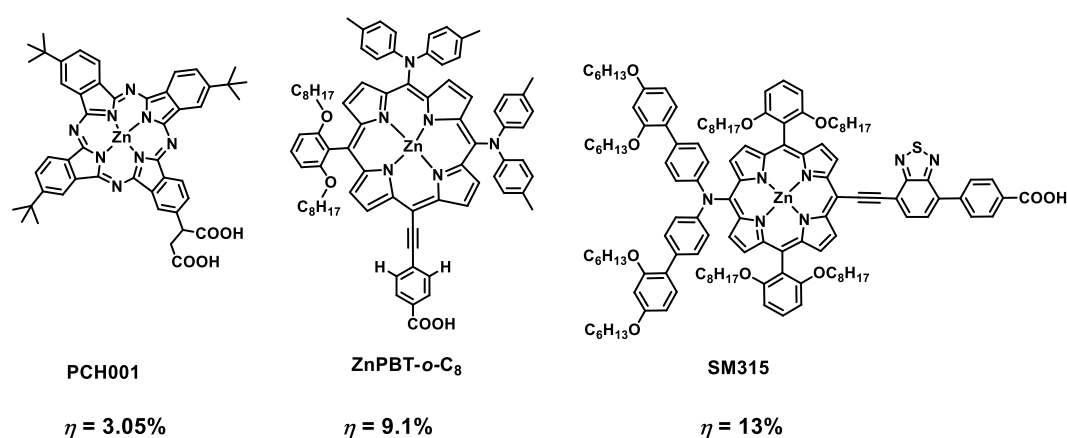


**Figure 20.** Examples of NIR absorbing Zinc-porphyrin dyes.

It is very essential to discover dyes with intense absorptions in both the visible and the NIR regions in order to efficiently absorb more solar light and obtain higher photocurrent. Organic sensitizers such as squaraine, cyanine, and merocyanine dyes have been also reported with strong and intense absorptions in both the visible and the NIR.<sup>56</sup> Cyanine dyes are cationic dyes; they have high molar absorption coefficient ( $\sim 10^5 \text{ M}^{-1} \text{ cm}^{-1}$ ) and an intense but narrow absorption band in the long wavelength region. For example, using the CM204 dye a highest efficiency of 5.5% of PCE under  $100 \text{ mW/cm}^2$  illuminations has been obtained.<sup>57</sup> However, the photovoltaic performances of DSSCs based on these dyes are quite low, as they forms aggregates upon adsorption on the TiO<sub>2</sub> surface.



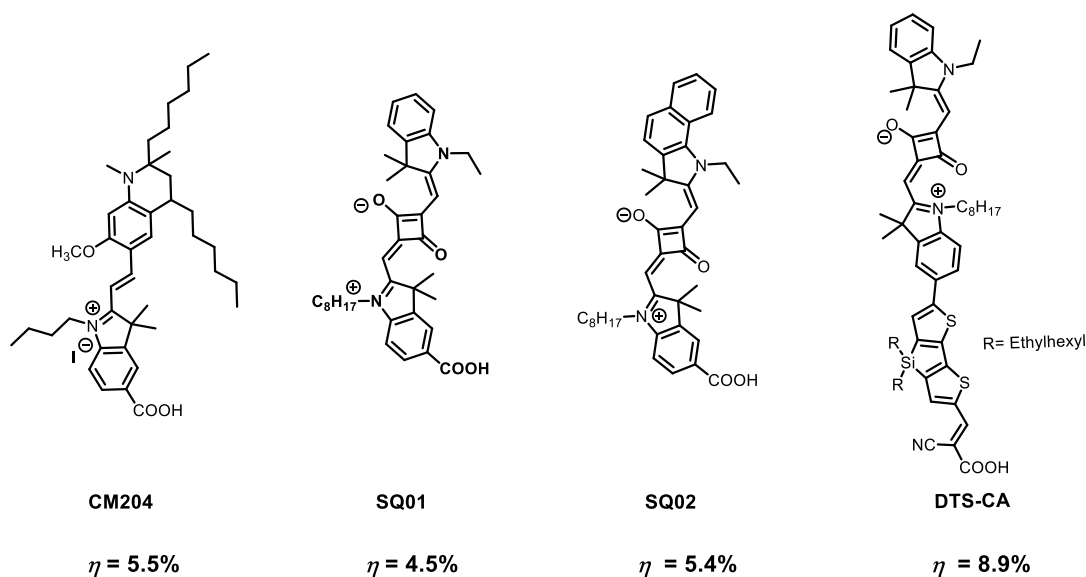


**Figure 21.** Molecular structures of NIR dye belonging cyanine and squaraine family.

Squaraines are also well-known NIR absorbing dyes for their intense absorption in the red/NIR as a result they are outstanding dyes to explore for solar cell applications. Grätzel and co-workers reported the squaraine dyes of SQ1 and SQ2 dyes which have given relatively high conversion efficiencies i.e. 4.5% and 5.4% respectively (**Figure 21**).<sup>58</sup> These NIR dye exhibits high molar extinction coefficient and strong electronic coupling with the TiO<sub>2</sub> semiconductor surface. Moreover, a highest efficiency obtained with DTS-CA unsymmetrical squaraine dyes; it is reached to 8.9% and also extended the spectrum to the near infrared region.<sup>59</sup>

## 1.7 Characterization Techniques

### 1.7.1 Device fabrication of solar cells

A transparent photo anode made of fluoride-doped tin dioxide (SnO<sub>2</sub>:F) deposited on the back of a glass plate. On the back of this conductive plate, mesoporous TiO<sub>2</sub> layer (TiO<sub>2</sub> particle size of < 20 nm) and TiO<sub>2</sub> scattering layer (TiO<sub>2</sub> particle size of 150 to 250 nm) is deposited, which forms into a highly porous structure with an extremely high surface area. This TiO<sub>2</sub> is chemically bound by a process called sintering. The working electrode was prepared by immersing the 10-12 μm (6 μm thick transparent layer +5 μm thick scattering layer) TiO<sub>2</sub> film into the dye solution for 6-12 h. After soaking the film in the dye solution, a thin layer of the dye is left covalently bonded to the surface of the TiO<sub>2</sub> via the bond that can be an ester, chelating, or bidentate bridging linkage. Then a spacer is placed around the photoanode layer, and then a drop of electrolyte is added on the active area. Devices were completed by placing the Pt counter electrode. The two plates of photoanode and counter

electrode are then joined and sealed together to avoid the electrolyte from leaking. The current-voltage characteristics of the cell are measured by Keithley digital source meter (2420, Keithley, USA) controlled by a computer and standard AM 1.5G solar simulator (PET, CT200AAA, USA). To measure the photocurrent and voltage, an external bias of AM 1.5G light was applied using a xenon lamp (450 W, USHIO INC, Philippines) and recorded the cell efficiencies.<sup>55,58</sup>

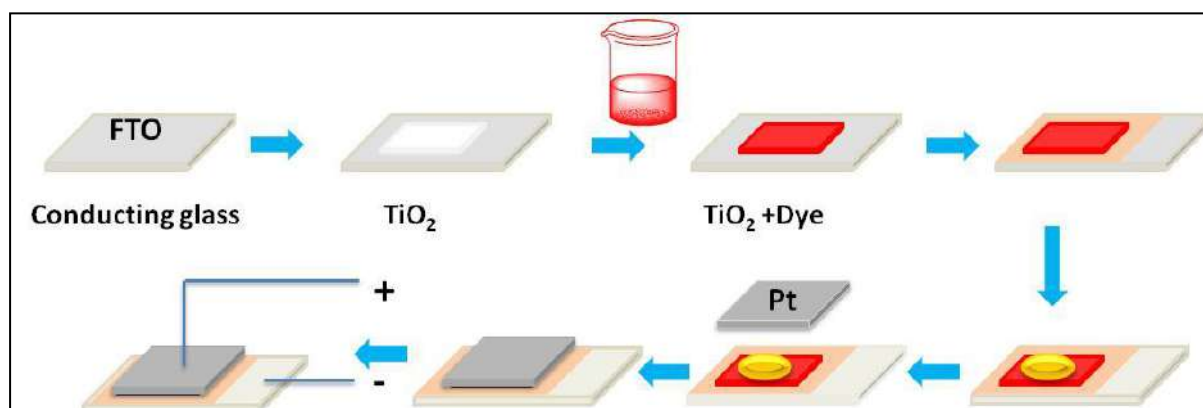


**Figure 22.** Pictorial presentation of DSSCs device fabrication.

### 1.7.2 Efficiency Measurements (*I-V*, IPCE)

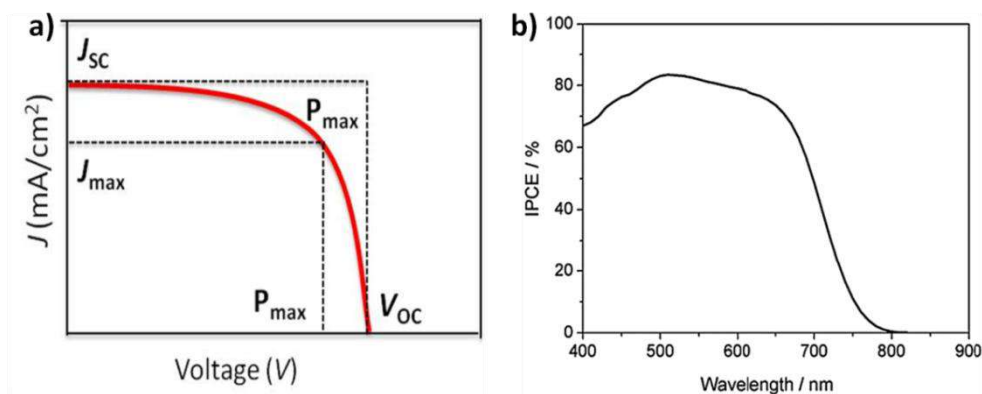


**Figure 23.** a) Typical *J-V* curve and b) Typical IPCE curve of DSSCs.

There are two extensively used techniques for photovoltaic characterizations are: current-voltage measurements under simulated sunlight (*J-V* curves) and incident photon-to-current conversion efficiency (IPCE) measurements.<sup>38</sup> The current-voltage (*I-V*) characteristics of a solar cell under illumination are used to determine the power conversion efficiency ( $\eta$ ). The photovoltaic parameters including short-circuit photocurrent density ( $J_{sc}$ ), open circuit voltage ( $V_{oc}$ ), fill factor ( $ff$ ) and overall power conversion efficiency (PCE) can be obtained by the current-voltage measurements. The standard solar spectrum used for the efficiency

measurements of solar cells is AM 1.5G irradiation, corresponding to the irradiance of 100 mW cm<sup>-2</sup>, namely,  $P_{in} = 100 \text{ mW cm}^{-2}$ .

In below equation, the  $J_{SC}$  is the photocurrent per unit area (mA cm<sup>-2</sup>) when the applied bias potential is zero and when no current is flowing through the cell, the potential equals the  $V_{OC}$ .

$$\eta = \frac{V_{OC} \times J_{SC} \times ff}{P_{in}} \dots\dots\dots (1)$$

The fill factor ( $ff$ ) is calculated using the maximum power output ( $J_{max} \times V_{max}$ ) divided by the product of  $J_{SC}$  and  $V_{OC}$ :  $ff = (J_{max} \times V_{max}) / (J_{SC} \times V_{OC})$ . The  $ff$  defines the quality of the DSSCs; it is the ratio between the areas of the two rectangles shown in **Figure 23**.

$$ff = \frac{P_{max}}{V_{OC} \times J_{SC}} \dots\dots\dots (2)$$

The spectral response of dye-sensitized solar cells is determined by measuring the monochromatic incident photon-to-current conversion efficiency (IPCE). IPCE measurements were carried out with a Newport QE measurement kit by focusing a monochromatic beam of light from 300 W Xe lamp onto the devices. IPCE is another important parameter to estimate the  $J_{SC}$ , it has to be taken into account. The IPCE value corresponds to the  $J_{SC}$  that is produced in the external circuit divided by the photon flux that strikes the cell under monochromatic illumination of the cell. A typical IPCE spectrum is shown in **Figure 23b**. Generally in DSSCs, a low IPCE value causes low  $J_{SC}$ . The IPCE is expressed by the product of the absorbed photon-to-current conversion efficiency and the light harvesting efficiency (LHE).

$$IPCE = LHE(\lambda) \Phi_{inj} \eta_{reg} \eta_{cc} \dots\dots\dots (3)$$

The LHE at the maximum absorption wavelength can be estimated using the following equation:  $LHE = 1 - 10^{-A}$ , where  $A$  is the absorbance of the dye on TiO<sub>2</sub> at the maximum wavelength. IPCE is governed by the light harvesting ability, the amount of adsorbed dyes on the TiO<sub>2</sub> surface, the overall charge collective efficiency and the overall electron injection efficiency. Generally, the maximum IPCEs for DSSCs are smaller than 90% because of the reflection and absorption loss due to the FTO glass.<sup>39</sup>

### 1.7.3 Electrochemical Impedance Spectroscopy (EIS)

EIS is a useful technique to study the kinetic processes of DSSCs.<sup>60</sup> Using this technique the several processes can be investigated such as electron transport in the mesoscopic TiO<sub>2</sub> film, electron recombination at the TiO<sub>2</sub>-electrolyte interface, charge transfer at the counter

electrode, and diffusion of the redox species in an electrolyte. This can be determined from the spectral shapes of the impedance response as a function of frequency. The impedance is described as the frequency domain ratio of the voltage to the current. The impedance measured in a wide range of frequencies, can be explained in terms of an equivalent circuit (Figure 24b) consisting of series and parallel connected elements R, C, L, and W, which is the Warburg element so as to describes diffusion processes. The Nyquist plot usually consist of three semicircles which is in the order of increasing frequency are ascribed to the Nernst diffusion within the electrolyte ( $\omega_1$ ), the electron transfer at the semiconductor/electrolyte interface ( $\omega_2$ ), and the redox reaction at the platinum counter electrode ( $\omega_3$ ).<sup>61</sup>

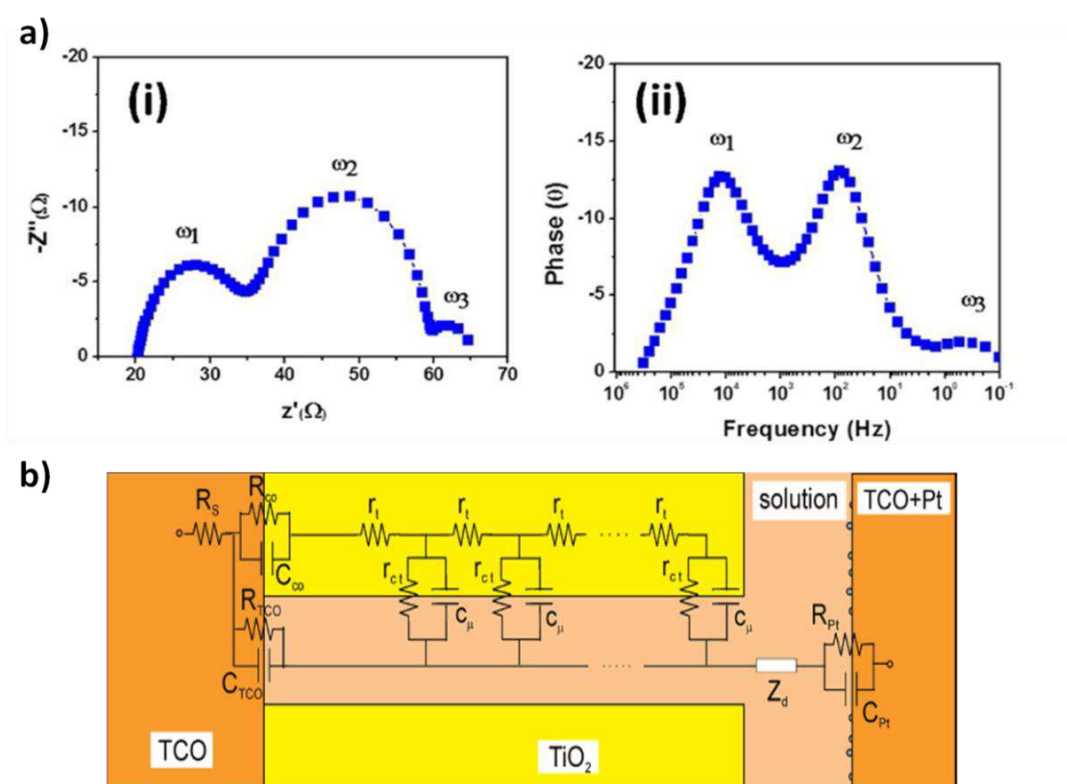


**Figure 24.** a) Typical (i) Nyquist and (ii) Bode plots of DSSCs and (b) General transmission line model of DSSCs. Adapted from reference<sup>62</sup>.

The charge transfer resistance at different interfaces in DSSCs can be easily estimated from the corresponding semicircles in the Nyquist plot whereas capacitive elements or kinetic parameters can't be obtained from the Nyquist plot. In this state, a Bode imaginary plot is the option for representing the EIS spectrum where the frequency maxima in this plot reflect the frequency maxima of the Nyquist plot. It is possible to calculate the corresponding capacitance and kinetic parameters from the frequency maxima of Bode plots.

## 1.8 Challenges and Perspectives

### 1.8.1 Dye aggregation on the semiconductor surface

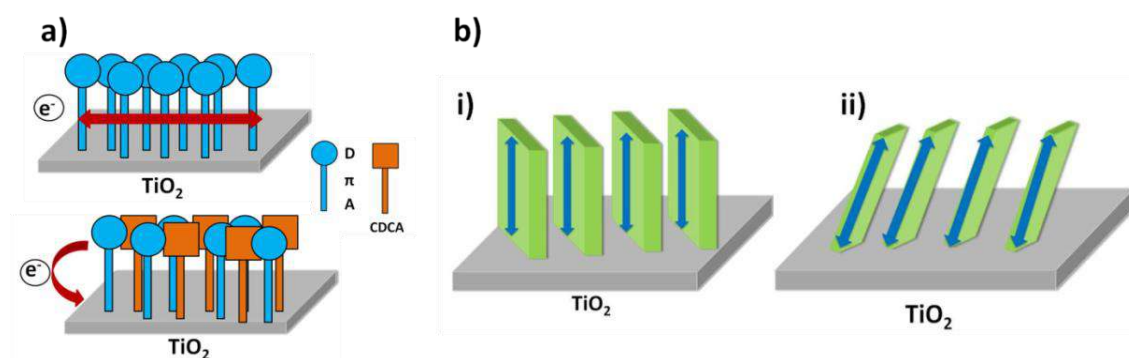


**Figure 25.** a) Schematic representation of aggregation of dyes on a  $\text{TiO}_2$  surface with and without co-adsorbents, and b) i) J-type and ii) H- type aggregation on the semiconductor surface.

The major drawbacks of D- $\pi$ -A dyes are the formation of strong  $\pi$ -stacked aggregates between dye molecules on the  $\text{TiO}_2$  surfaces. It reduces the electron-injection yields from the dyes to the CB of  $\text{TiO}_2$ , due to intermolecular energy transfer between dyes. These dye aggregation affects the directionality of electrons in the excited state of a dye through poor electronic coupling between the LUMO of the dye and the CB of  $\text{TiO}_2$ . Squaraine dyes are known to form H-aggregates, which notably affects their efficiency in DSSCs. The absorption maximum of cyanine class of dyes adsorbed on the  $\text{TiO}_2$  film is blue- or red-shifted relative to those in solution, which may be ascribed to H- or J-aggregation of the dyes on the  $\text{TiO}_2$  surface. It is known that H-aggregation cannot contribute to photosensitization usually it quenches the excited states.<sup>63</sup>

The coadsorption of CDCA with dyes has been used to avoid aggregation of dye molecules on  $\text{TiO}_2$  surface. Another approach is the introduction of sterically hindered substituents such as hydrophobic long alkyl and alkoxy chains, on the periphery of donor part or in a  $\pi$ -conjugated bridge.<sup>64</sup> The addition of CDCA or an introduction of sterically hindered substituent causes a decrease in the amount of dyes adsorbed on the  $\text{TiO}_2$  surface, resulting in a reduction of the LHE and number of injected electrons. Therefore, in DSSCs it is very important to find an efficient and convenient strategy to suppress the dye-aggregation on the  $\text{TiO}_2$  surface.

### 1.8.2 Charge recombination

The charge recombination between the injected electrons in the CB of  $\text{TiO}_2$  and the dye cations or electrolyte can seriously affects the  $J_{SC}$  value. A key loss mechanism is rate of

charge recombination between the injected electrons and the dye cation.<sup>65</sup> It depends on the molecular structures of the dyes and the molecular orientation and arrangement of the dyes on the TiO<sub>2</sub> surface. The hydrophobic group on the dye structure act as barriers to prevent hydrophilic I<sub>3</sub><sup>-</sup> ions from reaching the TiO<sub>2</sub> surface, thereby retarding charge recombination resulting in an increase in the electron lifetime ( $\tau$ ) and  $V_{OC}$  value. The charge recombination process for NIR dyes, such as squaraine, Pc, and cyanine dyes, are faster than those of typical D- $\pi$ -A dyes. It may be attributed to more positive charge density on the cationic dyes in the photo-excited state.

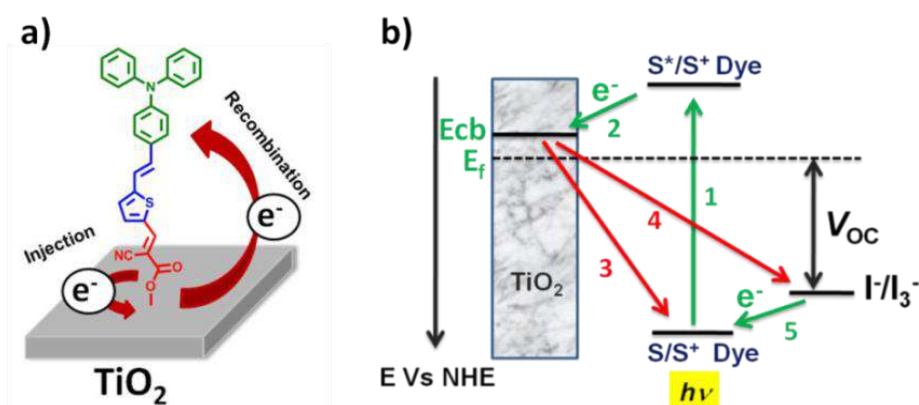


**Figure 26.** a) Pictorial presentation of charge recombination in dyes and b) Schematic diagram of the operation kinetics of DSSCs: forward electron transfer (1, 2, 5) and electron loss pathways (3, 4).

### 1.8.3 Poor optical response of the dyes in the NIR region

The  $J_{SC}$  is strongly depends on the molecular structures of dyes, their photophysical and electrochemical properties. Hence, the organic dyes with strong and intense absorptions in both the visible and the NIR regions is essentially required to cover the solar spectrum of different wavelengths to obtain higher  $J_{SC}$ . The solar light spectrum and obtained  $J_{SC}$  calculated with an assumed IPCE of 100% integrated from the UV region to the band edge of the sensitizer is represented in **Figure 27**. If the IPCE onset is reached at 800 nm,  $J_{SC}$  value of 27.3 mA cm<sup>-2</sup> can be obtained. When the IPCE onset expanded to 920 nm, the photocurrent can be achieved up to 34.7 mA cm<sup>-2</sup>. To achieve a broad light harvesting spectrum, narrow band gap is required between the HOMO and the LUMO of the sensitizer molecule.<sup>66</sup>

As a successful strategy is to improve the LHE of organic dyes, it would be very helpful to use NIR dye skeletons, which affords good absorption of light in the red/NIR region of the solar spectrum. This is mainly because of red/NIR radiation (600-1000 nm) providing about

25% of the solar energy arriving on the earth's surface whereas visible radiation (350–700 nm) provide about solar energy of 45%.

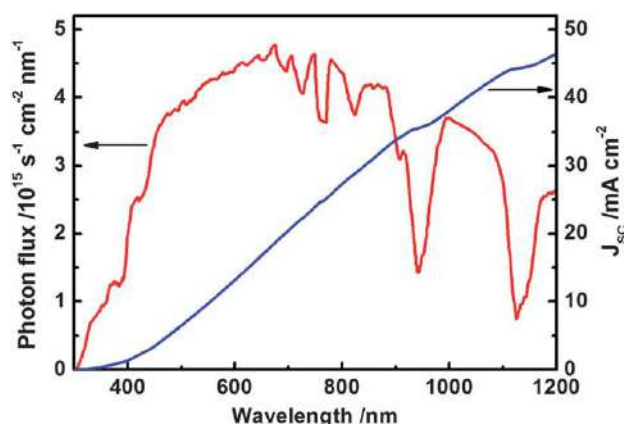


**Figure 27.** Solar light spectrum (red) and calculated photocurrent (blue) with an assumed IPCE of 100% integrated from 300 nm to the corresponding wavelength.

#### 1.8.4 Dipole moment effect on conduction band of $\text{TiO}_2$ and $V_{OC}$

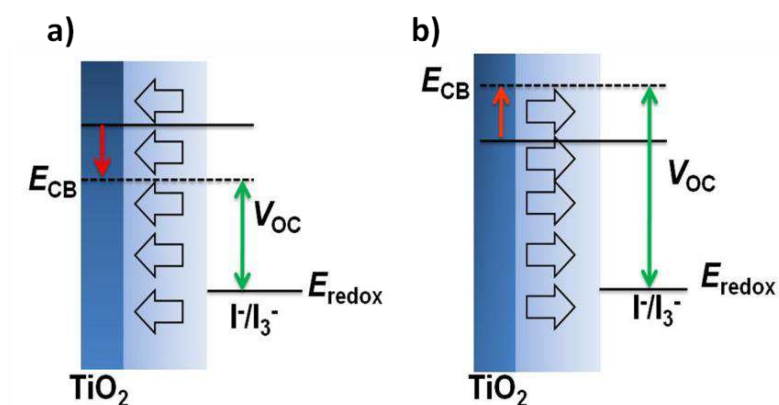


**Figure 28.** Interfacial dipole moment affects conduction band of  $\text{TiO}_2$ : a) negative and b) positive dipole direction for  $V_{OC}$ .

The control of directionality of the dipole moment of the dye molecules on the semiconductor surface result in better  $V_{OC}$  values. Also the reduction of charge recombination between the injected electrons in the CB of  $\text{TiO}_2$  and the  $\text{I}_3^-$  ion in the electrolyte causes increase in the  $V_{OC}$ . Furthermore, regulating the appropriate direction of interfacial dipole moment, which arises from dyes arrangement on the oxide electrode surface, is one more approach to enhance the  $V_{OC}$  in DSSCs. First of all, the dipole moment initiates from electron localization within a dye molecule in the excited state. Eventually, the shift of the  $E_{CB}$  of the oxide electrode consistently influences by the magnitude and the direction of the interfacial dipole moment. For D-A type organic dyes, the direction of the generated dipole in is commonly from the electron-acceptor moiety to the donor moiety, because the majority electrons are



localized around the electron-withdrawing unit in the excited state. Thus, the dyes containing an anchoring unit are an electron acceptor which has the potential advantage to produce a suitable direction of the dipole moment to provide a higher  $V_{OC}$ . A probable explanation for relatively low  $V_{OC}$  of cationic organic dyes, such as merocyanine, hemicyanine, and cyanine derivatives could also be due to the dipole moment effect. Moreover, D-A type dye should have the vertical orientation on the surface of the semiconducting oxide electrode in order to get high  $V_{OC}$ .<sup>67</sup>

Therefore, the dyes have a significant impact on both the  $J_{SC}$ ,  $V_{OC}$  and also on the performance of the devices. In the D- $\pi$ -A type organic dyes, modification of donor, exchange of  $\pi$ -spacer, and acceptor parts are the main strategies to control their frontier energy levels and enhance the molecular extinction coefficient to get maximum efficiency.

## Section B: Organic Field Effect Transistors

### 1.1 Introduction

The transistors are invented by John Bardeen, William Shockley and Walter Brattain in 1947 is regarded as one of the greatest discovery of the 20th century. It is the basic component in modern electronics. However, the inorganic electronics have some technological limitations associated with them; due to this organic-based devices have recently emerged in the market to replace amorphous silicon. Organic electronics have great possibility to find their place in a wide range of new applications. The main advantage is the solution processability, thus organic materials offer the possibility to fabricate low-cost and flexible devices, and are also suitable for large area applications.<sup>68</sup>



**Figure 29.** Conventional electronics are based on inorganic materials e.g., Si, oxides.

Organic electronics is used in displays, sensors, photovoltaics and electronics circuits and components present several advantages over the conventional inorganic-based electronics (Si, oxides) because they are comparatively inexpensive, flexible, unbreakable, optically transparent, and lightweight, and have low power consumption. Organic Field Effect Transistors (OFETs) and Organic Light Emitting Diodes (OLEDs) are the essential electronic

building blocks of organic electronic circuits. It includes the materials which has ability to modify chemical structure that could directly impact the properties of the materials when deposited in thin film form. Organic materials for example anthracene have been known for almost a century. It is the first studied material for their optical and an electronic property which have been reported in the 1910s. An interest in such materials was intensified in the 1960s and 1970s by the discovery of electroluminescence in molecular crystals and conducting polymers.<sup>69</sup> Organic thin films demonstrated useful number of applications; some of them now arrived to the consumer market. First exhibition of a low voltage and efficient thin film light emitting diode by Ching Tang and Steven van Slyke at Kodak was done in the mid-1980s.<sup>70</sup> The organic light emitting device is most successful which is currently used in long-lived and highly efficient color displays. Specifically, organic displays show high brightness, fast response time, wide viewing angle, and low operating voltage. However, in past 20 years organic electronic is showing major improvements in material design and purification that led to a significant boost in the materials performance.<sup>71</sup>



**Figure 30.** Organic electronics and their applications in display, flexible solar cells etc.

## 1.2 Organic Field Effect Transistors

Currently, OFETs are the subject of intense research because they are inexpensive, solution processed, and mechanically flexible electronic devices. OFETs are important building blocks for the next generation of cheap and flexible organic circuits; they also give an important insight into the charge transport of  $\pi$ -conjugated system. Research on OFETs incorporates the discovery, design, and synthesis of  $\pi$ -conjugated systems for OFETs, device optimization, development of applications in radio frequency identification (RFID) tags, flexible displays, electronic papers and sensors.<sup>72</sup>



**Figure 31.** OFETs applications: A) Flexible electrophoretic ink display driven by an active-matrix of 1.2 million OFETs and B) Plastic foils comprising 8-bit microprocessors with 3381 OFETs each.<sup>68</sup>

### 1.3 Components of OFETs

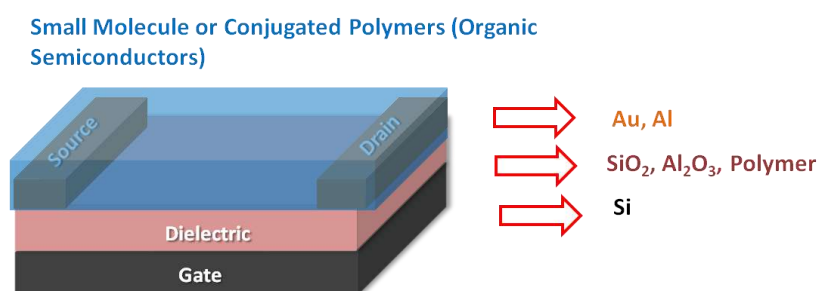


**Figure 32.** Common OFET configurations bottom gate/bottom contact.

OFETs device consists of an organic semiconducting layer, a gate insulator layer, and three terminals (drain, source, and gate electrodes). In the Bottom gate/bottom contact configuration, the gate electrode is located directly on the substrate; frequently a silicon wafer functions as both substrate and gate. The insulator, thermally grown silicon dioxide is situated on top. The basic circuit of a bottom-contact OFET is shown in **Figure 32**, the source and drain electrodes are above of dielectric, and on the top of that the semiconductor layer is deposited by drop casting or spin coating method. The gate dielectrics can be inorganic insulators, such as, for example,  $\text{SiO}_2$  (thermally grown on Si or sputtered),  $\text{Al}_2\text{O}_3$ , and  $\text{Si}_3\text{N}_4$ , or polymeric insulators, such as, for example, poly(methyl methacrylate) (PMMA) are commonly used depending on the transistor structure. The source and drain electrodes helps to inject charges into the semiconductor, are usually high work function metals such as gold (also  $\text{Pd}^{25}$ ,  $\text{Pt}^{26}$ , and  $\text{Ag}^{27}$ ) and conducting polymers (e.g., PEDOT: PSS<sup>29-31</sup>, PANI<sup>32-34</sup>).

OFETs are mainly divided into four types: (A) device configuration the bottom gate bottom contact, (B) the bottom gate top contact, (C) the top gate top contact and (D) the top gate bottom contact as shown in **Figure 33**.<sup>73</sup>

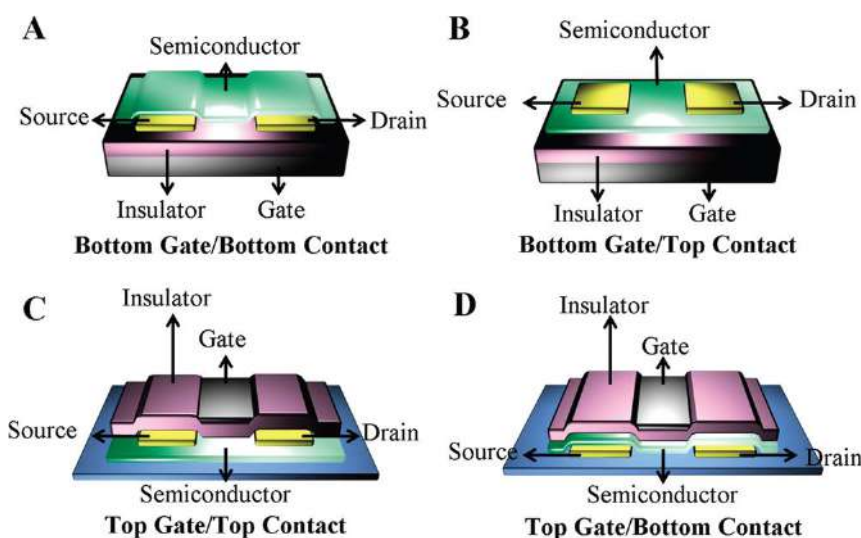


**Figure 33.** Four different types of OFETs (A) Bottom gate/bottom contact, (B) Bottom gate/top contact, (C) Top gate/top contact, and (D) Top gate/bottom contact.<sup>74</sup>

Definitely, the OFETs device configuration plays a key role in the device performance. It is found that devices of the type B and D always give superior performances than devices A and C. This is credited to the better contact between the organic semiconductor and the electrode.

#### 1.4 Operation of OFETs

The voltage applied to the gate shifts the HOMO and LUMO energy levels with respect to the metal Fermi level ( $E_F$ ) of the source-drain contacts, which permit the formation of the conducting channel. When a negative gate voltage applied it shifts the orbitals up and results in the alignment of the HOMO with  $E_F$ , making it feasible to get hole conduction. If a positive gate voltage is applied, the HOMO and LUMO will move down and LUMO become close with  $E_F$ , then the electrons will flow from the metal to the LUMO. However, the orbital shift induces bending of the bands near the source-drain electrodes and as a result there is an energy barrier at these contacts.<sup>75</sup>

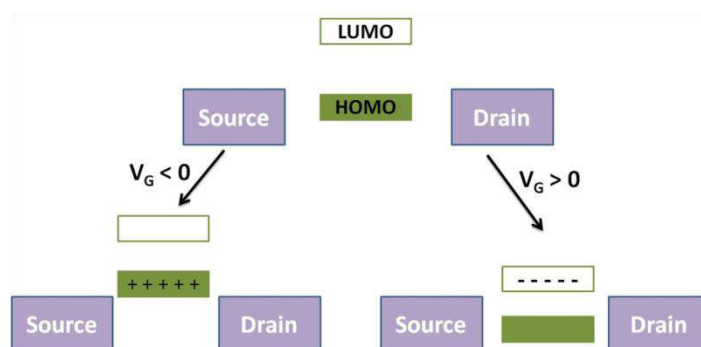


**Figure 34.** Schematic representation of the HOMO and LUMO of the organic semiconductor with respect to the source-drain metal Fermi level.

Primarily, OFETs can be considered as a capacitor in which the semiconductor layer and the gate electrode act as electrodes to sandwich the gate insulator. When the gate voltage is applied, the source electrode injects charges that will be attracted to the interface of the gate insulator and organic semiconductor. If a drain-source voltage is applied, a current between the source and drain electrodes will be generated, which in turn can be tuned by the gate voltage. For the inorganic semiconductors transport occurs through band-like transport mechanisms where the structure is covalently bound. Organic structures are Van der Waals bound and conduct charges by “electron/hole hopping” mechanism between molecules. In this mechanism the activation energy should rise above for charge transport to occur, resulting in slowed  $e^-/h^+$  flow through the semiconducting media.

### 1.5 Working of OFETs

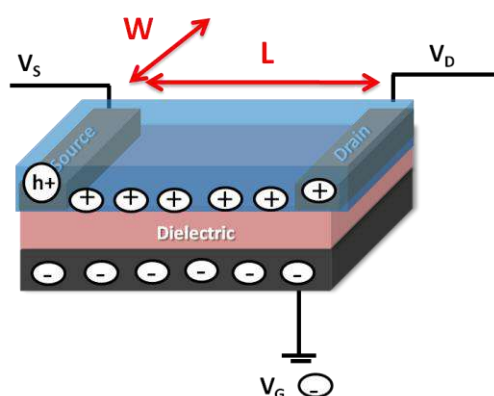


**Figure 35.** Schematic structure of a field-effect transistor and applied voltages for hole transport:  $L$  = channel length;  $W$  = channel width;  $V_D$  = drain voltage;  $V_G$  = gate voltage,  $V_S$  = source voltage.

The source and drain electrode is highly important because all other voltages are given in relation to this electrode. When a negative voltage  $V_G$  is applied to the gate electrode (with p-

semiconductors), an electric field is formed perpendicular to the layers. As a consequence, the development in positive charge carriers occurs at the interface between semiconductor and gate insulator. When a voltage  $V_D$  is applied at the same time on the drain electrode, holes can be moved from the source electrode to the drain electrode (**Figure 35**). This conducting condition is called the “on” state;  $V_G = 0$  defines the “off” state. The FETs are determined by the three most important characteristics that are the threshold voltage  $V_{Th}$ , the  $I_{on}/I_{off}$  ratio, and the charge-carrier mobility  $\mu_{FET}$ . The threshold voltage  $V_{Th}$  describes the voltage  $V_D$  at which the field effect sets in; it principally quantifies the number of the charge-carrier traps in the semiconductor interface that must be overcome. The  $I_{on}/I_{off}$  ratio is described as the ratio of the source-drain current in the “on” and the “off” state of the FETs. The charge-carrier mobility  $\mu_{FET}$  in turn mainly finds out the size of the voltage to be applied and thus the power consumption of the transistor.<sup>72</sup>

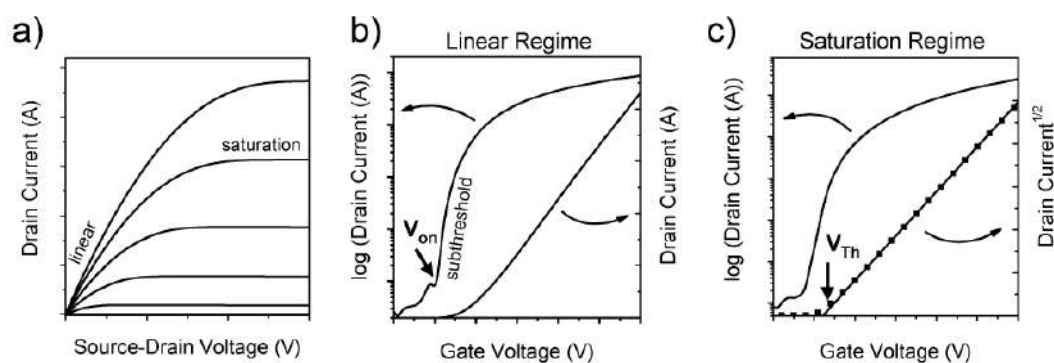


**Figure 36.** Representative current-voltage characteristics of an n-channel organic field-effect transistor: (a) Output characteristics representing the linear and saturation regimes; (b) Transfer characteristics in the linear regime ( $V_D, V_G$ ), representing the onset voltage ( $V_{on}$ ) when the drain current increases suddenly and (c) Transfer characteristics in the saturation regime ( $V_{DS} > V_G - V_{Th}$ ), representing the threshold voltage  $V_{Th}$ , where the linear fit to the square root of the drain current intersects with the x-axis.<sup>73</sup>

The output characteristic curve of the transistor is a plot of the source-drain current  $I_D$  against the drain voltage  $V_D$  at different gate voltages  $V_G$ . It is used to determine the charge-carrier mobility. Two regions of the characteristic curve can be distinguished: at low drain voltage, the source-drain current increases almost linearly (linear region) then converts into a saturation region (**Figure 36**). For the linear region, the field-effect mobility is calculated directly from the slope of the so-called transfer characteristic curve, a plot of the source-drain current against the gate voltage at constant drain voltage. The slope is considered according to Equation (4), which is based on the hypothesis of  $V_D \ll (V_G - V_{Th})$ . In the second region of the output characteristic curve (the saturation region), Equation (5) relates for the source-drain

current when  $V_D > (V_G - V_{Th})$ . The charge-carrier mobility  $\mu_{FET,sat}$  in the saturation region is calculated from the slope of the current-voltage curve in a plot of  $ID^{1/2}$  against  $V_G$ . In the case of organic semiconductors, the mobility is usually extensively dependent on the gate voltage and the temperature; Equations (4) and (5) are used to estimate the charge-carrier mobility.<sup>76</sup>

Linear regimes

$$I_{D,L} = (\mu_{FET} WC_i/L)(V_G - V_{Th}) V_{ds} \quad \dots\dots\dots (4)$$

Saturation regimes

$$I_{D,S} = (\mu_{FET} WC_i/2L)(V_G - V_{Th})^2 \quad \dots\dots\dots (5)$$

At last, the selection of the organic semiconductor will be solution to achieve a high mobility. The mobility is also depends on the purity of organic semiconductors, the thickness of the dielectric and semiconducting layers, the channel length, and the testing environment. The semiconductor layer is associated to the chemical structure and intermolecular interaction of organic semiconductor, the morphology and molecular arrangement in the active layer. Furthermore, the materials used for the electrodes and the gate insulator, the interface and energy alignments between the organic semiconductor and the gate insulator etc., all takes part an important roles in the ultimate performance of OFETs.

## 1.6 Field effect mobility of an organic FET depends on the:

- i) Molecular Structure
- ii) The Intermolecular Packing (reorganisation energy and the transfer integral)

### 1.6.1 Molecular Structure

In the solid state, small molecules have the benefit that they order themselves very well. This generally gives the high charge-carrier mobility. Primarily, the mobility depends on the intermolecular interactions but also limited to processability of the compounds from solution. Solution-processable semiconductor materials are mainly focused on backbone repeating units, side chains and different substituents. The choice of the backbone repeating units is important to maximize the intermolecular interactions; such intermolecular interactions are responsible for the formation of a conduction path. Therefore, the mobility in organic semiconductors is highly dependent on the molecular ordering. And also it depends on the highest occupied molecular orbital (HOMO) and lowest unoccupied molecular orbital (LUMO) energy levels with respect to the metal Fermi level ( $E_F$ ) of the source-drain contacts. The solubility and processability of organic semiconductor can be enhanced by insertion of



the side chains. The substituent plays an important role in extending their  $\pi$ -conjugation, and also usually improves their solubility, stability, and molecular packing. The addition of substituents to the conjugated core can strongly modify the crystal packing of the organic semiconductors.<sup>77</sup>

### 1.6.2 The Intermolecular Packing (reorganisation energy and the transfer integral)

The intermolecular packing is determined by the reorganisation energy and transfer integral in organic semiconductors. The transfer integral explains the splitting of the highest occupied molecular orbital (HOMO) and the lowest unoccupied molecular orbital (LUMO). This is mostly depends on the  $\pi$ -overlap between neighbouring molecules. The reorganization energy is the nothing but the energy loss when a charge carrier passes through a molecule. It is dependent on the conjugation length, degree, and packing of the organic molecules in the active layer. Typically, the smaller the reorganization energy and the larger the transfer integral gives the high mobility. Both are extremely dependent on the packing of the organic molecules. As a result, the packing mode of the organic semiconductors becomes very important for the analysis of the charge transport between molecules. So there are four different kinds of packing as shown in **Figure 37**.<sup>74</sup>

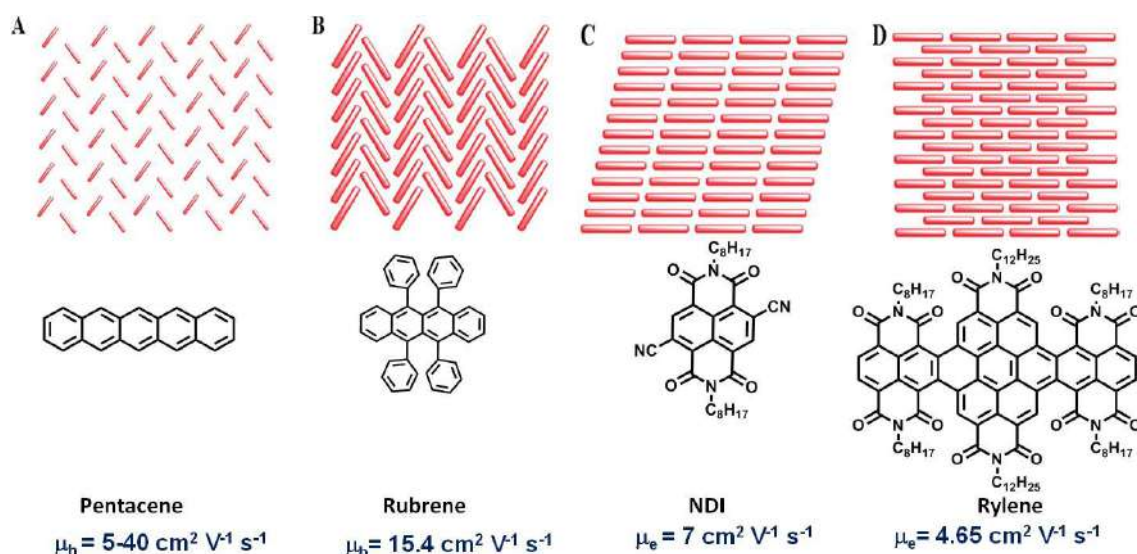


**Figure 37.** Molecular packing in organic semiconductors (A) Herringbone packing (face-to-edge) without  $\pi$ - $\pi$  overlap (face-to-face) between adjacent molecules (example: pentacene); (B) Herringbone packing with  $\pi$ - $\pi$  overlap between adjacent molecules (example: rubrene); (C) Lamellar motif, 1-D  $\pi$  stacking (example: hexyl substituted naphthalene diimide); (D) Lamellar motif, 2-D  $\pi$  stacking.<sup>74,77</sup>

The herringbone structure is not the most favorable packing for transport due to their large angle between the planes of adjacent molecules along the herringbone diagonal. Ideally, to

achieve a more efficient charge transport, the organic molecules should pack along the current direction in the conducting channel. Among a variety of new materials for organic electronics, at present the conjugated liquid crystals (discotic molecules) have been found as a new generation of organic semiconductors because they convey high ordering and dynamics. It is found that the two-dimensional chemical structure (one-dimensional charge transport) is believed to be the most efficient for charge transport (**Figure 38**). It can increase the transfer integrals to the maximum and transport the charge carriers through an approximately straight line.<sup>78</sup> Now days, the research has focused on molecular design and crystal engineering in order to obtain high mobility.

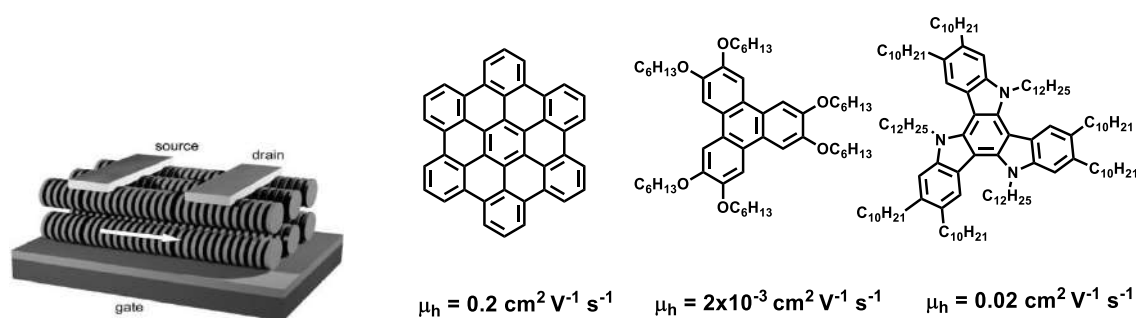


**Figure 38.** 2-D lamellar packing and Discotic shaped organic semiconductors.

## 1.7 Molecular Engineering of Organic Semiconductor

Predominantly, the mobility of the organic semiconductor should be as high as possible to get efficient charge transport from one molecule to another. The organic semiconductors that can be used in OFETs are classified into two main families: (i) Small conjugated molecules with low molecular weight (e.g. pentacene, oligothiophene, tetrathiafulvalene) ii) Conjugated polymers.

### 1.7.1 Small molecules

The mobility of small molecule is closely related to the chemical structure, their intermolecular interaction in films, the morphology, their packing structure and molecular arrangement on the substrate. Metal phthalocyanines (MPcs) are versatile conjugated macrocycles showed a great deal of interest as active materials in organic electronic device. Phthalocyanines (Pcs) are made up of a nitrogen-linked tetrameric diiminoisindoline conjugated macrocycle. They are ideal candidates for OFETs because of their molecular planarity, ability to stack and their tendency to form crystalline, and polycrystalline films. Small molecule like CuPc302 showed a hole mobility of  $0.02 \text{ cm}^2 \text{ V}^{-1} \text{ s}^{-1}$  an  $I_{\text{on}}/I_{\text{off}}$  ratio of  $10^5$ . Pentacene is widely studied organic semiconductor and it is the benchmark in the field of

OFETs, it has given superior hole mobilities in the range of  $5\text{-}40\text{ cm}^2\text{ V}^{-1}\text{ s}^{-1}$ . PCBM is typically used as an acceptor (n-type) in organic photovoltaic cells, and its good charge transport properties made it an ideal candidate for n-channel OFETs, it showed a mobility of  $4.5 \times 10^{-3}\text{ cm}^2\text{ V}^{-1}\text{ s}^{-1}$ . Oligothiophenes form planar structures and also it is very easy to modify thiophene than benzene rings. For example,  $\alpha$ -6T262 molecules have a hole mobility that is improved from  $10^{-4}\text{ cm}^2\text{ V}^{-1}\text{ s}^{-1}$  to  $0.1\text{ cm}^2\text{ V}^{-1}\text{ s}^{-1}$  within the last few decades. In the perylene diimide semiconductor PDI8-CN<sub>2</sub>, core-cyanated derivatives showed electron mobilities at  $0.16\text{ cm}^2\text{ V}^{-1}\text{ s}^{-1}$ . The sulfur-containing bis(1,2,5-thiadiazolo)-p-quinobis(1,3-dithiole) (BTQBT) has the TTF units separated by a cyclohexane unit. These materials showed higher OFET mobility when they are deposited at a high rate and reaching a maximum hole mobility of  $0.7\text{ cm}^2\text{ V}^{-1}\text{ s}^{-1}$ . The tetrafluoro-substituted derivatives (111b) were also synthesized and showed ambipolar behaviour in OFETs.<sup>79</sup>

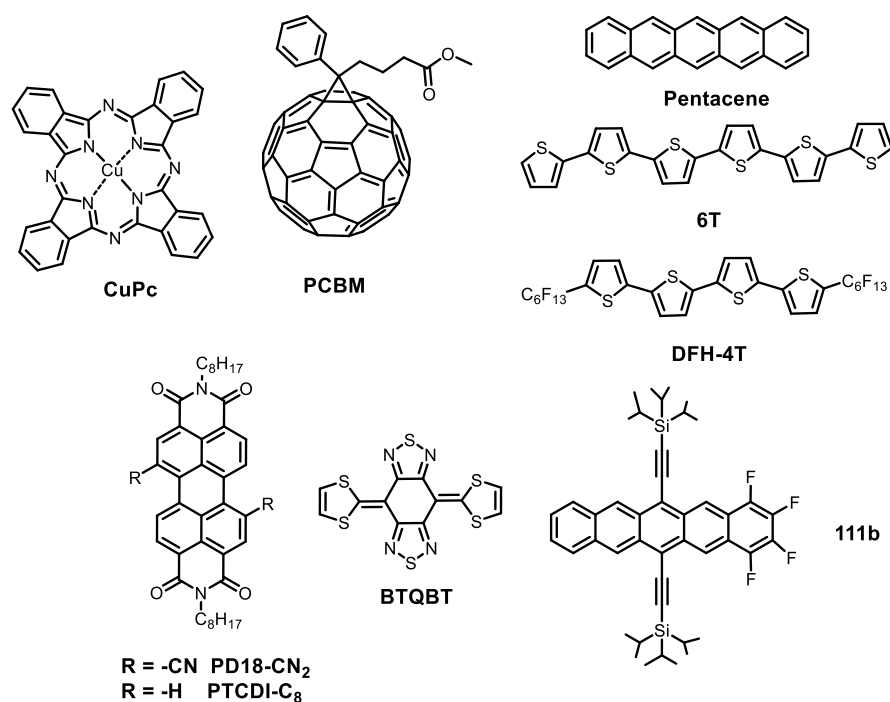


**Figure 39.** Examples of small molecules as organic semiconductors.

### 1.7.1.1 n-type semiconductors

n-type semiconductors are electron-accepting materials for transporting electrons owing to their electron-deficient nature. Charge carrier mobility is the main device parameter for many of the applications of organic field-effect transistors (OFETs).<sup>73</sup> Naphthalene tetracarboxylic diimides (NDIs) are the first small molecule based on n-type organic semiconductors which showed great potential for OFETs. Unfortunately, very few n-type organic semiconductors have been reported and their mobility values are still inferior as compared to p-type organic

semiconductors. The low performances of n-type semiconductors in OFETs are mainly because of: (1) the less stability of organic radical anions in the presence of oxygen and water (2) the large injection obstacle of electrons between the LUMO of the semiconductor and the work function of source or drain metals.<sup>80</sup> In order to inject electrons into the LUMO level from gold electrode, the LUMO level must be arranged in a line with the work function of the metal. For example, isoindigo derivative based on the fusion of benzofuran showed n-type semiconductor performance with higher electron mobilities of  $0.074 \text{ cm}^2 \text{ V}^{-1} \text{ s}^{-1}$ .<sup>81</sup> Dicyanomethylene-terminated quinoidal oligothiophenes (QOTs) are another class of well-known n-type semiconductors. Dicyanomethylene-substituted fused tetrathienoquinoid has a deep LUMO energy of  $-4.3 \text{ eV}$  and showed electron mobilities as high as  $0.9 \text{ cm}^2 \text{ V}^{-1} \text{ s}^{-1}$  with an  $I_{\text{on}}/I_{\text{off}}$  of  $10^5$ .<sup>82</sup>

### 1.7.1.2 p-type semiconductors

p-type semiconductors are hole transporting material; they are electron rich in nature. For p-type organic semiconductors, several small molecules with high mobility values have been achieved. This area of research is more explored and a number of small molecules are designed as p-type organic semiconductors, still the search for more efficient materials is always continues. Apart from high mobility, major objectives are stability under ambient conditions and easy processing from solution which can make organic semiconductors a feasible alternative to amorphous silicon.<sup>74</sup> For small molecule, like pentacene is still the material with the highest mobility but it should be vacuum sublimed, but solution processing is technologically more convenient.<sup>83</sup> Primarily, the mobility of the organic semiconductor supposed to be as high as possible so that efficient charge transport from one molecule to another is achievable. Ideally, the p-type organic semiconductor should have high solubility, high stability and finally an optimized energy alignment with the electrodes. For example, Dibenzo[d,d0]-thieno[3,2-b;4,5-b0]dithiophene (DBTDT) was showing HOMO energy level of DBTDT was about  $5.6 \text{ eV}$ , this suggests DBTDT has good stability. Thin films of DBTDT showed mobilities as high as  $0.5 \text{ cm}^2 \text{ V}^{-1} \text{ s}^{-1}$  with an  $I_{\text{on}}/I_{\text{off}}$  ratio of up to  $10^6$ .<sup>84</sup> Dihexyl substituted BDT derivative (DH-BDT) showed hole mobilities of only  $10^{-2} \text{ cm}^2 \text{ V}^{-1} \text{ s}^{-1}$ .<sup>85</sup>

### 1.7.2 Conjugated polymers

Polymer semiconductors are one of the most suitable candidates for OFETs due to their outstanding electronic and optoelectronic properties. In addition, they have simple processability, very good film-forming properties and the high flexibility of the films relative to many small molecules onto a range of desirable substrates.

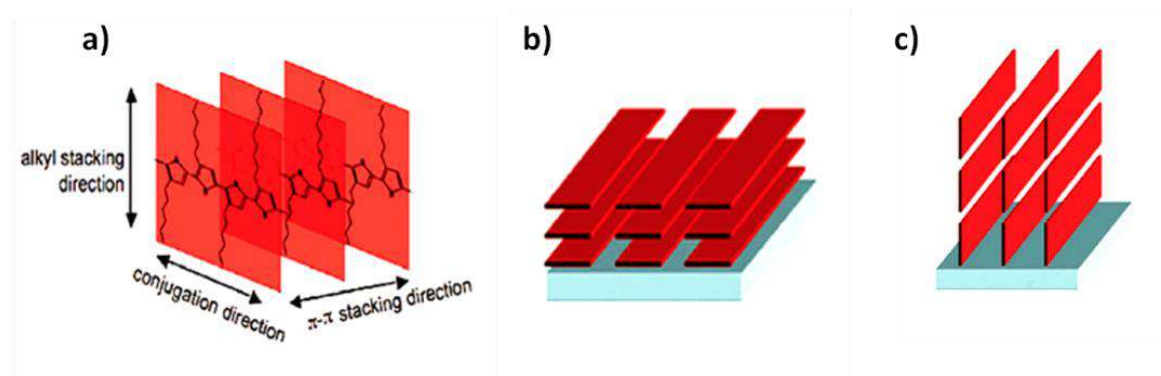


**Figure 40.** (a) Possible charge transport mechanisms in crystalline polymer films (using P3HT) (b) Face-on and (c) edge-on orientation of the polymer molecules on the substrates.<sup>86</sup>

There are two kinds of charge transports in polymer transistors found in polymers i.e. interchain transport ( $\pi$ - $\pi$  stacking orientation) and intrachain transport (**Figure 40**). The intrachain transport occurs faster than the interchain. The most studied polymer for OFETs is regioregular poly (3-hexylthiophene) (P3HT) gave one of the highest hole mobilities ( $0.1\text{-}0.2\text{ cm}^2\text{ V}^{-1}\text{ s}^{-1}$ ). This high mobility is credited to structural order in the polymer film which brings the regioregular head-to-tail coupling of the hexyl side chains results into a lamellar structure. The varieties of thiophene-based polymers are reported for the fabrication of OFETs. Another example is the copolymer poly(2,5-bis(thiophene-2-yl)-3,7-ditridecanyltetrathienoacene, P2TDC13FT4) designed to enlarge the rigidity of the thiophene monomer through the use of an alkyl-substituted core that consists of four fused thiophene rings. This polymer showed a field-effect hole mobility exceeding  $0.3\text{ cm}^2\text{ V}^{-1}\text{ s}^{-1}$ . Cyclopentadithiophenebenzothiadiazole copolymer (CDT-BTZ) have superior macroscopic order, achieved a mobility of up to  $0.67\text{ cm}^2\text{ V}^{-1}\text{ s}^{-1}$  in films deposited by spin-coating followed by an annealing step. OFETs based poly (2,5-bis- (3-alkylthiophene-2-yl)thieno[3,2-b]thiophene (PBTTT) gave mobilities as high as  $0.7\text{ cm}^2\text{ V}^{-1}\text{ s}^{-1}$ . A new n-type of polymer based on a naphthalenebis(dicarboximide) (P(NDI2OD-T2) showed a very high electron mobility ( $0.45\text{-}0.85\text{ cm}^2\text{ V}^{-1}\text{ s}^{-1}$ ) with solution processability and air stability.<sup>75</sup>

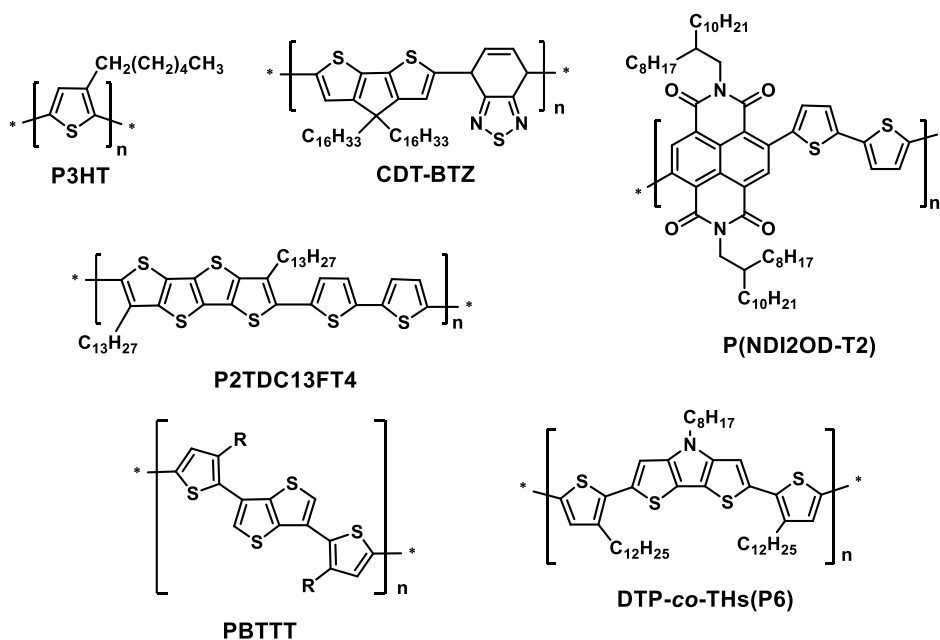


**Figure 41.** Examples of conjugated polymers as organic semiconductors.

Organic field-effect transistors made a huge impact for the applications in microelectronics industry in the near future. It showed reduce in cost and large area coverage for flexible devices. Therefore, the mobility in organic materials is highly dependent on the molecular structure, ordering, and molecular packing in the active layer and molecular. Small structural modifications or even by varying the experimental fabrication conditions, a high OFET performance can be obtained. Currently, great efforts are dedicated to the understanding of the transport mechanisms and the structure/ performance correlation.

## Outline of Thesis

This thesis describes a detailed introduction on the Dye-Sensitized Solar Cells (third generation solar cells) and Organic Field Effect Transistors. The second chapter involves the synthesis of HT based unsymmetrical squaraine dyes for DSSCs applications. The strategy is to include strong HT donor and the variation of in-plane and out-of-plane alkyl chains on the acceptor groups. Herein, the synergistic effect of HT moieties on extending the conjugation and avoiding the dye aggregations by in-plane and out-of-plane alkyl groups played important roles for obtaining high PCE efficiency. The third chapter describes the synthesis of HT based hemicyanine dye for DSSCs applications. Herein, the strong HT donor and long or branched alkyl groups is to modulate the photophysical, electrochemical properties, the band edge movement and the recombination process of D-A hemicyanine dyes. The fourth chapter presents the synthesis of unsymmetrical squaraine sensitizers comprising HT donor followed by  $\pi$ -spacer, in-plane and out-of-plane alkyl chains on acceptor groups, and characterize for DSSCs applications. This group of dyes utilizes additional  $\pi$ -spacer and variation of in-plane and out-of-plane alkyl chains on acceptor units to investigate the effects of molecular orientation and arrangement of dyes on the  $\text{TiO}_2$  surface. The fifth chapter describes the synthesis HT-squaraine based and HT-hexacyano based small molecules and their application for OFETs. In order to see the synergistic effect of planarization and side chain engineering, a series of HT-based small molecules have been designed for fabricating n-channel transistors or p-channel transistors. HT moiety was suitably functionalized with electron deficient  $-\text{CN}$  groups and systematically included the low-band gap squaraine molecules to realize the structure and charge carrier mobility relationship.



## REFERENCES

1. Pérez-Lombard, L.; Ortiz, J.; Pout, C. *Energy and buildings* **2008**, *40*, 394.
2. Weber, C.; Perrels, A. *Energy Policy* **2000**, *28*, 549.
3. <https://www.bp.com/content/dam/bp/en/corporate/pdf/energyeconomics/statistical-review-2017/bp-statistical-review-of-world-energy-2017-full-report.pdf>
4. Crompton, P.; Wu, Y. *Energy Economics* **2005**, *27*, 195.
5. Garg, P. J. *Sustainable Energy & Environment* **2012**, *3*.
6. Dorian, J. P.; Franssen, H. T.; Simbeck, D. R. *Energy Policy* **2006**, *34*, 1984.
7. Dudley, B. *London, UK* **2012**.
8. Panwar, N.; Kaushik, S.; Kothari, S. *Renewable and Sustainable Energy Rev.* **2011**, *15*, 1513.
9. Heinberg, R.; Fridley, D. *Nature* **2010**, *468*, 367.
10. Owen, A. D. *Energy policy* **2006**, *34*, 632.
11. Turner, J. A. *Science* **1999**, *285*, 687.
12. Glaser, P. E. *Science* **1968**, *162*, 857.
13. Lewis, N. S. *Science* **2007**, *315*, 798.
14. Hagfeldt, A.; Grätzel, M. *Acc. Chem. Res.* **2000**, *33*, 269.
15. Barlev, D.; Vidu, R.; Stroeve, P. *Sol. Energy Mater. Sol. Cells* **2011**, *95*, 2703.
16. Gates, D. M. *Science* **1966**, *151*, 523.
17. McCartney, H.; Unsworth, M. H. *Q. J. Royal Meteorol. Soc* **1978**, *104*, 699.
18. Fernández, E. F.; Almonacid, F.; Ruiz-Arias, J.; Soria-Moya, A. *Sol. Energy Mater Sol. Cells* **2014**, *127*, 179.
19. Becquerel, A. *C.R. Acad. Sci.* **1839**, *9*, 14.
20. Chapin, D. M.; Fuller, C.; Pearson, G. *J. Appl. Phys.* **1954**, *25*, 676.
21. Shockley, W.; Queisser, H. J. *J. Appl. Phys.* **1961**, *32*, 510.
22. Bube, R. H. *Phys. Rev.* **1955**, *98*, 431.
23. Fthenakis, V. *Renewable and Sustainable Energy Rev.* **2009**, *13*, 2746.
24. Beard, M. C.; Luther, J. M.; Semonin, O. E.; Nozik, A. J. *Acc. Chem. Res.* **2012**, *46*, 1252.
25. Kamat, P. V. *J. Phys. Chem. C* **2008**, *112*, 18737.
26. Kongkanand, A.; Tvrđy, K.; Takechi, K.; Kuno, M.; Kamat, P. V. *J. Am. Chem. Soc.* **2008**, *130*, 4007.
27. Benten, H.; Mori, D.; Ohkita, H.; Ito, S. *J. Mater. Chem. A* **2016**, *4*, 5340.
28. Lu, L.; Zheng, T.; Wu, Q.; Schneider, A. M.; Zhao, D.; Yu, L. *Chem. Rev.* **2015**, *115*, 12666.
29. Kumaresan, P.; Vegiraju, S.; Ezhumalai, Y.; Yau, S. L.; Kim, C.; Lee, W.-H.; Chen, M.-C. *Polymers* **2014**, *6*, 2645.
30. Nie, W.; Tsai, H.; Asadpour, R.; Blancon, J.-C.; Neukirch, A. J.; Gupta, G.; Crochet, J. J.; Chhowalla, M.; Tretiak, S.; Alam, M. A. *Science* **2015**, *347*, 522.
31. Mei, A.; Li, X.; Liu, L.; Ku, Z.; Liu, T.; Rong, Y.; Xu, M.; Hu, M.; Chen, J.; Yang, Y. *Science* **2014**, *345*, 295.
32. Liu, X.; Feng, Y.; Cui, H.; Liu, F.; Hao, X.; Conibeer, G.; Mitzi, D. B.; Green, M. *Prog. in Photovolt: Res. Appl.* **2016**, *24*, 879.
33. Katagiri, H.; Sasaguchi, N.; Hando, S.; Hoshino, S.; Ohashi, J.; Yokota, T. *Sol. Energy Mater. Sol. Cells* **1997**, *49*, 407.

34. Wang, W.; Winkler, M. T.; Gunawan, O.; Gokmen, T.; Todorov, T. K.; Zhu, Y.; Mitzi, D. B. *Adv. Energy Mater.* **2014**, *4*.
35. Todorov, T. K.; Reuter, K. B.; Mitzi, D. B. *Adv. Mater.* **2010**, *22*.
36. Siebentritt, S.; Schorr, S. *Prog. in Photovolt: Res. Appl.* **2012**, *20*, 512.
37. Grätzel, M. J. *Photochem. Photobio. C: Photochem. Rev* **2003**, *4*, 145.
38. Hagfeldt, A.; Boschloo, G.; Sun, L.; Kloo, L.; Pettersson, H. *Chem. Rev.* **2010**, *110*, 6595.
39. Liang, M.; Chen, J. *Chem. Soc. Rev.* **2013**, *42*, 3453.
40. Del Canizo, C.; Del Coso, G.; Sinke, W. *Prog. Photovolt.: Res. Appl.* **2009**, *17*, 199.
41. Reddy, K. G.; Deepak, T.; Anjusree, G.; Thomas, S.; Vadukumpully, S.; Subramanian, K.; Nair, S. V.; Nair, A. S. *Phys. Chem. Chem. Phys.* **2014**, *16*, 6838.
42. O'regan, B.; Grätzel, M. *Nature* **1991**, *353*, 737.
43. Mishra, A.; Fischer, M. K.; Bäuerle, P. *Angew. Chem. Int. Ed.* **2009**, *48*, 2474.
44. Bisquert, J.; Fabregat-Santiago, F.; Mora-Sero, I.; Garcia-Belmonte, G.; Giménez, S. *J. Phys. Chem. C* **2009**, *113*, 17278.
45. Gonçalves, L. M.; de Zea Bermudez, V.; Ribeiro, H. A.; Mendes, A. M. *Energy Environ. Sci.* **2008**, *1*, 655.
46. Ito, S.; Rothenberger, G.; Liska, P.; Comte, P.; Zakeeruddin, S. M.; Péchy, P.; Nazeeruddin, M. K.; Grätzel, M. *Chem. Commun.* **2006**, 4004.
47. Park, N.-G.; Van de Lagemaat, J.; Frank, A. J. *J. Phys. Chem. B* **2000**, *104*, 8989.
48. Ning, Z.; Fu, Y.; Tian, H. *Energy Environ. Sci.* **2010**, *3*, 1170.
49. Snaith, H. J.; Schmidt-Mende, L. *Adv. Mater.* **2007**, *19*, 3187.
50. Murakami, T. N.; Grätzel, M. *Inorg. Chim. Acta* **2008**, *361*, 572.
51. Nazeeruddin, M. K.; Zakeeruddin, S.; Humphry-Baker, R.; Jirousek, M.; Liska, P.; Vlachopoulos, N.; Shklover, V.; Fischer, C.-H.; Grätzel, M. *Inorg. Chem.* **1999**, *38*, 6298.
52. Nazeeruddin, M. K.; Pechy, P.; Renouard, T.; Zakeeruddin, S. M.; Humphry-Baker, R.; Comte, P.; Liska, P.; Cevey, L.; Costa, E.; Shklover, V. *J. Am. Chem. Soc.* **2001**, *123*, 1613.
53. Lee, C. W.; Lu, H. P.; Lan, C. M.; Huang, Y. L.; Liang, Y. R.; Yen, W. N.; Liu, Y. C.; Lin, Y. S.; Diao, E. W. G.; Yeh, C. Y. *Chem. Eur. J.* **2009**, *15*, 1403.
54. Wang, C.-L.; Lan, C.-M.; Hong, S.-H.; Wang, Y.-F.; Pan, T.-Y.; Chang, C.-W.; Kuo, H.-H.; Kuo, M.-Y.; Diao, E. W.-G.; Lin, C.-Y. *Energy Environ. Sci.* **2012**, *5*, 6933.
55. Mathew, S.; Yella, A.; Gao, P.; Humphry-Baker, R.; Curchod, B. F.; Ashari-Astani, N.; Tavernelli, I.; Rothlisberger, U.; Nazeeruddin, M. K.; Grätzel, M. *Nat. Chem.* **2014**, *6*, 242.
56. Saccone, D.; Galliano, S.; Barbero, N.; Quagliotto, P.; Viscardi, G.; Barolo, C. *Eur. J. Org. Chem.* **2016**, *2016*, 2244.
57. Cheng, M.; Yang, X.; Li, J.; Zhang, F.; Sun, L. *ChemSusChem* **2013**, *6*, 70.
58. Geiger, T.; Kuster, S.; Yum, J. H.; Moon, S. J.; Nazeeruddin, M. K.; Grätzel, M.; Nüesch, F. *Adv. Funct. Mater.* **2009**, *19*, 2720.

59. Jradi, F. M.; Kang, X.; O'Neil, D.; Pajares, G.; Getmanenko, Y. A.; Szymanski, P.; Parker, T. C.; El-Sayed, M. A.; Marder, S. R. *Chem. Mater.* **2015**, *27*, 2480.
60. Wang, Q.; Moser, J.-E.; Grätzel, M. *J. Phys. Chem. B* **2005**, *109*, 14945.
61. Bisquert, J. *J. Phys. Chem. B* **2002**, *106*, 325.
62. Fabregat-Santiago, F.; Bisquert, J.; Palomares, E.; Otero, L.; Kuang, D.; Zakeeruddin, S. M.; Grätzel, M. *J. Phys. Chem. C* **2007**, *111*, 6550.
63. Qin, C.; Wong, W. Y.; Han, L. *Chem. Asian J.* **2013**, *8*, 1706.
64. Koumura, N.; Wang, Z.-S.; Mori, S.; Miyashita, M.; Suzuki, E.; Hara, K. *J. Am. Chem. Soc.* **2006**, *128*, 14256.
65. Haque, S. A.; Tachibana, Y.; Klug, D. R.; Durrant, J. R. *J. Phys. Chem. B* **1998**, *102*, 1745.
66. Zhang, S.; Yang, X.; Numata, Y.; Han, L. *Energy Environ. Sci.* **2013**, *6*, 1443.
67. Kim, B. G.; Chung, K.; Kim, J. *Chem. Eur. J.* **2013**, *19*, 5220.
68. Sirringhaus, H. *Adv. Mater.* **2014**, *26*, 1319.
69. Ostroverkhova, O. *Chem. Rev.* **2016**, *116*, 13279.
70. Tang, C. W.; VanSlyke, S. A. *Appl. Phys. Lett.* **1987**, *51*, 913.
71. Coropceanu, V.; Cornil, J.; da Silva Filho, D. A.; Olivier, Y.; Silbey, R.; Brédas, J.-L. *Chem. Rev.* **2007**, *107*, 926.
72. Allard, S.; Forster, M.; Souharce, B.; Thiem, H.; Scherf, U. *Angew. Chem. Int. Ed.* **2008**, *47*, 4070.
73. Zaumseil, J.; Sirringhaus, H. *Chem. Rev.* **2007**, *107*, 1296.
74. Wang, C.; Dong, H.; Hu, W.; Liu, Y.; Zhu, D. *Chem. Rev.* **2011**, *112*, 2208.
75. Mas-Torrent, M.; Rovira, C. *Chem. Rev.* **2011**, *111*, 4833.
76. Horowitz, G. *Adv. Mater.* **1998**, *10*, 365.
77. Dong, H.; Wang, C.; Hu, W. *Chem. Commun.* **2010**, *46*, 5211.
78. Sergeev, S.; Pisula, W.; Geerts, Y. H. *Chem. Soc. Rev.* **2007**, *36*, 1902.
79. Mei, J.; Diao, Y.; Appleton, A. L.; Fang, L.; Bao, Z. *J. Am. Chem. Soc.* **2013**, *135*, 6724.
80. Quinn, J. T.; Zhu, J.; Li, X.; Wang, J.; Li, Y. *J. Mater. Chem. C* **2017**, *5*, 8654.
81. Xu, S.; Ai, N.; Zheng, J.; Zhao, N.; Lan, Z.; Wen, L.; Wang, X.; Pei, J.; Wan, X. *RSC Adv.* **2015**, *5*, 8340.
82. Wu, Q.; Li, R.; Hong, W.; Li, H.; Gao, X.; Zhu, D. *Chem. Mater.* **2011**, *23*, 3138.
83. Afzali, A.; Dimitrakopoulos, C. D.; Breen, T. L. *J. Am. Chem. Soc.* **2002**, *124*, 8812.
84. Gao, J.; Li, R.; Li, L.; Meng, Q.; Jiang, H.; Li, H.; Hu, W. *Adv. Mater.* **2007**, *19*, 3008.
85. Hunziker, C.; Zhan, X.; Losio, P. A.; Figi, H.; Kwon, O.-P.; Barlow, S.; Günter, P.; Marder, S. R. *J. Mater. Chem.* **2007**, *17*, 4972.
86. Salleo, A. *Mater. Today* **2007**, *10*, 38.

# CHAPTER II

---

## **Heterotriangulene Based Unsymmetrical Squaraine Dyes for Dye-Sensitized Solar Cells**

## 2.1 INTRODUCTION

Organic dyes are represented by judicious arrangement of donor (D),  $\pi$ -spacer, and acceptor (A) moieties connected by covalent bonds. This D- $\pi$ -A dye structure is essential for efficient intramolecular charge transfer (ICT) from the donor to the acceptor through the  $\pi$ -bridge in the excited state. Although, significant improvement has been made in the organic dyes as sensitizers for DSSCs, optimization of their chemical structures is still needed for further enhancement in performance. Preferably, the dye sensitizer in DSSCs should have the strong light absorption ability in visible and the near-IR (NIR) regions. Out of many non-radiative pathways for the excited states, i) self quenching ii) Torsional distortion initiates de-excitation of molecules are in the main.<sup>1</sup> A suitable structure is needed to avoid aggregation among the dyes and should suppress the charge recombination of electrons in the TiO<sub>2</sub> film and with I<sub>3</sub><sup>-</sup>. One of the most numerous ways to alter the absorption of all organic dyes is the extension of the efficient conjugation length by planarization of the donor. Therefore, integrating planar donors and acceptors with branched alkyl chain collectively in a conjugated framework is a successful approach to modulate absorption band of all-organic dyes.<sup>2</sup>

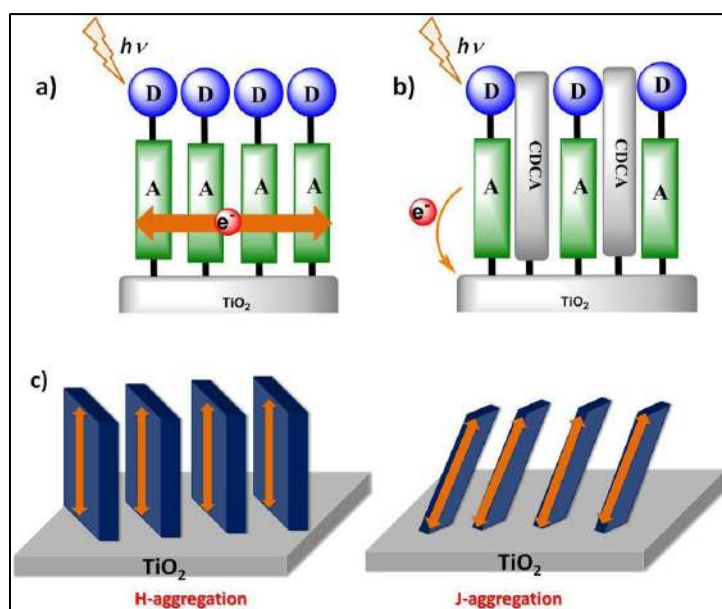


**Figure 1.** Molecular arrangement of dye adsorbed on a TiO<sub>2</sub> film: a)  $\pi$ -stacked dye aggregation, b) co-adsorption of CDCA with dyes, and c) H and J-aggregation of dyes on a TiO<sub>2</sub> surface.

In DSSCs, dyes tend to cause  $\pi$ -stacked aggregation through the formation of intermolecular  $\pi$ - $\pi$  interactions between dye molecules on the  $\text{TiO}_2$  surface; these interactions affect the electron injection into the  $\text{TiO}_2$  (**Figure 1a**).<sup>3,4</sup> The dye aggregation influences absorption shift to the blue (H-aggregation) or red (J-aggregation) regions relative to the absorption of the monomeric dye on the surface of  $\text{TiO}_2$ . Predominantly, H-aggregation normally quenches the excited state which severely hampers the electron injection (**Figure 1c**). The co-adsorption of chenodeoxycholic acid (CDCA) with dye molecule is found as one of the solution for reducing the dye aggregations on the  $\text{TiO}_2$  surface and showed drastically increase in the conversion efficiency. Still, the co-adsorption methods need cumbersome optimizations for each dye so it is necessary to find an efficient and suitable approach to suppress the dye-aggregation on the  $\text{TiO}_2$  surface (**Figure 1b**).<sup>5</sup> The fluorene and oligo(4,4-dihexyl-4H-cyclopenta[1,2-b:5,4-b']dithiophene) (CPDT) functionalities have been used as  $\pi$ -spacer in the D- $\pi$ -A dye structure and offer the dye with favorable steric properties.<sup>6</sup> The fluorene core or CPDT core is substituted with out-of-plane alkyl chains sufficiently insulates the  $\text{TiO}_2$  surface from the electrolyte, and inhibits charge recombination and avoid the dye aggregation.<sup>7</sup> The most successful strategy to improve the LHE of organic dyes is the use NIR dye skeletons, which afford good absorption of light in the visible and NIR region of the solar spectrum and get higher photocurrent.<sup>8</sup> Squaraines are one of the polymethine dyes which have created a center of attention in DSSCs because of their intense absorption in the far-red and NIR regions, and high molar extinction coefficient ( $\epsilon$ ) [ $\sim 10^5 \text{ M}^{-1} \text{ cm}^{-1}$ ].<sup>9,10</sup> Even though, these dyes are having potential to harvest NIR light still their performance has been limited by a comparatively low open-circuit potential ( $V_{oc}$ ) and major dye aggregation, which greatly affects the short-circuit current density ( $J_{sc}$ ). These squaraine dye forms either H- or J- type aggregates or affects the excited state electron lifetime on the  $\text{TiO}_2$  surface.<sup>11,12</sup>

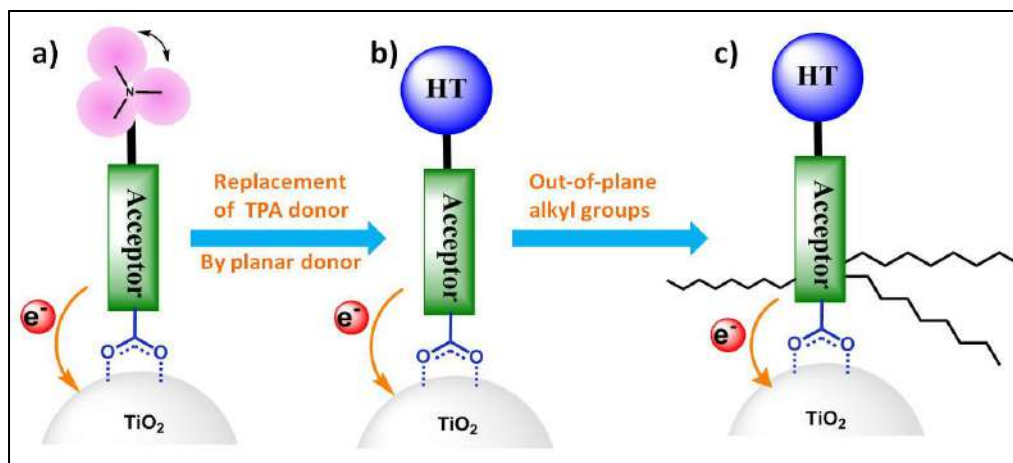


**Figure 2.** Schematic representation of sequential structural modification of NSQ dyes: a) TPA donor based dyes b) Replacement of TPA by planar HT donor c) Introduction of alkyl chain to suppress the dye aggregation and charge recombination on the TiO<sub>2</sub> surface.

In this chapter, synthesized four new unsymmetrical dyes, which are designed by adopting two different donors [triphenyl amine (TPA) or heterotriangulene (HT)] and varying the alkyl functionalities on acceptor unit.<sup>13</sup> In these dyes, squaric acid unit is linked between either HT or TPA donor and indolium moiety having a carboxylic acid as an anchoring group to get target sensitizers of **NSQ1-3** or **NSQR**. Herein, the main approach is to extend the light absorption by replacing the propeller shaped TPA by HT unit followed by introduction of out-of-plane alkyl chain on the acceptor units to avoid the dye aggregation. The photophysical, electrochemical, and related ICT properties of a D- $\pi$ -A dye strongly depend on the planarity and electron-donating ability of D, and the electron-accepting ability of A.<sup>14</sup> TPA unit is widely used as donor in several dye structures because of their intrinsic electron-donating properties.<sup>15,16</sup> Still owing to their propeller shape, these dyes are lacking in rigidity also it has poor extension of  $\pi$ -conjugation over the whole molecule due to the large dihedral angles between the phenyl rings and the plane of the N-bonded carbon atoms (**Figure 2**).<sup>17</sup> Such dye structure affects intermolecular charge transfer and hampers electron injection from dye to the electrode. However, planar and strong donor i.e. heterotriangulene (HT) was confirmed to achieve facile electron injection, increases the electronic coupling between donor and acceptor moieties of the dye, and localizes the positive charge of oxidized dyes.<sup>18</sup> This



donor moiety tends to assemble via  $\pi$ - $\pi$  stacking when anchored on  $\text{TiO}_2$ . Additionally to an electron-donating effect in organic dyes, the donor moiety should be organized in a way that the dye should not be interact with neighbouring dyes and suppress the dye aggregation on the  $\text{TiO}_2$ .<sup>19</sup>

Furthermore, to prevent aggregation of dye molecules on the  $\text{TiO}_2$  surface and recombination of injected electrons with the dye cations and  $\text{I}_3^-$  ions in the electrolyte, the introduction of in-plane and out-of-plane alkyl substituent on an acceptor part is needed (**Figure 3**).<sup>20</sup> The introduction of long and branched alkyl chains on indolium unit is to increase the solubility, reduce the undesirable dye aggregation and avoid dye desorption by reducing the infiltration of solvent to the  $\text{TiO}_2$  surface.<sup>21,22</sup> Here in, systematically connected alkyl groups in the N- and  $\text{sp}^3$ -C atoms of indolium unit to give an in-plane and out-of-plane branching of hydrophobic chains, respectively.

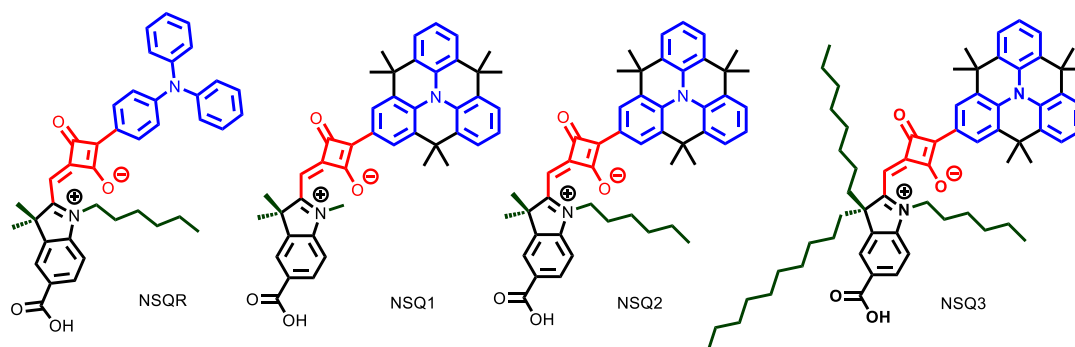


**Figure 3.** Molecular structures of the unsymmetrical squaraine **NSQR** and **NSQ1-3** sensitizers.

## 2.2 EXPERIMENTAL SECTION

### 2.2.1 Materials and Characterization

All reagents were purchased from commercial sources. Solvents were dried and distilled immediately prior to use by standard procedures. All reactions were carried out under an argon atmosphere. Procedure for the synthesis of **NSQ1-3** and **NSQR** are given in **Scheme 1 and Scheme 2**. Characterizations of all compounds are provided in section 2.5.  $^1\text{H}$  NMR and  $^{13}\text{C}$  NMR were recorded in  $\text{CDCl}_3$ ,  $\text{MeOH-}d_4$  or  $\text{DMSO-}d_6$  on 200 MHz NMR, 400 MHz NMR and 500 MHz NMR spectrometers. High-resolution mass spectrometric measurements (HR-MS) were carried out using the ESI method and an ion-trap mass analyzer. Absorption spectra were recorded at room temperature in quartz cuvette using Analytik Jena UV-Visible spectrophotometer. Electrochemical measurement was carried out using a Bio-Logic potentiostat (model no: SP300). The cyclic voltammetric analysis (CV) was carried out in dry acetonitrile solvent by using 0.1 M tetrabutylammonium perchlorate as supporting electrolyte and  $\text{Fc}/\text{Fc}^+$  as external reference. The experiments were performed at room temperature in nitrogen atmosphere with a three-electrode cell consisting of a platinum foil as counter electrode, an  $\text{Ag}/\text{Ag}^+$  reference electrode, and a platinum wire as working electrode.

### 2.2.2 Solar cells preparation and characterization

FTO (F-doped  $\text{SnO}_2$  glass; 6 - 8  $\Omega$  /sq; Pilkington TEC 7) was cleaned by mucasol (2 % in water), deionised water and ethanol, successively. To grow a  $\text{TiO}_2$  under layer, the substrate was immersed in freshly prepared 50 mM  $\text{TiCl}_4$  aqueous solution at 70  $^\circ\text{C}$  for 30 min, and washed with deionised water before drying at 100  $^\circ\text{C}$  for 10 min. A paste of  $\text{TiO}_2$  nanocrystal (< 20 nm, Ti-Nanoxide T/SP, Solaronix) was deposited by the doctor-blade technique on  $\text{TiO}_2$  buffer layer coated FTO substrate, kept in air for 5 min and then annealed at 125  $^\circ\text{C}$  in air for 15 min. The films were about 6 - 8  $\mu\text{m}$  thick. The annealed films were coated with scattering layer  $\text{TiO}_2$  paste (WER2-O, Dyesol) and annealed at 125  $^\circ\text{C}$  in air for 15 min. The annealed films were sintered at 325  $^\circ\text{C}$  for 5 min, 375  $^\circ\text{C}$  for 5 min, 450  $^\circ\text{C}$  for 15 min and 500  $^\circ\text{C}$  for 15 min with heating rate of 5  $^\circ\text{C}$  per min in air. After reaching the furnace temperature at 50  $^\circ\text{C}$ , sintered films were immersed in freshly prepared 50 mM aqueous  $\text{TiCl}_4$  solution at 70  $^\circ\text{C}$  for 30 min. After sintering the  $\text{TiCl}_4$ -

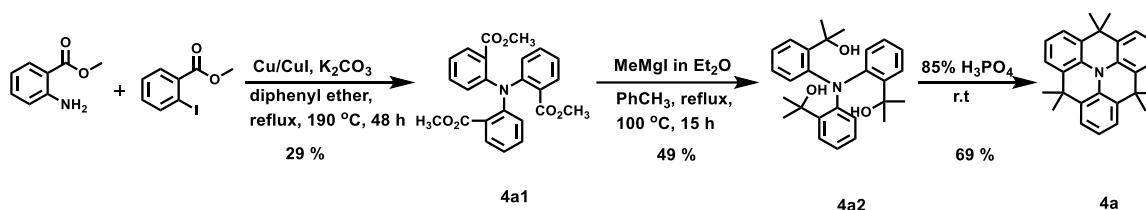
treated TiO<sub>2</sub> films at 500 °C for 30 min, they were immediately immersed in 0.1 mM NSQ dye solution in CH<sub>3</sub>CN for 2.5 h, washed and dried at 80 °C. In case of CDCA added experiments, different ratio of CDCA added to 0.1 mM dye solution and photoanode dipped for 2.5 h. Sandwich type cell configuration was completed using platinum as cathode, 0.5 M DMII, 0.1 M LiI, 0.1 M I<sub>2</sub> and 10 mM TBP in CH<sub>3</sub>CN was used as electrolyte and 25 μm spacer. *J-V* characteristics of the cells were measured using Keithley digital source meter (2420, Keithley, USA) controlled by a computer and standard AM 1.5 solar simulator (PET, CT200AAA, USA). To measure the photocurrent and voltage, an external bias of AM 1.5G light was applied using a xenon lamp (450 W, USHIO INC, Philippines) and recorded. IPCE measurements were carried out with a Newport QE measurement kit by focusing a monochromatic beam of light from 300 W Xe lamp onto the devices. The electrochemical impedance spectroscopy (EIS) measurements of the DSSCs were recorded with a Bio-Logic potentiostat (model no: SP300), equipped with an FRA2 module, with different potentials applied in dark. The frequency range explored was 1 mHz to 1 MHz with an ac perturbation of 10 mV. The impedance spectra were analyzed using an equivalent circuit model. OCVD profile was measured with a Bio-Logic potentiostat (model no: SP300), equipped with an FRA2 module, the dye cell was illuminated for 10 sec at 1 sun intensity (100 mW/cm<sup>2</sup>) and V<sub>OC</sub> decay recorded in dark.

### 2.2.3 Dye desorption from the photoanode

The TiO<sub>2</sub> coated FTO electrodes (0.22 cm<sup>2</sup>, thickness of TiO<sub>2</sub> layer 8 + 4 μm) were dipped in 0.1 mM of **NSQR**, **NSQ1-3** in CH<sub>2</sub>Cl<sub>2</sub> for 6 h at room temperature, and then washed with CH<sub>2</sub>Cl<sub>2</sub> to remove the physisorbed dyes. The electrodes were immersed in 2 M ethanolic HCl for 30 min until all the dyes completely desorbed and the amount of adsorbed dye is calculated by UV-Vis experiments.

### 2.2.4 SYNTHETIC PROCEDURE AND CHARACTERIZATION DATA

4,4,8,8,12,12-Hexamethyl-4H,8H,12H-benzo[9,1]quinolizino[3,4,5,6,7,-defg]acridine (**HBQA,4a**) was synthesized using a procedure of previous references.<sup>23,24</sup>



**Scheme 1.** Synthesis of HT donor units [4,4,8,8,12,12-Hexamethyl-4H,8H,12H-benzo[9,1]quinolizino[3,4,5,6,7,-defg]acridine (HBQA, **4a**).

### Trimethyl 2,2',2''-nitritotribenzoate (**4a1**)

A mixture of Methyl anthranilate (10 g, 66.19 mmol), Methyl 2-iodobenzoate (49.44 g, 188.66 mmol),  $K_2CO_3$  (21 g, 150.91 mmol), Cu (0.84 g, 13.23 mmol) and CuI (1.22 g, 6.42 mmol) in diphenylether (100 mL) was heated at 190 °C under argon for 48 h. The solvent was removed under reduced pressure and the residue was purified by silica gel chromatography using pet ether–ethyl acetate as eluent to give **4a1** (8 g, 29 %) as a yellow solid.  $^1H$  NMR (200 MHz,  $CDCl_3$ )  $\delta$ : 7.58 (d,  $J = 6.2$  Hz, 3 H), 7.42 - 7.30 (m, 3 H), 7.17 - 6.91 (m, 6 H), 3.36 (br. s., 9 H).  $^{13}C$  NMR (50 MHz,  $CDCl_3$ )  $\delta$ : 167.8, 147.0, 132.3, 131.1, 127.5, 126.3, 123.6, 51.7. HRMS (ESI):  $m/z$  calcd for  $C_{24}H_{21}O_6NNa$  ( $[M + Na]^+$ ): 442.1261. Found: 442.1261.

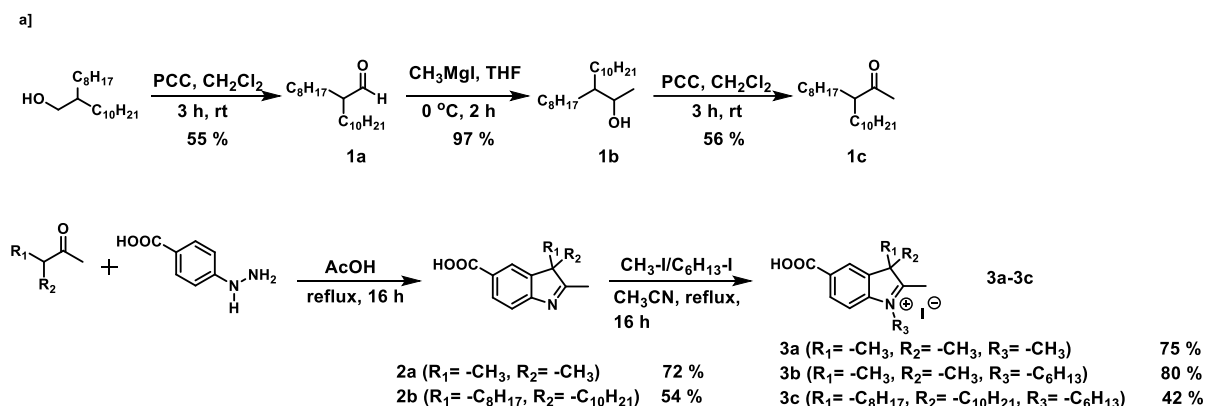
### Synthesis of 2,2',2''-(Nitritotris(benzene-2,1-diyl))tris(propan-2-ol) **4a2**

To a stirred solution of **4a1** (8 g, 19.07 mmol) in toluene (180 mL) methyl magnesium iodide [3 M solution in diethyl ether] (114.4 mL, 343.32 mmol) and refluxed for 15 h at 110 °C. The reaction mixture was cooled and poured into aq. solution of ammonium chloride (150 mL). Then mixture was extracted with ethyl acetate and washed with water, dried over  $Na_2SO_4$ , concentrated and purified by column chromatography to afford **4a2** (3.9 g, 49 %) as pale yellow solid.  $^1H$  NMR (400 MHz,  $CDCl_3$ )  $\delta$ : 7.33 (dd,  $J = 2.0, 7.6$  Hz, 3 H), 7.15 - 7.03 (m, 6 H), 6.67 (dd,  $J = 1.7, 7.6$  Hz, 3 H), 5.40 (br. s., 2 H), 1.66 (s, 9 H), 0.84 (s, 9 H).  $^{13}C$  NMR (100 MHz,  $CDCl_3$ )  $\delta$ : 149.0, 142.7, 129.9, 129.6, 127.2, 124.7, 74.1, 34.5, 30.3. HRMS calcd for  $C_{27}H_{34}NO_3$  ( $[M + H]^+$ ): 420.2533; found: 420.2530.

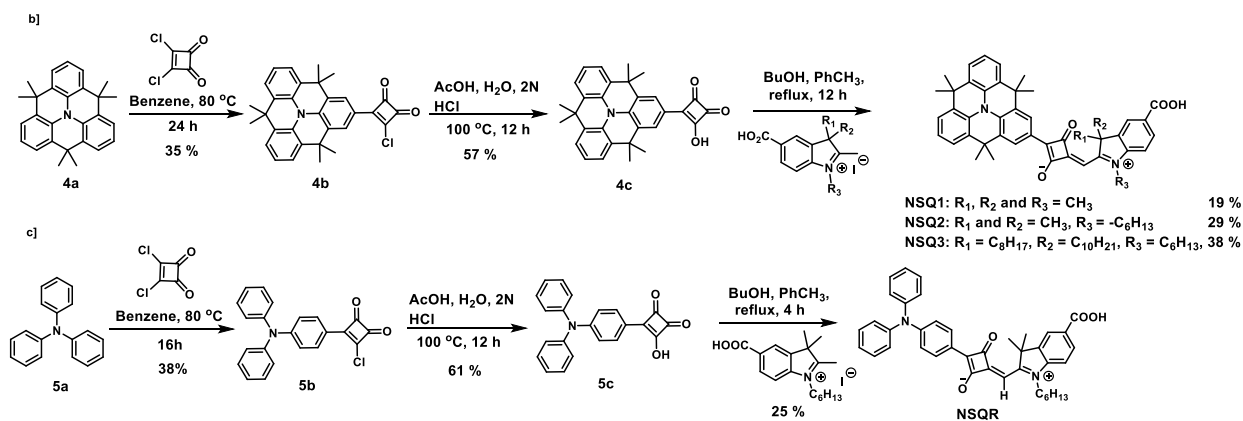
### 4,4,8,8,12,12-Hexamethyl-8,12-dihydro-4H-benzo[9,1]quinolizino[3,4,5,6,7-defg]acridine 4a

2,2',2''-(Nitrilotris(benzene-2,1-diyl))tris(propan-2-ol) (3 g, 7.15 mmol) was dispersed in 85% H<sub>3</sub>PO<sub>4</sub> (20 mL) and stirred it for 6 h. The reaction mixture was poured into ice cold solution of 2 M NaOH, extracted with CH<sub>2</sub>Cl<sub>2</sub>, washed with water, dried and purified by column chromatography to afford **4a** (1.8 g, 69 %) as a light orange solid. <sup>1</sup>H NMR (400 MHz, CDCl<sub>3</sub>) δ: 7.38 (d, *J* = 7.8 Hz, 6 H), 7.13 (t, *J* = 7.8 Hz, 3 H), 1.64 (s, 18 H). <sup>13</sup>C NMR (100 MHz, CDCl<sub>3</sub>) δ: 132.0, 129.9, 123.6, 122.9, 35.6, 33.2. HRMS calcd for C<sub>27</sub>H<sub>27</sub>N (M<sup>+</sup>): 365.2138; found: 365.2137.

### Synthesis of indolium units:



### Synthesis of NSQR and NSQ1-3



**Scheme 2.** (a) Syntheses of indolium iodide (**3a–3c**), (b) **NSQ1–3** dyes and (c) **NSQR** dye.

**2-Octyldodecanal (1a)**<sup>25</sup>

To a solution of 2-Octyldodecan-1-ol (4 g, 13.4 mmol) in CH<sub>2</sub>Cl<sub>2</sub> (30 mL), pyridiniumchlorochromate (7.2 g, 33.5 mmol) was added and stirred at room temperature for 3 h. The crude mixture was filtered through silica gel column chromatography, washed with pet ether, solvent was evaporated and dried under reduced pressure to afford **1a** (2.2 g, 55 %) as pale yellow liquid. <sup>1</sup>H NMR (400 MHz, CDCl<sub>3</sub>) δ: 9.55 (d, J = 3.2 Hz, 1 H), 2.40 - 2.29 (m, 1 H), 1.62 - 1.56 (m, 2 H), 1.47 - 1.43 (m, 2 H), 1.25 (br. s., 28 H), 0.89 - 0.87 (m, 6 H). <sup>13</sup>C NMR (100 MHz, CDCl<sub>3</sub>) δ: 211.9, 182.8, 161.1, 77.3, 77.2, 76.7, 74.6, 72.1, 45.5, 42.8, 37.4, 34.0, 32.2, 31.9, 31.8, 29.7, 29.6, 29.6, 29.5, 29.5, 29.3, 29.3, 29.3, 29.1, 27.4, 25.6, 25.2, 23.9, 22.7, 14.1. MALDI-TOF (m/z): [M]<sup>+</sup> calcd for C<sub>20</sub>H<sub>40</sub>O: 296.3079; found: 296.2517.

**3-Octyltridecan-2-ol (1b)**

2-Octyldodecanal (2 g, 6.74 mmol) was dissolved in dry THF (20 mL) at 0 °C, and then CH<sub>3</sub>MgI (3.37 mL, 10.1 mmol) was slowly added. The mixture was stirred at 0 °C for 2 h, then quenched by adding saturated aqueous solution of ammonium chloride, extracted with ethyl acetate and dried over Na<sub>2</sub>SO<sub>4</sub>. The organic layer was concentrated under reduced pressure to afford **1b** (2.03 g, 97 %) as pale yellow liquid. This product was used further without purification. <sup>1</sup>H NMR (200 MHz, CDCl<sub>3</sub>) δ: 3.81 (q, J = 5.8 Hz, 1 H), 1.70 (br. s., 1 H), 1.26 (br. s, 33 H), 1.12 (d, J = 6.3 Hz, 3 H), 0.94 - 0.84 (m, 6 H). <sup>13</sup>C NMR (100 MHz, CDCl<sub>3</sub>) δ: 69.7, 44.8, 37.4, 32.2, 31.9, 31.9, 30.2, 30.1, 30.1, 30.1, 29.7, 29.6, 29.6, 29.5, 29.5, 29.4, 29.3, 29.3, 27.4, 27.4, 25.6, 22.7, 19.8, 14.1.

**3-Octyltridecan-2-one (1c)**

To a solution of 3-Octyltridecan-2-ol (2 g, 6.34 mmol) in CH<sub>2</sub>Cl<sub>2</sub> (30 mL), pyridiniumchlorochromate (2.76 g, 12.68 mmol) and celite (PCC: celite, 1:1, 2.76 g) were added and stirred at room temperature for 3 h. The reaction mixture was filtered through silica gel column chromatography, washed with dichloromethane, solvent was evaporated and purified by column chromatography to afford **1c** (1.1 g, 56 %) as colorless liquid. <sup>1</sup>H NMR (200 MHz, CDCl<sub>3</sub>) δ: 2.45 - 2.32 (m, 1 H), 2.06 (s, 3 H), 1.57 - 1.48 (m, 2 H), 1.42 - 1.30 (m, 2 H), 1.21 (br. s, 28 H), 0.88 - 0.78 (m, 6 H). <sup>13</sup>C NMR (100 MHz, CDCl<sub>3</sub>) δ: 212.9, 53.3, 31.8, 31.8, 31.7, 29.7, 29.5, 29.4, 29.4, 29.3, 29.2,

29.1, 28.5, 27.4, 22.6, 14.0. HRMS (ESI):  $m/z$  calcd for  $C_{21}H_{43}O$  ( $[M + H]^+$ ): 311.3308. Found: 311.3316.

### **2,3,3-Trimethyl-3H-indole-5-carboxylic acid (2a)**

4-Hydrazinobenzoic acid hydrochloride (4 g, 21.2 mmol) and 3-methyl-2-butanone (3.92 mL, 36.69 mmol) were dissolved into glacial acetic acid (40 mL) and refluxed under nitrogen for 16 h. The mixture was cooled and the solvent was removed under reduced pressure. The residue was dissolved by adding  $CH_2Cl_2$ , and then washed with saturated solution of  $NaHCO_3$  and dried over  $Na_2SO_4$ . The organic layer was concentrated to afford **2a** (3.1 g, 72 %) as a light red solid.  $^1H$  NMR (200 MHz,  $CDCl_3$ )  $\delta$ : 10.56 (br. s., 1 H), 8.15 (dd,  $J = 8.1, 1.6$  Hz, 1 H), 8.07 (d,  $J = 1.6$  Hz, 1 H), 7.69 (d,  $J = 8.1$  Hz, 1 H), 2.39 (s, 3 H), 1.37 (s, 6 H).  $^{13}C$  NMR (100 MHz,  $CDCl_3$ )  $\delta$ : 192.5, 170.9, 156.9, 145.4, 130.7, 127.2, 123.2, 119.5, 53.8, 22.8, 15.4. HRMS (ESI):  $m/z$  calcd for  $C_{12}H_{14}NO_2$  ( $[M + H]^+$ ): 204.1019. Found: 204.1018.

### **3-Decyl-2-methyl-3-octyl-3H-indole-5-carboxylic acid (2b)**

4-Hydrazinobenzoic acid hydrochloride (0.6 g, 3.18 mmol) and 3-octyltridecan-2-one (1.18 g, 3.82 mmol) were dissolved into glacial acetic acid (12 mL) and refluxed under nitrogen for 12 h. The mixture was cooled and the solvent was removed under vacuum. The crude product was extracted with  $CH_2Cl_2$ , washed with saturated solution of  $NaHCO_3$ , dried over  $Na_2SO_4$  and solvent was evaporated. The reaction mixture was purified by silica gel chromatography to afford **2b** (0.74 g, 54 %) as a light red liquid.  $^1H$  NMR (400 MHz,  $CDCl_3$ )  $\delta$ : 11.78 (br. s., 1 H), 8.17 (dd,  $J = 8.0, 1.6$  Hz, 1 H), 7.99 (s, 1 H), 7.70 (d,  $J = 8.0$  Hz, 1 H), 2.33 (s, 3 H), 2.02 - 1.88 (m, 2 H), 1.83 - 1.71 (m, 2 H), 1.25 - 1.07 (m, 24 H), 0.85 - 0.80 (m, 6 H), 0.75 - 0.65 (m, 2 H), 0.61 - 0.52 (m, 2 H).  $^{13}C$  NMR (100 MHz,  $CDCl_3$ )  $\delta$ : 191.4, 171.2, 158.4, 142.2, 130.7, 127.1, 123.3, 119.2, 63.0, 36.9, 31.8, 31.7, 29.7, 29.5, 29.5, 29.4, 29.3, 29.3, 29.2, 29.1, 29.1, 23.5, 22.6, 22.5, 16.0, 14.0, 14.0. HRMS (ESI):  $m/z$  calcd for  $C_{28}H_{46}NO_2$  ( $[M + H]^+$ ): 428.3523. Found: 428.3524.

### **5-Carboxy-1,2,3,3-tetramethyl-3H-indol-1-ium iodide (3a)**

In a 50 mL round bottom flask, 2,3,3-Trimethyl-3H-indole-5-carboxylic acid (1.5 g, 7.38 mmol) and 1-iodomethane (1.15 mL, 18.45 mmol) were dissolved in  $CH_3CN$  (12 mL),



and refluxed under nitrogen for 16 h. The solvent was evaporated and the crude product was washed with diethyl ether to afford **3a** (1.2 g, 75 %) as red solid.  $^1\text{H}$  NMR (400 MHz,  $\text{DMSO-}d_6$ )  $\delta$ : 8.37 (s, 1 H), 8.18 (d,  $J = 8.2$  Hz, 1 H), 8.02 (d,  $J = 8.2$  Hz, 1 H), 3.99 (s, 3 H), 2.81 (s, 3 H), 1.57 (s, 6 H).  $^{13}\text{C}$  NMR (100 MHz,  $\text{DMSO-}d_6$ )  $\delta$ : 199.0, 166.5, 145.3, 141.9, 131.6, 130.4, 124.2, 115.4, 54.3, 35.0, 21.5, 14.6. HRMS (ESI):  $m/z$  calcd for  $\text{C}_{13}\text{H}_{16}\text{NO}_2$  ( $\text{M}^+$ ): 218.1176. Found: 218.1175.

### 5-Carboxy-1-hexyl-2,3,3-trimethyl-3H-indol-1-ium iodide (3b)

In a 50 mL round bottom flask, 2,3,3-Trimethyl-3H-indole-5-carboxylic acid (1.5 g, 7.38 mmol) and 1-iodohexane (2.72 mL, 18.45 mmol) were dissolved in  $\text{CH}_3\text{CN}$  (12 mL) and refluxed under nitrogen for 16 h. The solvent was evaporated and the crude product was washed with diethyl ether to afford **3b** (1.7 g, 80 %) as red solid.  $^1\text{H}$  NMR (200 MHz,  $\text{DMSO-}d_6$ )  $\delta$ : 8.39 (br. s., 1 H), 8.25 - 8.04 (m, 2 H), 4.54 - 4.35 (m, 2 H), 2.89 (br. s., 3 H), 1.57 (br. s., 6 H), 1.32 (d,  $J = 7.7$  Hz, 8 H), 0.93 - 0.83 (m, 3 H).  $^{13}\text{C}$  NMR (100 MHz,  $\text{DMSO-}d_6$ )  $\delta$ : 192.9, 167.4, 155.6, 145.7, 129.7, 127.7, 122.9, 118.7, 53.6, 22.2, 21.9, 15.4, 13.8. HRMS (ESI):  $m/z$  calcd for  $\text{C}_{18}\text{H}_{26}\text{NO}_2$  ( $\text{M}^+$ ): 288.1958. Found: 288.1956.

### 5-Carboxy-3-decyl-1-hexyl-2-methyl-3-octyl-3H-indol-1-ium iodide (3c)

3-Decyl-2-methyl-3-octyl-3H-indole-5-carboxylic acid (0.7 g, 1.64 mmol) and 1-iodohexane (0.48 mL, 3.27 mmol) were dissolved in  $\text{CH}_3\text{CN}$  (10 mL) in a 25 mL round bottom flask and refluxed at 100 °C under nitrogen for 72 h. The solvent was evaporated and the crude product was purified by silica gel chromatography to afford 3-Decyl-1-hexyl-3-methyl-2-methyleneindoline-5-carboxylic acid (0.35 g, 42 %) as a light red liquid.  $^1\text{H}$  NMR (200 MHz,  $\text{CDCl}_3$ )  $\delta$ : 7.96 (dd,  $J = 1.5, 8.3$  Hz, 1 H), 7.68 (d,  $J = 1.5$  Hz, 1 H), 6.50 (d,  $J = 8.3$  Hz, 1 H), 4.12 (s, 1 H), 3.87 (s, 1 H), 3.53 (t,  $J = 7.1$  Hz, 2 H), 1.85 - 1.44 (m, 6 H), 1.40 - 1.02 (m, 35 H), 0.86 (dd,  $J = 2.7, 6.0$  Hz, 6 H), 0.73 - 0.58 (m, 2 H). In a 25 mL RB flask, 3-Decyl-1-hexyl-3-methyl-2-methyleneindoline-5-carboxylic acid (0.25 g, 0.49 mmol) was added in dry diethyl ether (5 mL). Then hydroiodic acid (57 wt% in water, 0.20 mL, 0.98 mmol) was added dropwise. The mixture was stirred at room temperature for 2 h. The diethyl ether was removed in vacuum to give **3c** (0.22 g, 88 %) as brown liquid.  $^1\text{H}$  NMR (500 MHz,  $\text{CDCl}_3$ )  $\delta$ : 8.36 (d,  $J = 8.2$  Hz, 1 H), 8.20 (s, 1 H), 7.95 (d,  $J = 8.2$  Hz, 1 H), 4.96 - 4.75 (m, 2 H), 3.15 (s, 3 H), 2.30 - 2.18 (m, 2 H),

2.17 - 2.10 (m, 2 H), 1.99 - 1.91 (m, 2 H), 1.60 - 1.45 (m, 2 H), 1.42 - 1.26 (m, 6 H), 1.25 - 1.15 (m, 11 H), 1.13 (br. s., 13 H), 0.88 - 0.81 (m, 9 H), 0.72 - 0.63 (m, 2 H).  $^{13}\text{C}$  NMR (100 MHz,  $\text{CDCl}_3$ )  $\delta$ : 198.8, 168.3, 145.6, 139.1, 132.1, 131.5, 125.0, 115.9, 64.1, 50.9, 37.3, 31.8, 31.6, 31.3, 29.6, 29.4, 29.2, 29.0, 28.9, 28.6, 26.6, 24.2, 22.6, 22.5, 22.4, 17.5, 14.1, 14.0, 13.9. HRMS (ESI):  $m/z$  calcd for  $\text{C}_{34}\text{H}_{58}\text{NO}_2$  ( $\text{M}^+$ ): 512.4462. Found: 512.4462.

### **3,4-Dichlorocyclobut-3-ene-1,2-dione<sup>26</sup>**

Squaric acid (1 g, 8.76 mmol) was dissolved in 15 mL of benzene in a 50 mL round bottom flask. Thionyl chloride (1.27 mL, 17.53 mmol) was added dropwise, after half of the addition was over, a drop of dry DMF was added and then continued the dropwise addition of thionyl chloride at room temperature. The mixture was refluxed for 6 h and cooled to room temperature. Excess of solvent was removed and the residue was dissolved in hexane and kept in refrigerator to isolate pale yellow crystals of the required 3,4-Dichlorocyclobut-3-ene-1,2-dione (Yield: 0.56 g, 42 %).

### **3-Chloro-4-(4,4,8,8,12,12-hexamethyl-8,12-dihydro-4H-benzo[9,1]quinolizino[3,4,5,6,7-defg]acridin-2-yl)cyclobut-3-ene-1,2-dione (4b)**

A mixture of 4,4,8,8,12,12-Hexamethyl-8,12-dihydro-4H-benzo[9,1]quinolizino[3,4,5,6,7-defg]acridine (**4a**) (1 g, 2.74 mmol) and 3,4-dichlorocyclobut-3-ene-1,2-dione (0.45 g, 3 mmol) in benzene (15 mL) was heated at 80 °C for 24 h in a 50 mL round bottom flask. The resultant reaction mixture was cooled and solvents were removed under reduced pressure and purified by column chromatography to give 3-Chloro-4-(4,4,8,8,12,12-hexamethyl-8,12-dihydro-4H-benzo[9,1]quinolizino[3,4,5,6,7-defg]acridin-2-yl)cyclobut-3-ene-1,2-dione (**4b**) (0.46 g, 35 %) as yellow solid.  $^1\text{H}$  NMR (200 MHz,  $\text{CDCl}_3$ )  $\delta$ : 8.26 (s, 2 H), 7.48 - 7.37 (m, 4 H), 7.24 - 7.17 (m, 2 H), 1.67 (s, 6 H), 1.64 (s, 12 H).  $^{13}\text{C}$  NMR (100 MHz,  $\text{CDCl}_3$ )  $\delta$ : 195.4, 190.3, 186.9, 175.0, 138.5, 131.2, 130.6, 130.2, 130.1, 124.9, 124.8, 124.3, 123.4, 121.1, 35.6, 35.4, 34.3, 32.2. HRMS (ESI):  $m/z$  calcd for  $\text{C}_{31}\text{H}_{26}\text{ClNO}_2\text{Na}$  ( $[\text{M} + \text{Na}]^+$ ): 502.1544. Found: 502.1544.

### **3-(4,4,8,8,12,12-Hexamethyl-8,12-dihydro-4H-benzo[9,1]quinolizino[3,4,5,6,7-defg]acridin-2-yl)-4-hydroxycyclobut-3-ene-1,2-dione (4c)**

A mixture of 3-Chloro-4-(4,4,8,8,12,12-hexamethyl-8,12-dihydro-4H-benzo[9,1]quinolizino[3,4,5,6,7-defg]acridin-2-yl)cyclobut-3-ene-1,2-dione (**4b**) (0.4 g, 0.83 mmol), acetic acid (5 mL), water (5 mL) and 2 N HCl (2 mL) was refluxed for 16 h in a 50 mL round bottom flask, the resultant mixture was concentrated under reduced pressure, and washed with aq. NaHCO<sub>3</sub> (50 mL) and brine (50 mL) to give 3-(4,4,8,8,12,12-hexamethyl-8,12-dihydro-4H-benzo[9,1]quinolizino[3,4,5,6,7-defg]acridin-2-yl)-4-hydroxycyclobut-3-ene-1,2-dione (**4c**) (0.22 g, 57 %) as brown solid. <sup>1</sup>H NMR (400 MHz, CDCl<sub>3</sub>) δ: 8.28 (s, 2 H), 7.48 - 7.40 (m, 4 H), 7.27 - 7.20 (m, 2 H), 1.69 (s, 6 H), 1.65 (s, 12 H). <sup>13</sup>C NMR (100 MHz, CDCl<sub>3</sub>) δ: 195.4, 190.4, 186.9, 175, 138.5, 131.2, 130.6, 130.2, 130.1, 124.9, 124.7, 124.3, 123.4, 121.1, 35.6, 35.4, 34.3, 32.1. HRMS (ESI): m/z calcd for C<sub>31</sub>H<sub>28</sub>NO<sub>3</sub> ([M + H]<sup>+</sup>): 462.2064. Found: 462.2061.

### 2.2.5 General procedure for synthesis of NSQ dyes

A mixture of 3-(4,4,8,8,12,12-Hexamethyl-8,12-dihydro-4H-benzo[9,1]quinolizino[3,4,5,6,7-defg]acridin-2-yl)-4-hydroxycyclobut-3-ene-1,2-dione (**4c**) (150 mg, 0.32 mmol) and **3a-3c** (0.36 mmol, 1.1 eq.) in toluene (3 mL), 1-butanol (3 mL) and pyridine (1 mL) was added in 25 mL round bottom flask and refluxed with a Dean-Stark apparatus for 5 h. The resultant mixture was concentrated under reduced pressure, then diluted with dichloromethane, dried over Na<sub>2</sub>SO<sub>4</sub>, and concentrated under vacuum to give a residue, which was purified with dichloromethane/ methanol to give **NSQ1-NSQ3** as green solid.

#### 5-Carboxy-2-[[3-[(4,4,8,8,12,12-hexamethyl-8,12-dihydro-4H-benzo[9,1]quinolizino[3,4,5,6,7-defg]acridine-2-yl)]-4-oxo-2-cyclobuten-2-olate-1-ylidene]methyl]-1,3,3-trimethyl-3H-indolium (NSQ1)

Yield: 19 %. <sup>1</sup>H NMR (200 MHz, DMSO-*d*<sub>6</sub>) δ: 8.24 (s, 2 H), 8.15 - 8.05 (m, 1 H), 7.78 (d, J = 8.46 Hz, 1 H), 7.44 - 7.44 (m, 5 H), 7.27 - 7.12 (m, 2 H), 6.26 (s, 1 H), 3.92 (s, 3 H), 1.81 (s, 6 H), 1.60 (br. s., 18 H). <sup>13</sup>C NMR (100 MHz, DMSO-*d*<sub>6</sub>) δ: 197.2, 191.7, 183.0, 179.5, 178.8, 168.3, 145.5, 142.9, 133.8, 130.3, 130.0, 129.9, 129.8, 126.4, 124.8, 124.3, 124.2, 123.8, 123.7, 123.5, 123.5, 121.9, 119.1, 113.1, 91.7, 50.9, 48.6, 35.2, 35.1, 34.0, 33.5, 32.8, 32.8, 32.4, 25.04. HRMS (ESI): m/z calcd for C<sub>44</sub>H<sub>41</sub>N<sub>2</sub>O<sub>4</sub> ([M + H]<sup>+</sup>): 661.3061. Found: 661.3059.

**5-Carboxy-2-[[3-[(4,4,8,8,12,12-hexamethyl-8,12-dihydro-4H-benzo[9,1]quinolizino [3,4,5,6,7-defg]acridine-2-yl)]-4-oxo-2-cyclobuten-2-olate-1-ylidene]methyl]-3,3-dimethyl-1-hexyl-3H-indolium (NSQ2)**

Yield: 29 %. <sup>1</sup>H NMR (400 MHz, DMSO-*d*<sub>6</sub>) δ: 8.24 (s, 2 H) 8.13 - 8.05 (m, 1 H), 7.79 (d, J = 8.31 Hz, 1 H), 7.56 - 7.36 (m, 5 H), 7.22 (t, J = 8.31 Hz, 2 H), 6.28 (s, 1 H), 4.39 (t, J = 6.60 Hz, 2 H), 1.81 (s, 6 H), 1.61 (s, 6 H), 1.59 (s, 12 H), 1.40 (br. s., 2 H), 1.35 - 1.18 (m, 6 H), 0.84 (t, J = 6.60 Hz, 3 H). <sup>13</sup>C NMR (100 MHz, DMSO-*d*<sub>6</sub>) δ: 192.3, 182.8, 179.3, 178.1, 169.2, 166.8, 144.7, 143.1, 133.9, 130.3, 129.9, 129.9, 129.8, 128.9, 126.3, 124.8, 124.3, 123.7, 123.7, 121.9, 113.1, 91.2, 50.9, 44.8, 35.2, 34.0, 32.4, 30.8, 27.2, 25.7, 25.2, 21.9, 13.8. HRMS (ESI): m/z calcd for C<sub>49</sub>H<sub>51</sub>N<sub>2</sub>O<sub>4</sub> ([M + H]<sup>+</sup>): 731.3843. Found: 731.3833.

**5-Carboxy-2-[[3-[(4,4,8,8,12,12-hexamethyl-8,12-dihydro-4H-benzo[9,1]quinolizino [3,4,5,6,7-defg]acridine-2-yl)]-4-oxo-2-cyclobuten-2-olate-1-ylidene]methyl]-3-decyl-1-hexyl-3-octyl-3H-indolium (NSQ3)**

Yield: 38 %. <sup>1</sup>H NMR (400 MHz, CDCl<sub>3</sub>) δ: 8.46 (s, 2 H), 8.24 (d, J = 8.8 Hz, 1 H), 8.12 (s, 1 H), 7.45 - 7.40 (m, 5 H), 7.21 (d, J = 8.8 Hz, 2 H), 6.48 (s, 1 H), 4.28 (br. s., 2 H), 3.14 (br. s., 2 H), 2.18 - 2.12 (m, 2 H), 1.86 (t, J = 7.3 Hz, 2 H), 1.70 (s, 12 H), 1.67 (s, 6 H), 1.47 - 1.44 (m, 2 H), 1.11 (br. s., 14 H), 1.05 (br. s., 10 H), 0.88 (t, J = 6.8 Hz, 6 H), 0.79-0.73 (m, 11.7 Hz, 9 H), 0.46 (br. s., 2 H). <sup>13</sup>C NMR (100 MHz, CDCl<sub>3</sub>) δ: 185.3, 180.1, 175.8, 170.0, 147.4, 136.0, 131.1, 130.9, 130.6, 130.3, 127.3, 126.1, 124.4, 124.3, 124.1, 123.6, 110.4, 91.7, 60.3, 45.1, 40.2, 39.9, 35.6, 35.4, 34.0, 32.7, 31.8, 31.7, 31.4, 29.7, 29.5, 29.4, 29.3, 29.2, 29.1, 29.0, 27.8, 26.7, 24.8, 24.1, 22.5, 22.5, 22.4, 14.0, 13.9. HRMS (ESI): m/z calcd for C<sub>65</sub>H<sub>83</sub>N<sub>2</sub>O<sub>4</sub> ([M + H]<sup>+</sup>): 955.6347. Found: 955.6331.

**3-Chloro-4-(4-(diphenylamino) phenyl)cyclobut-3-ene-1,2-dione (5b)**

In a 50 mL round bottom flask, a mixture of triphenylamine (**5a**) (0.8 g, 3.3 mmol) and 3,4-dichlorocyclobut-3-ene-1,2-dione (0.54 g, 3.6 mmol) in toluene (15 mL) was heated at 80 °C for 24 h. The resultant reaction mixture was evaporated under reduced pressure to give residue, which was purified by column chromatography to give 3-chloro-4-(4-(diphenylamino) phenyl)cyclobut-3-ene-1,2-dione (**5b**) (0.45 g, 38 %) as yellow solid. <sup>1</sup>H NMR (500 MHz, CDCl<sub>3</sub>) δ: 8.07 (m, J = 9.16 Hz, 2 H), 7.42 - 7.35 (m, 4 H), 7.27 - 7.18

(m, 6 H), 7.02 (m, J = 9.16 Hz, 2 H).  $^{13}\text{C}$  NMR (100 MHz,  $\text{CDCl}_3$ )  $\delta$ : 195.3, 190.4, 186.7, 174.6, 153.8, 145.2, 130.8, 129.9, 126.7, 126.0, 118.6, 118.0. HRMS (ESI): m/z calcd for  $\text{C}_{22}\text{H}_{14}\text{ClNO}_2\text{Na}$  ( $[\text{M} + \text{Na}]^+$ ): 382.0605. Found: 382.0604.

### 3-(4-(Diphenylamino) phenyl)-4-hydroxycyclobut-3-ene-1, 2-dione (5c)

In a 50 mL round bottom flask, a mixture of 3-chloro-4-(4-(diphenylamino) phenyl) cyclobut-3-ene-1,2-dione (**5b**) (0.4 g, 1.1 mmol), acetic acid (7 mL), water (7 mL) and 2 N HCl (2 mL) was refluxed for 16 h, the resultant mixture was concentrated under vacuum to give residue. The residue was washed with  $\text{NaHCO}_3$  aq. and brine to give 3-(4-(diphenylamino)phenyl)-4-hydroxycyclobut-3-ene-1,2-dione (**5c**) (0.23 g, 61 %) as brown solid.  $^1\text{H}$  NMR (400 MHz,  $\text{CDCl}_3$ )  $\delta$ : 8.07 (d, J = 8.80 Hz, 2 H), 7.42 - 7.34 (m, 4 H), 7.25 - 7.18 (m, 6 H), 7.02 (d, J = 8.80 Hz, 2 H).  $^{13}\text{C}$  NMR (100 MHz,  $\text{CDCl}_3$ )  $\delta$ : 195.3, 190.4, 186.8, 174.7, 153.8, 145.2, 130.8, 129.9, 126.7, 126.0, 118.6, 118.0. HRMS (ESI): m/z calcd for  $\text{C}_{22}\text{H}_{16}\text{NO}_3$  ( $[\text{M} + \text{H}]^+$ ): 342.1125. Found: 341.1123.

### 5-carboxy-2-[[3-[N,N-diphenyl-anilin-4-yl]-4-oxo-2-cyclobuten-2-olate-1-ylidene] methyl]-3, 3-dimethyl-1-hexyl-3H-indolium (NSQR)

A mixture of 3-(4-(diphenylamino)phenyl)-4-hydroxycyclobut-3-ene-1,2-dione (**5b**) (0.15 g, 0.44 mmol) and **3b** (0.14 g, 0.48 mmol, 1.1 eq.) in toluene (5 mL), 1-butanol (5 mL) and pyridine (0.5 mL) was added in 25 mL RB flask and refluxed with a Dean-Stark apparatus for 5 h. The resultant mixture was concentrated under reduced pressure, washed with 2 N HCl, extracted with dichloromethane and dried over  $\text{Na}_2\text{SO}_4$ , then concentrated under vacuum to give a residue, which was purified with dichloromethane/methanol to give **NSQR** as blue solid (67 mg, 25 %).  $^1\text{H}$  NMR (200 MHz,  $\text{DMSO}-d_6$ )  $\delta$ : 8.22 (s, 1 H), 8.11 - 7.95 (m, 3 H), 7.78 (d, J = 8.84 Hz, 1 H), 7.45 - 7.31 (m, 4 H), 7.24 - 7.08 (m, 6 H), 6.92 (d, J = 8.84 Hz, 2 H), 6.24 (s, 1 H), 4.39 (br. s., 2 H), 1.76 (s, 6 H), 1.45 - 1.16 (m, 8 H), 0.87 - 0.79 (m, 3 H).  $^{13}\text{C}$  NMR (100 MHz,  $\text{CDCl}_3$ )  $\delta$ : 192.67, 182.7, 179.0, 178.0, 169.8, 166.8, 149.8, 145.9, 144.7, 143.0, 130.3, 129.9, 128.9, 128.3, 125.8, 125.0, 123.9, 123.6, 120.1, 113.0, 91.2, 50.9, 30.8, 27.2, 25.7, 25.2, 21.9, 13.8. HRMS (ESI): m/z calcd for  $\text{C}_{40}\text{H}_{39}\text{N}_2\text{O}_4$  ( $[\text{M} + \text{H}]^+$ ): 611.2904. Found: 611.2899.

## 2.3 RESULTS AND DISCUSSION

### 2.3.1 Synthesis and Characterization

The synthetic route of NSQ sensitizers are displayed in **Scheme 2**. The indolium salt of  $sp^3$ -C atom functionalized with alkyl groups is synthesized by suitably substituted branched methyl ketone. The branched methyl ketone was synthesized starting from oxidation of branched alcohol to the corresponding aldehyde (**1a**). Then reaction with  $CH_3MgI$  afforded the corresponding secondary alcohol (**1b**) which was oxidized to provide the required 3-octyltridecan-2-one in moderate yield. 3-Methylbutan-2-one and 3-Octyltridecan-2-one reacted with 4-carboxyphenylhydrazine to give the intermediate **2a** and **2b**, respectively. Then, the corresponding indolium salts (**3a-3c**) were prepared by reacting with alkyl halide to get with either N- or  $sp^3$ -C or both atoms functionalized with alkyl groups. The semi-squaraine derivatives **4c** and **5c** were synthesized by reaction of **4a** and **5a** with squaryl chloride followed by acid hydrolysis of the semi-squaryl chloride derivatives.<sup>27</sup> A condensation reaction between semi-squaryl chloride derivatives of **4c** or **5c** and 5-carboxy-2,3,3-trialkyl-1-alkylindolium units (**3a-3c**) provided the targeted NSQ sensitizers. All the sensitizers showed good solubility in  $CH_3CN$ ,  $CH_2Cl_2$ ,  $CHCl_3$ , DMSO and limited solubility in MeOH.

The structure of all intermediates and final compound were analyzed by  $^1H$  NMR,  $^{13}C$  NMR and HR-MS spectra. **Figure 3** shows the labeled  $^1H$  NMR spectrum of NSQ2. This compound showed broad singlet (**a**) at 1.59 ppm (12 H) and another singlet (**a'**) at 1.60 ppm (6 H) which correspond to 18 protons of bridged methyl groups. The 2-methyl group attached to  $sp^3$ -C atom of indolium group showed singlet (**b**) at 1.81 ppm. The  $-CH_2$  group which is connected to N-atom of indolium units shows triplet (**c**) at 4.38-4.41 ppm. The peak corresponds to  $=CH$  protons shows singlet (**d**) at 6.28 ppm. **Figure 4** shows the labeled  $^{13}C$  NMR spectrum of NSQ2. The peak at 192 ppm (**a**) corresponds to enolate carbon whereas peak at 183 ppm (**b**) corresponds to carbonyl carbon of squaraine units. The carboxylic acid containing carbonyl carbon exhibits peak around 178 ppm. The  $=CH$  containing carbon shows peak at 133 ppm. The final compounds were subjected to HRMS analysis using the ESI method and an ion-trap mass analyzer. The molecular ion peaks were obtained for cationic species such as  $M + 1$ ,  $M + Na$  etc.

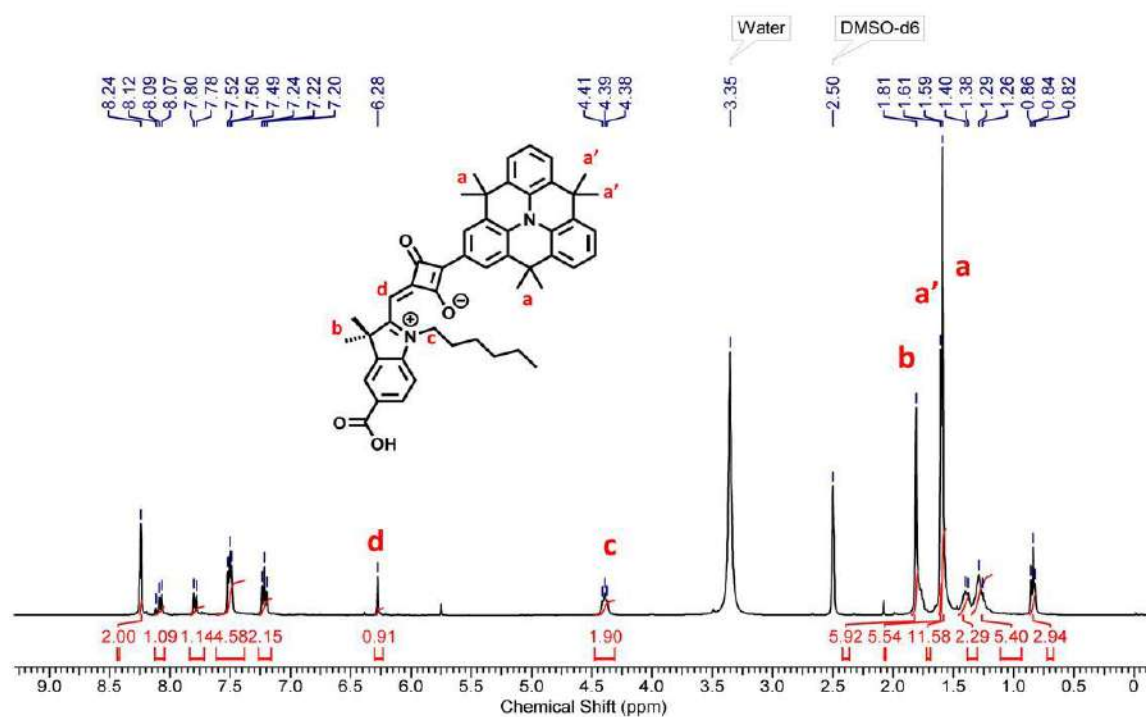


**Figure 3.**  $^1\text{H}$  NMR (400 MHz,  $\text{DMSO-}d_6$ ) spectrum of compound NSQ2.

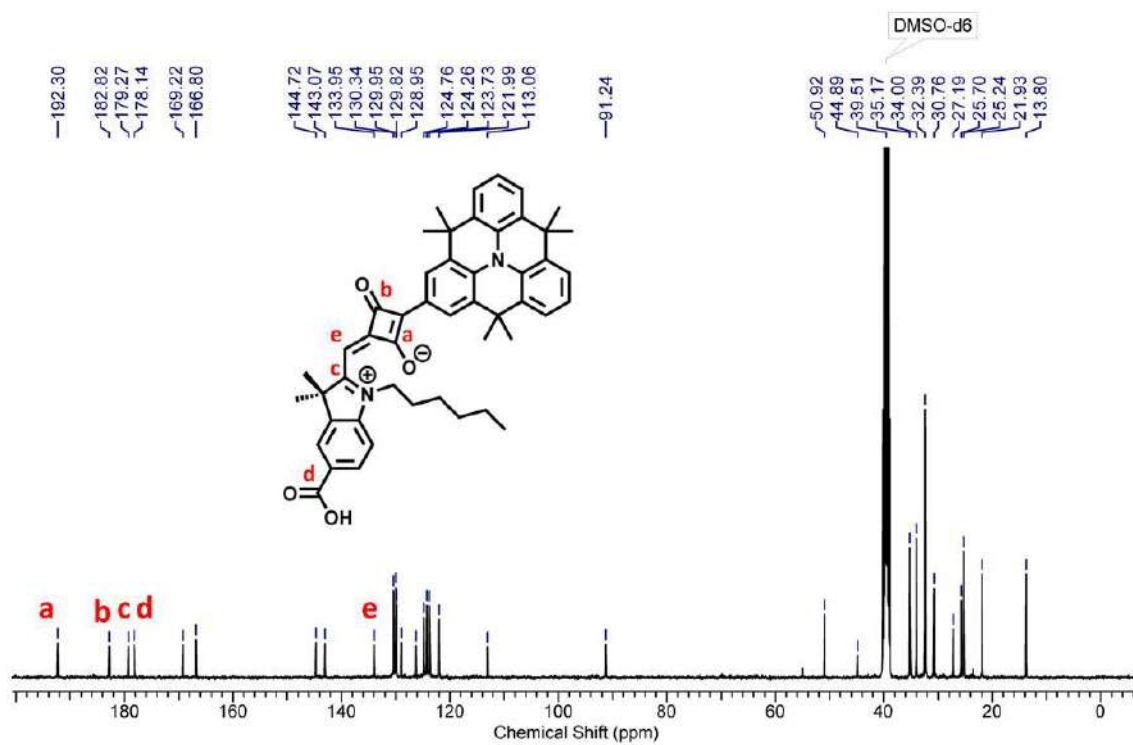


**Figure 4.**  $^{13}\text{C}$  NMR (100 MHz,  $\text{DMSO-}d_6$ ) spectrum of compound NSQ2.

### 2.3.2 Photophysical Properties

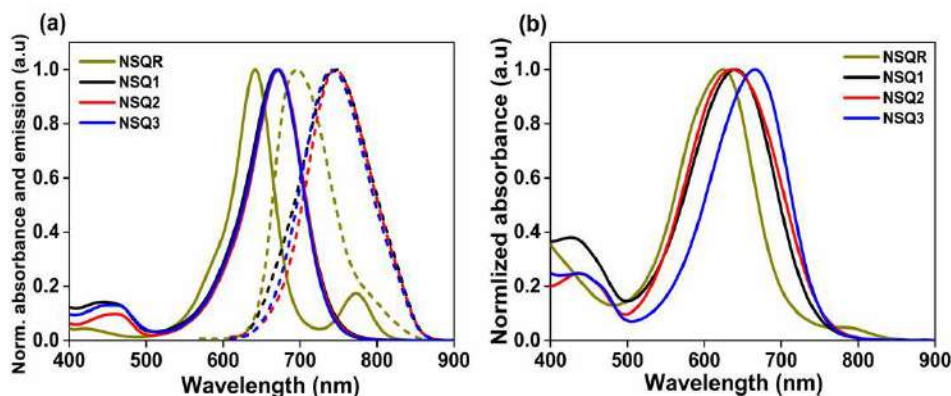


**Figure 5.** (a) Absorption (solid line) and emission (dot line) spectra of **NSQ** dyes in  $\text{CH}_3\text{CN}$  solution [excitation wavelength for **NSQR** 560 nm and **NSQ1-3** 600 nm] (b) Absorption spectra of **NSQ** sensitizers (0.1 mM in  $\text{CH}_3\text{CN}$ ) adsorbed on the transparent  $\text{TiO}_2$  film (6  $\mu\text{m}$ ), dipped for 10 min.

The absorption spectra of **NSQR** and **NSQ1-3** in  $\text{CH}_3\text{CN}$  solution are shown in **Figure 5a**. **NSQ1**, **NSQ2** and **NSQ3** were exhibited an intense absorption band centered at 673, 674 and 674 nm, respectively, corresponding to internal charge transfer (ICT) transition. Compared to reference dye (**NSQR**), **NSQ1-3** dyes are red shifted by 30 nm is mainly because of extended conjugation due to planar HT donor. All of these sensitizers show a high  $\epsilon$  in the range of  $10^4 \text{ M}^{-1} \text{ cm}^{-1}$ . **NSQ1-3** shows  $\pi$ - $\pi^*$  transition between 400-500 nm apart from the ICT band, with lower  $\epsilon$  values ( $\sim 10^3 \text{ M}^{-1} \text{ cm}^{-1}$ ). **Figure 5b** shows absorption spectra on transparent mesoporous  $\text{TiO}_2$  film, these spectra are broadened on  $\text{TiO}_2$  thin film due to the interaction of carboxylic acid groups with the surface titanium ions.<sup>28</sup> The  $\lambda_{\text{max}}$  is blue shifted by 32 and 38 nm towards higher energy for **NSQ1** and **NSQ2**, respectively, because of H-type of aggregation on  $\text{TiO}_2$  surface.<sup>29</sup> On the other hand, **NSQ3** is shifted by only 8 nm because of the presence of out-of-plane alkyl segments on indolium  $\text{sp}^3$ -C atom, which efficiently suppresses dye aggregation on the  $\text{TiO}_2$  surface. The emission  $\lambda_{\text{max}}$  of **NSQ** sensitizers are shifted to longer wavelength and giving maximum stokes shift of  $\sim 70$  nm for **NSQ1-3** sensitizers, which is comparatively small for **NSQR** ( $\sim 50$  nm). This result supports the larger dipole moments in excited state for **NSQ1-3** in solution is due to increased conjugation from HT unit (**Figure 5a**).



## 2.3.3 Electrochemical Properties

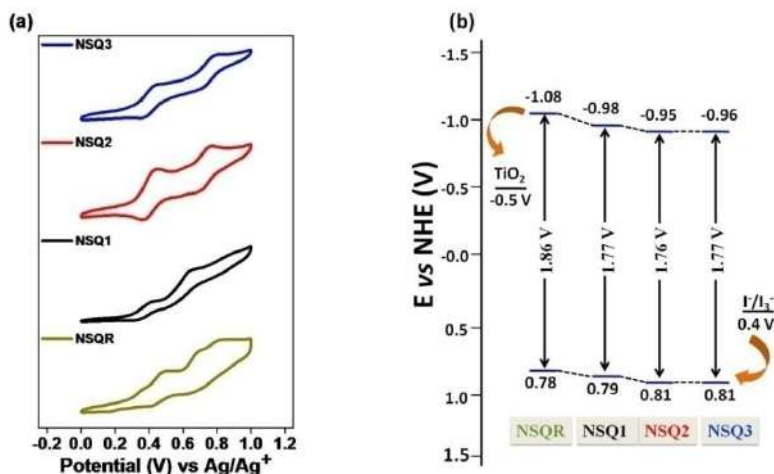


**Figure 6.** (a) Cyclic voltammograms of **NSQR** and **NSQ1-3** measured in CH<sub>3</sub>CN, with TBAClO<sub>4</sub> (0.1 M) at the scan rate of 50 mV s<sup>-1</sup> and (b) Energy level diagram for the **NSQ** sensitizers vs NHE.

The electrochemical properties of **NSQ** dyes were studied using cyclic voltammetry (CV) in CH<sub>3</sub>CN to understand the possibility of electron transfer from the excited state of the sensitizers to the CB of the TiO<sub>2</sub> and the regeneration of oxidized dyes by the electrolyte. The redox potentials of **NSQR** and **NSQ1-3** dyes were measured as shown in **Figure 6** and **Table 1**. **NSQR** exhibited the quasi-reversible first ground-state oxidation potential ( $E_{ox}$ ) of at 0.78 and for **NSQ1-3** at 0.79 (**NSQ1**), 0.81 (**NSQ2**) and 0.81 (**NSQ3**) V vs NHE. The  $E_{ox}$  level of **NSQs** was low enough to get regenerated by iodide (0.4 V vs NHE). The HOMO levels of the **NSQR** were not affected after substituting with heterotriagulene, **NSQ1-3**, as listed in **Table 1**. The LUMO of **NSQ** dyes are found to be -1.08, -0.98, -0.95 and -0.96 V vs NHE for **NSQR**, **NSQ1**, **NSQ2** and **NSQ3**, respectively, which lie above the conduction band edge (CB) of TiO<sub>2</sub> (-0.5 V vs NHE) that permits an efficient electron injection into the conduction band of TiO<sub>2</sub> as shown in **Figure 6b**.<sup>30</sup> **NSQR** and **NSQ1-3** displayed a band gap ( $E_g$ ) in the range of 1.7-1.9 eV, which are in good agreement to the band gaps determined from the DFT studies.

**Table 1.** Photophysical and electrochemical properties of squaraine dyes

SQ Dyes	$\lambda_{\max}$ /CH <sub>3</sub> CN (nm) <sup>a</sup>	$\lambda_{\max}$ /TiO <sub>2</sub> (nm) <sup>b</sup>	$\lambda_{\max}$ /em(nm) <sup>a</sup>	$\epsilon \times 10^4$ (M <sup>-1</sup> cm <sup>-1</sup> ) <sup>a</sup>	$E_{g/DF}$ T (eV)	$E_{ox/onset}$ (V vs Ag/Ag <sup>+</sup> )	$E_{HOMO}$ (V vs NHE) <sup>c</sup>	$E_{0-0}$ (eV) <sup>d</sup>	$E_{LUMO}$ (V vs NHE) <sup>e</sup>
<b>NSQR</b>	643	624	696	5.5	2.13	0.28	0.78	1.86	-1.08
<b>NSQ1</b>	673, 458	641	746	6.1, 0.86	2	0.29	0.79	1.77	-0.98
<b>NSQ2</b>	674, 464	636	746	6.9, 0.73	2.01	0.31	0.81	1.76	-0.95
<b>NSQ3</b>	674, 464	666	743	6.5, 0.92	2.01	0.31	0.81	1.77	-0.96

<sup>a</sup>Absorption and emission spectra, molar extinction coefficients ( $\epsilon$ ) were measured in CH<sub>3</sub>CN. <sup>b</sup>On 6  $\mu$ m transparent TiO<sub>2</sub> film. <sup>c</sup>The oxidation potentials were measured in CH<sub>3</sub>CN solutions with tetrabutylammonium perchlorate (TBAClO<sub>4</sub>) as supporting electrolyte, ferrocene/ferrocenium (Fc/Fc<sup>+</sup>) as an internal reference and converted to NHE by addition of 0.63 V. <sup>d</sup>Optical energy gaps ( $E_{0-0}$ ) were deduced from the intersection of absorption and emission spectra,  $E_{0-0}$  (eV) = 1240/ $\lambda$ . <sup>e</sup> $E_{LUMO}$  was calculated from  $E_{LUMO}$  (V vs NHE) =  $E_{HOMO}$  (V vs NHE) -  $E_{0-0}$ .

### 2.3.4 Theoretical Investigations

In order to elucidate the molecular geometries of **NSQ** sensitizers, density functional theory (DFT) calculations were performed with at B3LYP/6-31G (d, p) basis set using Gaussian 09 program.<sup>31</sup> The isosurface plots for HOMO-1, HOMO, LUMO, and LUMO+1 are shown in **Figure 7**. The electron density in HOMO and HOMO-1 of **NSQ1-3** was more delocalized on donor part and also well distributed throughout squaric acid, whereas the LUMO was delocalized towards indolium unit contains electron withdrawing carboxylic acid.

The calculation reveals that the HOMO and LUMO overlap facilitates the effective charge transfer from donor to anchoring unit and hence shows a red-shifted  $\lambda_{\max}$  in the absorption spectrum. On the other hand, LUMO+1 for all sensitizers were mainly located near to anchoring group. The HOMO-1 of **NSQR** was located on squaric acid unit, which shows the inability of triarylamine to regenerate the dye after injection of electron to TiO<sub>2</sub> compared to **NSQ1-3** dyes. These overall DFT results illustrate that the HOMO-LUMO or HOMO-LUMO+1 excitations can move electron flow from the donor unit to the anchoring group.

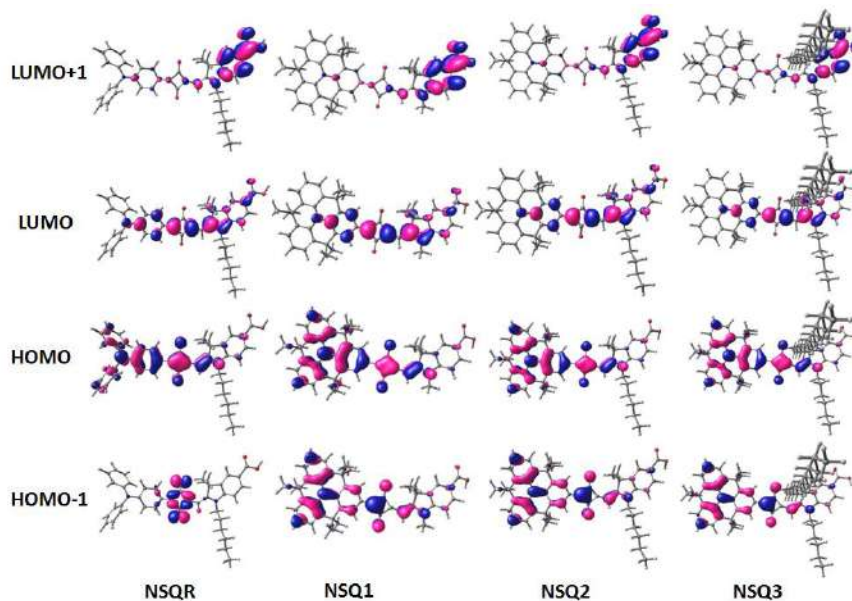


**Figure 7.** Isodensity surface plots of the HOMO, HOMO-1, LUMO and LUMO+1 of NSQ sensitizers.

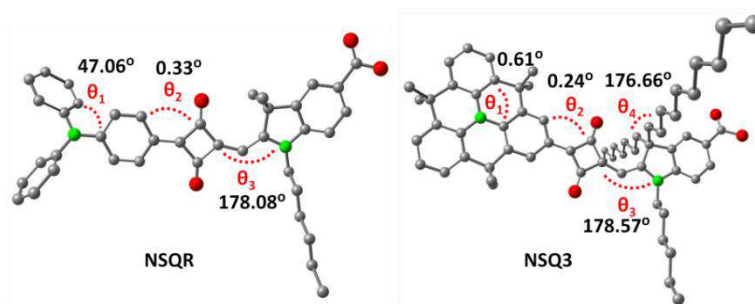


**Figure 8.** Selected dihedral angles of NSQR and NSQ3 calculated from the optimized ground state geometry using density functional theory (DFT) at B3LYP/6-31G (d, p) basis set with the Gaussian 09 program (hydrogen atoms are removed for better clarity).

The ICT process between donor and acceptor is influenced by dihedral angle between benzene and nitrogen atom of TPA or HT donor ( $\theta_1$ ), donor and squaric acid unit ( $\theta_2$ ), and squaric acid and indolium unit  $\theta_3$ .<sup>32</sup> In NSQR,  $\theta_1$  is more deviated than NSQ1-3 dyes, shows a superior co-planarity of donor-acceptor parts in HT based dyes (**Figure 8**). The  $\theta_1$  value of NSQ1-3 is close to  $0^\circ$  whereas for NSQR it is  $47.06^\circ$  (**Table 2**). Bulky alkyl functionalities of indolium unit shows extended conformation with  $\theta_4$  of  $176.6^\circ$ , which facilitates to improve the photo-physical properties by reducing the dye aggregation as well as by extending the conjugation.

**Table 2.** Selected dihedral angles of **NSQs** were calculated from the optimized ground state geometry

NSQ Dyes	Dihedral angle (degree)			
	$\theta_1$	$\theta_2$	$\theta_3$	$\theta_4$
<b>NSQR</b>	47.06	-0.33	-178.08	-
<b>NSQ1</b>	-0.05	0.05	-179.6	-
<b>NSQ2</b>	-0.43	0.57	-177.65	-
<b>NSQ3</b>	0.61	-0.24	-178.57	-176.66

The distance between (i)  $sp^3$ -C (methylene group of HT) to  $-O$  atom of carboxylic acid, (ii) terminal carbon atoms of  $sp^3$ -branched alkyl chain and (iii)  $sp^3$ -C (indoline) to  $-O$  atom of carboxylic acid were found to be 19.6 Å, 23.1 Å, and 6.2 Å, respectively for **NSQ3** (**Figure 9**). These structural features may show the way to better exposed HOMO for efficient dye regeneration, diminishes the dye aggregation and reduces charge recombination due to the presence of long and branched hydrophobic alkyl chains near to the  $TiO_2$  surface.

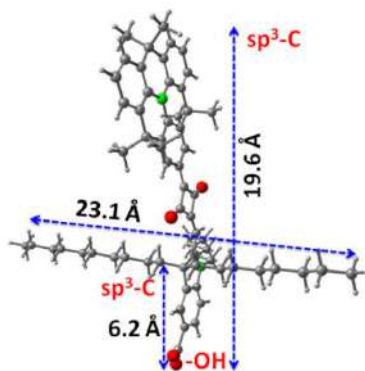


**Figure 9.** Distance between  $sp^3$ -C (methyl group of HT) to  $-O$  atom of carboxylic acid, distance between the terminal carbon atoms of  $sp^3$ -branched alkyl chain and  $sp^3$ -C (indoline) to  $-O$  atom of carboxylic acid of **NSQ3** calculated from the optimized ground state geometry using density functional theory (DFT) at B3LYP/6-31G (d, p) basis set with the Gaussian 09 program.

### 2.3.5 Photovoltaic Performance of DSSCs

The current density-voltage ( $J$ - $V$ ) characteristics of DSSCs based on **NSQR** and **NSQ1-3** using the optimized CDCA/dye ratios were evaluated under simulated AM 1.5G solar light ( $100 \text{ mW cm}^{-2}$ ), and the corresponding  $J$ - $V$  curves are presented in **Figure 10a** and

**11a.** In the case of **NSQR**, **NSQ1** and **NSQ2**, the moderate performance is achieved without any co-absorbent, because of the aggregation of dyes in the absence of CDCA.

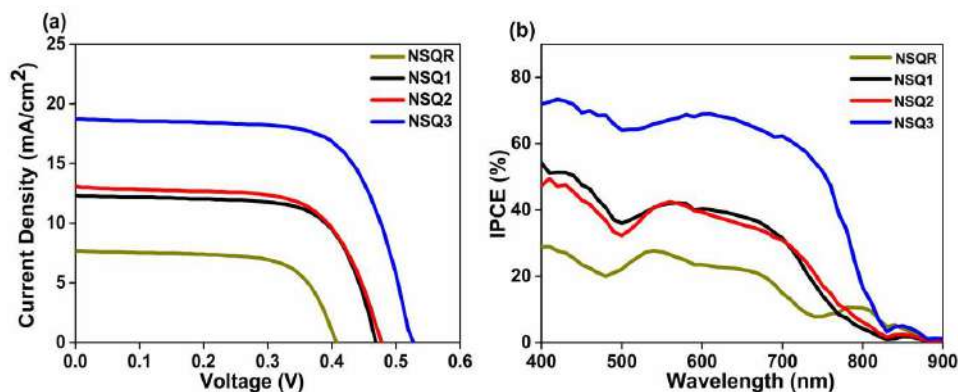


**Figure 10.** (a)  $J$ - $V$  curve and (b) IPCE spectrum of **NSQR**, and **NSQ1-3** sensitizers without co-adsorbent (CDCA).

Among the **NSQs**, **NSQ3** sensitized cells confers better performance without CDCA and reached an overall power conversion efficiency ( $\eta$ ) of 6.73% with a short-circuit current density ( $J_{SC}$ ) of 18.74 mA cm<sup>-2</sup> and open-circuit potential ( $V_{OC}$ ) of 0.53 V. Particularly, among the four dyes the **NSQ3** exhibits the maximum  $V_{OC}$  of 0.54 V and 0.53 V with and without CDCA, respectively. It is proving the strong capability of branched and long alkyl side chain on chromophore that avoids surface aggregation and reduces the charge recombination even without any co-adsorbent.<sup>33</sup> The photovoltaic performances are summarized in **Table 3**, and also the results of five cells with deviation for optimized dye/ CDCA are shown in **Figure 12**. It is known that the addition of CDCA has a positive impact on improving the  $V_{OC}$  and  $J_{SC}$  values of **NSQ** sensitizers based DSSCs. As expected, after the addition of 10 equivalents of CDCA, the **NSQ2** sensitized cells gives an overall PCE of 7.4% with a  $J_{SC}$  of 20.57 mA cm<sup>-2</sup>,  $V_{OC}$  of 0.53 V and  $ff$  of 0.68 whereas triphenylamine based **NSQR** sensitized cells were showed a relatively poor performance with an overall  $\eta$  of 4.63% at the same amount of co-adsorbent due to lesser  $J_{SC}$  (14.95 mA cm<sup>-2</sup>) and  $V_{OC}$  (0.47 V) values.

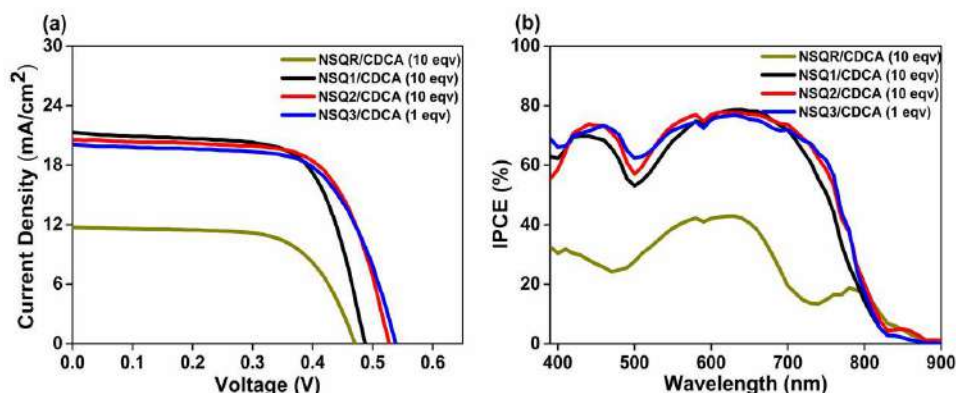


**Figure 11.** (a)  $J$ - $V$  curve and (b) IPCE spectra of NSQR, and NSQ1-3 in the presence of CDCA.

**Table 3.** Photovoltaic parameters for NSQ1-3 and NSQR with and without co-adsorbent.<sup>a</sup>

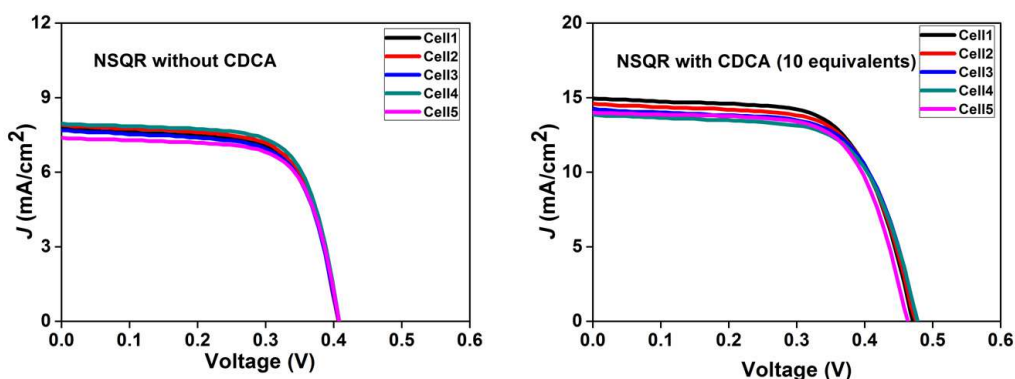
NSQ Dye Cell	$V_{oc}$ [ V ]	$J_{sc}$ [ mA/cm <sup>2</sup> ]	$ff$ [ % ]	$\eta$ [ % ]	Amount of adsorbed dyes (×10 <sup>-7</sup> mol cm <sup>-2</sup> ) <sup>b</sup>
NSQR	0.406±0.002	7.4±0.29	66.8±0.8	2.01±0.11	2.12
NSQR/CDCA (1:10)	0.467±0.004	14.64±0.31	64.4±1.3	4.40±0.23	1.56
NSQ1	0.465±0.004	11.93±0.38	68.7±0.5	3.81±0.18	1.81
NSQ1/CDCA (1:10)	0.486±0.002	20.77±0.55	67.6±0.4	6.82±0.25	1.01
NSQ2	0.474±0.002	12.90±0.18	65.1±1.0	3.98 ±0.13	1.23
NSQ2/CDCA (1:10)	0.526±0.001	20.35±0.22	66.9±1.2	7.16±0.22	0.87
NSQ3	0.521±0.004	18.38±0.36	68.1±0.20	6.53±0.20	1.13
NSQ3/CDCA (1:1)	0.540±0.001	20±0.11	65.7±0.25	7.09±0.08	0.94

<sup>a</sup>Photovoltaic performance of NSQR and NSQ1-3 with deviation of 5 cells, thickness of electrode: 8+4 μm (transparent+ scattering) layer of TiO<sub>2</sub>, Electrolyte: 0.5 M DMII, 0.1 M LiI, 0.1 M I<sub>2</sub> and 10 mM TBP in CH<sub>3</sub>CN. Dipping time was 6 h. Active area of 0.22 cm<sup>2</sup> and measurements were carried out under 1 sun intensity (100 mW/cm<sup>2</sup>), <sup>b</sup>by dye desorption method, carried out in 2M ethanolic HCl at rt.

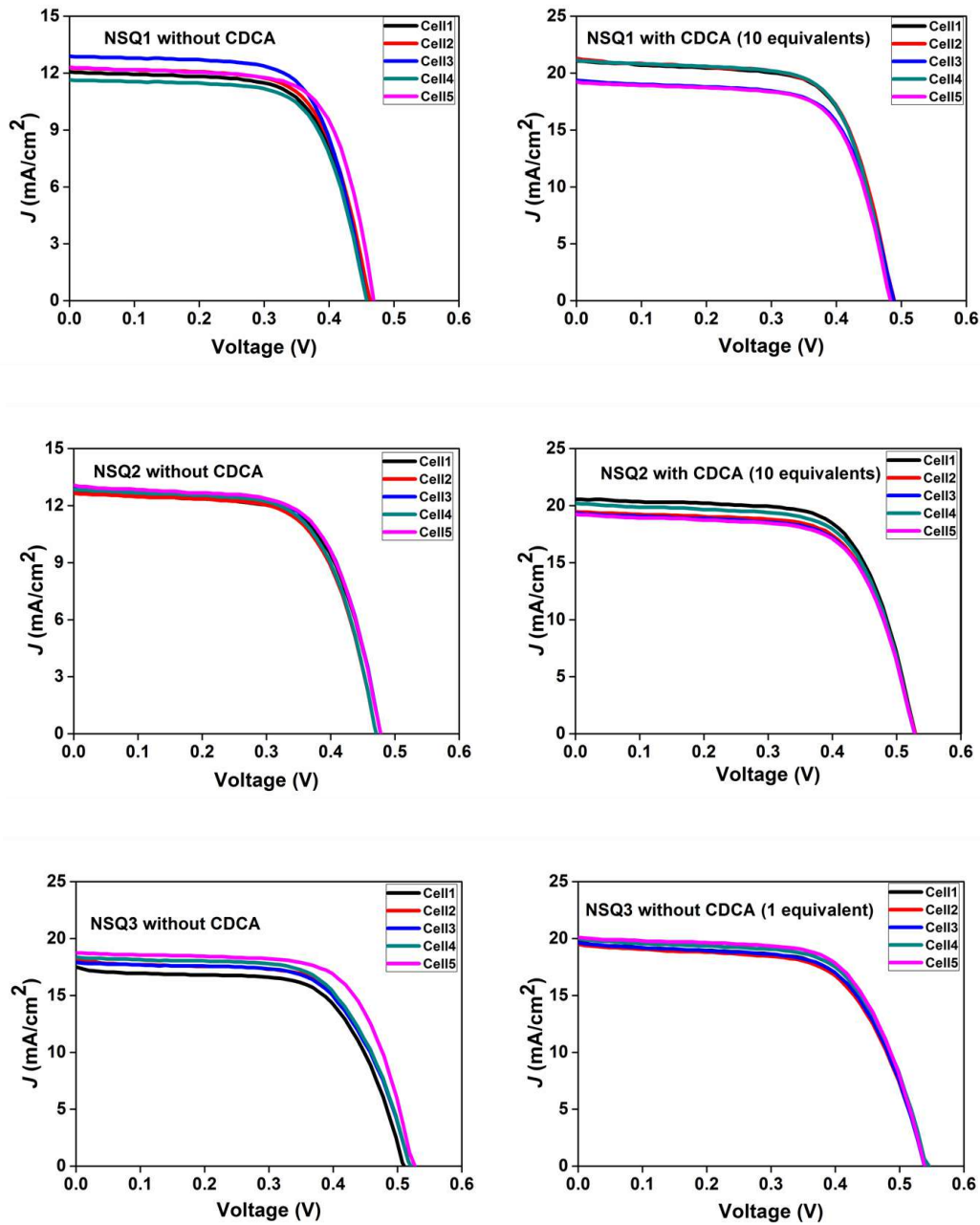
The NSQ1 sensitized cell was attained a  $J_{sc}$  value of 21.32 mA cm<sup>-2</sup>,  $V_{oc}$  of 0.49 V, and  $ff$  of 0.68, corresponding to  $\eta$  of 7.07%. NSQ3 sensitized cell reached at a  $J_{sc}$  of 20.11 mA cm<sup>-2</sup>,  $V_{oc}$  of 0.54 V,  $ff$  of 0.66 and overall conversion efficiency of 7.17% with the addition of least amount of CDCA (1 equivalent), and the  $J$ - $V$  curves are shown in **Figure**

**11a.** The  $J_{SC}$  and  $V_{OC}$  of **NSQ3** dye reduces with further addition of CDCA due to competitive binding of CDCA over dyes. These results specify that the addition of large amount of CDCA is not helpful for **NSQ3** to improve the photovoltaic performance (**Table 4**). The dye desorption study show the modulated adsorption of dyes on  $TiO_2$  with respect to their molecular structure (**Table 3** and **Figure 13**). It is found that the dye loading ability decreases in the order of **NSQR** > **NSQ1** > **NSQ2**  $\approx$  **NSQ3**, owing to progressive increase of alkyl groups near  $TiO_2$  surface which blocks the dye anchoring to the pentacoordinated Ti center. In **NSQ3** dye cell, addition of 10 equivalents of CDCA promptly changes the quantity of adsorbed dyes and leads to decreased device efficiency (**Table 4**).

HT-based dyes showed high  $J_{SC}$  with and without CDCA than triphenylamine donor. As considering very similar configuration of **NSQ1-3** and **NSQR**, the incorporated HT donor and branching at chromophore extends the light harvesting ability and decreases the charge recombination property of **NSQ1-3** dyes. **NSQ1-3** showed distinct enhancement of  $J_{SC}$  and  $V_{OC}$  suggests that the incorporation of planar donor unit and branched alkyl groups into the dye structure would be a significant approach to increase the PCE of metal-free unsymmetrical squaraine dyes.





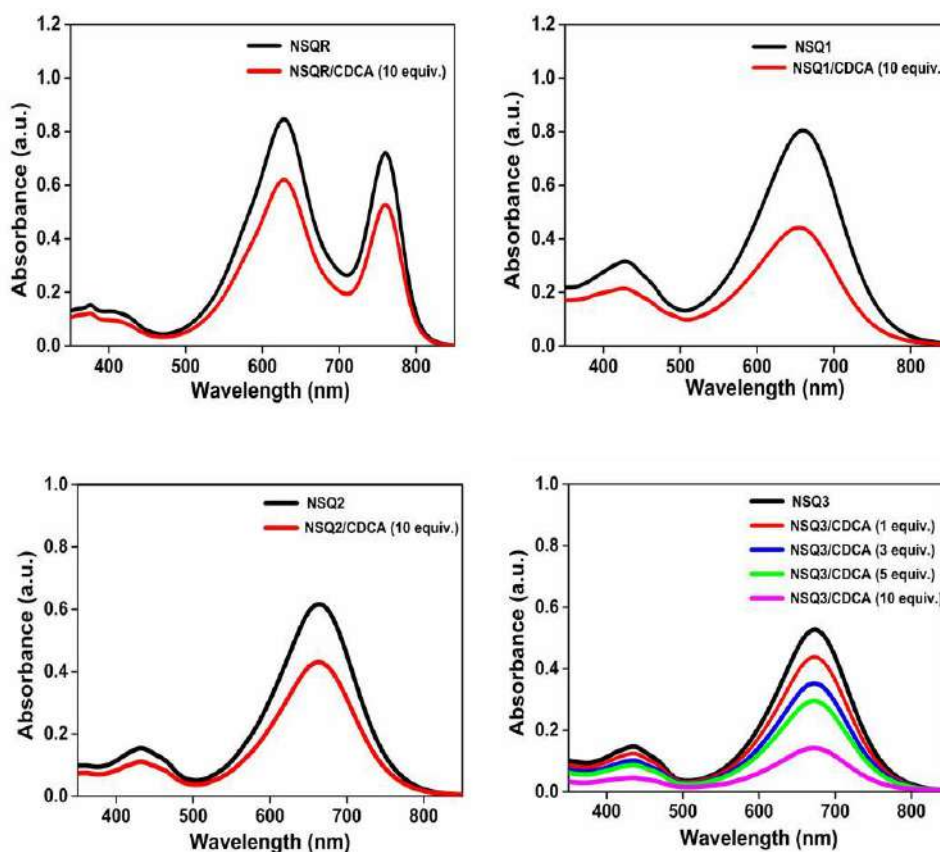


**Figure 12.**  $J$ - $V$  characteristics of NSQR and NSQ1-3 with deviation of 5 cells measured under simulated AM 1.5 G simulated sunlight ( $100 \text{ mW cm}^{-2}$ ).



**Table 4.** Photovoltaic performance of **NSQ3** with different ratios of CDCA.

Dye	$V_{OC}$ (V)	$J_{SC}$ (mA/cm <sup>2</sup> )	$ff$ (%)	$\eta$ (%)	Amount of adsorbed dyes (x 10 <sup>-7</sup> mol cm <sup>-2</sup> )
<b>NSQ3/CDCA (1:1)</b>	0.541	20.11	65.6	7.14	0.94
<b>NSQ3/CDCA (1:3)</b>	0.544	20.01	64.1	6.99	0.76
<b>NSQ3/CDCA (1:5)</b>	0.541	19.51	63.2	6.67	0.64
<b>NSQ3/CDCA (1:10)</b>	0.550	14.28	69.4	5.45	0.32

**Figure 13:** UV-Vis absorption spectra of desorbed **NSQ** dyes in 2 M HCl in EtOH.

The incident photon-to-current conversion efficiencies (IPCEs) as a function of incident wavelength for DSSCs based on **NSQR** and **NSQ1-3** dyes are plotted as shown in **Figure 10b** and **11b**. The higher  $J_{SC}$  values of **NSQ1-3** are reflected in the IPCE spectra, it shows higher and broader IPCE in the range of 400 to 800 nm. In the absence of CDCA, IPCE

of NSQ3 reaching to a maximum of 73% and 69% at 420 and 635 nm, respectively. NSQ3 dye can efficiently converted 50% of the photons at 750 nm, while NSQR displays IPCE response only 8% at the same wavelength. The NIR photons are efficiently converted when the TiO<sub>2</sub> sensitized with NSQ3 than any other dyes in the series without CDCA, with the IPCE of 30% at 780 nm, but NSQ1 and NSQ2 shows below 10%. NSQs show further increase in IPCE at higher wavelength region after the addition of CDCA. At 750 nm, NSQ1, NSQ2 and NSQ3 exhibit IPCE of 50%, 58% and 62%, respectively, while for NSQR, IPCE response is 15% around 750 nm at the same condition.

### 2.3.6 Electrochemical Impedance Spectroscopy (EIS)

EIS measurement was carried out under dark conditions to explain the interfacial charge recombination process in NSQ dye cells. In general,  $V_{OC}$  and  $J_{SC}$  of dye cells are seriously affected by the charge recombination dynamics at the interface of TiO<sub>2</sub>-dye-electrolyte.<sup>6</sup> In DSSCs, the  $V_{OC}$  of dye cell is determined by the difference between quasi-Fermi level of TiO<sub>2</sub> ( $E_{F,n}$ ) and Fermi level ( $E_{F,redox}$ ) of the redox couple (for e.g. I<sup>-</sup>/I<sub>3</sub><sup>-</sup>), as expressed in Equation 1.

$$V_{oc} = E_{F,redox} - E_{F,n} \quad (1)$$

$$E_{F,n} = E_{CB} + k_B T \ln \left( \frac{n_c}{N_c} \right) \quad (2)$$

The ambiguity of the photo-voltage initiates from a shift of the TiO<sub>2</sub> electron quasi-Fermi-level, Equation 2, where  $k_B$  is the Boltzmann constant,  $T$  is the absolute temperature (293 K),  $n_c$  the free electron density, and  $N_c$  the density of accessible states in the conduction band, which may be attributed to two major reasons: i) a shift in the TiO<sub>2</sub> conduction band edge ( $E_{CB}$ ), which can be concluded from the chemical capacitance ( $C_\mu$ ), and ii) a fluctuation of electron density, which is related to the electron lifetime ( $\tau$ ) which is determined by the charge recombination rate.<sup>20</sup> Therefore, using Nyquist and Bode plots of EIS analysis, corresponding charge transfer resistance ( $R_{ct}$ ),  $C_\mu$  and  $\tau$  is calculated to clarify the charge transfer process at TiO<sub>2</sub>-dye-electrolyte interface.

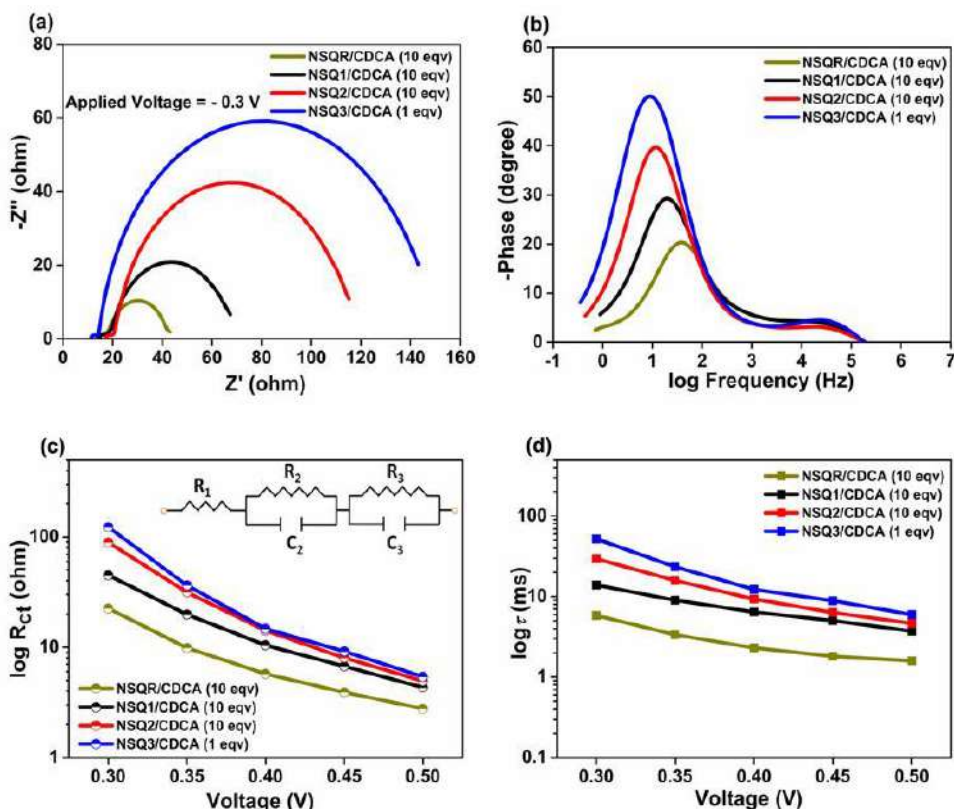


**Figure 14.** Plots of EIS analysis of NSQ dye cells. (a) Nyquist plot (b) Bode plot, (c) and (d)  $R_{ct}$  and  $\tau$  as a function of voltage, respectively

In general, the Nyquist diagram shows three semicircles that in the order of increasing frequency are ascribed to the Nernst diffusion within the electrolyte, the electron transfer at the TiO<sub>2</sub>-dye-electrolyte interface, and the redox reaction at the counter electrode. **Figure 14a** shows, Nyquist plot of NSQR and NSQ1-3 dye cells, the second semi-circle corresponding to the charge transfer reaction processes at the TiO<sub>2</sub>-dye-electrolyte interface, for NSQ3 was larger than other dyes, it is in the order of NSQ3 > NSQ2 > NSQ1 > NSQR. The peak frequency of Bode plot has moved towards the lowest value for NSQ3 as shown in **Figure 14b**. Generally, a long electron life time implies slower electron recombination rate at the interface and hence increases the free electron density. These observations show the effective passivation of surface by hydrophobic alkyl chains near to TiO<sub>2</sub> surface through Van der Waals interaction. **Figure 14c** and **14d** shows plot of  $R_{ct}$  and  $\tau$  which are extracted after fitting the Nyquist plot using an equivalent circuit (inset **Figure 14c**). The  $\tau$  of NSQ3 is longer than NSQR, NSQ1 and NSQ2 which is

steady with observed improvement in  $V_{OC}$ . The strong  $\pi$ - $\pi$  interaction and better screening of semiconductor surface showed maximum  $\tau$  around 52 ms at applied bias of -0.3 V. **NSQ1** and **NSQ2** showed  $\tau$  of 13.8 and 29.5 ms under same condition, indicating increase in charge recombination rates. **NSQ1-3** shows increased  $R_{ct}$  and  $C_{\mu}$  (**Figure 15**) which is further supported the high  $J_{SC}$  and  $V_{OC}$  values than **NSQR**. The increase in rate of electron injection and decrease in interfacial recombination can bring the difference in electron density in conduction band of metal oxide.<sup>34</sup> The successful approach for increasing the efficiency of unsymmetrical squaraine dyes is to mainly focus on improving  $V_{OC}$ .<sup>35</sup> In particular, the performance of **NSQ3** provides new approach to design co-adsorbent free and highly efficient unsymmetrical squaraine dyes.

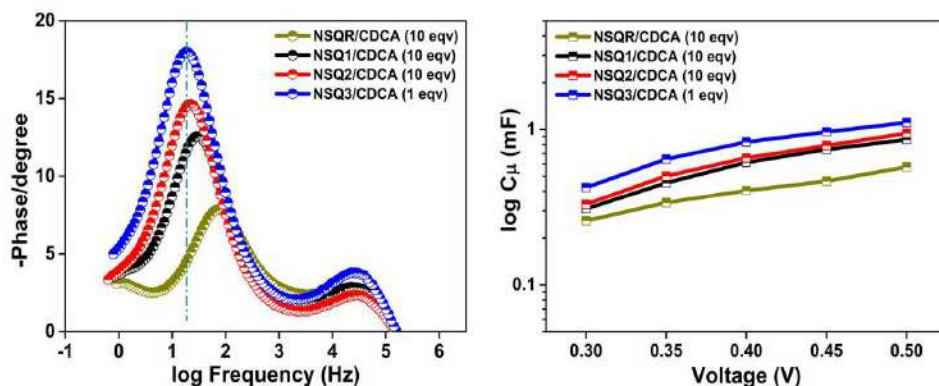


**Figure 15.** (a) Bode plot of **NSQ** dye cells (with an applied potential of -0.5 V) and (b)  $C_{\mu}$  as a function of voltage (with an applied potential of -0.3 V).

### 2.3.7 Open-circuit voltage decay measurement

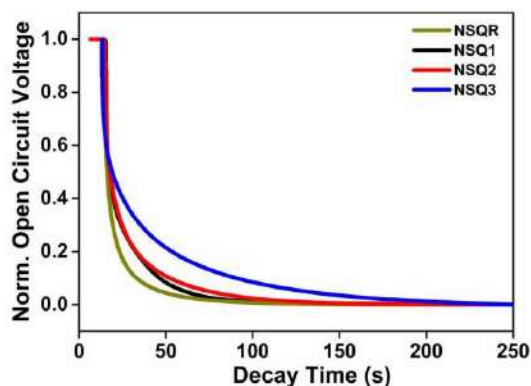


**Figure 16.** OCVD profile of DSSCs based on **NSQR** and **NSQ1-3** sensitizers.

In addition, transient recombination kinetics of **NSQ** sensitized cells was studied after illuminating the devices. Open-circuit voltage decay-time profile indicates the electron recombination kinetics after generating triiodide at TiO<sub>2</sub>-dye-electrolyte interface.<sup>36</sup>

**Equation 3** is used to calculate the relationship between  $V_{OC}$  decay and electron lifetime ( $\tau_n$ ), where  $k_B T$  the thermal energy and  $e$  is the positive elementary charge:

$$\tau_n = - \frac{k_B T}{e} \left( \frac{dV_{oc}}{dt} \right)^{-1} \quad (3)$$

According to this equation, the  $\tau$  of the devices is extracted from the slope of the photo voltage decay curves and  $V_{OC}$  decay were measured in the dark after illuminating the cell at 1 sun intensity for 10 s. The decay profile of **NSQR** and **NSQ1-3** dye cells are as shown in **Figure 16**. **NSQ3** dye cell confirms the slowest decay (78% at 50 s) where as **NSQR** shows the fast voltage decay (95% at 50 s). The minimum rate of recombination in **NSQ3** sensitized dye cell was ascribed to the effective passivation of mesoporous TiO<sub>2</sub> surface by introducing hydrophobic alkyl functionalities near to the anchoring group. The experimentally observed 120 mV difference in the  $V_{OC}$  of **NSQ3** compared to **NSQR** without any co-adsorbent shows the slow recombination of injected electron with triiodide. The results of EIS experiment in the dark and OCVD measurement in the presence of light successively indicates the deceleration of charge recombination, via dark reaction and back electron transfer, for **NSQ3** compared to other **NSQs**.

## 2.4 CONCLUSION

In this second chapter, the effects of HT and TPA donor moieties and alkyl functionalities in unsymmetrical squaraine dyes are studied in details. HT based **NSQ1-3** sensitizers have shown significant improvement in PCE as compared to TPA based **NSQR**. **NSQ3** sensitized device reached to a PCE of 6.73% without co-adsorbent, and in presence of CDCA **NSQ2** and **NSQ3** achieved PCE of 7.4% and 7.17%, respectively. IPCE spectra for **NSQ1-3** was broader and Higher, owing to extended conjugation and strong donor-acceptor coupling, gives the better NIR light harvesting efficiency than **NSQR**. The EIS and OCVD studies proved the alkyl-functionalized indolium unit attached to carboxylic acid suppresses the undesirable charge recombination and shows long electron lifetime, and therefore significantly enhancing the PCE. This chapter suggests that introducing an in-plane and out-of-plane alkyl chains on indolium group of unsymmetrical squaraine increases the  $J_{SC}$  and  $V_{OC}$ , and avoiding the use of co-adsorbent in dye cell fabrication. Most importantly, the hydrophobic alkyl functionalities on squaraine chromophore near to the semiconductor surface leads to better control over the recombination process between electrolyte and  $TiO_2$ .

## 2.5 NMR Spectra

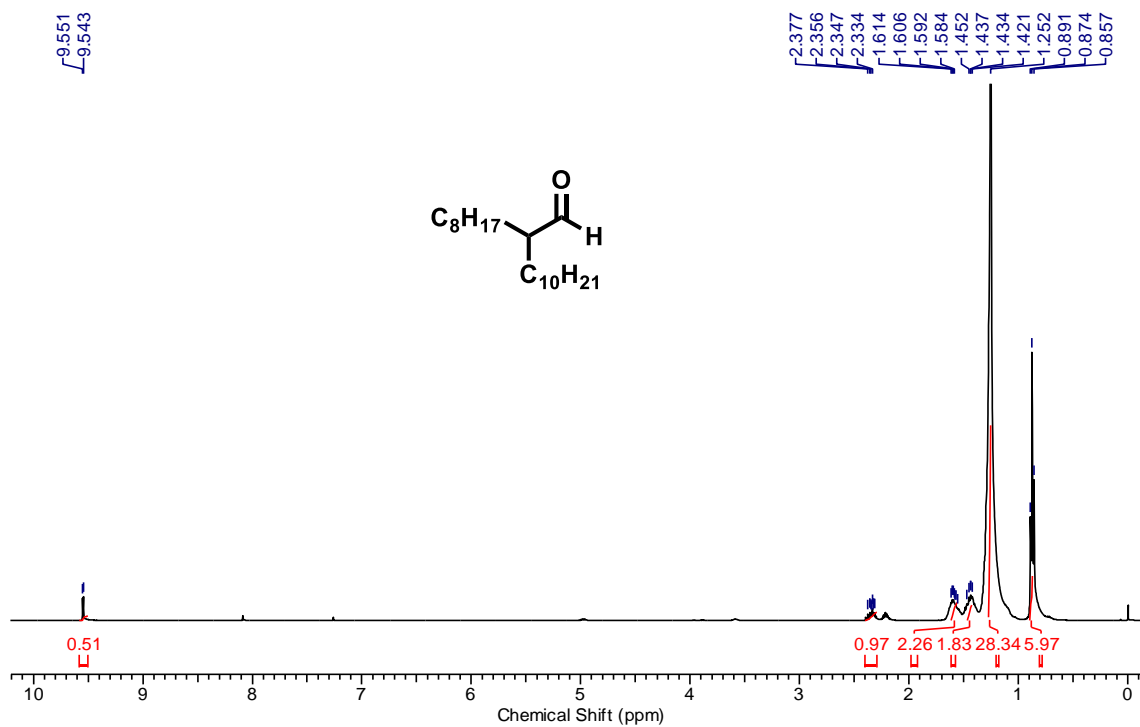


Figure 17. <sup>1</sup>H NMR (400 MHz, CDCl<sub>3</sub>) spectrum of compound **1a**.

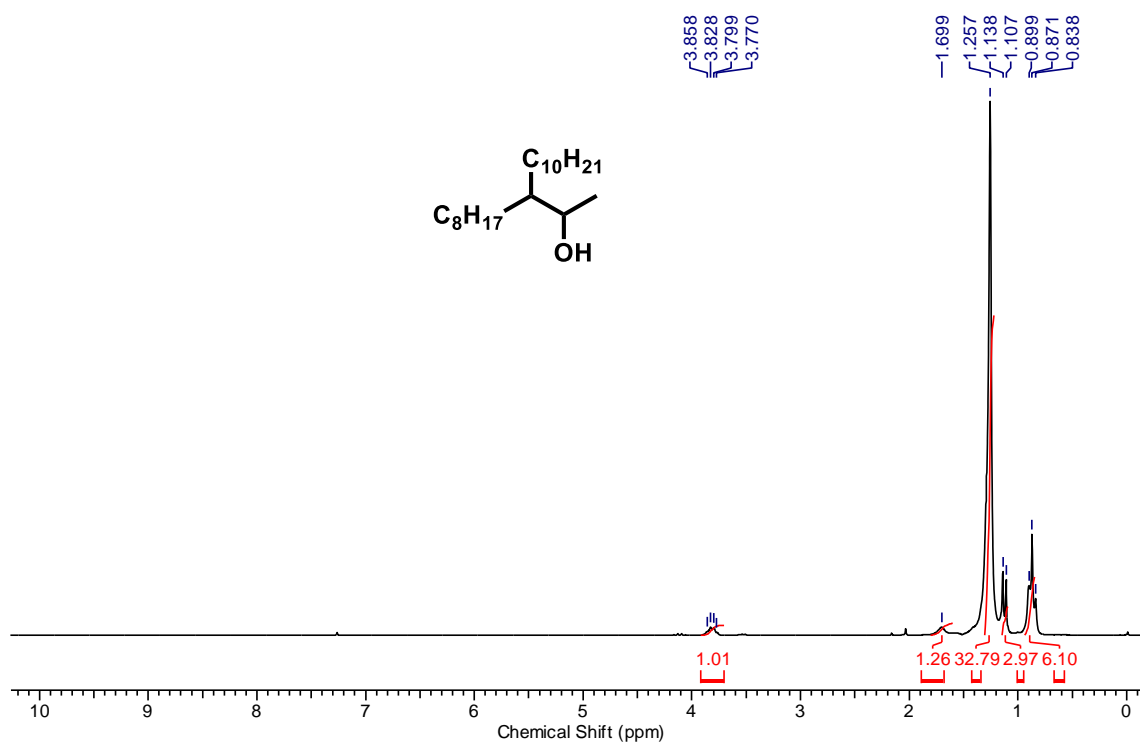
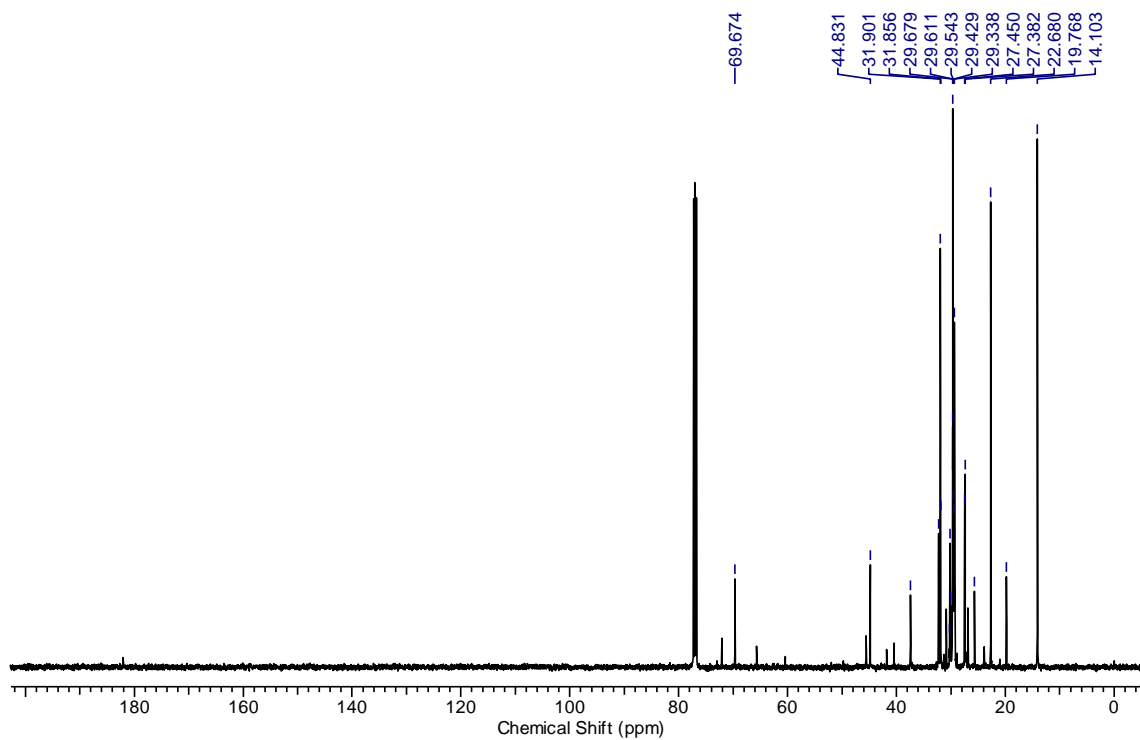
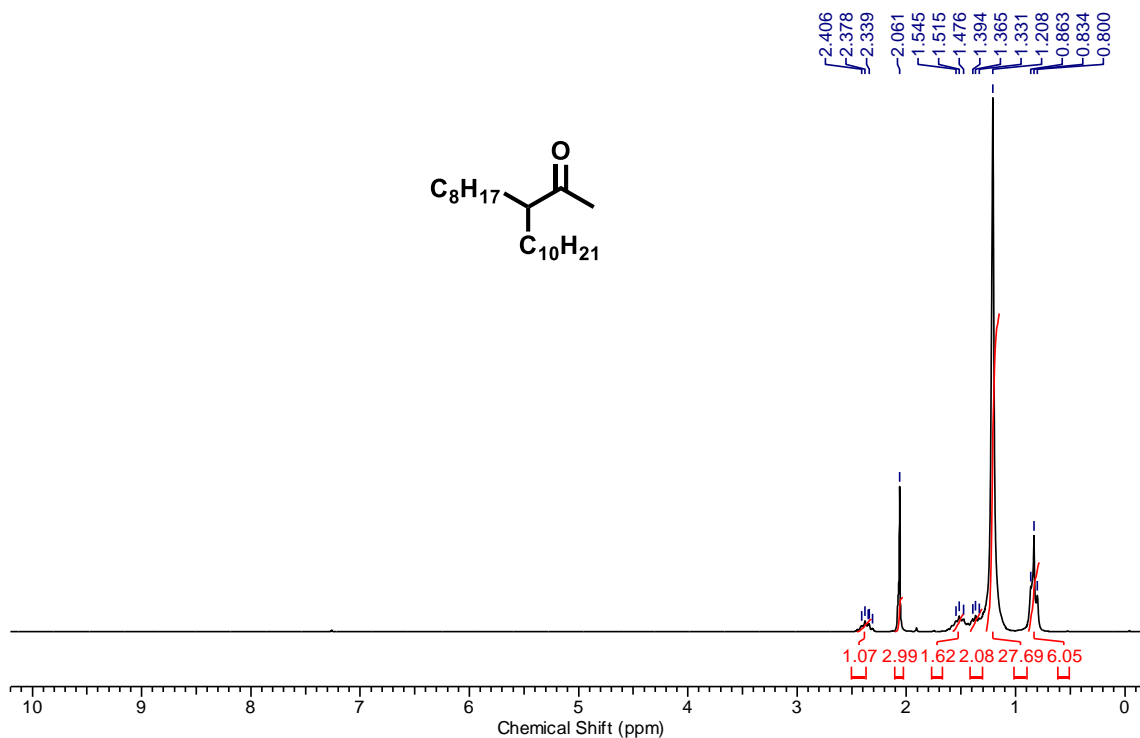


Figure 18. <sup>1</sup>H NMR (200 MHz, CDCl<sub>3</sub>) spectrum of compound **1b**.



**Figure 19.**  $^{13}\text{C}$  NMR (100 MHz,  $\text{CDCl}_3$ ) spectrum of compound **1b**.



**Figure 20.**  $^1\text{H}$  NMR (200 MHz,  $\text{CDCl}_3$ ) spectrum of compound **1c**.



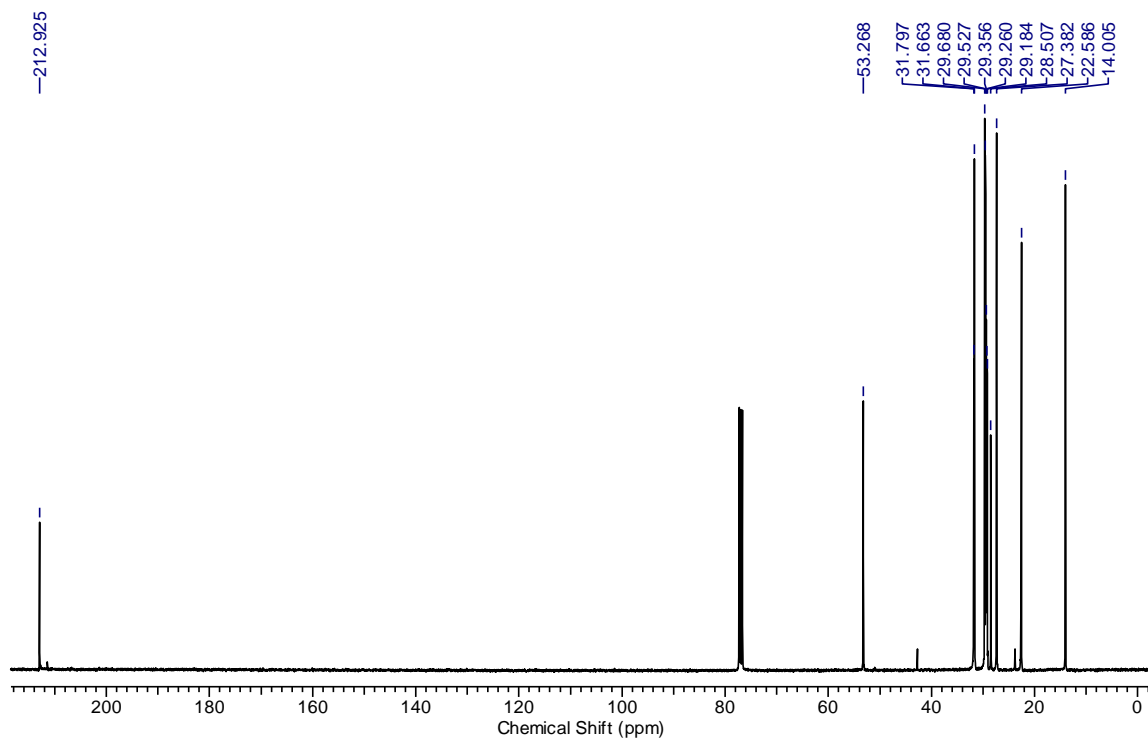


**Figure 21.**  $^{13}\text{C}$  NMR (100 MHz,  $\text{CDCl}_3$ ) spectrum of compound **1c**.

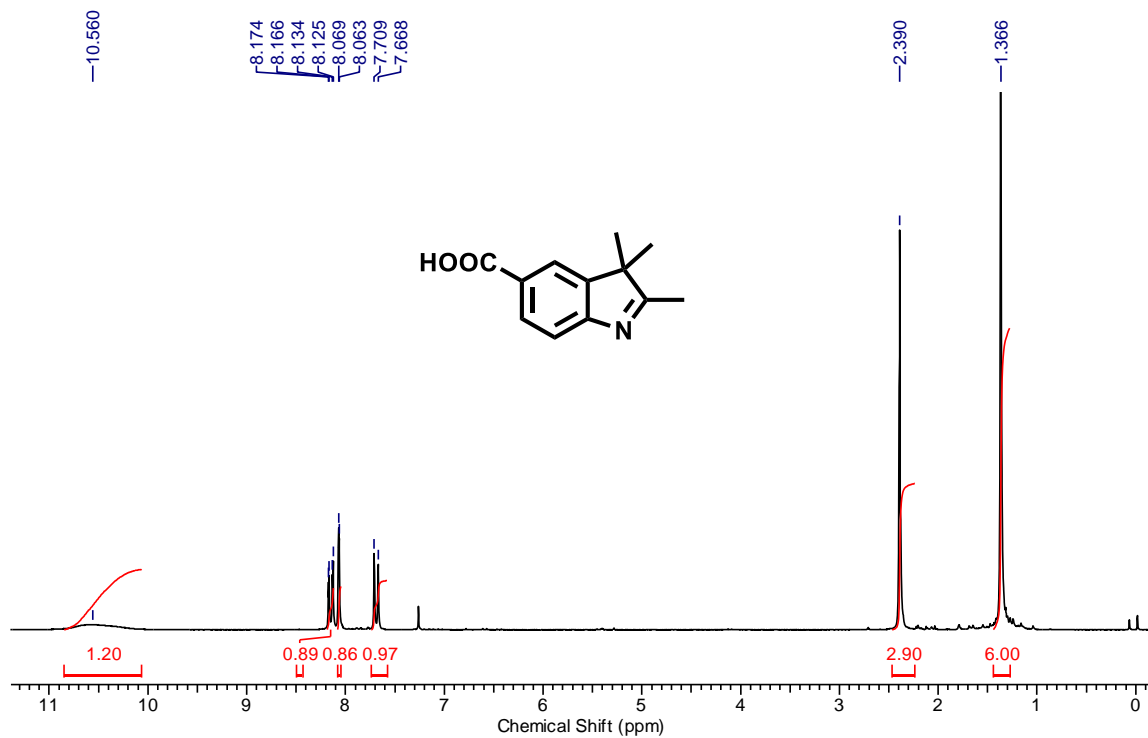


**Figure 22.**  $^1\text{H}$  NMR (200 MHz,  $\text{CDCl}_3$ ) spectrum of compound **2a**.

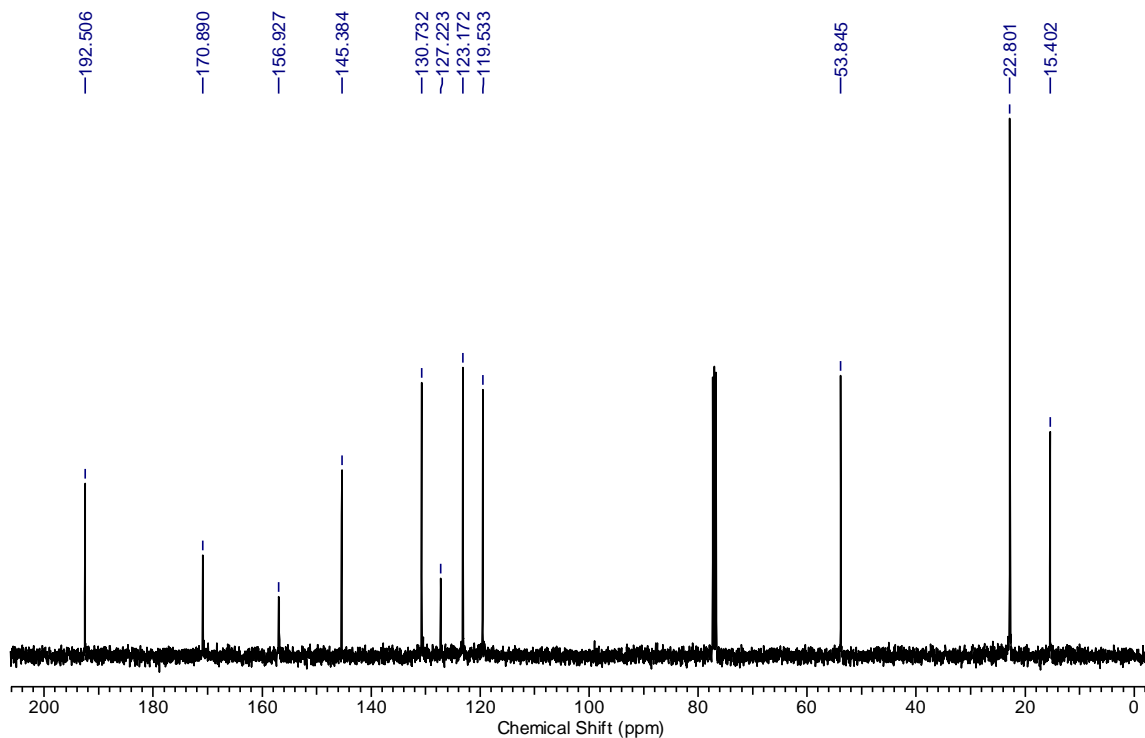


Figure 23.  $^{13}\text{C}$  NMR (100 MHz,  $\text{CDCl}_3$ ) spectrum of compound **2a**.

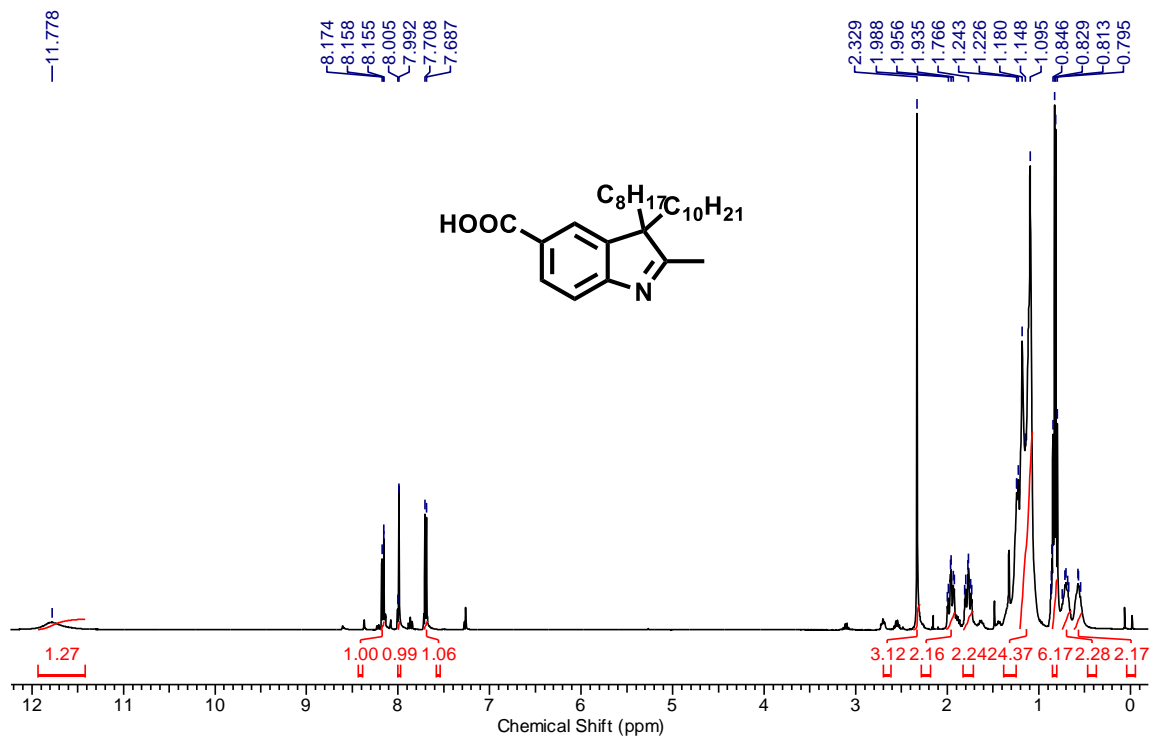


Figure 24.  $^1\text{H}$  NMR (400 MHz,  $\text{CDCl}_3$ ) spectrum of compound **2b**.

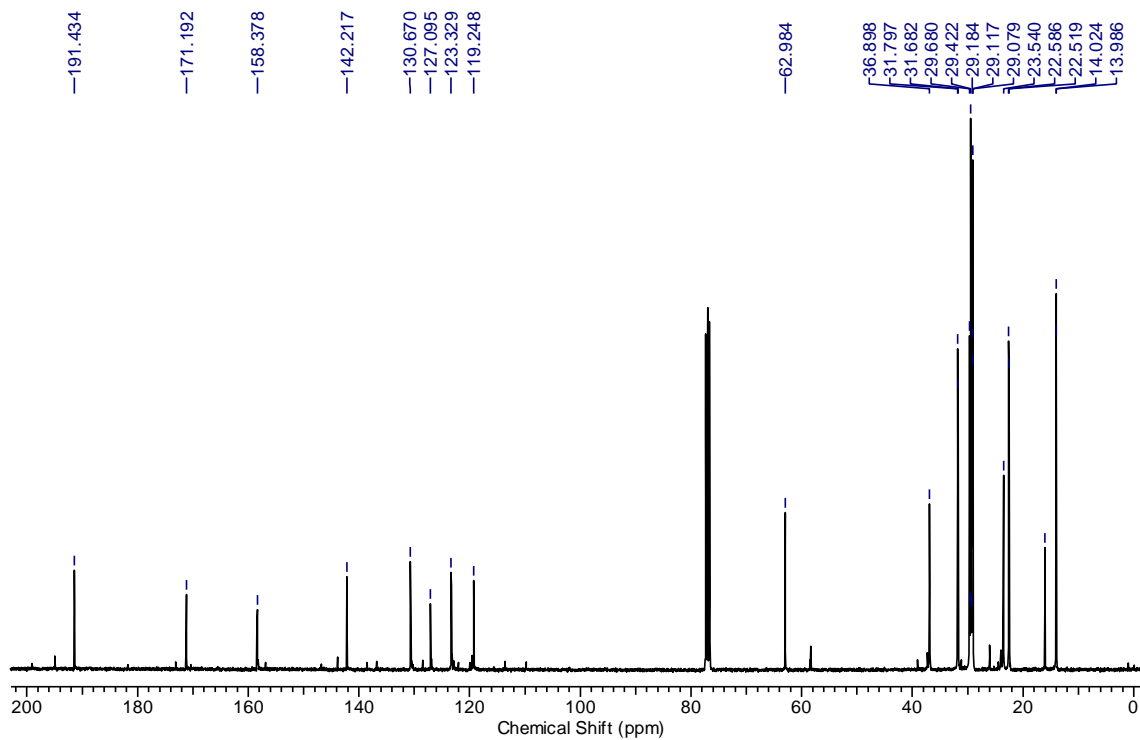


Figure 25. <sup>13</sup>C NMR (100 MHz, CDCl<sub>3</sub>) spectrum of compound **2b**.

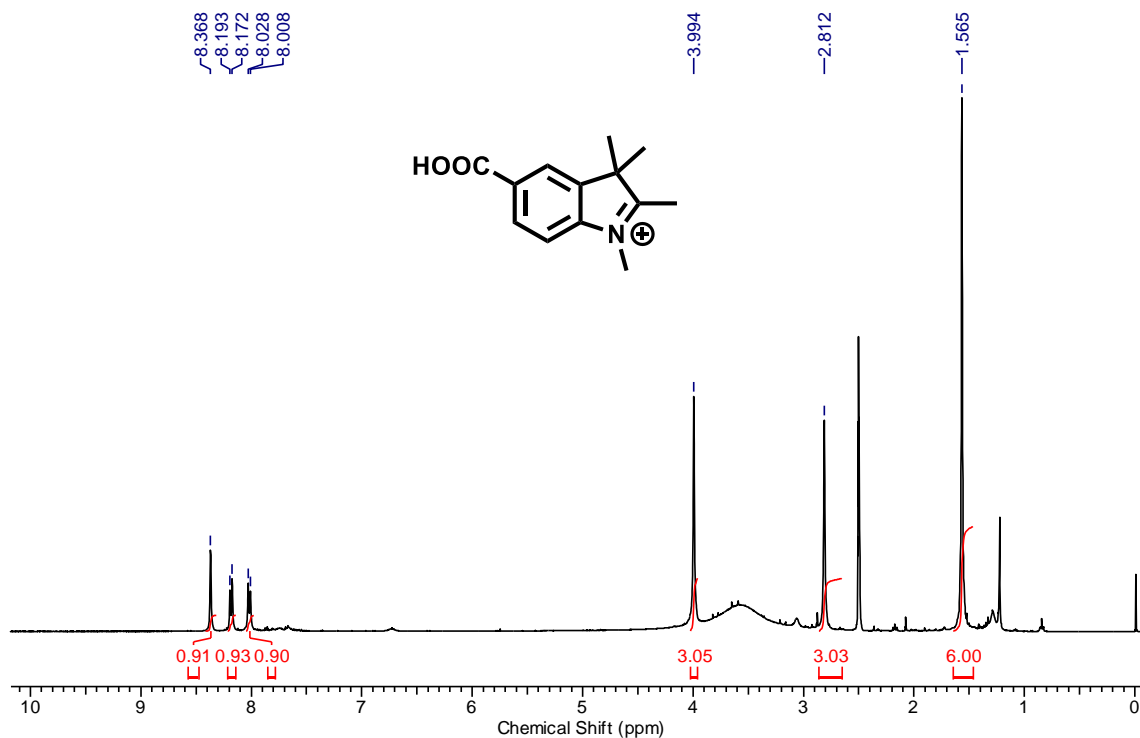


Figure 26. <sup>1</sup>H NMR (400 MHz, DMSO-*d*<sub>6</sub>) spectrum of compound **3a**.

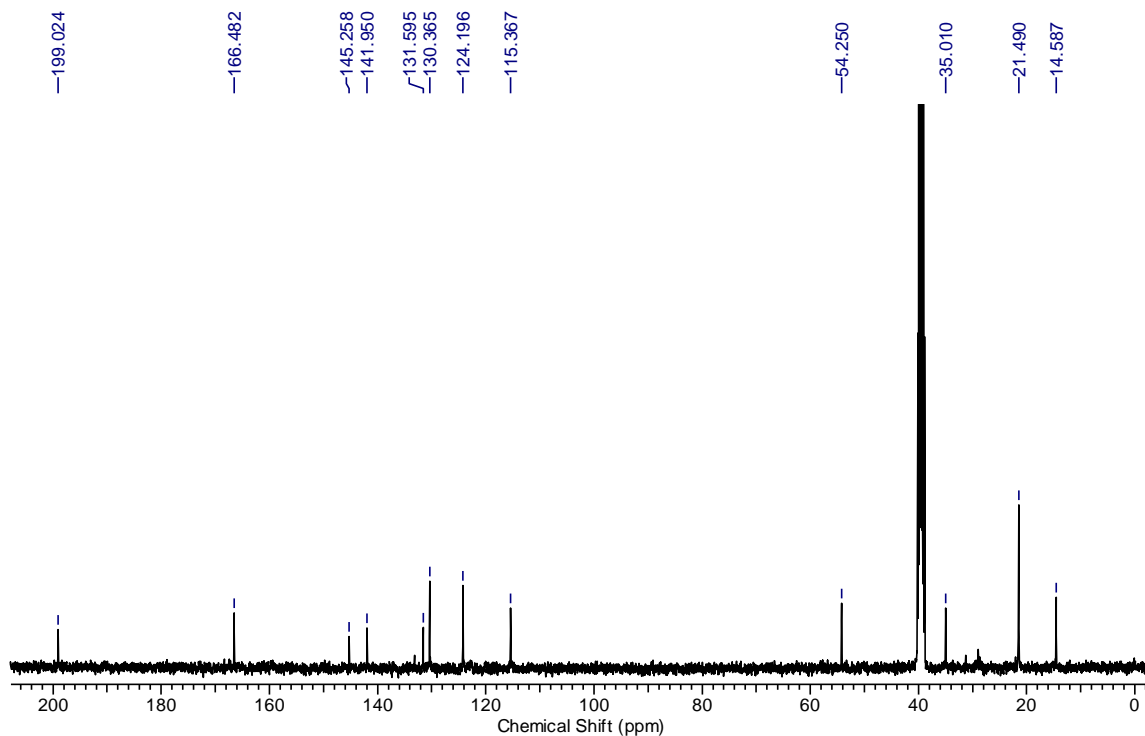


Figure 27.  $^{13}\text{C}$  NMR (100 MHz,  $\text{DMSO-}d_6$ ) spectrum of compound **3a**.

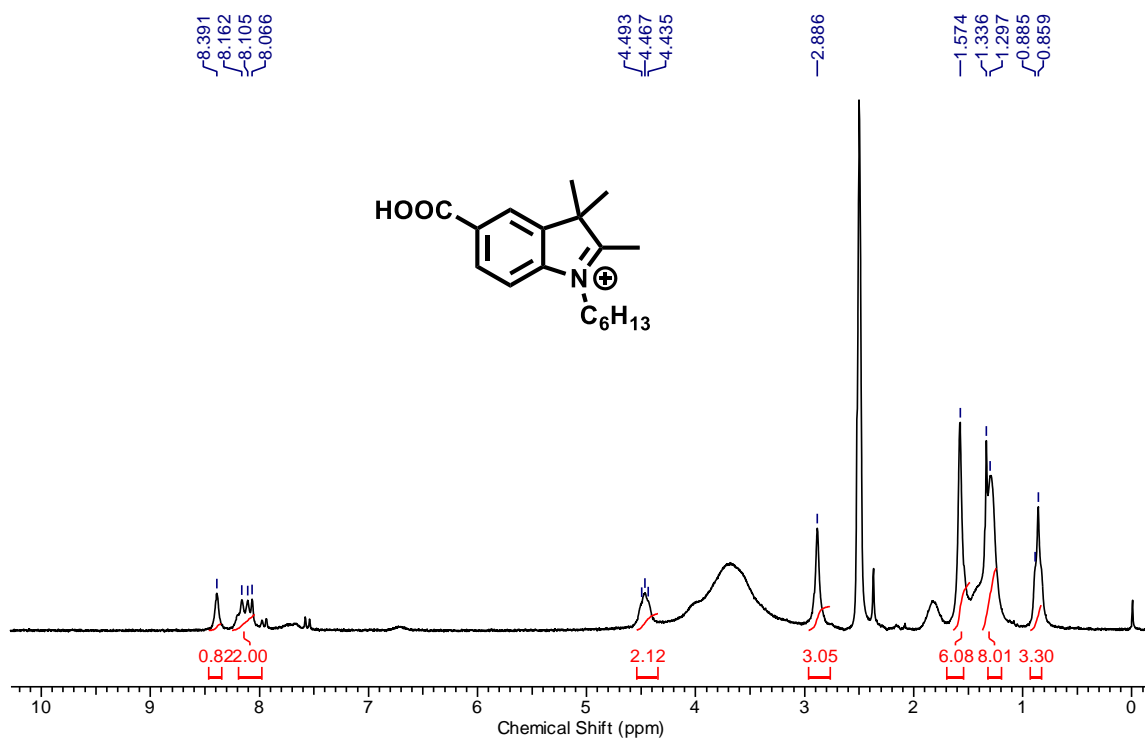
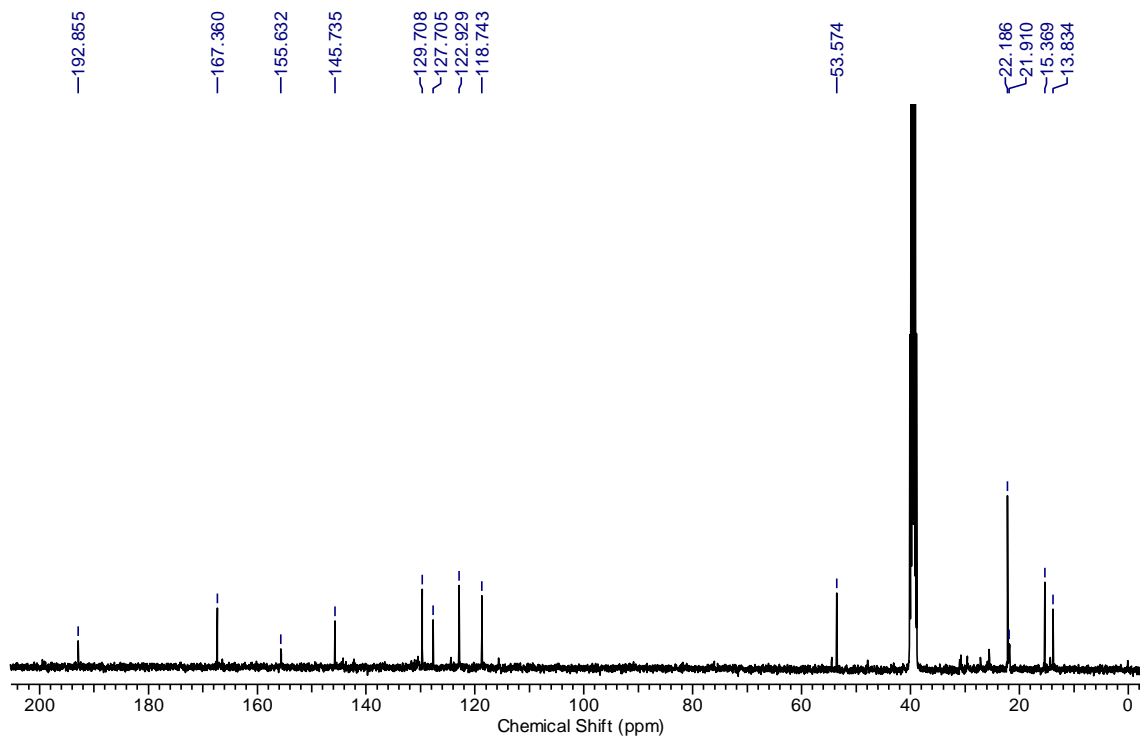
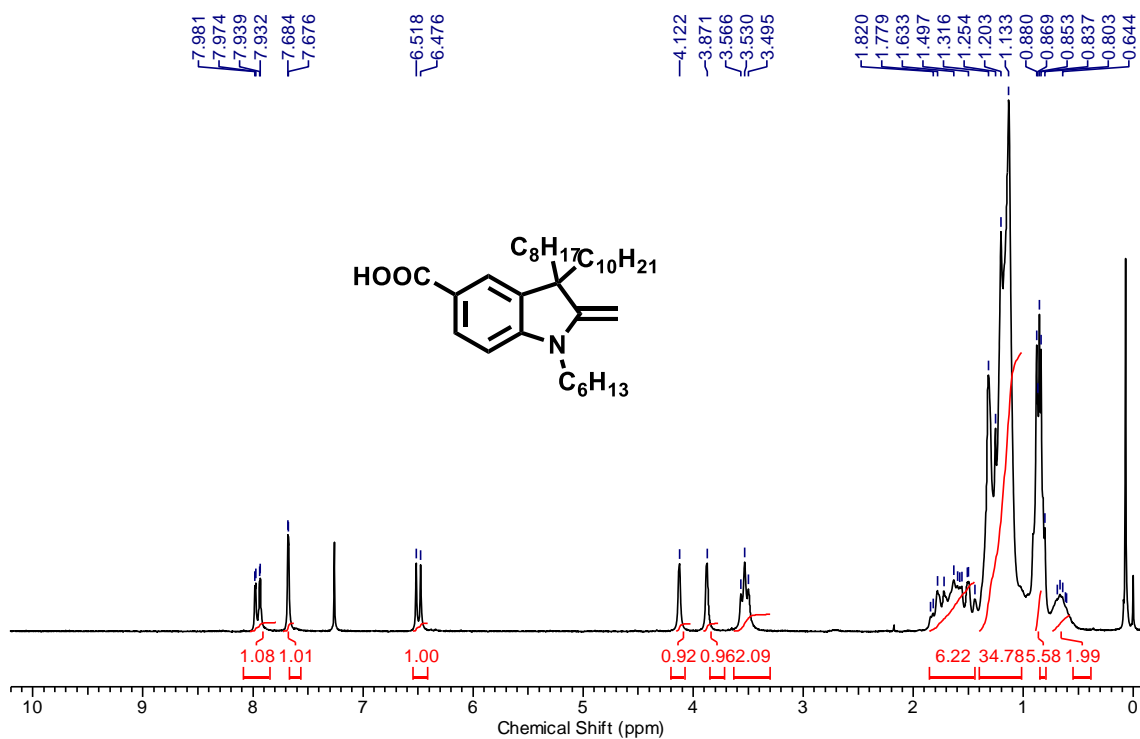


Figure 28.  $^1\text{H}$  NMR (200 MHz,  $\text{DMSO-}d_6$ ) spectrum of compound **3b**.



**Figure 29.**  $^{13}\text{C}$  NMR (100 MHz,  $\text{DMSO-}d_6$ ) spectrum of compound **3b**.



**Figure 30.**  $^1\text{H}$  NMR (200 MHz,  $\text{CDCl}_3$ ) spectrum of compound 3-decyl-1-hexyl-3-methyl-2-methyleneindoline-5-carboxylic acid.

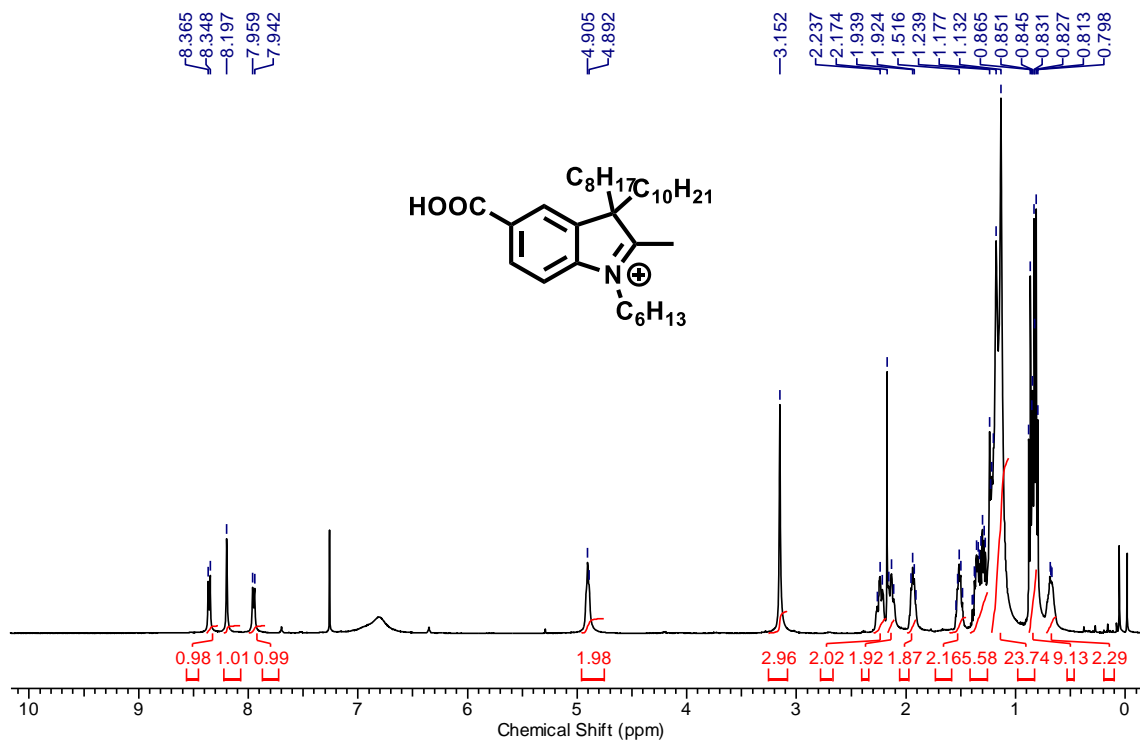


**Figure 31.**  $^1\text{H}$  NMR (500 MHz,  $\text{CDCl}_3$ ) spectrum of compound 3c.

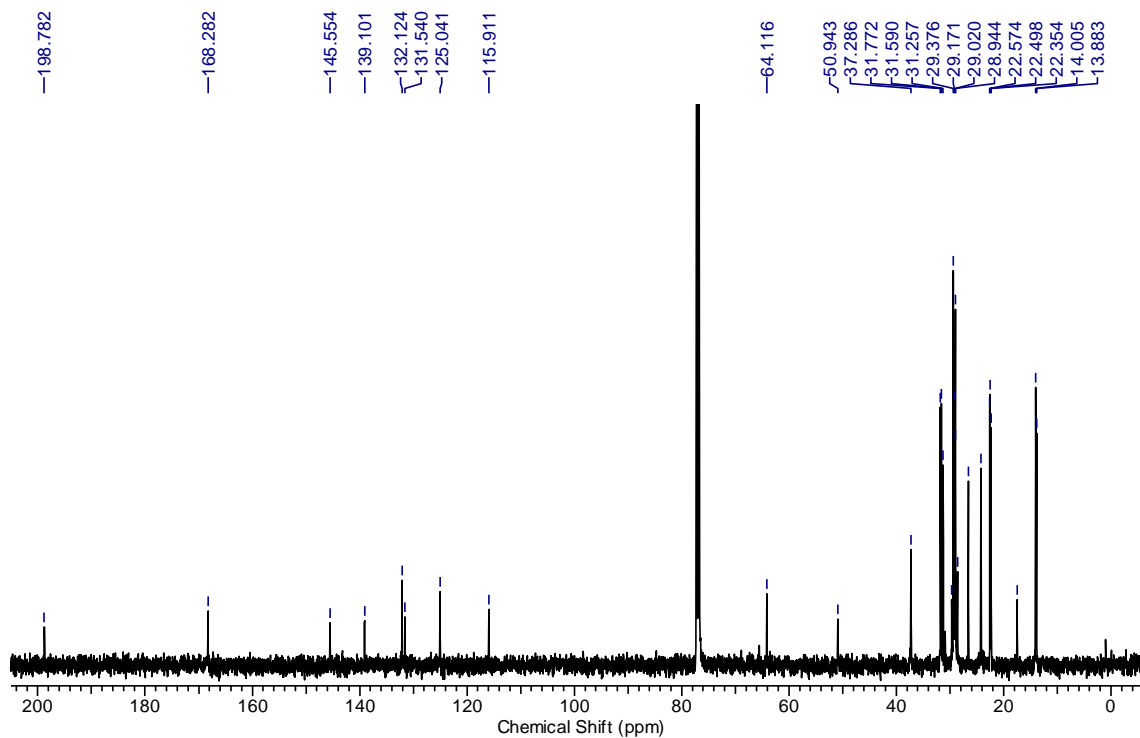


**Figure 32.**  $^{13}\text{C}$  NMR (100 MHz,  $\text{CDCl}_3$ ) spectrum of compound 3c.

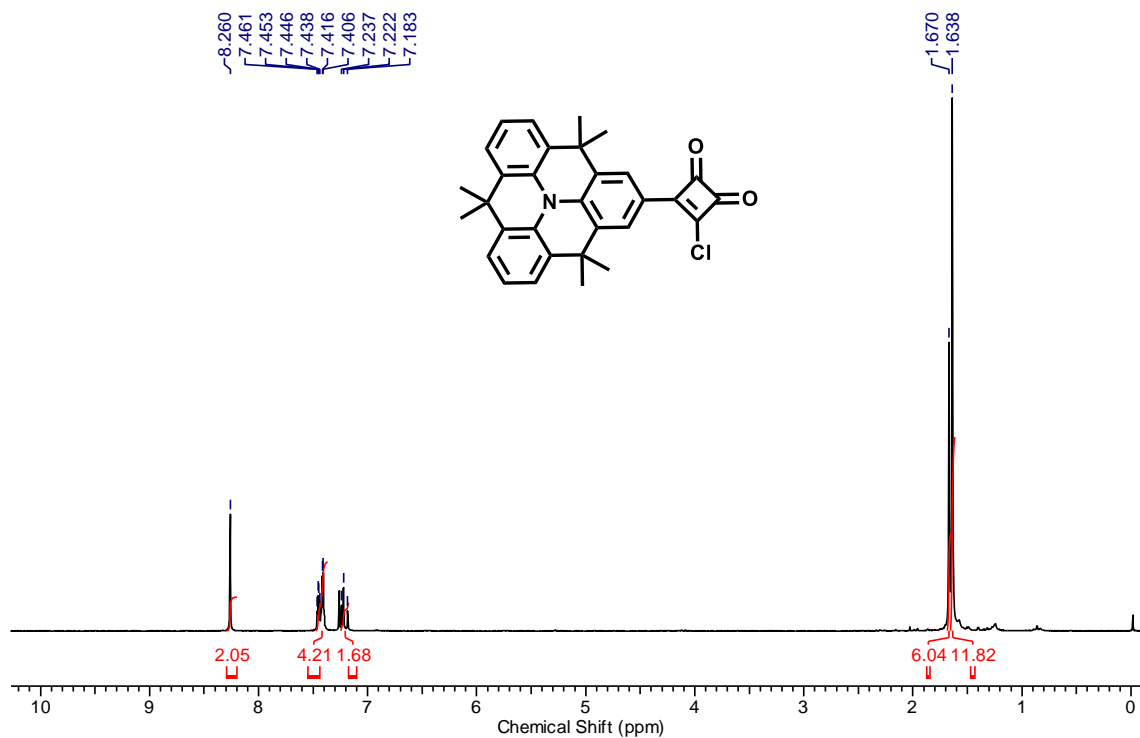


Figure 33. <sup>1</sup>H NMR (200 MHz, CDCl<sub>3</sub>) spectrum of compound **4b**.

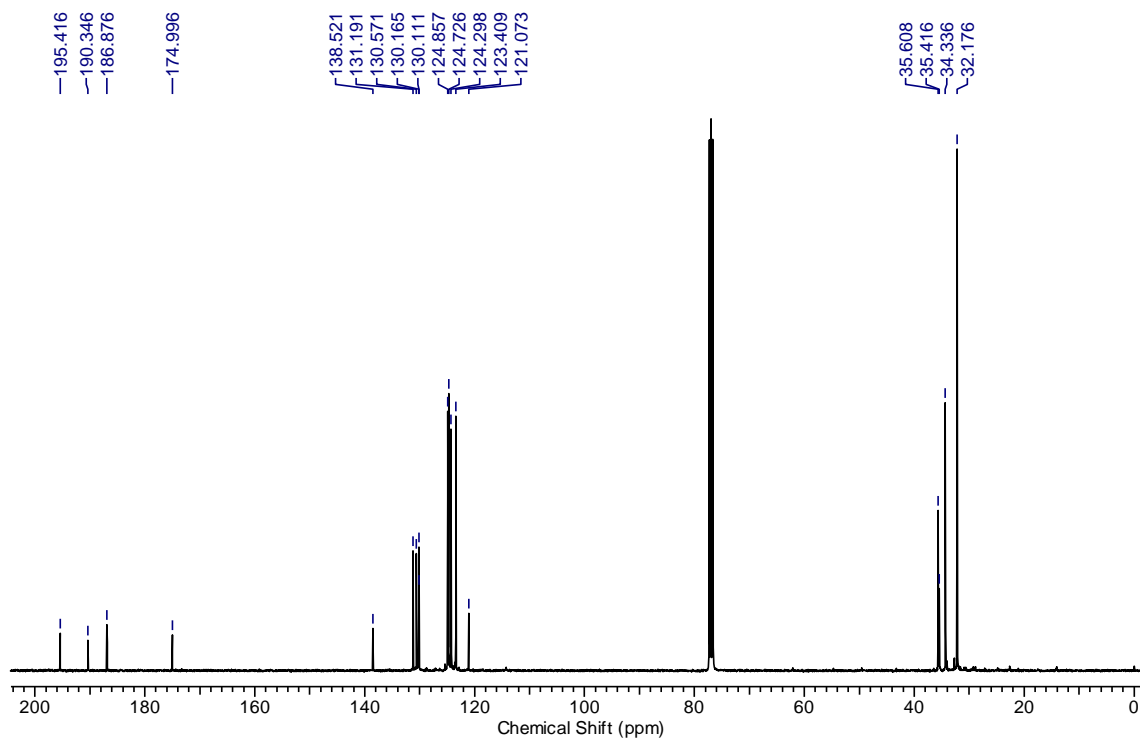


Figure 34. <sup>13</sup>C NMR (100 MHz, CDCl<sub>3</sub>) spectrum of compound **4b**.

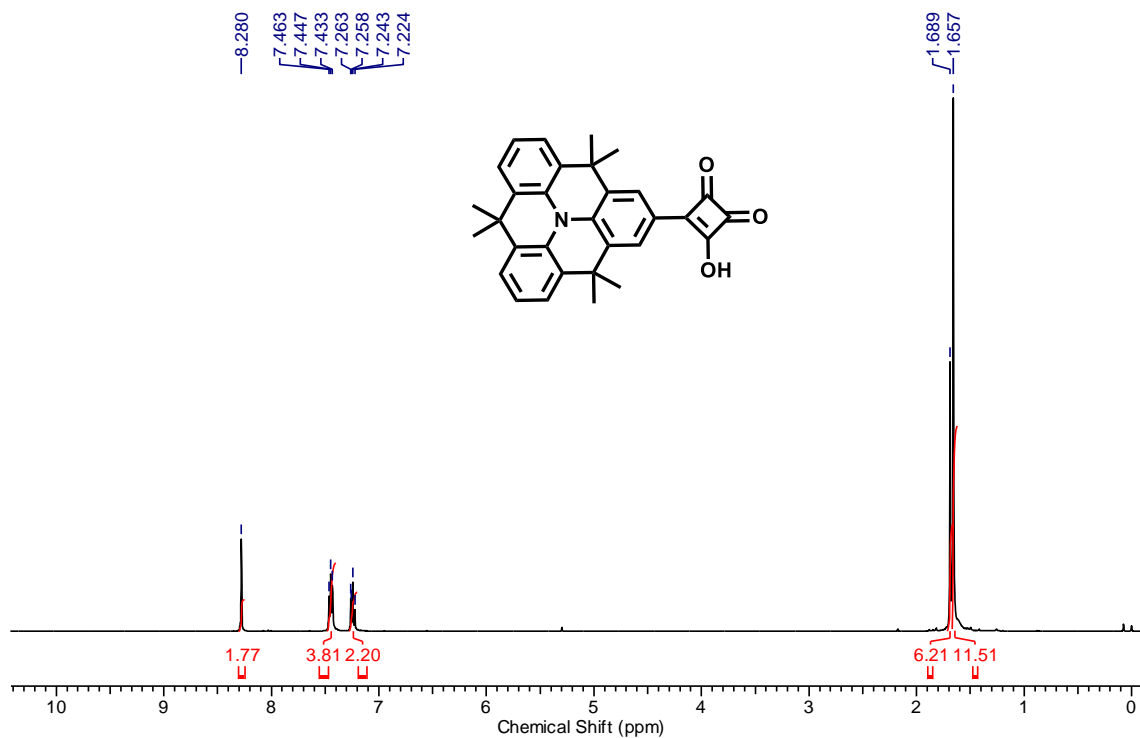


Figure 35. <sup>1</sup>H NMR (400 MHz, CDCl<sub>3</sub>) spectrum of compound 4c.

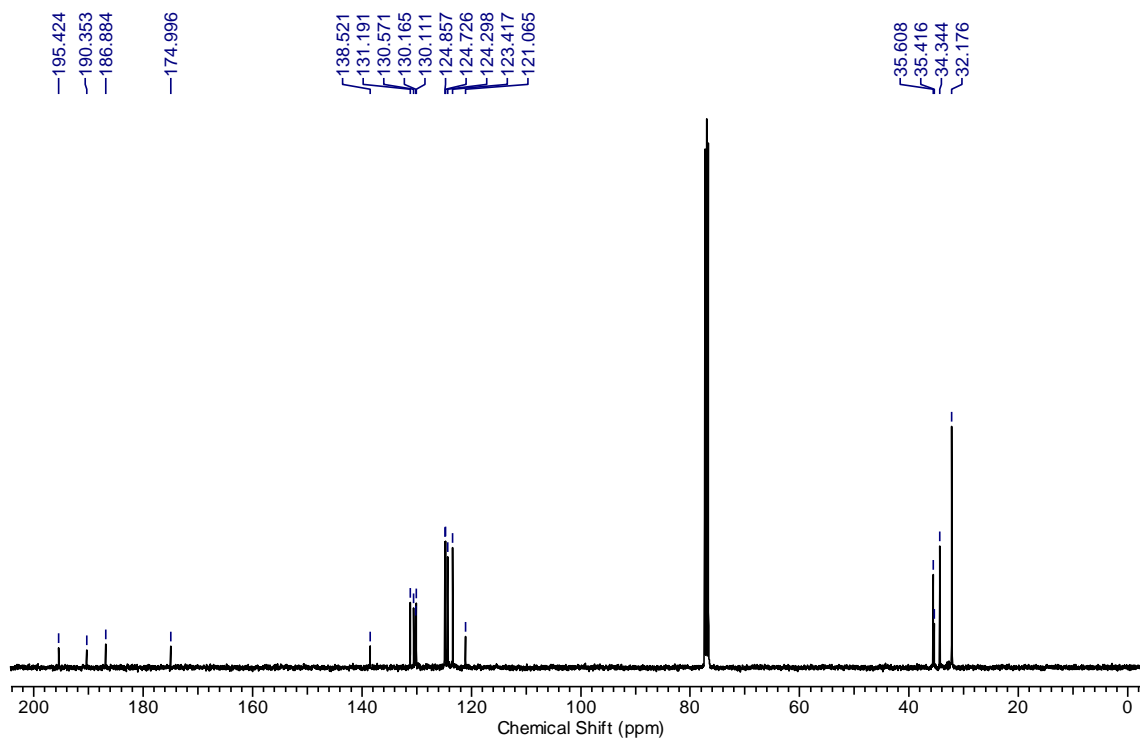


Figure 36. <sup>13</sup>C NMR (100 MHz, CDCl<sub>3</sub>) spectrum of compound 4c.



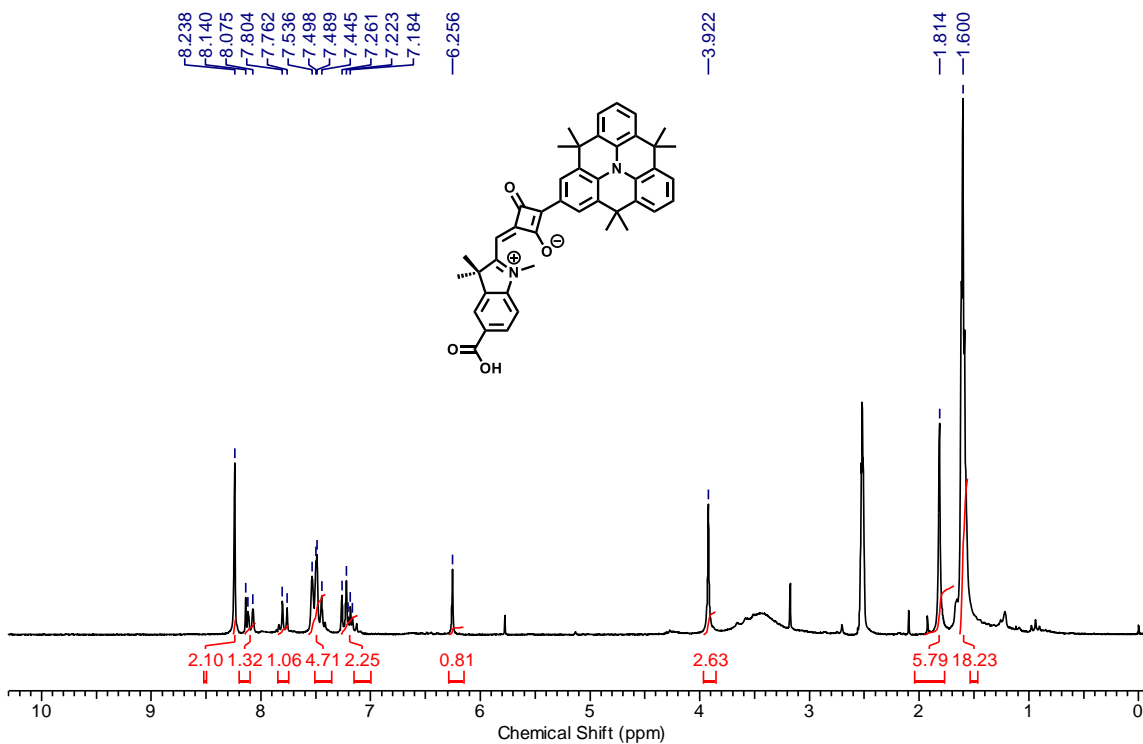


Figure 37.  $^1\text{H}$  NMR (200 MHz,  $\text{DMSO-}d_6$ ) spectrum of compound NSQ1.

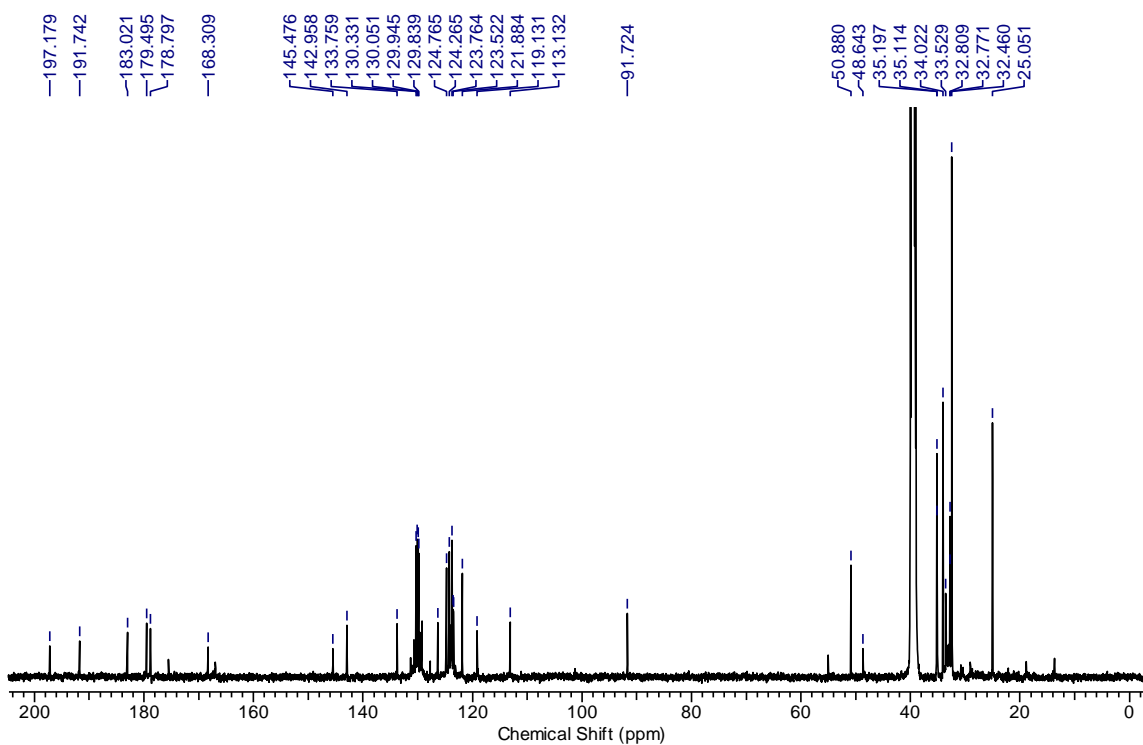
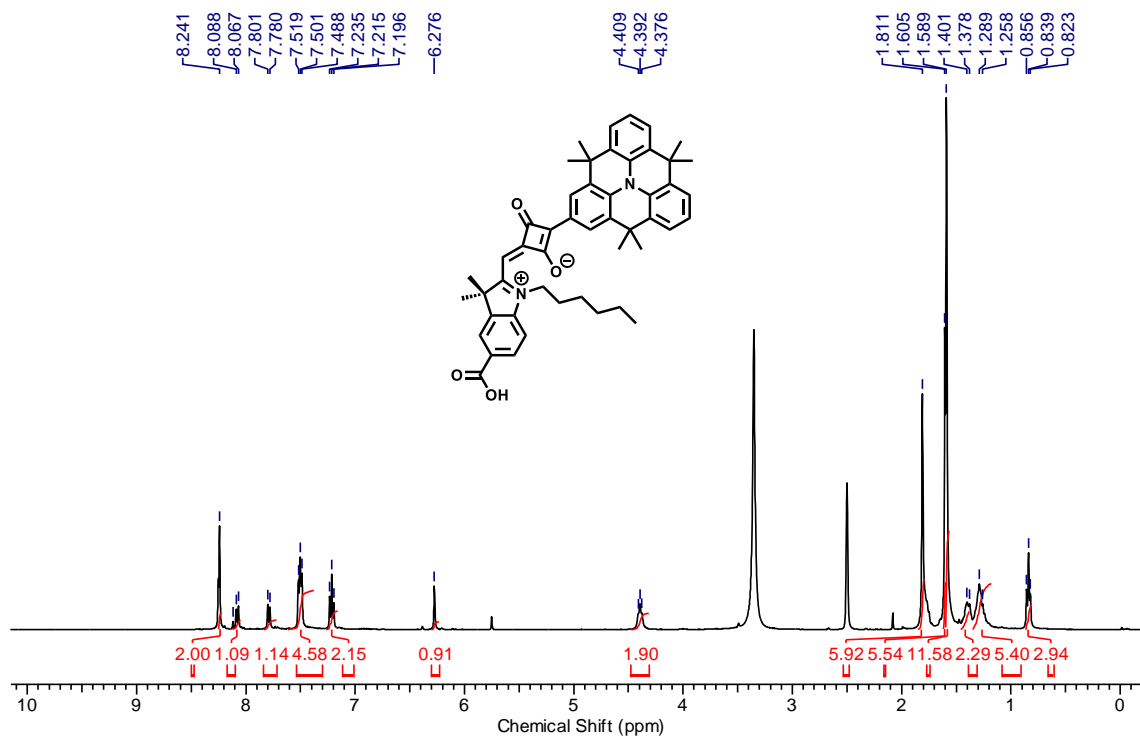
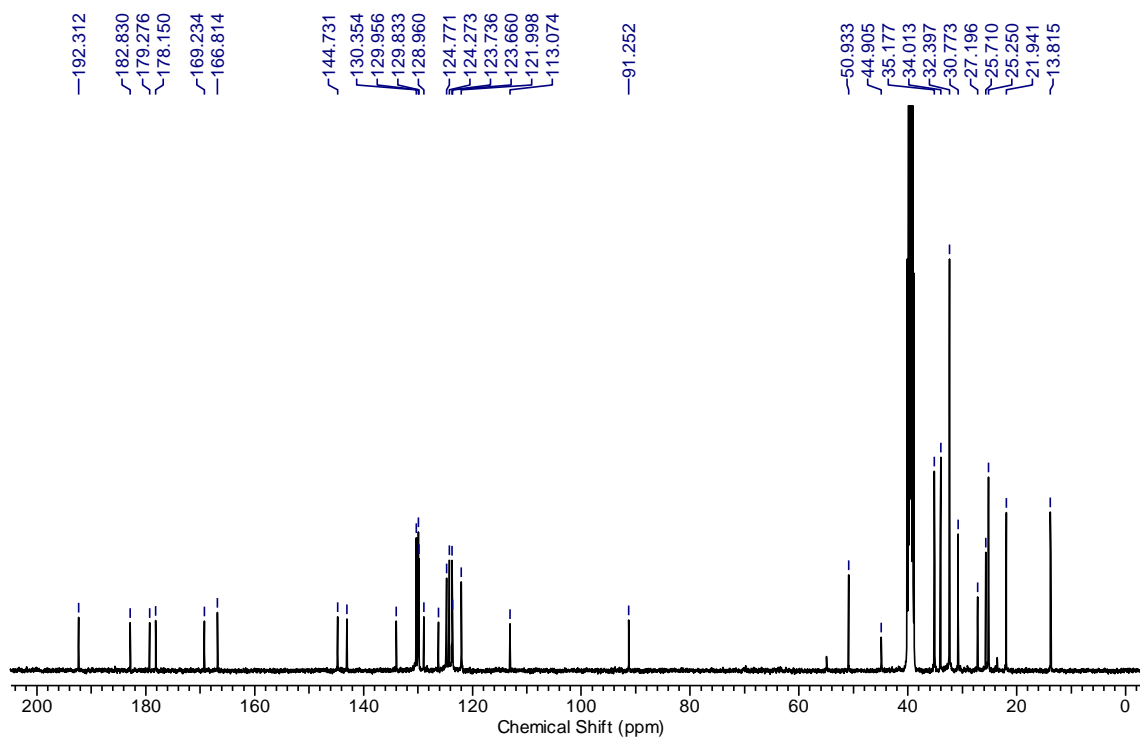


Figure 38.  $^{13}\text{C}$  NMR (100 MHz,  $\text{DMSO-}d_6$ ) spectrum of compound NSQ1.



**Figure 39.** <sup>1</sup>H NMR (400 MHz, DMSO-*d*<sub>6</sub>) spectrum of compound NSQ2.



**Figure 40.** <sup>13</sup>C NMR (100 MHz, DMSO-*d*<sub>6</sub>) spectrum of compound NSQ2.

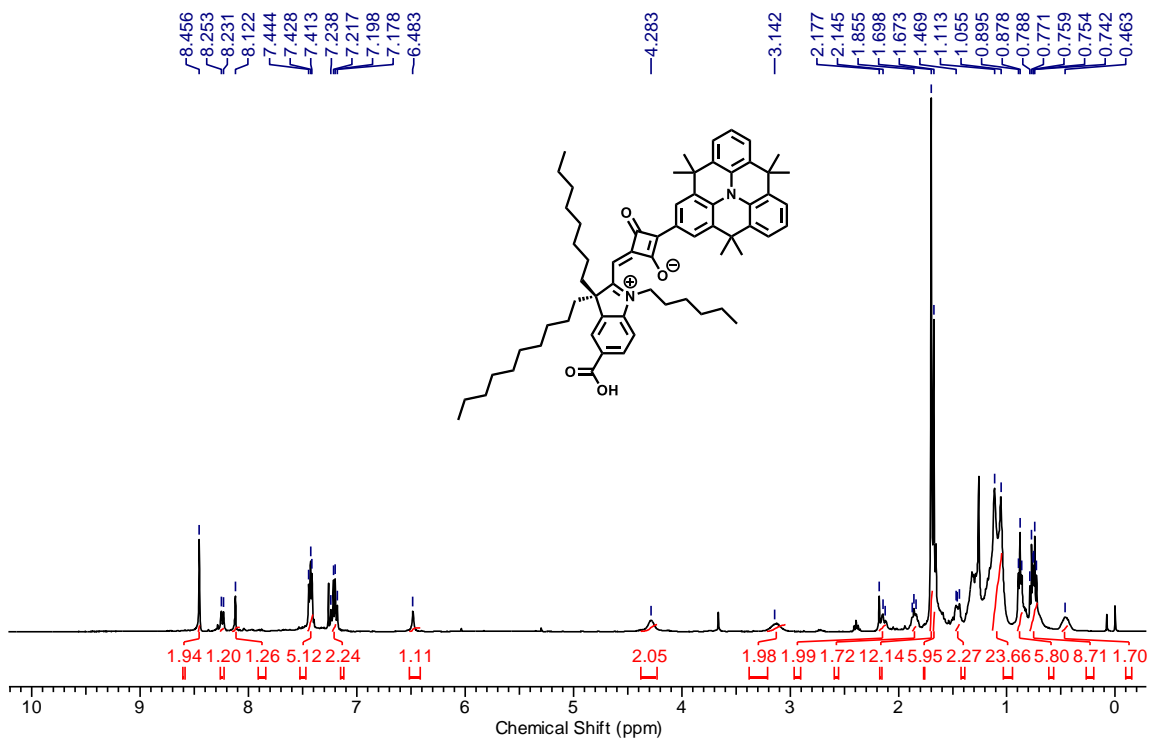


**Figure 41.** <sup>1</sup>H NMR (400 MHz, CDCl<sub>3</sub>) spectrum of compound NSQ3.

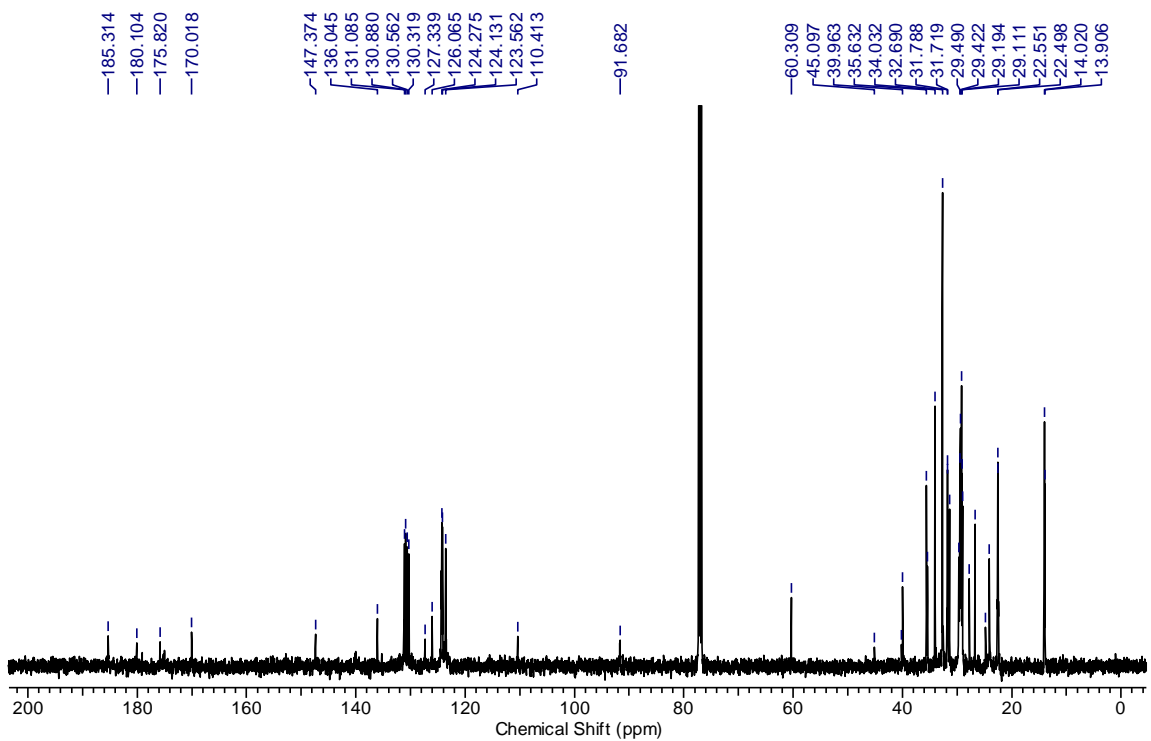


**Figure 42.** <sup>13</sup>C NMR (100 MHz, CDCl<sub>3</sub>) spectrum of compound NSQ3.

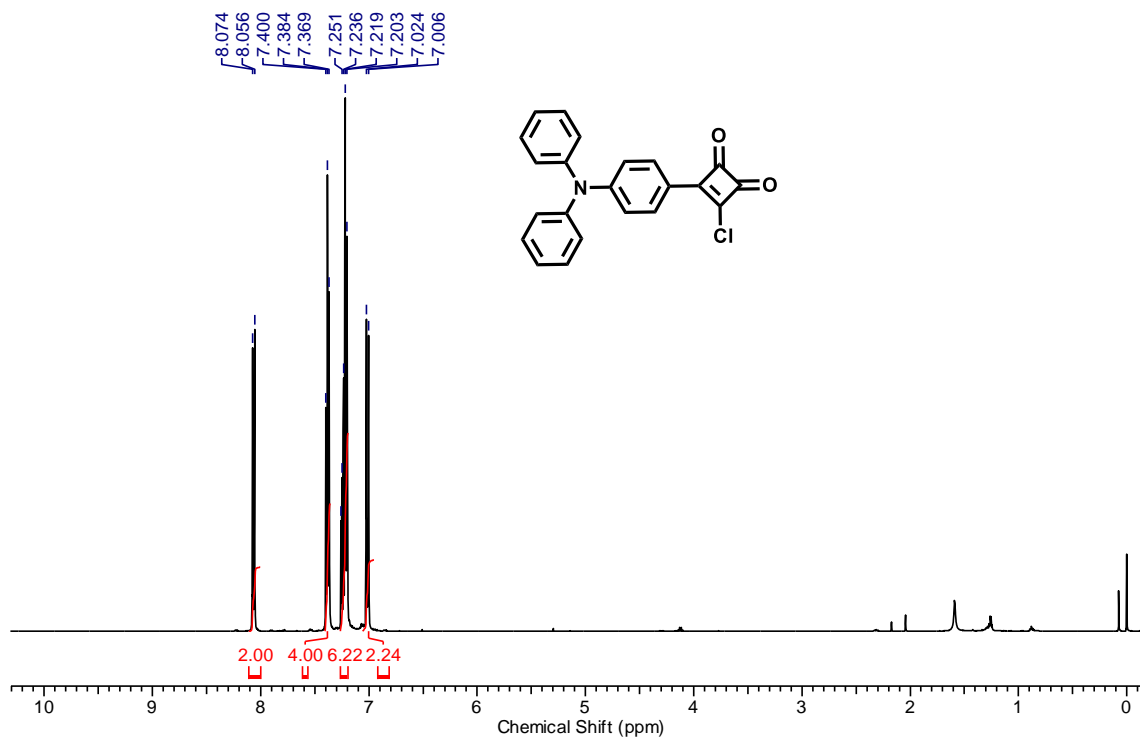


**Figure 43.** <sup>1</sup>H NMR (500 MHz, CDCl<sub>3</sub>) spectrum of compound **5b**.

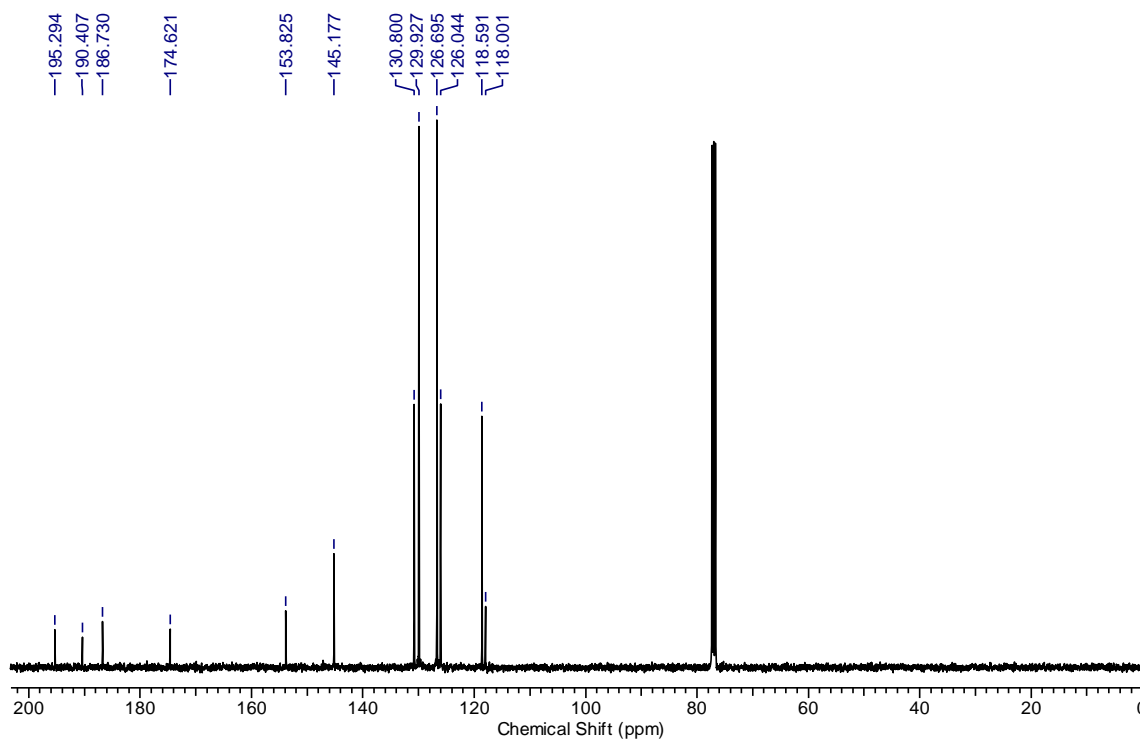


**Figure 44.** <sup>13</sup>C NMR (100 MHz, CDCl<sub>3</sub>) spectrum of compound **5b**.

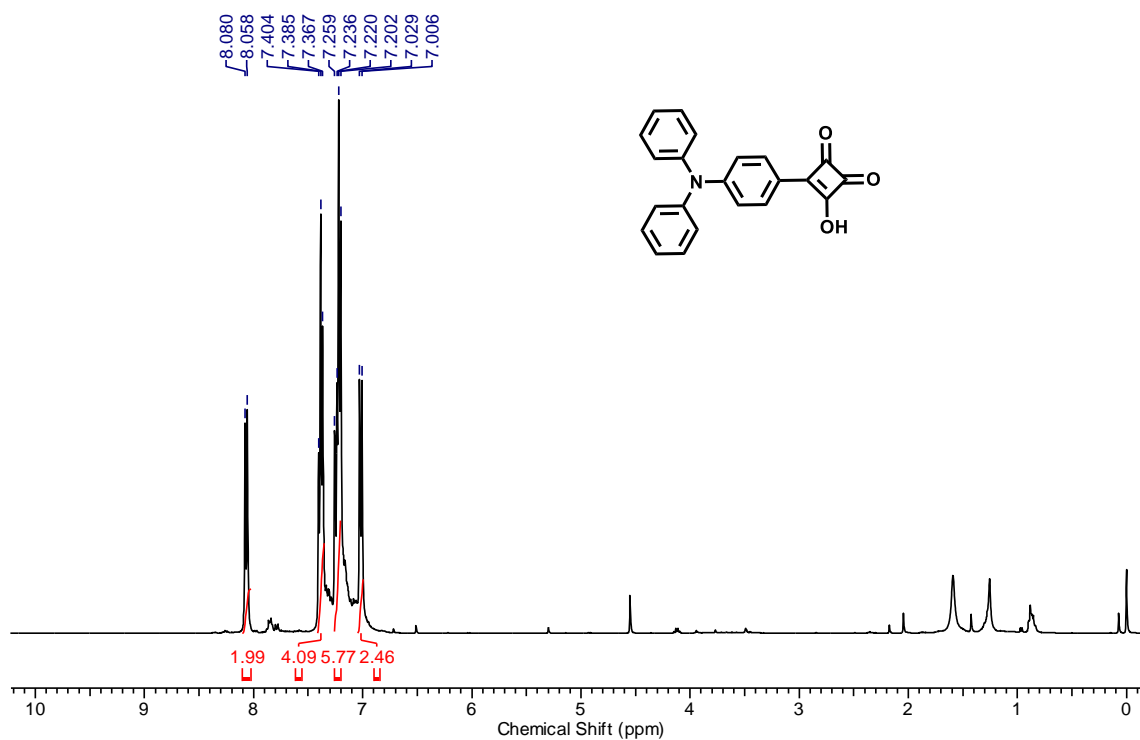


Figure 45. <sup>1</sup>H NMR (400 MHz, CDCl<sub>3</sub>) spectrum of compound 5c.

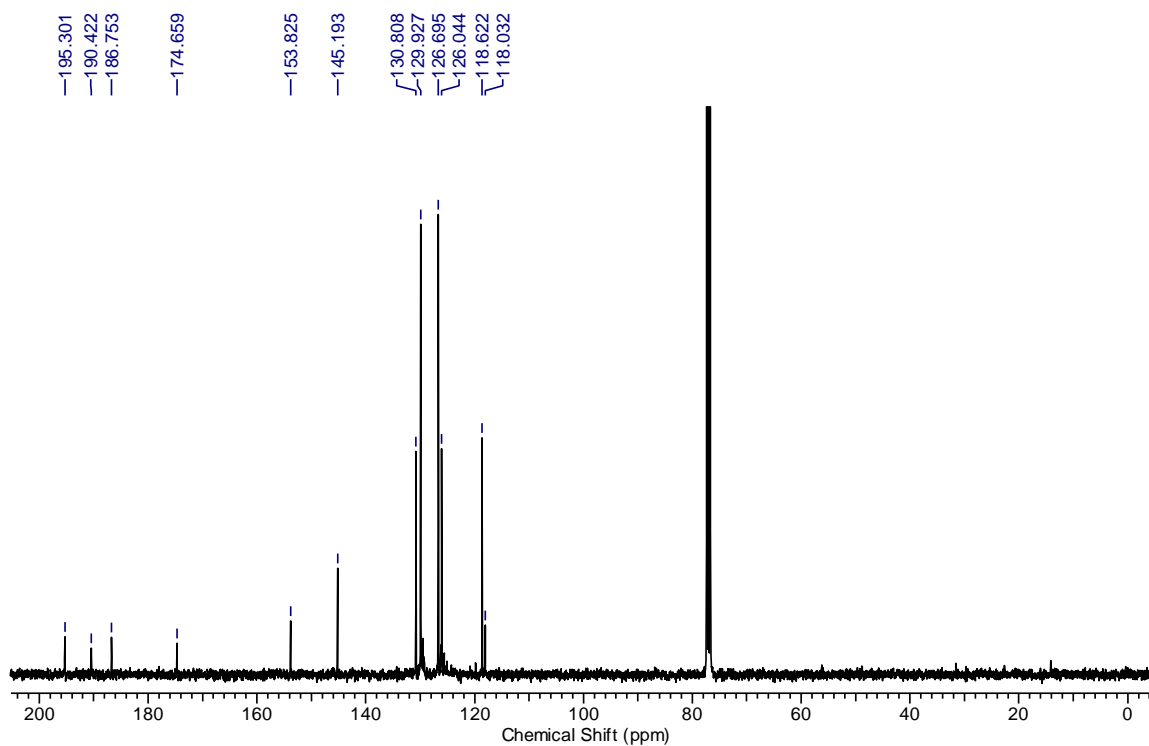
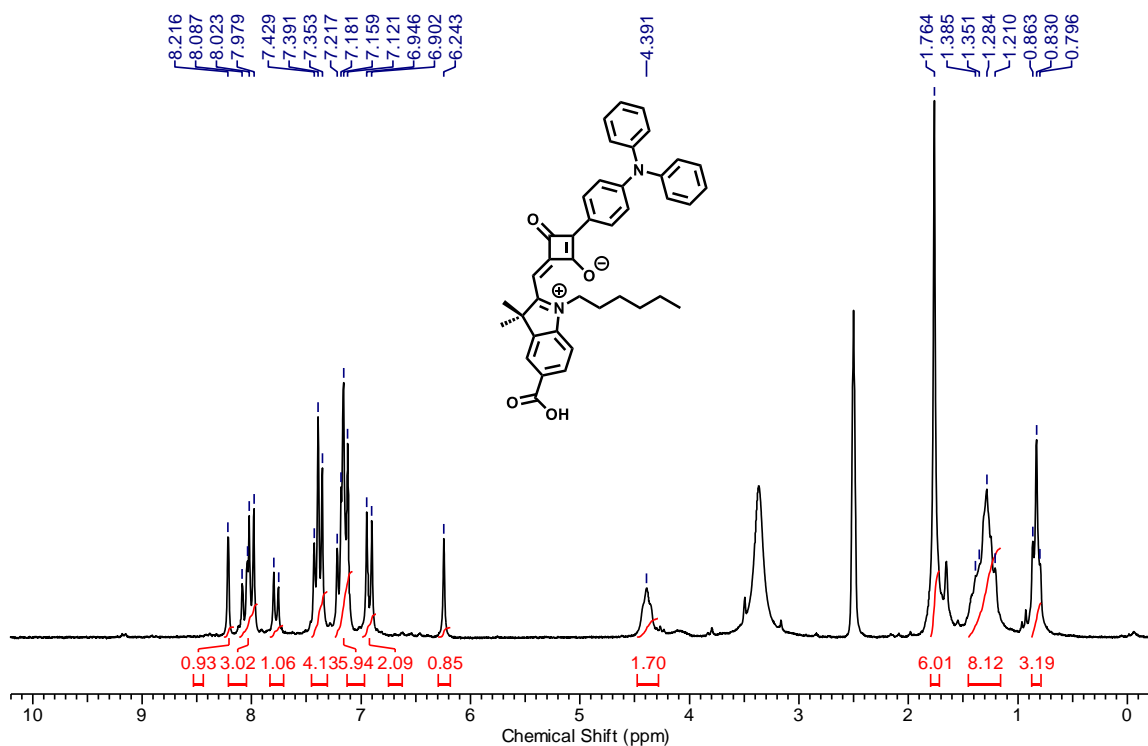
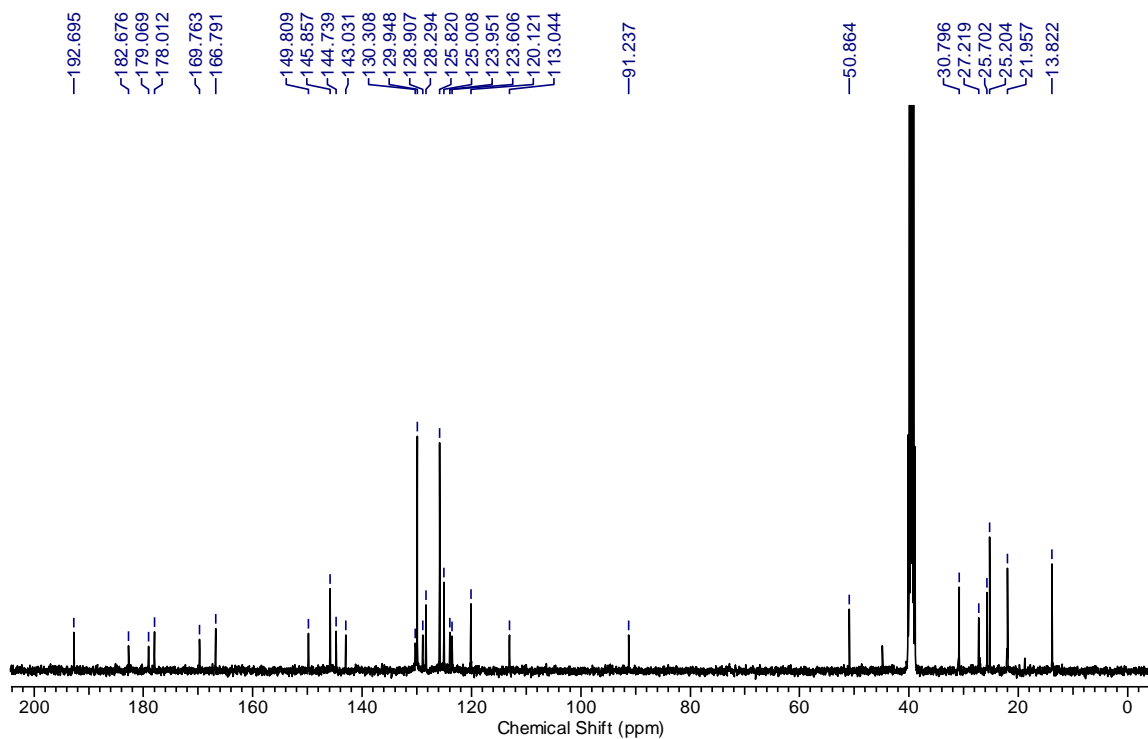


Figure 46. <sup>13</sup>C (100 MHz, CDCl<sub>3</sub>) spectrum of compound 5c.



**Figure 47.** <sup>1</sup>H NMR (200 MHz, DMSO-*d*<sub>6</sub>) spectrum of compound NSQR.



**Figure 48.** <sup>13</sup>C NMR (100 MHz, CDCl<sub>3</sub>) spectrum of compound NSQR.

**2.6 REFERENCES**

1. Hagfeldt, A.; Boschloo, G.; Sun, L.; Kloo, L.; Pettersson, H. *Chem. Rev.* **2010**, *110*, 6595.
2. Liang, M.; Chen, J. *Chem. Soc. Rev.* **2013**, *42*, 3453.
3. Maeda, T.; Hamamura, Y.; Miyanaga, K.; Shima, N.; Yagi, S.; Nakazumi, H. *Org. Lett.* **2011**, *13*, 5994.
4. Kuster, S.; Sauvage, F.; Nazeeruddin, M. K.; Grätzel, M.; Nüesch, F. A.; Geiger, T. *Dyes Pigm.* **2010**, *87*, 30.
5. Zhang, S.; Yang, X.; Numata, Y.; Han, L. *Energy Environ Sci.* **2013**, *6*, 1443.
6. Yella, A.; Humphry-Baker, R.; Curchod, B. F.; Ashari Astani, N.; Teuscher, J. I.; Polander, L. E.; Mathew, S.; Moser, J.-E.; Tavernelli, I.; Rothlisberger, U. *Chem. Mater.* **2013**, *25*, 2733.
7. Zhang, W.; Wu, Y.; Li, X.; Li, E.; Song, X.; Jiang, H.; Shen, C.; Zhang, H.; Tian, H.; Zhu, W.-H. *Chem. Sci.* **2017**, *8*, 2115.
8. Mishra, A.; Fischer, M. K.; Bäuerle, P. *Angew. Chem., Int. Ed.* **2009**, *48*, 2474.
9. Saccone, D.; Galliano, S.; Barbero, N.; Quagliotto, P.; Viscardi, G.; Barolo, C. *Eur. J. Org. Chem.* **2016**, *2016*, 2244.
10. Ajayaghosh, A. *Acc. Chem. Res.* **2005**, *38*, 449.
11. Qin, C.; Wong, W. Y.; Han, L. *Chem. Asian J.* **2013**, *8*, 1706.
12. Liang, Y.; Cheng, F.; Liang, J.; Chen, J. *J. Phys. Chem. C* **2010**, *114*, 15842.
13. Karjule, N.; MK, M. F.; Nithyanandhan, J. *J. Mater. Chem. A* **2016**, *4*, 18910.
14. Ooyama, Y.; Harima, Y. *ChemPhysChem* **2012**, *13*, 4032.
15. Li, J.-Y.; Chen, C.-Y.; Lee, C.-P.; Chen, S.-C.; Lin, T.-H.; Tsai, H.-H.; Ho, K.-C.; Wu, C.-G. *Org. Lett.* **2010**, *12*, 5454.
16. Velusamy, M.; Justin Thomas, K.; Lin, J. T.; Hsu, Y.-C.; Ho, K.-C. *Org. Lett.* **2005**, *7*, 1899.
17. Sobolev, A.; Belsky, V.; Romm, I.; Chernikova, N. Y.; Guryanova, E. *Acta Crystallogr. C* **1985**, *41*, 967.
18. Cai, L.; Tsao, H. N.; Zhang, W.; Wang, L.; Xue, Z.; Grätzel, M.; Liu, B. *Adv. Energy Mater.* **2013**, *3*, 200.
19. Do, K.; Kim, D.; Cho, N.; Paek, S.; Song, K.; Ko, J. *Org. Lett.* **2011**, *14*, 222.
20. Jradi, F. M.; Kang, X.; O'Neil, D.; Pajares, G.; Getmanenko, Y. A.; Szymanski, P.; Parker, T. C.; El-Sayed, M. A.; Marder, S. R. *Chem. Mater.* **2015**, *27*, 2480.
21. Otsuka, A.; Funabiki, K.; Sugiyama, N.; Yoshida, T.; Minoura, H.; Matsui, M. *Chem. Lett.* **2006**, *35*, 666.
22. Chen, C. Y.; Wu, S. J.; Wu, C. G.; Chen, J. G.; Ho, K. C. *Angew. Chem., Int. Ed.* **2006**, *118*, 5954.
23. Fang, Z.; Chellappan, V.; Webster, R. D.; Ke, L.; Zhang, T. F.; Liu, B.; Lai, Y. H. *J. Mater. Chem.* **2012**, *22*, 15397.
24. Hellwinkel, D.; Melan, M. *Chem. Ber.* **1974**, *107*, 616.
25. Lim, C. J.; Lei, Y.; Wu, B.; Li, L.; Liu, X.; Lu, Y.; Zhu, F.; Ong, B. S.; Hu, X.; Ng, S.-C. *Tetrahedron Lett.* **2016**, *57*, 1430.
26. Malicka, J. M.; Sandeep, A.; Monti, F.; Bandini, E.; Gazzano, M.; Ranjith, C.; Praveen, V. K.; Ajayaghosh, A.; Armaroli, N. *Chem. Eur. J.* **2013**, *19*, 12991.

27. Funabiki, K.; Mase, H.; Saito, Y.; Otsuka, A.; Hibino, A.; Tanaka, N.; Miura, H.; Himori, Y.; Yoshida, T.; Kubota, Y. *Org. Lett.* **2012**, *14*, 1246.
28. Hara, K.; Wang, Z.-S.; Sato, T.; Furube, A.; Katoh, R.; Sugihara, H.; Dan-oh, Y.; Kasada, C.; Shinpo, A.; Suga, S. *J. Phys. Chem. B* **2005**, *109*, 15476.
29. de Miguel, G.; Ziółek, M.; Zitnan, M.; Organero, J.; Pandey, S.; Hayase, S.; Douhal, A. *J. Phys. Chem. C* **2012**, *116*, 9379.
30. Hagfeldt, A.; Gratzel, M. *Chem. Rev.* **1995**, *95*, 49.
31. Frisch, M. J.; Trucks, G. W.; Schlegel, H. B.; Scuseria, G. E.; Robb, M. A.; Cheeseman, J. R.; Scalmani, G.; Barone, V.; Mennucci, B.; Petersson, G. A.; Nakatsuji, H.; Caricato, M.; Li, X.; Hratchian, H. P.; Izmaylov, A. F.; Bloino, J.; Zheng, G.; Sonnenberg, J. L.; Hada, M.; Ehara, M.; Toyota, K.; Fukuda, R.; Hasegawa, J.; Ishida, M.; Nakajima, T.; Honda, Y.; Kitao, O.; Nakai, H.; Vreven, T.; Montgomery, J. A., Jr.; Peralta, J. E.; Ogliaro, F.; Bearpark, M.; Heyd, J. J.; Brothers, E.; Kudin, K. N.; Staroverov, V. N.; Kobayashi, R.; Normand, J.; Raghavachari, K.; Rendell, A.; Burant, J. C.; Iyengar, S. S.; Tomasi, J.; Cossi, M.; Rega, N.; Millam, J. M.; Klene, M.; Knox, J. E.; Cross, J. B.; Bakken, V.; Adamo, C.; Jaramillo, J.; Gomperts, R.; Stratmann, R. E.; Yazyev, O.; Austin, A. J.; Cammi, R.; Pomelli, C.; Ochterski, J. W.; Martin, R. L.; Morokuma, K.; Zakrzewski, V. G.; Voth, G. A.; Salvador, P.; Dannenberg, J. J.; Dapprich, S.; Daniels, A. D.; Farkas, O.; Foresman, J. B.; Ortiz, J. V.; Cioslowski, J.; Fox, D. J. *Gaussian 09, Revision A.01*; Gaussian, Inc.: Wallingford, CT, **2009**.
32. Feng, S.; Li, Q.-S.; Sun, P.-P.; Niehaus, T. A.; Li, Z.-S. *ACS Appl. Mater. Interfaces* **2015**, *7*, 22504.
33. Kroeze, J. E.; Hirata, N.; Koops, S.; Nazeeruddin, M. K.; Schmidt-Mende, L.; Grätzel, M.; Durrant, J. R. *J. Am. Chem. Soc.* **2006**, *128*, 16376.
34. Clifford, J. N.; Martínez-Ferrero, E.; Viterisi, A.; Palomares, E. *Chem. Soc. Rev.* **2011**, *40*, 1635.
35. Islam, A.; Akhtaruzzaman, M.; Chowdhury, T. H.; Qin, C.; Han, L.; Bedja, I. M.; Stalder, R.; Schanze, K. S.; Reynolds, J. R. *ACS Appl. Mater. Interfaces* **2016**, *8*, 4616.
36. Zaban, A.; Greenshtein, M.; Bisquert, J. *ChemPhysChem* **2003**, *4*, 859.



# CHAPTER III

---

## **Heterotriangulene Based Unsymmetrical Hemicyanine Dyes for Dye-Sensitized Solar Cells**

### 3.1. INTRODUCTION

The hemicyanine and cyanine dyes are class of metal-free ionic dyes with Donor-Acceptor (D-A) configuration, which are very much attractive in terms of its feasible synthesis and strong absorption in the far-red region as compared to the metal complexes.<sup>1,2</sup> In DSSCs, aryl amine are frequently used as donors such as triphenylamine, indoline, phenothiazine, fluorene and carbazole based dyes have been designed and established as efficient D-A systems.<sup>3</sup> However, the molar extinction coefficient ( $\epsilon$ ) of the NIR absorbing dyes is very high, for example hemicyanine,<sup>4,5</sup> merocyanine<sup>6,7</sup> and squaraines.<sup>8,9</sup> This makes them very beneficial for the design of organic dyes possessing tunable absorption in the far-red to NIR region. The squaraines are well studied NIR dyes, but the effort towards high performance hemicyanine class of dyes is not much investigated although it shows good light capturing ability towards NIR region. The hemicyanine dyes comprising triphenylamine,<sup>10,11</sup> fluoranthene,<sup>12</sup> phenothiazine<sup>13</sup> and tetrahydroquinoline<sup>14</sup> as donor units exhibited a strong absorption in the range of 500-650 nm in solution with  $\epsilon$  of  $\sim 10^4$ - $10^5$  M<sup>-1</sup> cm<sup>-1</sup>. But, the power conversion efficiency (PCE) of these dyes was moderate (2–5.5%) compared to other far-red active dyes under simulated AM 1.5G illumination (100 mW cm<sup>-2</sup>). This is mainly because of aggregate formation upon adsorption on the semiconductor surface, also most of the cationic dyes gave a relatively low open-circuit potential ( $V_{OC}$ ) in DSSCs could be attributable to the dipole moment effect. Cationic dyes usually have the direction of the generated dipole from the donor moiety to the acceptor moiety which is opposite dipole direction comparative to the conventional D-A type dyes.<sup>15</sup>

In D-A dyes, it is easy to improve the further light capturing ability through different structural modifications. Mostly, the molecular energy levels of the dyes need to be properly matched with conduction band edge ( $E_{CB}$ ) of the TiO<sub>2</sub> and the redox energy level of I<sup>-</sup>/I<sub>3</sub><sup>-</sup> to facilitate efficient charge injection and dye regeneration.<sup>16</sup> The selection of electrolyte is most important for the hemicyanine sensitization due to their ionic nature, so the use of additives such as protons,<sup>17</sup> TBP (tert-butyl pyridine),<sup>18</sup> lithium salts (Li<sup>+</sup>),<sup>19</sup> and ionic liquids<sup>20</sup> critically control the  $V_{OC}$ , short-circuit current density ( $J_{SC}$ ) and fill factor ( $ff$ ) parameters of the device. And also the adsorption of charged species on the TiO<sub>2</sub> surface greatly influences the  $E_{CB}$  position. Notably, the  $J_{SC}$  and  $V_{OC}$  of

hemicyanine class of dye relatively less than the non-ionic ones because of less light-harvesting capability in the NIR region and downward movement of the  $\text{TiO}_2$   $E_{\text{CB}}$  on chemisorption, respectively.<sup>13</sup> For ionic dye cells, the key challenge is to enhance the  $J_{\text{SC}}$  and  $V_{\text{OC}}$  by utilizing the molecular structure, despite the fact that the intrinsic dipole moment plays a negative role. For hemicyanine dyes, the excited state electrons will be located on the cationic unit; due to this the cationic dyes usually have the dipole direction from donor to the acceptor, which induces a downward shift of the  $E_{\text{CB}}$  of the  $\text{TiO}_2$  and result into decreased  $V_{\text{OC}}$  (**Figure 1a**).

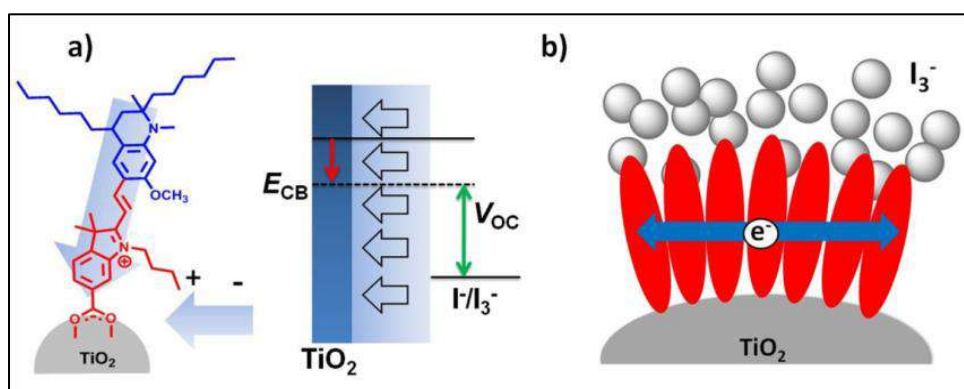


**Figure 1.** Pictorial presentation: a) Interfacial dipole moment inducing a downward shift of the  $E_{\text{CB}}$  of  $\text{TiO}_2$  and b) Dye aggregation on  $\text{TiO}_2$ .

The D-A structure of hemicyanine dyes shows broad absorption in the far-red region in solution, due to the presence of highly electron withdrawing indolium unit as an electron acceptor which gives the efficient intermolecular charge transfer (ICT). Besides to ICT, the self-aggregation of dyes in solution or on surfaces due to the strong intermolecular van der Waals forces forms H- or J- type aggregates which undergoes either blue- and red- shifted absorption, respectively (**Figure 1b**).<sup>2,13</sup>

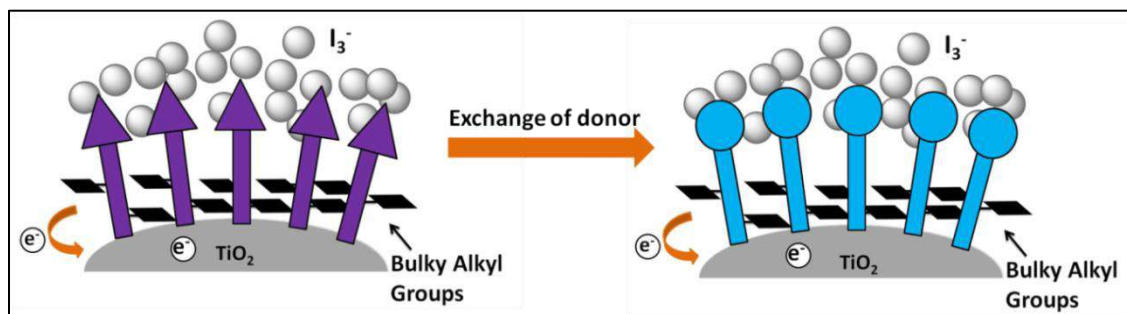


**Figure 2.** Pictorial presentation: Exchange of TPA by HT donor and introduction of alkyl chain on acceptor units to avoid aggregations.

The molecular structure of donor part and alkyl functionalities plays an important role in D-A hemicyanine ionic dyes to enhance the  $J_{SC}$  and  $V_{OC}$ . By introducing the strong donor, the photo responses of the sensitizers can extend towards the NIR region and also increase the injection efficiency, which in turn improves  $J_{SC}$  (**Figure 2**).<sup>3</sup> In this chapter, designed and synthesized six hemicyanine dyes using two different electron donor, heterotriangulenebased (**HT**) or triphenyl amine (**TPA**) as donor and 1-alkyl-5-carboxy-3,3-dialkyl-indol-1-ium moiety (indolium unit) as an electron acceptor contains anchoring group.<sup>21</sup> The molecular structures of **NC1-3** and **NC4-6** dyes are shown in **Figure 3**. TPA is a flexible donor, it has relatively large dihedral angles between the phenyl rings and the plane of the N-bonded carbon atoms gives poor the extension of  $\pi$ -conjugation over the whole molecule.<sup>22</sup> There are several reports in the literature for improvement of voltage and current after replacing a weak donor with a strong one. Bridged triphenylamine (heterotriangulene, **HT**) has been recognized as an efficient donor units in our earlier reports, for far-red harvesting squaraine sensitizers in DSSCs.<sup>23</sup> Herein, taking the advantage of strong and planar HT units that provides an excellent degree of conjugation between donor and acceptor and leads to faster electron injection (**Figure 2**). Also assemble via  $\pi$ - $\pi$  stacking even as anchoring on the  $TiO_2$  surface and most importantly localizes the positive charge resulting after injection.<sup>24</sup> HT units demonstrated red-shifted absorption spectrum and also showed remarkable improvement in photocurrent density and device efficiencies.<sup>25</sup>

The hemicyanine device efficiency is affected by the aggregation phenomenon on the  $TiO_2$  surface, therefore controlling the aggregation of ionic dyes helps to widen the absorption spectrum. This can contribute for photocurrent to reach high PCE. There are several strategies were aimed for diminishing the dye aggregation and charge recombination by focusing on the electron-donor,  $\pi$ -spacer, and acceptor unit to get the high performance. The optically transparent co-adsorbent like CDCA was employed, but the higher concentration of CDCA competes with dyes in chemisorption and reduces the  $J_{SC}$  after definite adsorbent/dye ratio.<sup>26</sup> The in-plane and out-of-plane alkyl chains with respect to conjugated backbone, enhance the  $J_{SC}$  and  $V_{OC}$  due to the increase in

intermolecular distance and efficient screening of  $\text{TiO}_2$  surface from  $\text{I}^-$  ions present in electrolyte, which retards the dark current.<sup>23</sup> Through this structural modification of hemicyanine dyes, possessing bulky alkyl groups near to the anchoring group can be employed to passivate the  $\text{TiO}_2$  surface from the iodide/triiodide electrolyte (**Figure 3**). In this chapter, elaborated the use of strong and planar HT donor instead of flexible TPA donor and out-of-plane alky groups which played an important role in improving the  $V_{oc}$ ,  $J_{sc}$  and related enhancement in the PCE without any co-adsorbent.<sup>27</sup> It is found that the rational molecular design of HT-based dyes having better spectral response, modulated the energy level, and better interfacial charge transfer property facilitated to reach high  $J_{sc}$  and  $V_{oc}$  compared to TPA-based dyes.

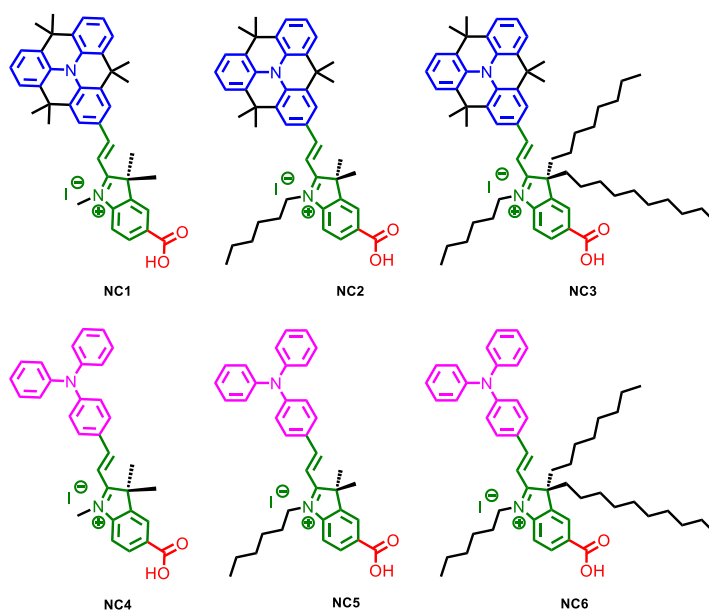


**Figure 3.** Molecular structures of HT-based **NC1-3** and TPA-based **NC4-6** based hemicyanine dyes.

## 3.2 EXPERIMENTAL SECTION

### 3.2.1 Materials and Characterization

All reagents were purchased from commercial sources. Solvents were dried and distilled immediately prior to use by standard procedures. All reactions were carried out under an argon atmosphere.  $^1\text{H}$  NMR and  $^{13}\text{C}$  NMRs were recorded in  $\text{MeOH-}d_4$  on 200 MHz, 400 MHz and 500 MHz NMR spectrometers. High-resolution mass spectrometric measurements were carried out using the ESI method and an ion-trap mass analyzer. Absorption spectra were recorded at room temperature in quartz cuvette using Analytik Jena UV-visible spectrophotometer. Electrochemical measurement was carried out using a Bio-Logic potentiostat (model no: SP300). The cyclic voltammetric analysis (CV) was carried out in dry  $\text{CH}_3\text{CN}$  solvent by using 0.1 M tetrabutylammonium perchlorate as supporting electrolyte and  $\text{Fc}/\text{Fc}^+$  as external reference. The experiments were performed at room temperature in nitrogen atmosphere with a three-electrode cell consisting of a platinum foil as counter electrode, non-aqueous  $\text{Ag}/\text{Ag}^+$  reference electrode, and a platinum wire as working electrode.

### 3.2.2 Solar cells preparation and characterization

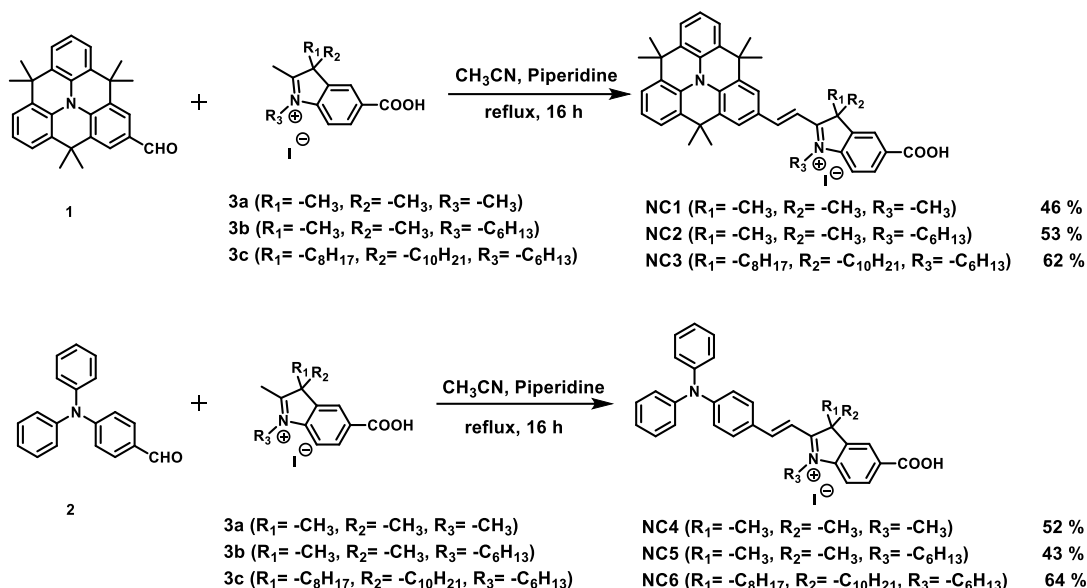
FTO (F-doped  $\text{SnO}_2$  glass; 6 - 8  $\Omega$  /sq; Pilkington TEC 7) was cleaned by mucasol (2 % in water), deionized water, and ethanol, successively. To grow a  $\text{TiO}_2$  under layer, the substrate was immersed in freshly prepared 50 mM  $\text{TiCl}_4$  aqueous solution at 70  $^\circ\text{C}$  for 30 min, and washed with deionized water before drying at 100  $^\circ\text{C}$  for 10 min. A paste of  $\text{TiO}_2$  nanocrystal (< 20 nm, Ti-Nanoxide T/SP, Solaronix) was deposited by the doctor-blade technique on  $\text{TiO}_2$  buffer layer coated FTO substrate, kept in air for 5 min and then annealed at 125  $^\circ\text{C}$  in air for 15 min. The films were about 6 - 8  $\mu\text{m}$  thick. The annealed films were coated with scattering layer  $\text{TiO}_2$  paste (WER2-O, Dyesol) and annealed at 125  $^\circ\text{C}$  in air for 15 min. The annealed films were sintered at 325  $^\circ\text{C}$  for 5 min, 375  $^\circ\text{C}$  for 5 min, 450  $^\circ\text{C}$  for 15 min and 500  $^\circ\text{C}$  for 15 min with heating rate of 5  $^\circ\text{C}$  per min in air. After reaching the furnace temperature of 50  $^\circ\text{C}$ , sintered films were immersed in freshly prepared 50 mM aqueous  $\text{TiCl}_4$  solution at 70  $^\circ\text{C}$  for 30 min. After sintering the  $\text{TiCl}_4$ -treated  $\text{TiO}_2$  films at 500  $^\circ\text{C}$  for 30 min, they were immediately immersed in 0.1 mM NC dye solution in  $\text{CH}_3\text{CN}$  for 2.5 h, washed and dried. In case of CDCA (an

additive to reduce the dye aggregation) added experiments, different ratios of CDCA added to 0.1 mM dye solution and photoanode dipped for 2.5 h. Sandwich type cell configuration was completed using platinum as cathode, 0.5 M LiI, 0.05 M I<sub>2</sub> in CH<sub>3</sub>CN was used as electrolyte and 25 μm spacer. *I-V* characteristics of the cells were measured using Keithley digital source meter (2420, Keithley, USA) controlled by a computer and standard AM 1.5G solar simulator (PET, CT200AAA, USA). To measure the photocurrent and voltage, an external bias of AM 1.5G light was applied using a xenon lamp (450 W, USHIO INC, Philippines) and recorded. IPCE measurements were carried out with a Newport QE measurement kit by focusing a monochromatic beam of light from 300 W Xe lamp onto the devices. The electrochemical impedance spectroscopy (EIS) measurements of the DSSCs were recorded with a Bio-Logic potentiostat (model no: SP300), equipped with an FRA2 module, with different potentials applied in dark. The frequency range explored was 25 mHz to 1 MHz with an ac perturbation of 10 mV. The impedance spectra were analyzed using an equivalent circuit model. The Mott-Schottky plots were measured with Bio-Logic potentiostat (model no: SP300) with a potential window of -1 V to 0 V.

### 3.2.3 Dye desorption from the photoanode

The TiO<sub>2</sub> coated FTO electrodes (0.22 cm<sup>2</sup>) were dipped in 0.1 mM solution of **NC1-3** and **NC4-6** dyes in CH<sub>3</sub>CN for 2.5 h at room temperature, and then washed with CH<sub>3</sub>CN to remove the physisorbed dyes. The electrodes were immersed in 2 M ethanolic HCl for 10 min until all the dyes completely desorbed and the amount of adsorbed dye is calculated by UV-Vis absorption study.

## 3.2.4 SYNTHETIC PROCEDURE AND CHARACTERIZATION DATA



**Scheme 1.** Synthesis of HT-based **NC1-3** and TPA-based **NC4-6** based hemicyanine dyes.

### Synthesis of 4,4,8,8,12,12-Hexamethyl-8,12-dihydro-4H-benzo[9,1]quinolizino[3,4,5,6,7,7-defg]acridine-2-carbaldehyde (**1**)

A solution of [4,4,8,8,12,12-Hexamethyl-4H,8H,12H-benzo[9,1]quinolizino[3,4,5,6,7,7-defg]acridine [see section 2.2.4] (1 g, 2.74 mmol) in dry DMF (100 mL) was cooled in an ice bath under nitrogen atmosphere. A solution of POCl<sub>3</sub> (3 mL, 32.82 mmol) in dry DMF (10 mL) was added slowly and stirred at 0 °C. Then the mixture was warmed to room temperature slowly and stirred for another 30 min. Then it was heated at 80 °C for 15 h. The reaction mixture was cooled then neutralized with sodium acetate and extracted with CH<sub>2</sub>Cl<sub>2</sub>, washed with water and dried over Na<sub>2</sub>SO<sub>4</sub>. The mixture was purified by silica gel chromatography to give **1** (0.8 g, 75 %) as a yellow liquid. <sup>1</sup>H NMR (400 MHz, CDCl<sub>3</sub>) δ: 9.93 (s, 1 H), 7.89 (s, 2 H), 7.45 - 7.39 (m, 4 H), 7.20 (t, *J* = 7.8 Hz, 2 H), 1.67 (s, 6 H), 1.65 (s, 12 H). <sup>13</sup>C NMR (100 MHz, CDCl<sub>3</sub>) δ: 191.1, 131.3, 130.9, 130.8, 130.4, 129.9, 125.3, 124.5, 124.3, 123.5, 35.8, 35.6, 34.1, 32.7. HRMS (ESI): *m/z* calcd for C<sub>28</sub>H<sub>28</sub>NO ([M + H]<sup>+</sup>): 393.2165. Found: 394.2159.



**Synthesis of 4-(Diphenylamino)benzaldehyde (2)**

Phosphoryl chloride (0.38 mL, 4.07 mmol) was added slowly to the N, N-Dimethylformamide (0.63 mL, 8.15 mmol) at 0 °C. The mixture was stirred at 0 °C for 1 h and additionally stirred at room temperature for 1 h. After the addition of triphenylamine (1 g, 4.07 mmol) in anhydrous dichloromethane (10 mL), the reaction mixture was heated to 100 °C for 5 h. After cooling to room temperature, the mixture was neutralized using ice cold solution of 2 M sodium hydroxide. After stirring for a further 30 minutes, the mixture was extracted with ethyl acetate, the organic layer dried with Na<sub>2</sub>SO<sub>4</sub> and then solvent was removed under reduced pressure. The crude residue was then purified by silica gel chromatography to afford **2** (0.620 g, 56 %) as pale yellow solid. <sup>1</sup>H NMR (500 MHz, CDCl<sub>3</sub>) δ: 9.81 (s, 1 H), 7.72 - 7.58 (m, 2 H), 7.37 - 7.31 (m, 4 H), 7.21 - 7.15 (m, 6 H), 7.04 - 7.01 (m, 2 H). <sup>13</sup>C NMR (125 MHz, CDCl<sub>3</sub>) δ: 190.5, 153.4, 146.2, 131.4, 129.8, 129.2, 126.4, 125.2, 119.4. HRMS (ESI): m/z calcd for C<sub>19</sub>H<sub>16</sub>NO ([M + H]<sup>+</sup>): 274.1226; found: 274.1226.

**General Procedure for synthesis of NC1-3 and NC4-6**

4,4,8,8,12,12-Hexamethyl-8,12-dihydro-4H-benzo[9,1]quinolizino[3,4,5,6,7-defg]acridine-2-carbaldehyde<sup>28</sup> (100 mg, 0.25 mmol) or 4-(diphenylamino)benzaldehyde<sup>29</sup> (100 mg, 0.37 mmol) and compound **3a-3c**<sup>23</sup> (1.2 eq.) [see section 2.2.4] were added into CH<sub>3</sub>CN (10 mL) with piperidine as the catalyst and refluxed for 16 h. Then solvent was removed under reduced pressure and the residue was purified by column chromatography on silica with methanol/dichloromethane as eluent to afford **NC1-3** as a blue solid and **NC4-6** as a violet solid.

**(E)-5-Carboxy-2-(2-(4,4,8,8,12,12-hexamethyl-8,12-dihydro-4H-benzo[9,1]quinolizino[3,4,5,6,7-defg]acridin-2-yl)vinyl)-1,3,3-trimethyl-3H-indol-1-ium (NC1):** Yield: 70 mg, 46 %. <sup>1</sup>H NMR (200 MHz, MeOH-*d*<sub>4</sub>) δ: 8.65 - 8.36 (m, 1 H), 8.31 - 8.09 (m, 4 H), 7.74 (d, *J* = 8.3 Hz, 1 H), 7.62 - 7.43 (m, 5 H), 7.33 - 7.15 (m, 2 H), 4.16 (s, 3 H), 1.89 (s, 6 H), 1.70 (s, 12 H), 1.65 (s, 6 H). <sup>13</sup>C NMR (100 MHz, MeOH-*d*<sub>4</sub>) δ: 184.1, 156.6, 145.7, 144.4, 139.7, 132.8, 132.4, 132.2, 132.1, 131.5, 130.8, 128.4, 126.3, 126.2, 124.9, 124.8, 114.8, 53.3, 37.0, 36.7, 34.7, 34.4, 32.9, 27. HRMS (ESI): m/z calcd for C<sub>41</sub>H<sub>41</sub>N<sub>2</sub>O<sub>2</sub> [M]<sup>+</sup>: 593.3163; found: 593.3163.

**(E)-5-Carboxy-2-(2-(4,4,8,8,12,12-hexamethyl-8,12-dihydro-4H-benzo[9,1]quinolizino[3,4,5,6,7-defg]acridin-2-yl)vinyl)-1-hexyl-3,3-dimethyl-3H-indol-1-ium**

**(NC2):** Yield: 90 mg, 53 %. <sup>1</sup>H NMR (200 MHz, MeOH-*d*<sub>4</sub>) δ: 8.57 (m, 1 H), 8.32 - 8.15 (m, 4 H), 7.76 (d, *J* = 8.5 Hz, 1 H), 7.60 - 7.47 (m, 5 H), 7.32 - 7.21 (m, 2 H), 4.70 (t, *J* = 7.3 Hz, 2 H), 1.90 (s, 6 H), 1.70 (s, 12 H), 1.67 (s, 6 H), 1.57 - 1.28 (m, 8 H), 0.95 - 0.85 (m, 3 H); <sup>13</sup>C NMR (100 MHz, MeOH-*d*<sub>4</sub>) δ: 183.7, 156.8, 144.7, 132.8, 132.5, 132.3, 132.1, 131.4, 128.4, 126.3, 126.2, 124.9, 114.9, 53.3, 47.5, 37.0, 36.7, 34.7, 32.8, 32.5, 29.6, 27.5, 27.2, 23.7, 14.4; HRMS (ESI): *m/z* calcd for C<sub>46</sub>H<sub>51</sub>N<sub>2</sub>O<sub>2</sub> [M]<sup>+</sup>: 663.3945; found: 663.3940.

**(E)-5-Carboxy-3-decyl-2-(2-(4,4,8,8,12,12-hexamethyl-8,12-dihydro-4Hbenzo[9,1]quinolizino[3,4,5,6,7-defg]acridin-2-yl)vinyl)-1-hexyl-3-octyl-3H-indol-1-ium (NC3):**

Yield: 140 mg, 62 %. <sup>1</sup>H NMR (200 MHz, MeOH-*d*<sub>4</sub>) δ: 8.68 - 8.52 (m, 1 H), 8.34 - 8.10 (m, 4 H), 7.75 (d, *J* = 8.3 Hz, 1 H), 7.62 - 7.40 (m, 5 H), 7.33 - 7.17 (m, 2 H), 4.73 (t, *J* = 6.9 Hz, 2 H), 2.63 (t, 2 H), 2.44 (t, 2 H), 2.02 - 1.90 (m, 2 H), 1.70 (s, 12 H), 1.64 (s, 6 H), 1.56 - 1.14 (m, 8 H), 1.02 (m, 25 H), 0.91-0.85 (m, 4 H), 0.67 (t, 6 H). <sup>13</sup>C NMR (100 MHz, MeOH-*d*<sub>4</sub>) δ: 182.1, 155.6, 146.1, 141.5, 140.3, 137.9, 132.9, 132.5, 132.4, 132.3, 131.4, 130.7, 128.4, 126.4, 126.3, 124.9, 114.5, 63.1, 47.5, 42.3, 42.2, 37.1, 36.7, 34.8, 33.0, 32.8, 32.7, 30.7, 30.5, 30.3, 30.2, 30.1, 30.0, 29.9, 29.8, 27.9, 24.7, 24.6, 23.7, 14.5 HRMS (ESI): *m/z* calcd for C<sub>62</sub>H<sub>83</sub>N<sub>2</sub>O<sub>2</sub> [M]<sup>+</sup>: 887.6449; found: 887.6448.

**(E)-5-Carboxy-2-(4-(diphenylamino)styryl)-1,3,3-trimethyl-3H-indol-1-ium(NC4):**

Yield: 90 mg, 52 %. <sup>1</sup>H NMR (500 MHz, MeOH-*d*<sub>4</sub>) δ: 8.46 - 8.34 (d, *J* = 15.0 Hz, 1 H), 8.32 - 8.17 (m, 2 H), 7.97 (d, *J* = 8.2 Hz, 2 H), 7.78 (d, *J* = 8.2 Hz, 1 H), 7.48 - 7.38 (m, 5 H), 7.32 - 7.19 (m, 6 H), 6.96 (d, *J* = 7.6 Hz, 2 H), 4.08 (s, 3 H), 1.85 (s, 6 H); <sup>13</sup>C NMR (100 MHz, MeOH-*d*<sub>4</sub>) δ: 184.4, 168.6, 157.3, 155.7, 146.9, 146.7, 144.5, 134.9, 132.4, 132.1, 131.3, 128.2, 127.7, 127.7, 125.0, 119.8, 115.2, 109.0, 53.1, 34.5, 27.1; HRMS (ESI): *m/z* calcd for C<sub>33</sub>H<sub>29</sub>N<sub>2</sub>O<sub>2</sub> [M]<sup>+</sup>: 473.2224; found: 473.2229.

**(E)-5-Carboxy-2-(4-(diphenylamino)styryl)-1-hexyl-3,3-dimethyl-3H-indol-1-ium**

**(NC5):** Yield: 85 mg, 43 %. <sup>1</sup>H NMR (200 MHz, MeOH-*d*<sub>4</sub>) δ: 8.46 - 8.38 (m, 1 H), 8.31 - 8.18 (m, 2 H), 7.94 (d, *J* = 8.5 Hz, 2 H), 7.75 (d, *J* = 8.5 Hz, 1 H), 7.52 - 7.39 (m, 5 H),

7.34 - 7.24 (m, 6 H), 6.97 (d,  $J = 9.0$  Hz, 2 H), 4.57 (t,  $J = 7.3$  Hz, 2 H), 1.85 (s, 6 H), 1.40 - 1.27 (m, 8 H), 0.92 - 0.85 (m, 3 H).  $^{13}\text{C}$  NMR (100 MHz, MeOH- $d_4$ )  $\delta$ : 183.7, 157.2, 155.8, 146.7, 145.4, 144.6, 134.8, 132.4, 131.3, 128.3, 127.8, 127.6, 125.1, 119.8, 115.0, 53.2, 47.4, 32.6, 30.9, 29.5, 27.5, 27.2, 23.7, 14.4. HRMS (ESI):  $m/z$  calcd for  $\text{C}_{37}\text{H}_{39}\text{N}_2\text{O}_2$   $[\text{M}]^+$ : 543.3006; found: 543.3014.

**(E)-5-Carboxy-3-decyl-2-(4-(diphenylamino)styryl)-1-hexyl-3-octyl-3H-indol-1-ium**

**(NC6):** Yield: 180 mg, 64 %.  $^1\text{H}$  NMR (200 MHz, MeOH- $d_4$ )  $\delta$ : 8.52 - 8.38 (m, 1 H), 8.29 - 8.15 (m, 2 H), 7.96 (d,  $J = 8.2$  Hz, 2 H), 7.74 (d,  $J = 8.2$  Hz, 1 H), 7.51 - 7.39 (m, 5 H), 7.36 - 7.24 (m, 6 H), 6.98 (d,  $J = 9.0$  Hz, 2 H), 4.61 (t,  $J = 6.8$  Hz, 2 H), 2.58 - 2.30 (m, 4 H), 1.96 - 1.82 (m, 2 H), 1.39 - 1.18 (m, 11 H), 1.11 (br. s., 21 H), 0.91 - 0.81 (m, 9 H), 0.60 - 0.48 (m, 2 H).  $^{13}\text{C}$  NMR (100 MHz, MeOH- $d_4$ )  $\delta$ : 182.1, 156.0, 146.7, 146.6, 141.5, 134.9, 132.4, 131.3, 128.3, 127.8, 127.6, 125.0, 119.9, 114.6, 63.0, 47.5, 42.4, 33.1, 33.0, 32.7, 30.7, 30.5, 30.3, 30.2, 30.1, 29.9, 29.9, 27.8, 24.7, 24.7, 23.8, 23.8, 23.7, 14.6, 14.6, 14.4. HRMS (ESI):  $m/z$  calcd for  $\text{C}_{53}\text{H}_{71}\text{N}_2\text{O}_2$   $[\text{M}]^+$ : 767.5510; found: 767.5515.

### 3.3 RESULTS AND DISCUSSION

#### 3.3.1 Synthesis and Characterization

We have synthesized six hemicyanine dyes **NC1-6**; the synthetic routes are depicted in **Scheme 1**. 4,4,8,8,12,12-Hexamethyl-8,12-dihydro-4H-benzo[9,1]quinolizino[3,4,5,6,7-defg]acridine-2-carbaldehyde (**1**), 4-(diphenylamino)benzaldehyde (**2**) were synthesized as per reported procedure whereas and 1-alkyl-5-carboxy-3,3-dialkyl-indol-1-ium units (**3a-3c**) was synthesized as per section 2.24. Finally, a condensation reaction between **3a-3c** and monoformlyated amine intermediate (**1** and **2**) giving the **NC1-6** dyes in good yield. The structures of targeted dyes are analyzed by  $^1\text{H}$ - and  $^{13}\text{C}$ -NMR spectroscopy and mass spectrometry (HRMS-ESI). All the compounds have good solubility in MeOH,  $\text{CH}_3\text{CN}$ ,  $\text{CHCl}_3$ , DMSO and *t*-BuOH.

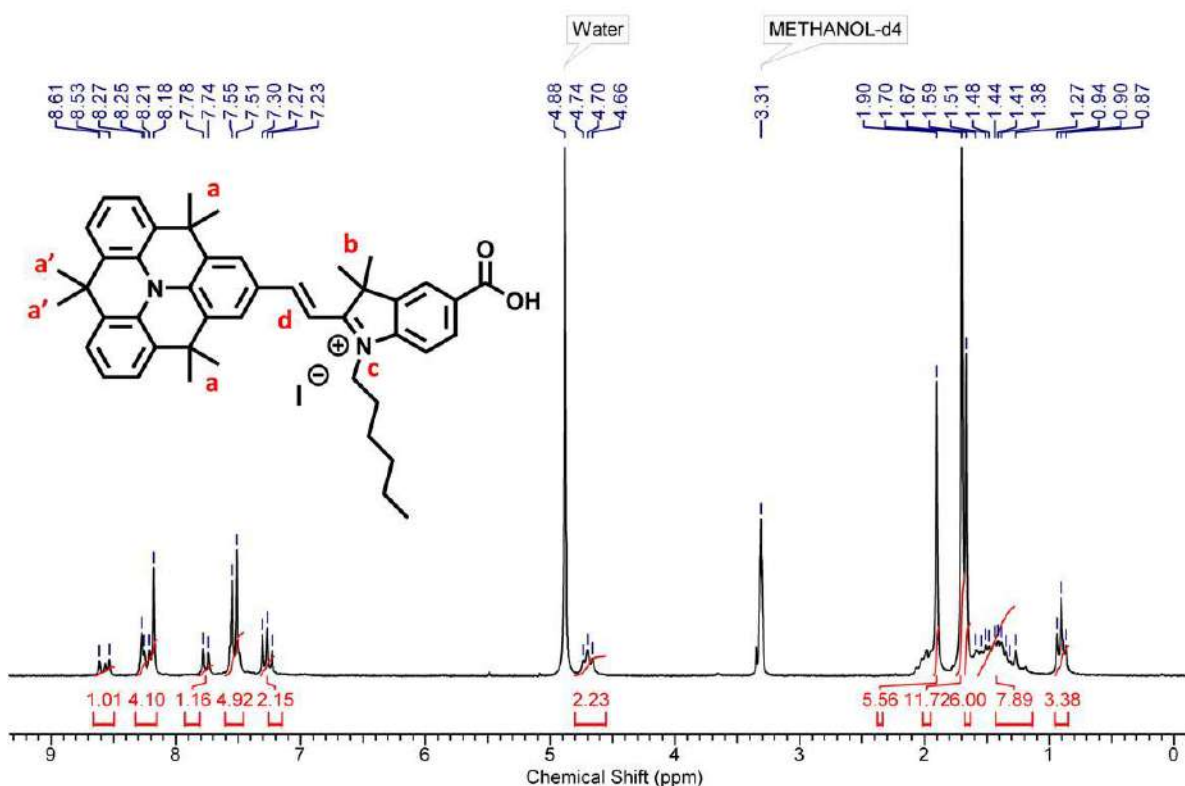


**Figure 4.**  $^1\text{H}$  NMR (400 MHz,  $\text{DMSO}-d_6$ ) spectrum of compound **NC2**.

**Figure 4** shows the labeled  $^1\text{H}$  NMR spectrum of **NC2** as a representative spectrum. This compound shows singlet (**a'**) at 1.67 ppm (6 H) and another singlet (**a**) at 1.70 ppm (12 H) which correspond to 18 protons of bridged methyl groups. The two methyl groups

attached to  $sp^3$ -C atom of indolium group shows singlet (**b**) at 1.90 ppm. The  $-CH_2$  group which is connected to N-atom of indolium units shows triplet (**c**) at 4.70 ppm. The peak corresponds to  $-CH=CH-$  protons shows multiplet (**d**) at 7.23-7.30 ppm.

### 3.3.2 Photophysical Properties

The absorption and emission spectra of **NC1-3** and **NC4-6** in MeOH solution are shown in **Figure 5a** and **5b**, and the corresponding properties are summarized in **Table 1**. **NC1-3** dyes display strong light absorption in far-red region in solutions. **NC1-3** dyes showed absorptions bands in the range of 440 to 730 nm are attributed to the ICT between donor and acceptor and apart from this a band between 350 to 450 nm ascribed to the a weak  $\pi$ - $\pi^*$  transition. In contrast, **NC4-6** displays strong absorption band between 400-680 nm and weak absorption between 300-380 nm. The strong and planar HT donor and electron withdrawing cationic indolium carboxylic acid acceptor units offer the broad and strong absorption in the ultraviolet and visible region. As shown in **Figure 5a**, **NC1-3** illustrated red shift in the maximum absorption wavelength ( $\lambda_{max}$ ), this arises from HT units, due to rigid coplanar structure and gives the better conjugation compared to propeller shaped TPA donor. For **NC1-3** or **NC4-6**, introducing the long or branched alkyl group gives red shifted absorption peak within each series. Such increase in the ICT character ascribed to the out-of-plane alkyl segments on indolium  $sp^3$ -C atom and linear chains at the N-atom of indolium units, and red shift in the transition is owing to the formation of dye-solvent complex which stabilizes the ICT state.<sup>30</sup> Among **NC1-3** dyes, the red-shifted absorption with respect to **NC1** was lay in the order of **NC2** (7 nm) < **NC3** (18 nm) and for **NC4-6**, red shift with respect to **NC4** was obtained in the order of **NC5** (2 nm) < **NC6** (10 nm). The  $\epsilon$  value for all the dyes at the  $\lambda_{max}$  was in the order of  $10^4 M^{-1} cm^{-1}$  (**Table 1**). As a result, red shift in the  $\lambda_{max}$  highlights the strategy to alter the optical properties of hemicyanine class of dyes by connecting different donors and a branched alkyl group at N- and  $sp^3$ -C atoms of indolium unit.

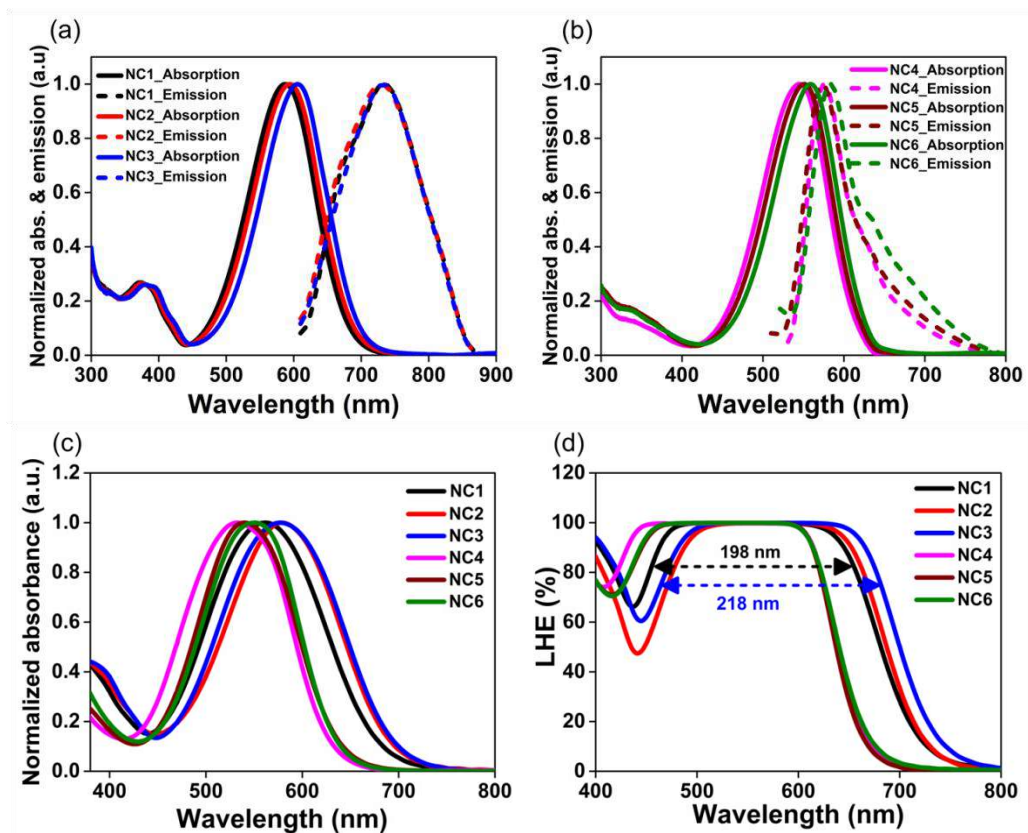


**Figure 5.** (a) Absorption and emission spectra of **NC1-3** in MeOH, excitation wavelength 610 nm, (b) Absorption and emission spectra of **NC4-6** in MeOH, excitation wavelength 520 nm, (c) Absorption spectra of **NC1-6** adsorbed on the transparent TiO<sub>2</sub> film (TiO<sub>2</sub> film thickness: 6  $\mu$ m, [Dye] = 0.1 mM in CH<sub>3</sub>CN and dipping time 10 min), and (d) LHE profile of **NC1-6** sensitizers without co-adsorbent on transparent TiO<sub>2</sub> films of 6  $\mu$ m thickness (dipping time 2.5 h).

**Figure 5c** shows the absorption spectra of dyes anchored on a transparent mesoporous TiO<sub>2</sub> film. When anchored on transparent TiO<sub>2</sub>, the absorption spectra of **NC** dyes showed broad and blue-shifted (10-30 nm) absorptions due to interaction of carboxylic acid groups with the surface titanium ions and formation of H-aggregate of dyes on the TiO<sub>2</sub> surface, respectively.<sup>31,32</sup> **Figure 5a** shows the emission  $\lambda_{\max}$  of **NC1-3** is shifted to longer wavelength compared to **NC4-6**. The maximum Stokes shift of ~135 nm was observed for HT-based dyes which indicates considerable dipole moment change upon photo excitation, and it is smallest for **NC4-6** (~25 nm). It can be associated with an excited-state ICT between the donor and acceptor in the **NC1-3**.<sup>33</sup> Therefore, the conjugation length provides the band gap between 1.92-1.88 eV, which results into broad absorption

and light-harvesting efficiency ( $LHE = 1-10^{-A}$ ) at longer wavelength. Furthermore, **NC** dyes displays negative solvatochromism with increased polarity of solvents where the  $\lambda_{\max}$  shifts to shorter wavelength (**Figure 6**). It confirms that the ground state is more stabilized than the excited state attributable to solvation by solvents of increased polarity.<sup>34</sup>

**Table 1.** Photophysical and electrochemical properties of the dyes **NC1-6** at room temperature

NC Dyes	$\lambda_{\max}$ /MeOH (nm) <sup>a</sup>	$\varepsilon \times 10^4$ ( $M^{-1}cm^{-1}$ ) <sup>b</sup>	$\lambda_{\max}$ /em (nm) <sup>a</sup>	$\lambda_{\max}$ /TiO <sub>2</sub> (nm) <sup>c</sup>	$E_g$ /DFT (eV)	$E_{HOMO}$ (V vs NHE) <sup>d</sup>	$E_{0-0}$ (eV) <sup>e</sup>	$E_{LUMO}$ (V vs NHE) <sup>f</sup>	$-\Delta G_{inj}$ (V) <sup>g</sup>	$-\Delta G_{reg}$ (V) <sup>h</sup>
<b>NC1</b>	372, 588	2.56	735	562	1.94	1.04	1.92	-0.88	0.38	0.64
<b>NC2</b>	375, 595	2.40	731	578	1.95	1.05	1.91	-0.86	0.36	0.65
<b>NC3</b>	380, 606	3.37	734	577	1.96	1.07	1.88	-0.81	0.31	0.67
<b>NC4</b>	549	3.01	576	532	2.35	1.24	2.20	-0.96	0.46	0.84
<b>NC5</b>	551	2.21	574	540	2.35	1.23	2.19	-0.96	0.46	0.83
<b>NC6</b>	559	5.15	583	551	2.37	1.21	2.16	-0.95	0.45	0.81

<sup>a</sup>Absorption and emission spectra were recorded in MeOH, <sup>b</sup>Molar extinction coefficients ( $\varepsilon$ ) were measured in CHCl<sub>3</sub>. <sup>c</sup>On 6  $\mu m$  transparent TiO<sub>2</sub> film. <sup>d</sup>The oxidation potentials were measured by differential pulse voltammetry (DPV) in CH<sub>3</sub>CN with tetrabutylammonium perchlorate (TBAClO<sub>4</sub>) as supporting electrolyte, ferrocene/ferrocenium (Fc/Fc<sup>+</sup>) as an external reference and NC1-6 oxidation peak potential vs Ag/Ag<sup>+</sup> converted to NHE by addition of 0.63 V using the equation  $E_{HOMO}$  (V vs NHE) =  $(E_{p/DPV} - E_{1/2}$  vs Fc/Fc<sup>+</sup>) + 0.63] V vs NHE. <sup>e</sup>Optical energy gaps ( $E_{0-0}$ ) were deduced from the intersection of absorption and emission spectra,  $E_{0-0}$  (eV) =  $1240/\lambda$ . <sup>f</sup> $E_{LUMO}$  was calculated from  $E_{LUMO}$  (V vs NHE) =  $E_{HOMO} - E_{0-0}$ . <sup>g</sup> $-\Delta G_{inj}$  is expressed as the energy difference between  $E_{LUMO}$  and  $E_{CB}$  ( $-\Delta G_{inj} = E_{CB/TiO_2} - E_{LUMO}$ ), <sup>h</sup> $-\Delta G_{reg}$  was calculated from  $-\Delta G_{reg} = E_{redox/electrolyte} - E_{HOMO}$ . The redox potential of I<sup>-</sup>/I<sub>3</sub><sup>-</sup> electrolyte is +0.4 V vs NHE.

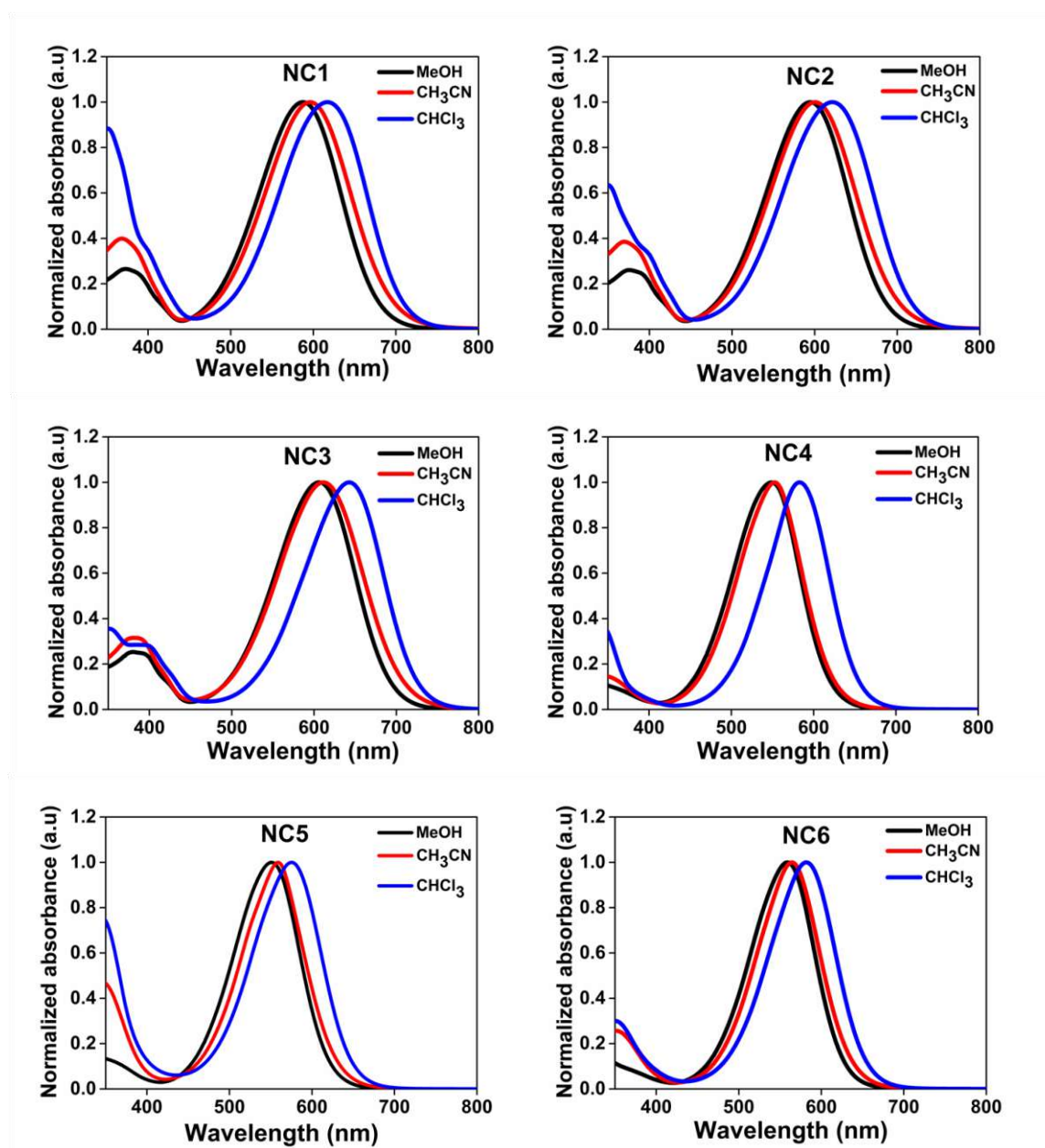


**Figure 6.** Absorption spectra of **NC1-6** dyes in different solvents (methanol, acetonitrile and chloroform).

LHE elucidates the ability of sensitizers to absorb different range of photons in the  $\text{TiO}_2$  films.<sup>35,36</sup> **NC** dyes showed LHE values of near unity over a wide spectral region as shown in **Figure 5d**. LHE of **NC1-3** sensitized electrodes confirmed the higher light-harvesting efficiency than **NC4-6** sensitized electrode. **NC1** sensitized electrode exhibited the spectral broadening with  $\Delta\lambda = 198$  nm whereas **NC3** sensitized electrode



showed superior spectral broadening of LHE profile ( $\Delta\lambda = 218$  nm), similarly UV-Vis absorption spectrum of **NC3** also exhibited red shifted peak in comparison to **NC1**. This is mainly due to presence of out-of-plane alkyl segments on indolium  $sp^3$ -C atoms which helps to suppress the aggregation of dye molecules on  $TiO_2$  film. As a result, **NC1-3** displayed more than 90% LHE from 430 to 720 nm, whereas **NC4-6** displayed 90% LHE in the region of 405 to 680 nm. This result confirms that **NC1-3** are constructive for harvesting the NIR photons together with visible.

### 3.3.3 Electrochemical Properties

The differential pulse voltammetry (DPV, **Figure 7a**) and cyclic voltammetry (CV, **Figure 8**) and was carried out to measure the oxidation potentials of the sensitizers and to determine the thermodynamic feasibility of charge injection from the excited dye into conduction band of the  $TiO_2$  and the dye regeneration by the electrolyte.<sup>37</sup> **NC1-3** displayed reversible first oxidation peak upon the application of positive potentials. **NC4-6** displayed different oxidation features than the **NC1-3**, with first quasi reversible oxidation and a reversible equilibrium oxidation peak at higher potential as shown in **Figure 8**. As depicted in **Figure 7a**, the redox potentials of all dyes were measured using DPV in  $CH_3CN$  and the results are summarized in **Table 1**. DPV analysis was carried out to get the clear difference in the oxidation potentials of NC dyes, and the curves are shown in **Figure 7a**. The HOMO level corresponding to oxidation potential of **NC1-3** are 1.04, 1.05 and 1.07 V vs NHE for **NC1**, **NC2** and **NC3**, respectively. And in **NC4-6**, these levels are 1.24, 1.23 and 1.21 V vs NHE for **NC4**, **NC5** and **NC6**, respectively. These HOMO values are more positive than that of  $I^-/I_3^-$  redox potential (0.4 V) vs. NHE indicating enough energy offset for dye regeneration by accepting electron from  $I^-$  ion (**Figure 7b**). The LUMO levels of all dyes are calculated by subtracting  $E_{0-0}$  from  $E_{HOMO}$  and are more negative than  $E_{CB}$  of  $TiO_2$  (-0.5 V vs. NHE) which ensures sufficient driving for electron injection from the excited dye into the CB of the  $TiO_2$ .

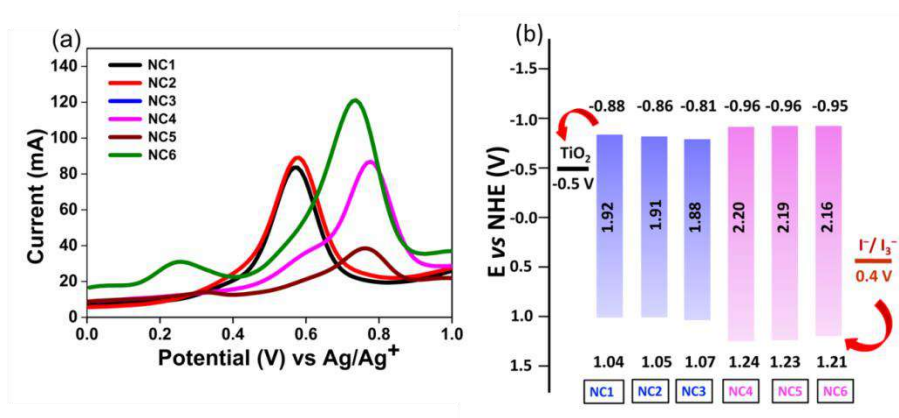


**Figure 7.** (a) Differential pulse voltammograms of NC1-6 dyes in CH<sub>3</sub>CN solution with scan rate of 50 mV s<sup>-1</sup> and (b) Energy level diagram for the NC1-6 dyes vs NHE.

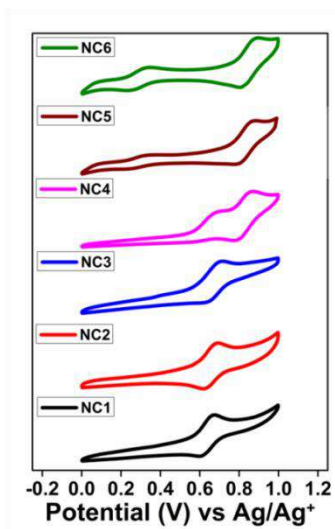


**Figure 8.** Cyclic voltammograms of NC1-6 dyes in CH<sub>3</sub>CN solution with scan rate of 50 mV s<sup>-1</sup>.

Generally, the incident photon-to-current conversion efficiency (IPCE) response of DSSCs is determined by LHE, the electron injection efficiency ( $\Phi_{inj}$ ), regeneration efficiency ( $\eta_{reg}$ ), collection efficiency ( $\eta_{cc}$ ), and; as expressed in **Equation 1**.<sup>38</sup>

$$\text{IPCE} = \text{LHE}(\lambda) \Phi_{inj} \eta_{reg} \eta_{cc} \quad (1)$$

The value of  $-\Delta G_{inj}$  explains the driving force for  $\Phi_{inj}$  from the excited states of dye molecules to the CB of TiO<sub>2</sub>. In DSSCs, the free energy change ( $-\Delta G_{inj}$ ) is major trait for determining the rate and efficiency of charge injection. This means that electron injection from excited dye to the CB of the TiO<sub>2</sub> can be so fast before competing with excited-state

decay processes.<sup>39</sup>  $-\Delta G_{inj}$  is the energy difference between  $E_{LUMO}$  and  $E_{CB}$  as expressed as follow:

$$-\Delta G_{inj} = E_{CB/TiO_2} - E_{LUMO} \quad (2)$$

Therefore,  $-\Delta G_{inj}$  should be suitably positive ( $> 0.2$  eV) to attain a high efficiency.<sup>40</sup> The calculated driving forces for electron injection are 0.38 V, 0.36 V, and 0.31 V for **NC1**, **NC2** and **NC3** respectively. For **NC4**, **NC5**, and **NC6**, the driving forces are 0.46 V, 0.46 V, and 0.45 V, respectively (**Table 1**). These all values are higher than 0.2 eV and offer adequate driving force for the fast injection of excited electrons.

The  $J_{SC}$  of DSSCs is affected by the regeneration efficiency of the dye ( $\eta_{reg}$ ), which is correlated to the driving force of regeneration  $-\Delta G_{reg}$ .<sup>41</sup> It can be expressed as follows:

$$-\Delta G_{reg} = E_{redox} (\Gamma/I_3^-) - E_{HOMO} \quad (3)$$

The calculated regeneration driving forces ( $-\Delta G_{reg}$ ) of HT-based dyes, **NC1**/0.64 V, **NC2**/0.65 V and **NC3**/0.67 V are higher than that of TPA-based dyes, **NC4**/0.84 V, **NC5**/0.83 V and **NC6**/0.81 V. The dye regeneration kinetics studies indicates that a driving force for dye regeneration is essential only  $\sim 150$ -200 mV using the  $\Gamma/I_3^-$  redox couple.<sup>42</sup> Even though, this large driving force is required for the complex regeneration kinetics that proceeds via formation of intermediates such as the  $I_2$  radical which results into lesser  $V_{OC}$ .<sup>43</sup>

### 3.3.4 Theoretical Calculations

The ground-state geometries of **NC** dyes were optimized using DFT at B3LYP/6-31G (d, p) basis set with the Gaussian 09 package.<sup>44,45</sup> Also time dependent density functional theory (TDDFT) was performed for excited states calculation at the B3LYP/6-31G (d, p) basis set on the optimized ground-state geometry. In TDDFT calculations, solvation effects (MeOH) were taken into account with the PCM model implemented in Gaussian 09.<sup>46</sup>

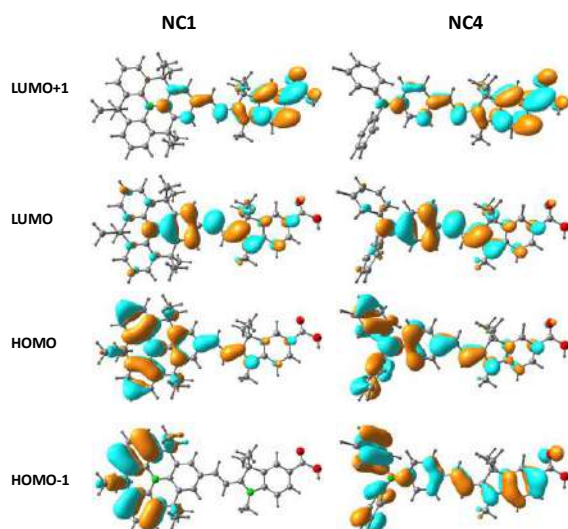


**Figure 9.** HOMO, HOMO-1, LUMO and LUMO+1 isosurface plots for **NC1** (left) and **NC4** (right), respectively.

As shown in **Figure 9**, the HOMO and LUMO of **NC1-6** are strongly distributed over the donor part and its adjacent  $\pi$ -spacer unit. In contrast, HOMO-1 of **NC1-3** dyes was mainly localized on the donor part. For **NC4-6**, HOMO-1 was distributed over the whole molecule. In LUMOs of **NC1-3** and **NC4-6**, there is basically no participation from the amino phenyl groups, and the electron density is reallocated toward the other end of the molecule which shows a good charge separated state. LUMO+1 of all dyes are delocalized inside the acceptors. The contribution of acceptor to LUMO strongly influences the electron injection. The electron density on the anchoring group implies that electron excitation from the HOMO to the LUMO or LUMO+1 levels can efficiently move the electron distribution from the donor unit (HT or TPA) to the acceptor anchoring moiety to recognize effective directional electron transfer into the CB of  $\text{TiO}_2$ .

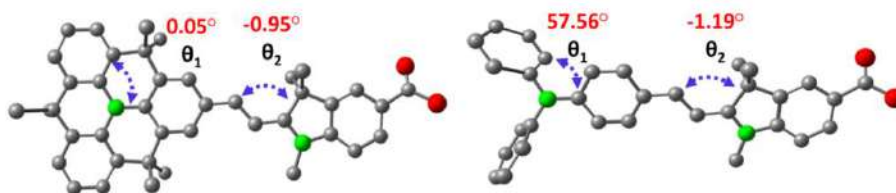


**Figure 10.** Selected dihedral angles of **NC1** and **NC4** calculated from the optimized ground state geometry using DFT at the B3LYP/6-31G (d, p) level with the Gaussian 09 program (hydrogen atoms are removed for better clarity).

The planarity of the dyes influences the ICT processes. However, for TPA-based dyes found that the large dihedral angle between phenyl ring plane and the plane of N-bonded C atoms break effective contribution of two phenyl groups to the ICT process.<sup>47</sup> As shown in **Figure 10**, **NC4-6** exhibited large dihedral angle ( $\theta_1$ ) of  $57.56^\circ$ , which may causes poor extension of  $\pi$ -conjugation over the whole molecule, while for **NC1-3** dihedral angle is almost close to  $0^\circ$ . The HT-based dyes create a more planar molecular structure as confirmed by decreased dihedral angles  $\theta_1$  and  $\theta_2$  and which support the red shift in absorption spectra. The dihedral angle between HT or TPA and indolium units ( $\theta_2$ ) was about  $0^\circ$  which control the degree of conjugation between donor and acceptor which is beneficial to electron transfer from donor to acceptor part then transfer into the CB of TiO<sub>2</sub> upon photo-excitation of dyes.

**Table 2.** Calculated maximum absorption wavelengths  $\lambda_{\max}/\text{nm}$ , corresponding vertical excitation energies  $E_{\text{ex}}$  (eV), and oscillator strengths ( $f$ ) by TD-B3LYP/6-311G (d, p)

Dye	$\lambda_{\max}/\text{MeOH}$ (nm) <sup>a</sup>	$\lambda_{\max}/\text{nm}$ (TDDFT)	$E_{\text{ex}}$ (eV)	$f$
<b>NC1</b>	372, 588	395, 624	1.99	0.48, 1.25
<b>NC2</b>	375, 595	393, 626	1.98	0.49, 1.22
<b>NC3</b>	380, 606	396, 634	1.96	0.43, 1.16
<b>NC4</b>	549	529	2.35	1.71
<b>NC5</b>	551	531	2.33	1.66
<b>NC6</b>	559	537	2.31	1.58

<sup>a</sup>Absorption were measured in MeOH.

The absorption spectra have been evaluated by using TD-DFT study at the B3LYP/6-31G (d, p). The result confirms that in all dyes the lowest excitation is a charge-transfer transition of predominantly HOMO-LUMO character. Thus, the transitions from HOMO to LUMO would give an efficient electron injection into the CB of TiO<sub>2</sub>. The calculated absorption wavelength for **NC1** to **NC3** or **NC4** to **NC6** dyes is in accordance with

experimental absorption spectra (**Figure 11**).<sup>48</sup> The determined oscillator strength is large in all dyes and hence the LHE, as shown in **Table 2**.<sup>49</sup> Moreover, calculated lowest excitation energies ( $E_{ex}$ ) of **NC1-6** dyes are extremely close to the experimentally obtained value. Particularly, **NC1-3** possesses smallest HOMO-LUMO energy gaps and features a broader light absorption window that has advantageous impact on PCE.

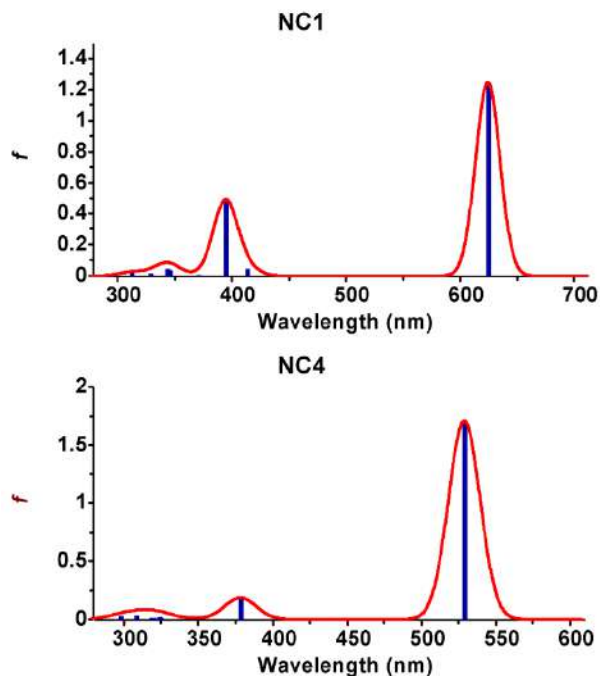


**Figure 11.** Simulated absorption spectrum of **NC1** and **NC4** by TD-DFT calculation using B3LYP/6-31G (d,p) basis set.

### 3.3.5 Photovoltaic Performance

The current-voltage ( $I$ - $V$ ) characteristics of solar cells sensitized with **NC1-6** measured under standard AM 1.5G simulated solar irradiation ( $100 \text{ mW cm}^{-2}$ ) with  $0.18 \text{ cm}^2$  active area without mask. To know the molecular control over PCE of **NC** series, the dye cells were measured using an electrolyte containing  $0.5 \text{ M LiI}$  and  $0.05 \text{ M I}_2$  in  $\text{CH}_3\text{CN}$  and without addition of TBP. The photocurrent density-voltage ( $J$ - $V$ ) curves and the IPCE profiles of the optimized DSSCs based on dyes **NC1-6** are depicted in **Figure 12** and **Figure 14**, and their photovoltaic parameters are listed in **Table 4**. An optically transparent additive chenodeoxycholic acid (CDCA) was co-adsorbed along with the

dyes to avoid the aggregation of dyes on TiO<sub>2</sub> surface, and the best device data with deviation for the NC dyes are summarized in **Table 4**, **Table 5** and **Table 6**.

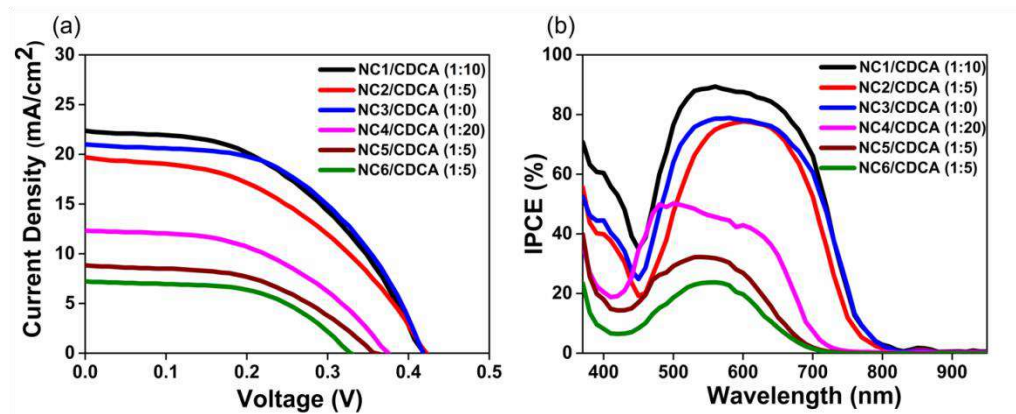


**Figure 12.** (a) *J-V* curves of DSSCs sensitized by NC1-6 and (b) IPCE spectra of NC1-6 dyes.

The choice of electrolyte is highly important to get good  $V_{OC}$  in a DSSCs device. Apart from redox species in the electrolyte, additives such as (i) presence of TBP, (ii) Li ion, (iii) ionic liquid, helps in modifying the  $V_{OC}$ ,  $J_{SC}$  and mass transport of species for improving the device performance.<sup>50</sup> The *I-V* characteristics of NC4 sensitized cells with different electrolytes summarized in **Table 3**. TBP is one of the most important additives in the electrolytes which help to move the semiconductor's conduction band edge upward and gives better  $V_{OC}$  by a significant charge rearrangement upon adsorption onto the semiconductor.<sup>51</sup> From this result, it was observed that the device efficiency of the NC4 sensitized cell was decreased severely upon the addition of TBP to the electrolyte (**Figure 13**). This devices data showed that the addition of TBP is not feasible for improving the  $V_{OC}$  of the hemicyanine dyes. Mott-Schottky analysis of photo anode was carried out to study the effect of TBP on  $E_{CB}$  of TiO<sub>2</sub> electrode; it is explained in EIS part (**Figure 18d**).

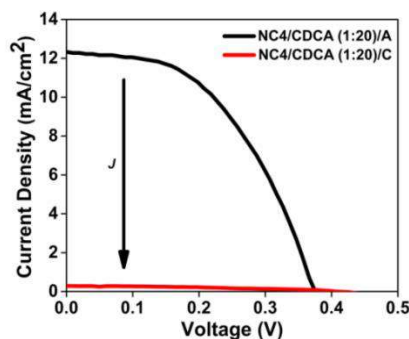


**Figure 13.** Current-voltage characteristics of DSSCs fabricated using **NC4** (TPA) in presence of 20 equivalents of CDCA with different electrolytes A: LiI (0.5 M)/I<sub>2</sub> (0.05 M), C: LiI (0.5 M)/I<sub>2</sub> (0.05 M)/DMII (0.6 M)/TBP (0.2 M).

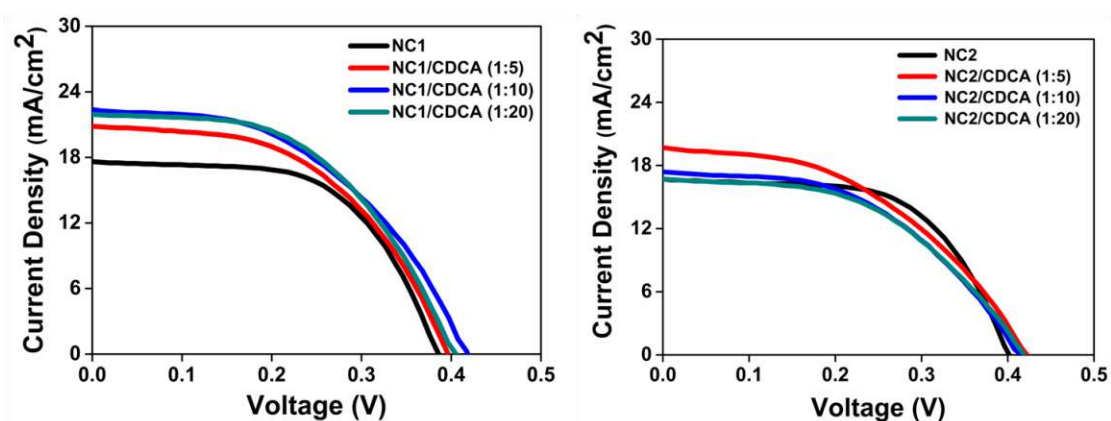
**Table 3.** Photovoltaic parameters for **NC4/CDCA** (1:20) with different electrolytes

Electrolyte	LiI	DMII	I <sub>2</sub>	GuSCN	TBP	PCE (%)	<i>J</i> <sub>SC</sub> (mA/cm <sup>2</sup> )	<i>V</i> <sub>OC</sub> (V)	<i>ff</i> (%)
<b>A</b>	0.5	-----	0.05	-----	-----	2.22	12.33	0.374	48.2
<b>B</b>	0.5	0.6	0.05	-----	-----	2.26	10.70	0.360	58.9
<b>B'</b>	0.5	0.6	0.1	-----	-----	2.12	9.83	0.363	59.3
<b>C</b>	0.5	0.6	0.05	-----	0.2	0.04	0.29	0.406	35.4
<b>C'</b>	0.5	0.6	0.1	0.05	-----	1.88	7.59	0.395	62.7
<b>E</b>	0.5	-----	0.05	-----	0.4	0.04	0.27	0.369	35.8
<b>E'</b>	0.5	0.6	0.1	-----	0.4	0.02	0.182	0.359	35.5

Furthermore, the addition of ionic liquid used to enhance the *ff*, though the device performance was not enhanced significantly. Therefore, 0.5 M LiI and 0.05 M I<sub>2</sub> in CH<sub>3</sub>CN was used as an electrolyte without TBP. HT-based **NC3** attained average PCE of 4.34% with maximum *J*<sub>SC</sub> of 20.04 mA cm<sup>-2</sup>, *V*<sub>OC</sub> of 0.416 V without co-adsorbents (**Figure 12a**). Under the same optimized condition, TPA-based **NC6** sensitized cell reached to average PCE of 0.98% with *J*<sub>SC</sub> of 4.99 mA cm<sup>-2</sup>, and *V*<sub>OC</sub> of 0.329 V. Between **NC1-3**, after addition of coadsorbent, only the **NC1** and **NC2** have positive effect on improving the *V*<sub>OC</sub> and *J*<sub>SC</sub>. After addition of 10 equivalent of coadsorbent, **NC1** dye showed average PCE of 4.33% with *J*<sub>SC</sub> of 21.67 mA cm<sup>-2</sup>, and *V*<sub>OC</sub> of 0.414 V and **NC4**



sensitized cell gave average best performance after addition of 20 equivalents of CDCA with PCE of 2.14%,  $J_{SC}$  of 11.94 mA cm<sup>-2</sup>, and  $V_{OC}$  of 0.372 V. The observed high  $J_{SC}$  with poor  $ff$  is mostly attributable to the high concentration of LiI present in the electrolyte the combination and such observations have been made earlier. Further addition of CDCA leads to improved device efficiency for **NC1** and **NC2** and **NC4** and **NC5** dyes but for **NC3** the  $J_{SC}$  and  $V_{OC}$  reduced with further addition of CDCA and in case of **NC6** for 1:5 equivalent coadsorbent/dye the efficiency was increased but addition of more equivalents of coadsorbent reduced the PCE (**Figure 14**). In NC dyes, dye loading capability decreases in the order of **NC1** > **NC2** > **NC3** and **NC4**  $\approx$  **NC5** > **NC6**, due to progressive increase of alkyl chains at N- and sp<sup>3</sup>-C atoms of indolium unit which is close to the TiO<sub>2</sub> surface that diminishes the dye anchoring to the Ti (V) sites (**Figure 15**). The long and branched alkyl groups on the indolium units contribute an important role for avoiding surface aggregation and suppress the charge recombination even without any co-adsorbent. Therefore, more addition of a large amount of CDCA is not useful for **NC3** or **NC6** dye to improve the photovoltaic performance.<sup>27</sup> The entire HT donor based dyes showed high  $J_{SC}$  with and without CDCA than TPA donor. The low  $V_{OC}$  of NC dyes with I<sup>-</sup>/I<sub>3</sub><sup>-</sup> redox couple are similar with that of previous reports on hemicyanine dyes.<sup>4,12</sup> The reduced PCE of **NC4-6** series is mostly because of lower  $J_{SC}$  and which is dropped by 48% going from **NC1** to **NC4** and the major  $J_{SC}$  loss for **NC6** is around 69%. Remarkably, HT donor connected to indolium units affords more conjugated and planar molecular structure that considerably showed high  $J_{SC}$  with and without CDCA than TPA donor.



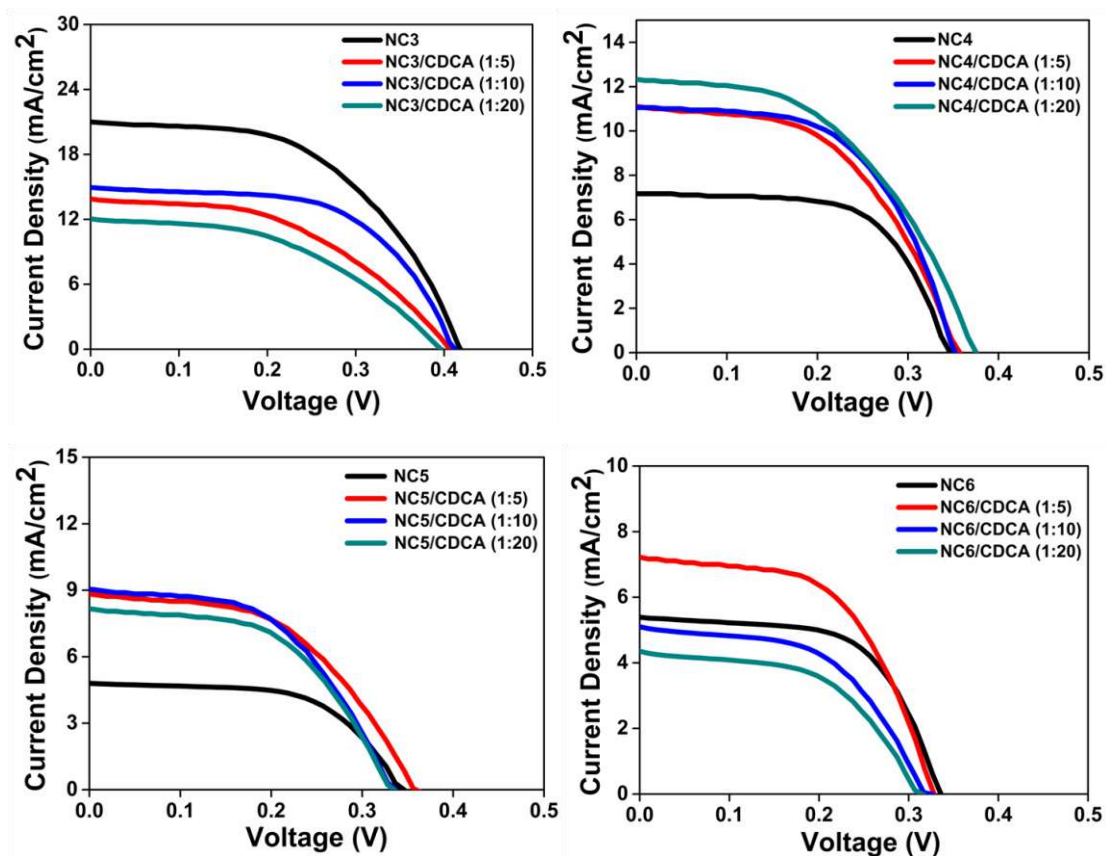


**Figure 14.** *J-V* curves of DSSCs sensitized by NC1-6.

**Table 4.** Photovoltaic parameters for NC1-3 and NC4-6 with and without co-adsorbent

NC Dyes	$J_{sc}$ (mA/cm <sup>2</sup> )	$V_{oc}$ (V)	$ff$ (%)	PCE (%) <sup>a</sup>	Dye Loading ( $\times 10^{-7}$ mol cm <sup>-2</sup> ) <sup>b</sup>
NC1	16.65 $\pm$ 0.95	0.385 $\pm$ 0.006	58.62 $\pm$ 0.61	3.76 $\pm$ 0.24	3.43
NC1/CDCA (1:10)	21.67 $\pm$ 0.74	0.414 $\pm$ 0.005	48.35 $\pm$ 0.61	4.33 $\pm$ 0.15	1.72
NC2	15.86 $\pm$ 0.83	0.399 $\pm$ 0.008	59.63 $\pm$ 0.57	3.78 $\pm$ 0.23	2.63
NC2/CDCA (1:5)	20.63 $\pm$ 1.24	0.412 $\pm$ 0.009	45.93 $\pm$ 1.87	3.90 $\pm$ 0.24	1.36
NC3	20.04 $\pm$ 0.94	0.416 $\pm$ 0.002	52.03 $\pm$ 0.37	4.34 $\pm$ 0.23	1.89
NC3/CDCA (1:5)	14.24 $\pm$ 0.69	0.404 $\pm$ 0.008	57.77 $\pm$ 0.53	3.32 $\pm$ 0.26	0.77
NC4	6.46 $\pm$ 0.51	0.347 $\pm$ 0.003	61.43 $\pm$ 1.33	1.37 $\pm$ 0.12	3.89

<b>NC4/CDCA (1:20)</b>	11.94±0.39	0.372±0.007	48.41±0.69	2.14±0.08	1.75
<b>NC5</b>	4.19±0.68	0.343±0.006	58.77±0.63	0.85±0.14	4.59
<b>NC5/CDCA (1:5)</b>	8.38±0.46	0.358±0.005	49.13±0.57	1.47±0.11	2.08
<b>NC6</b>	4.99±0.39	0.329±0.005	59.34±1.61	0.98±0.12	1.62
<b>NC6/CDCA (1:5)</b>	6.83±0.41	0.320±0.009	54.93±0.67	1.20±0.11	0.61

<sup>a</sup>Electrolyte: 0.5 M LiI and 0.05 M I<sub>2</sub> in CH<sub>3</sub>CN. Dye cell area was 0.18 cm<sup>2</sup> and measurements carried out under 1 sun intensity (100 mW/cm<sup>2</sup>), <sup>b</sup>The desorption experiment was carried out in 2 M ethanolic HCl at room temperature.

**Table 5.** Photovoltaic performance of **NC1-3** with different ratios of CDCA

NC Dyes	$J_{SC}$ (mA/cm <sup>2</sup> )	$V_{OC}$ (V)	$ff$ (%)	PCE (%)
<b>NC1</b>	16.65 ± 0.95	0.385 ± 0.006	58.62 ± 0.61	3.76 ± 0.24
<b>NC1/CDCA (1:5)</b>	20.30± 0.60	0.398± 0.002	50.63± 0.27	4.10± 0.11
<b>NC1/CDCA(1:10)</b>	21.67 ± 0.74	0.414 ± 0.005	48.35 ± 0.61	4.33 ± 0.15
<b>NC1/CDCA (1:20)</b>	20.75 ± 1.19	0.393 ± 0.011	50.86 ± 1.3	4.14 ± 0.38
<b>NC2</b>	15.86 ± 0.83	0.399 ± 0.008	59.63 ± 0.57	3.78 ± 0.23
<b>NC2/CDCA (1:5)</b>	20.63 ± 1.24	0.412 ± 0.009	45.93 ± 1.87	3.90 ± 0.24
<b>NC2/CDCA(1:10)</b>	16.52 ± 0.86	0.411 ± 0.010	50.47 ± 1.83	3.42 ± 0.07
<b>NC2/CDCA (1:20)</b>	15.87 ± 0.87	0.408 ± 0.11	49.37 ± 0.83	3.19 ± 0.25
<b>NC3</b>	20.04 ± 0.94	0.416 ± 0.002	52.03 ± 0.37	4.34 ± 0.23
<b>NC3/CDCA (1:5)</b>	14.24 ± 0.69	0.404 ± 0.008	57.77 ± 0.53	3.32 ± 0.26
<b>NC3/CDCA(1:10)</b>	13.30 ± 0.58	0.403 ± 0.007	47.60 ± 0.61	2.55 ± 0.08
<b>NC3/CDCA (1:20)</b>	11.75 ± 0.30	0.396 ± 0.005	45.93 ± 1.17	2.13 ± 0.06

**Table 6.** Photovoltaic performance of **NC4-6** with different ratios of CDCA

NC Dyes	$J_{SC}$ (mA/cm <sup>2</sup> )	$V_{OC}$ (V)	$ff$ (%)	PCE (%)
<b>NC4</b>	6.46 ± 0.51	0.347 ± 0.003	61.43 ± 1.33	1.37 ± 0.12
<b>NC4/CDCA (1:5)</b>	10.45 ± 0.68	0.362 ± 0.007	50.40 ± 0.71	1.90 ± 0.07
<b>NC4/CDCA(1:10)</b>	10.61 ± 0.45	0.350 ± 0.009	57.17 ± 1.67	2.12 ± 0.04
<b>NC4/CDCA (1:20)</b>	11.94 ± 0.39	0.372 ± 0.007	48.41 ± 0.69	2.14 ± 0.08
<b>NC5</b>	4.19 ± 0.68	0.343 ± 0.006	58.77 ± 0.63	0.85 ± 0.14
<b>NC5/CDCA (1:5)</b>	8.38 ± 0.46	0.358 ± 0.005	49.13 ± 0.57	1.47 ± 0.11
<b>NC5/CDCA(1:10)</b>	8.77 ± 0.26	0.331 ± 0.006	49.97 ± 1.13	1.45 ± 0.09
<b>NC5/CDCA (1:20)</b>	7.92 ± 0.14	0.318 ± 0.015	52.72 ± 0.42	1.34 ± 0.11
<b>NC6</b>	4.99 ± 0.39	0.329 ± 0.005	59.34 ± 1.61	0.98 ± 0.12
<b>NC6/CDCA (1:5)</b>	6.83 ± 0.41	0.320 ± 0.009	54.93 ± 0.67	1.20 ± 0.11
<b>NC6/CDCA(1:10)</b>	4.84 ± 0.26	0.319 ± 0.010	52.34 ± 0.76	0.81 ± 0.05
<b>NC6/CDCA (1:20)</b>	3.92 ± 0.43	0.319 ± 0.007	52.3 ± 0.50	0.66 ± 0.06

**NC1-3** dye cells were displayed impressive *I-V* and IPCE characteristics in contrast to the TPA counterparts. The **NC1-3** sensitized cell with displayed broader plateau region (400-700 nm) with the excellent light-harvesting in longer wavelength region it was extended to 780 nm than **NC4-6** (480-710 nm) (**Figure 12b**). Particularly, **NC3** exhibited maximum plateaus around 79% at 580 nm without co-adsorbents, showing that long and branched alkyl chains on the acceptor is an efficient way for the suppression of dye aggregation, and appreciably contribute to the high performance of **NC3** dye. **NC1** sensitized cell with CDCA displayed the IPCE maximum plateaus around 90% at 560 nm. On the other hand, with the same conditions **NC4** showed IPCE maximum plateaus around 50% at 500 nm. In fact, **NC1-3** has superior light harvesting ability than TPA based dyes, representing that the introduction of HT donor gives effective conjugation leading to a relative high  $J_{SC}$  and  $V_{OC}$ .

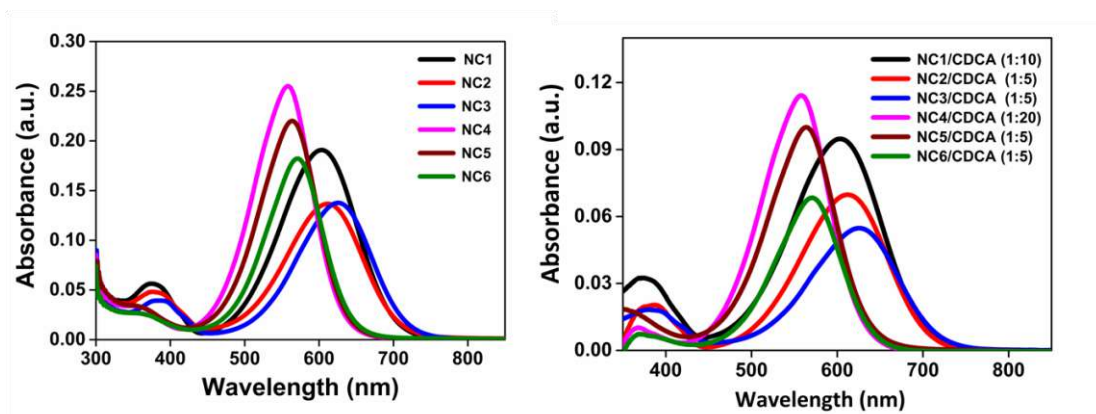


**Figure 15.** UV-Vis absorption spectra of desorbed NC dyes in 2 M HCl in EtOH.

### 3.3.6 Electrochemical Impedance Analysis

EIS measurement was employed to study the interfacial charge recombination process in DSSCs under dark conditions.<sup>52</sup> Principally;  $V_{OC}$  and  $J_{SC}$  are influenced by charge transfer processes happen at the  $TiO_2$ -dye-electrolyte interface. The  $V_{OC}$  is determined from the potential difference between the quasi-Fermi level of  $TiO_2$  ( $E_{F,n}$ ) and the chemical potential of redox species ( $E_{F,redox}$ ) in the electrolyte (Equation 4). The redox potential of electrolyte is considered as constant, while the same ( $I^-/I_3^-$ ) redox couple used in the experiment. A difference in  $V_{OC}$  value is elucidated by the position of  $TiO_2$  conduction band ( $E_{CB}$ ) and the electron density in the semiconductor ( $n_c$ ), it is intimately related to the surface charge and charge recombination, respectively as expressed in Equation 5.<sup>53</sup>

$$V_{OC} = E_{F,redox} - E_{F,n} \quad (4)$$

$$E_{F,n} = E_{CB} + k_B T \ln \left( \frac{n_c}{N_c} \right) \quad (5)$$

Where  $k_B$  is the Boltzmann constant,  $T$  is the absolute temperature (293 K),  $n_c$  is the free electron density, and  $N_c$  is the density of accessible states in the conduction band.

For better insights into the interface kinetics, we have analyzed **NC1**, **NC3**, **NC4** and **NC6**. The capacitance ( $C_\mu$ ) derived from the Nyquist plot with different applied potential using  $R_S+R_1/C_1+R_2/C_2$  circuit model (**Figure 16**). Nyquist plot of **NC3** with different applied potential showed in **Figure 17** and we have carried out similar experiment for

other dyes. The capacitive response of the cell under a series of applied voltage is plotted to study effect on the position of the  $\text{TiO}_2$  CB. The  $C_\mu$  was decreased in the order of  $\text{NC1} \geq \text{NC3} > \text{NC4} > \text{NC6}$  at a given applied potential as shown in **Figure 18a**, for best cells, showing a subsequent upward shift of  $E_{\text{CB}}$  (**Table 7**) which results to increase in  $V_{\text{OC}}$  in the order of  $\text{NC1} \geq \text{NC3} > \text{NC4} > \text{NC6}$ . For **NC3** without co-adsorbent, the increased  $V_{\text{OC}}$  is because of the upward shift in the  $E_{\text{CB}}$  due to the effective surface passivation of the  $\text{TiO}_2$  from ions ( $\text{Li}^+$  and  $\Gamma^-$ ) which are present in the electrolyte.<sup>16</sup> Indeed, after adsorption on to the  $\text{TiO}_2$  surfaces, the distinct dyes have some difference in dipole moment. Primarily, the dipole moments points from dyes to the  $\text{TiO}_2$  (vertical) upon dye adsorption in cationic dyes, which have an effect on CB shift and influences the  $V_{\text{OC}}$ .<sup>54</sup> However, within the HT based **NC1-3** dyes; the increased  $V_{\text{OC}}$  of **NC3** without co-adsorbents can be observed from the lesser recombination due to  $\text{sp}^3\text{-C}$  and N-alkyl chain.

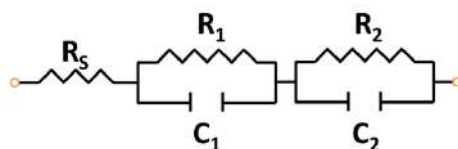


**Figure 16.** Equivalent circuit model ( $R_s + R_1/C_1 + R_2/C_2$ ).  $R_1/C_1$  represents Pt/ ( $\Gamma^- / \text{I}_3^-$ ) and  $R_2/C_2$  represents Dye/ $\text{TiO}_2$ / ( $\Gamma^- / \text{I}_3^-$ ) interfaces.

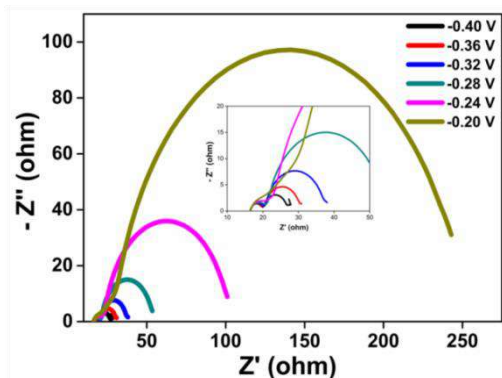


**Figure 17.** Nyquist plot of **NC3** cells.

The  $R_{\text{ct}}$  was obtained in the order of **NC1** ( $25.63 \Omega$ ) > **NC3** ( $18.91 \Omega$ ) > **NC4** ( $11.75 \Omega$ ) > **NC6** ( $9.82 \Omega$ ) at applied bias of  $-0.36 \text{ V}$  as shown in **Figure 18b**. For **NC1** sensitized cells, the  $R_{\text{ct}}$  was higher than that of **NC4**. As a result, **NC1** or **NC3** can suppress charge recombination more strongly than **NC4** or **NC6**, leading to the highest  $V_{\text{OC}}$ . The longer

electron lifetime shows slower charge recombination rate at the interface giving into a higher  $V_{OC}$ . The electron lifetime of **NC1** (17.86 ms) and **NC3** (11.32 ms) is longer than **NC4** (3.47 ms) and **NC6** (1.37 ms) at applied bias of -0.36 V, and which is consistent with experiential obtained  $V_{OC}$  (**Figure 18c**). **NC3** dyes can suppress charge recombination more effectively than other dyes even without any co-adsorbents and which is mostly because of the alkyl chain in the N- and  $sp^3$ -C atoms of indolium unit provides out-of-plane branching of hydrophobic chains that minimizes the intermolecular interactions to some level when adsorbed on  $TiO_2$  and also gives useful surface blocking for the charge recombination between electrons injected on the  $TiO_2$  film and  $I_3^-$ . The high charge transfer resistance and longer electron lifetime in **NC1-3** concludes the significant improvement in  $V_{OC}$  values as compared to **NC1-3** dyes.

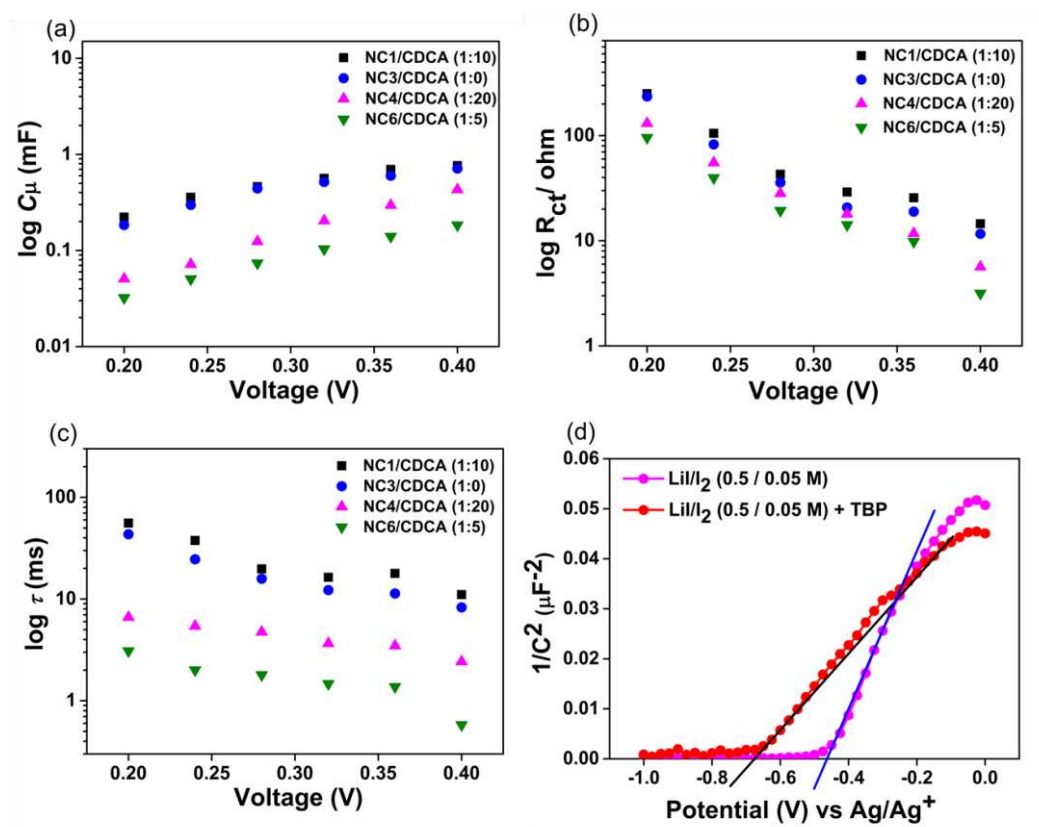


**Figure 18.** Plots of EIS analysis of **NC1**, **NC3**, **NC4** and **NC6** dye cells. (a), (b) and (c)  $C_{\mu}$ ,  $R_{ct}$  and  $\tau$  as a function of voltage, respectively, (d) Mott–Schottky plots at the semiconductor/electrolyte interface.

**Table 7.** EIS parameters for the DSSCs based on **NC1**, **NC2**, **NC3** and **NC4**.

NC Dyes	$R_{ct}$ (ohm)	$C_{\mu}$ (mF)	$\tau$ (ms)
<b>NC1/CDCA (1:10)</b>	25.63	0.70	17.86
<b>NC3/CDCA (1:0)</b>	18.91	0.60	11.32
<b>NC4/CDCA (1:20)</b>	11.75	0.29	3.47
<b>NC6/CDCA (1:5)</b>	9.82	0.14	1.37

EIS data measured at a applied bias of  $-0.36$  V under dark conditions,  $R_{ct}$ : charge transport resistance;  $C_{\mu}$ : chemical capacitance;  $\tau$ : electron lifetime.

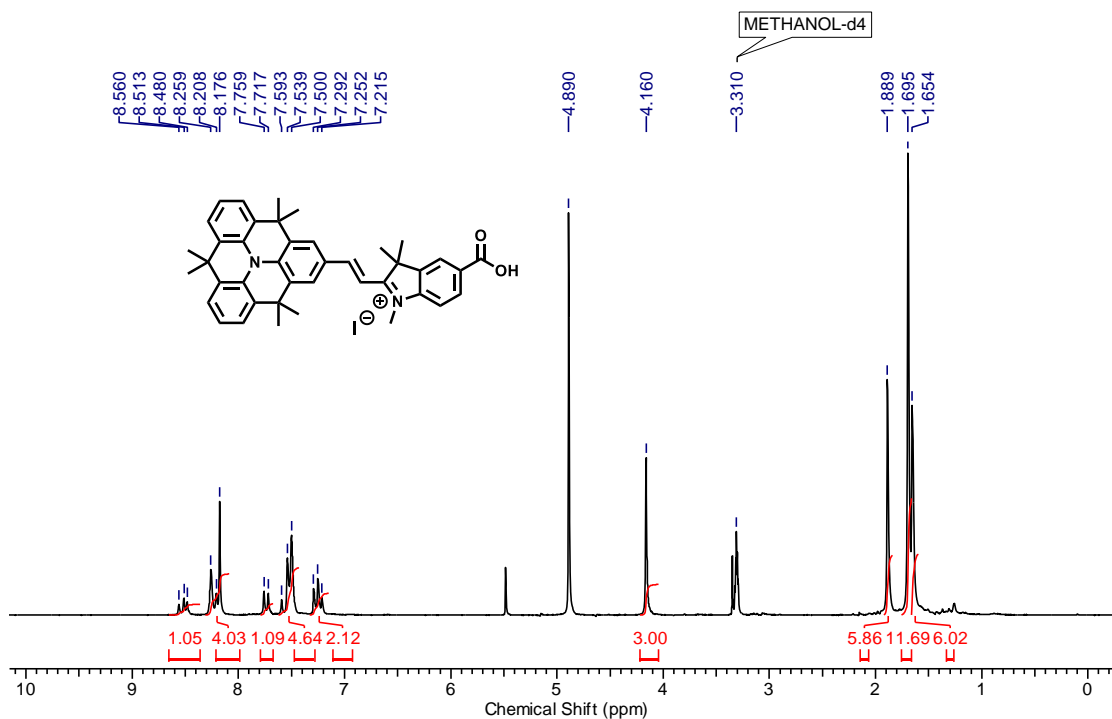
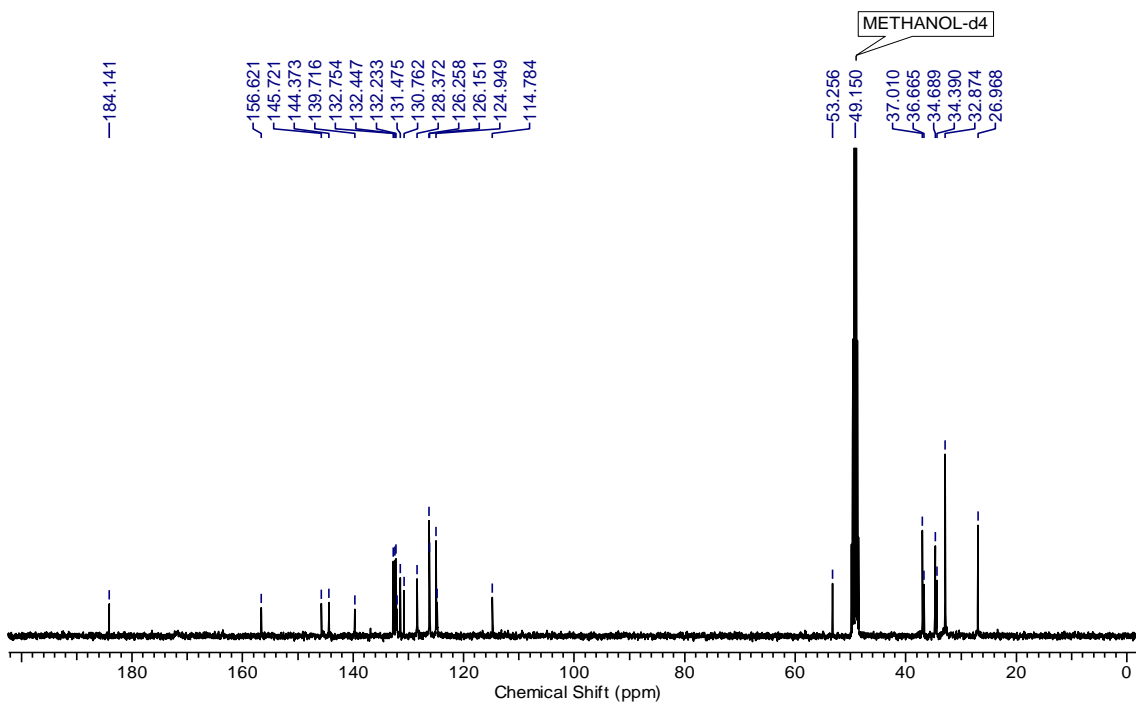
Herein, the addition of TBP is nearly impossible for improving the  $V_{OC}$  of the hemicyanine dyes because of the low lying LUMO and also the effect of TBP on  $E_{CB}$  of semiconductor.<sup>13,55</sup> TBP is one of the major important additives in the electrolytes which are adsorbed onto the  $TiO_2$ /electrolyte interface, therefore moves the semiconductor's conduction band edge upward and avoid charge recombination with triiodides.<sup>19</sup> Also, it helps to get better  $V_{OC}$  by a significant charge rearrangement upon adsorption onto the  $TiO_2$  surface. Also the electrostatic potential (dipole) produced by the dye can alter the  $TiO_2$  CB. For this explanation, an evident Fermi level of semiconductor/electrolyte interface was determined by electrochemical analysis.<sup>56</sup> Mott-Schottky analysis of photoanode was measured in presence of iodolyte redox couple (0.5 M LiI and 0.05 M  $I_2$  in  $CH_3CN$ ) with and without TBP (0.5 M) using three electrode assembly (**Figure 18d**).<sup>13</sup> This study showed that after the addition of TBP, around 220 mV up-shift (more negative) of  $TiO_2$  flat band potential was observed, which supports the drastic decrease in PCE of NC dyes using TBP based electrolyte (**Figure 13**). The efficiency of the NC sensitized cells was suppressed by a greater after TBP was added to the electrolyte (**Table 3**).



### 3.4 CONCLUSION

In this chapter, designed a new D-A type hemicyanine dyes by adopting two different donors and varying the alkyl functionalities on acceptor unit. Herein, modulated the electronic levels, corresponding photophysical properties, and conversion efficiencies of hemicyanine class of dyes by exchanging the donor. Most importantly, for avoiding the dye aggregations on the TiO<sub>2</sub> surface and to passivate the surface to suppress the charge recombination by in-plane and out-of-plane alky groups are incorporated in D-A dyes. HT is more planar and conjugated structure which is beneficial to the harvest longer wavelength photons, which reveals the higher IPCE response in **NC1-3** than **NC4-6**. The newly designed dyes **NC1-3** (HT-based) are very promising candidate for DSSCs which offers substantial improvement in  $J_{SC}$  and  $V_{OC}$  values. The **NC1-3** and **NC4-6** showed different IPCE profiles, **NC1** dye displayed plateau around 80% from 520 to 720 nm and it is only 40% from 480 to 620 nm for **NC4**. Density functional theory(DFT) calculations revealed that HT unit has a dihedral angle of 0.05° between the phenyl groups and the plane of the N-bonded C atoms, which is comparatively smaller than for TPA (57.56°) showing that the HT has outstanding electron delocalization than TPA. The electrochemical impedance measurement was carried out to elucidate the interfacial charge transfer processes for **NC1-6** dyes. The **NC3** sensitized cells exhibited photovoltaic efficiency of  $4.34 \pm 0.23\%$  without co-adsorbents ( $J_{SC} = 20.04 \pm 0.94$  mA cm<sup>-2</sup>,  $V_{OC} = 0.416 \pm 0.002$  V, and  $ff = 52.03 \pm 0.37\%$ ). The molecular engineering of D-A dye using strong donor and out-of-plane alkyl functionalities promote an upward shift in  $E_{CB}$  of TiO<sub>2</sub> even in presence of high concentration of Li<sup>+</sup> and which is evidently explained by large  $R_{ct}$ , and a longer  $\tau$  for HT-NC sensitized cells. Therefore, this D-A molecular structure of hemicyanine dye is an example of improving  $V_{OC}$  and  $J_{SC}$  without changing the electrolyte. This work illustrates controlled trade-off between  $E_{CB}$  and  $V_{OC}$  using new dye design and further increase in efficiency may be possible with sulfur-based electrolyte.

## 3.5 NMR data

Figure 19. <sup>1</sup>H NMR (200 MHz, MeOH-*d*<sub>4</sub>) spectrum of NC1.Figure 20. <sup>13</sup>C NMR (100 MHz, MeOH-*d*<sub>4</sub>) spectrum of NC1.

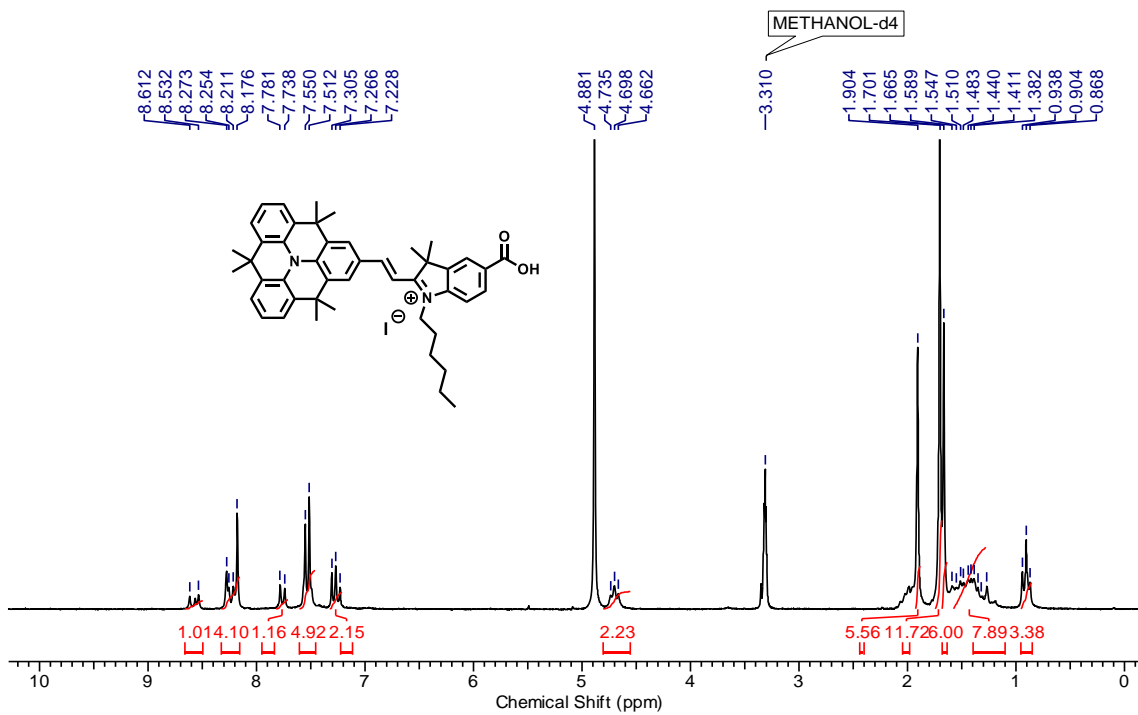


**Figure 21.**  $^1\text{H}$  NMR (200 MHz,  $\text{MeOH-}d_4$ ) spectrum of NC2.

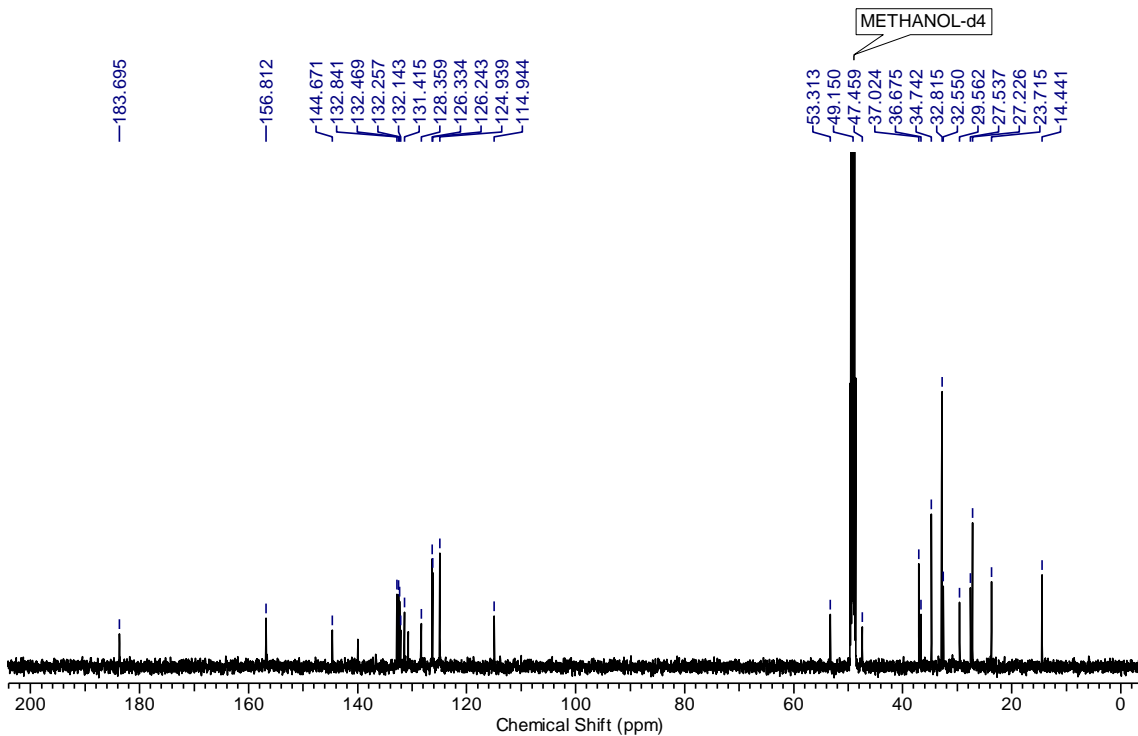


**Figure 22.**  $^{13}\text{C}$  NMR (100 MHz,  $\text{MeOH-}d_4$ ) spectrum of NC2.

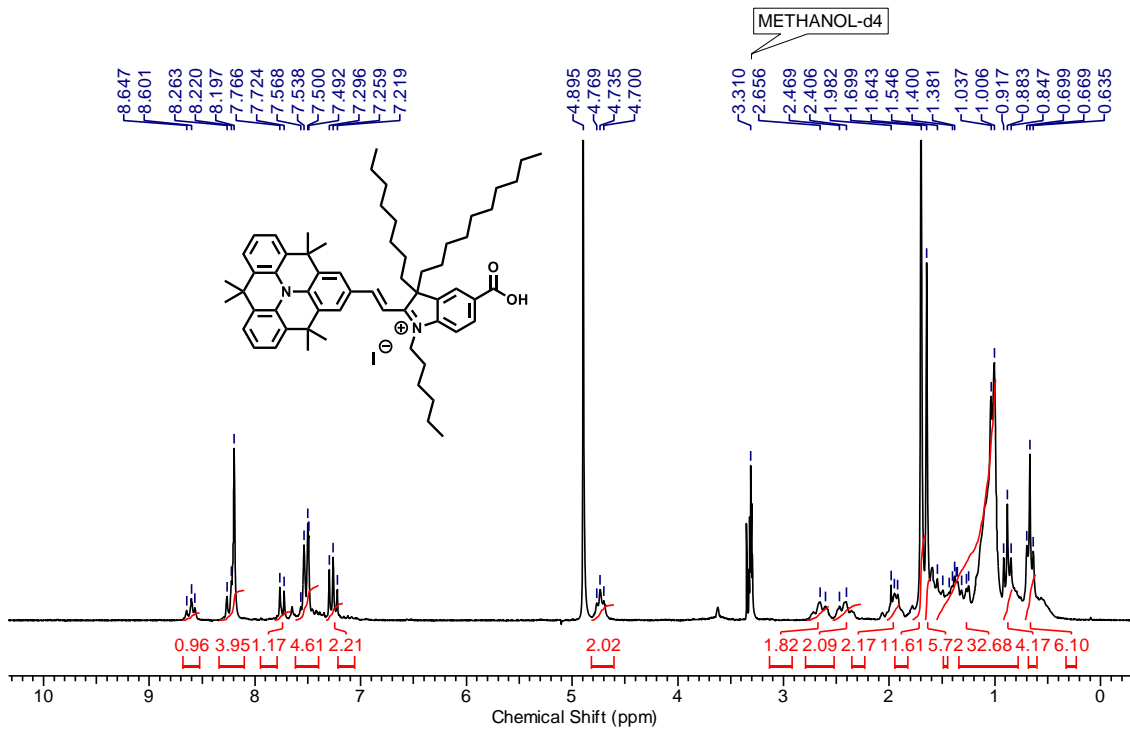


**Figure 23.**  $^1\text{H}$  NMR (200 MHz, MeOH- $d_4$ ) spectrum of NC3.

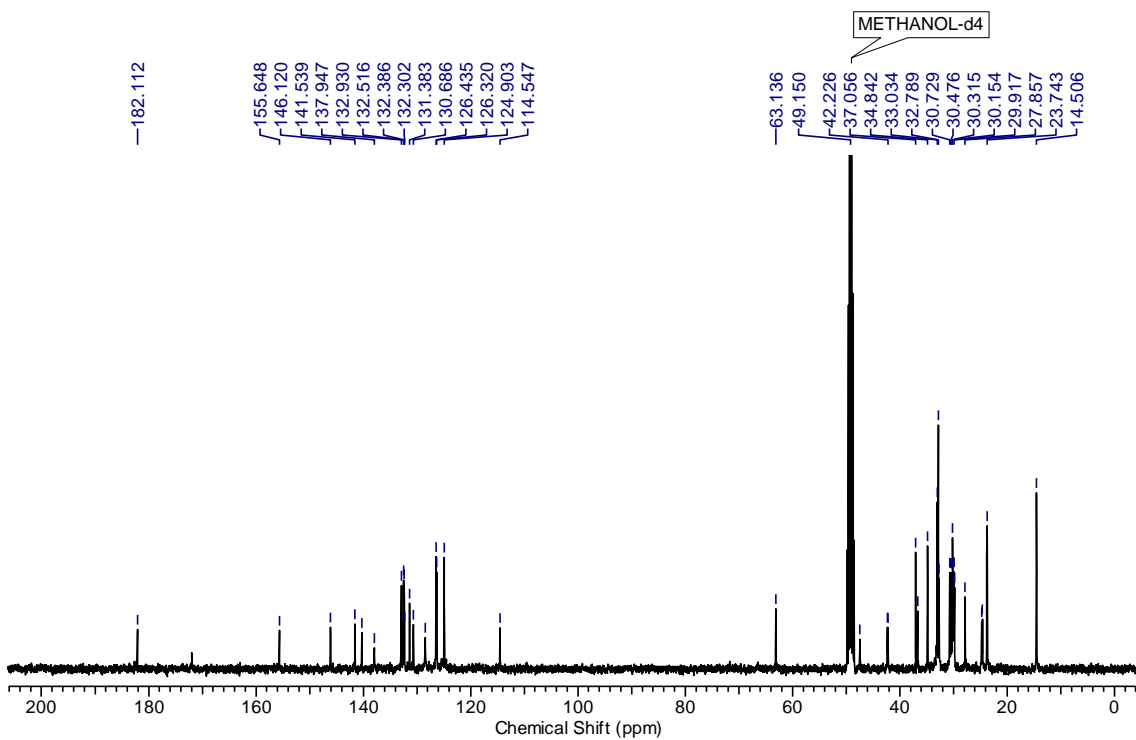


**Figure 24.**  $^{13}\text{C}$  NMR (100 MHz, MeOH- $d_4$ ) spectrum of NC3.

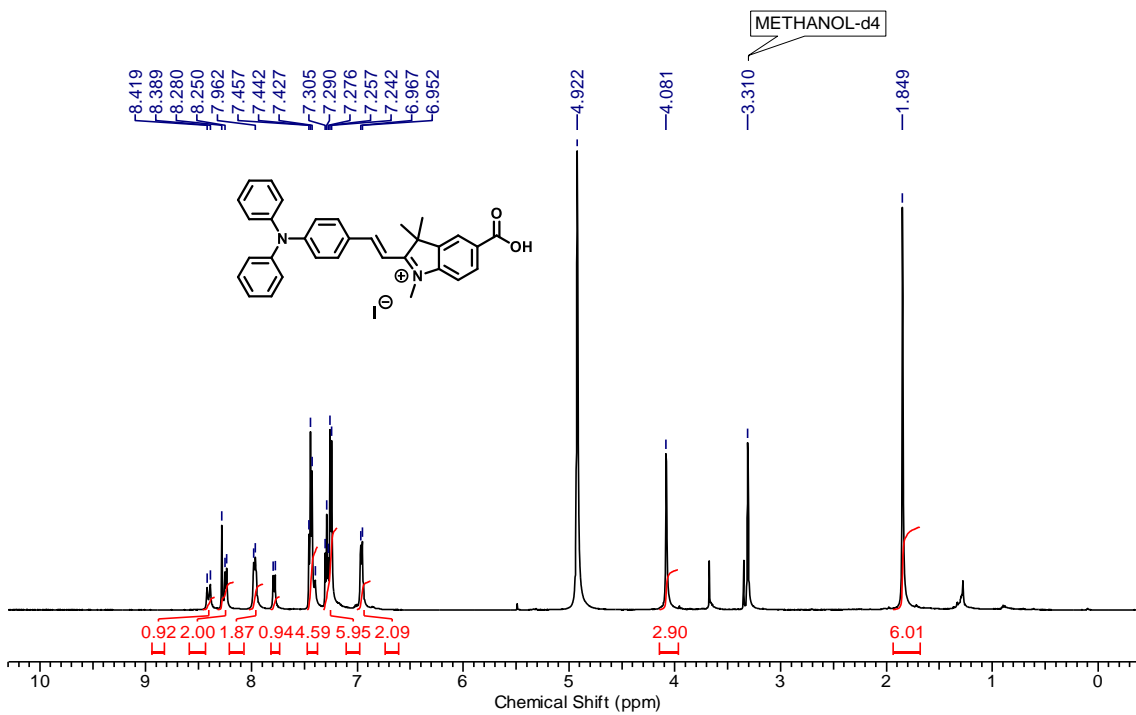


**Figure 25.** <sup>1</sup>H NMR (500 MHz, MeOH-*d*<sub>4</sub>) spectrum of NC4.

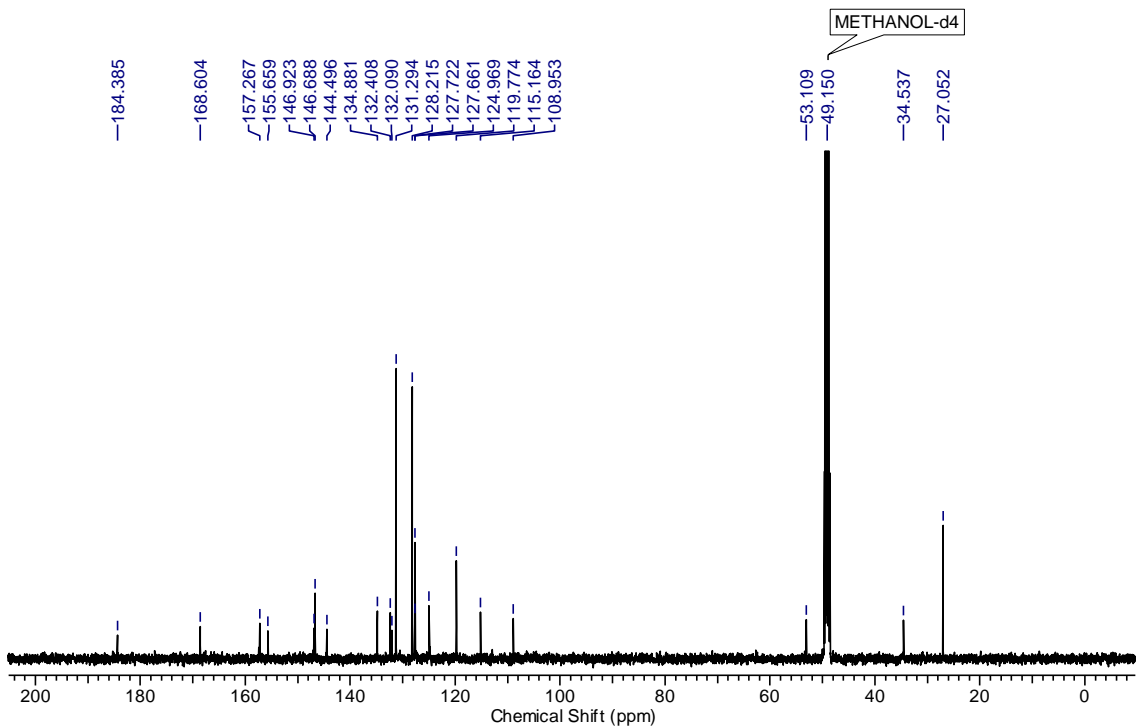


**Figure 26.** <sup>13</sup>C NMR (100 MHz, MeOH-*d*<sub>4</sub>) spectrum of NC4.

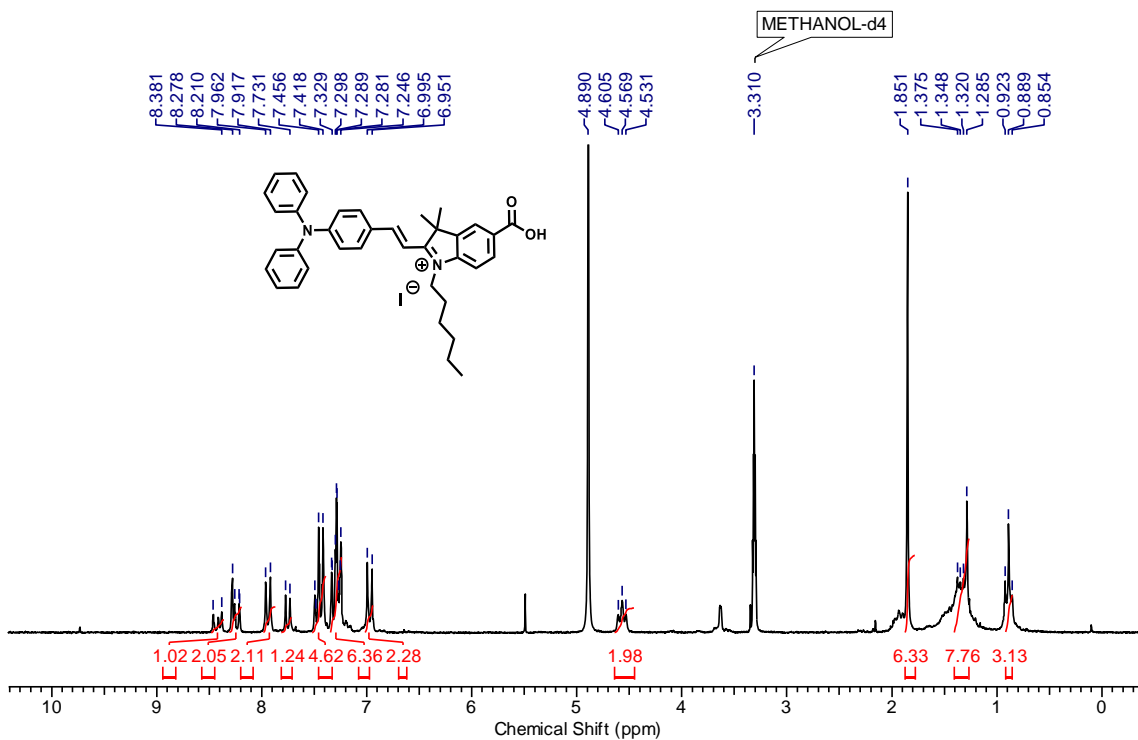


**Figure 27.**  $^1\text{H}$  NMR (200 MHz,  $\text{MeOH-}d_4$ ) spectrum of NC5.

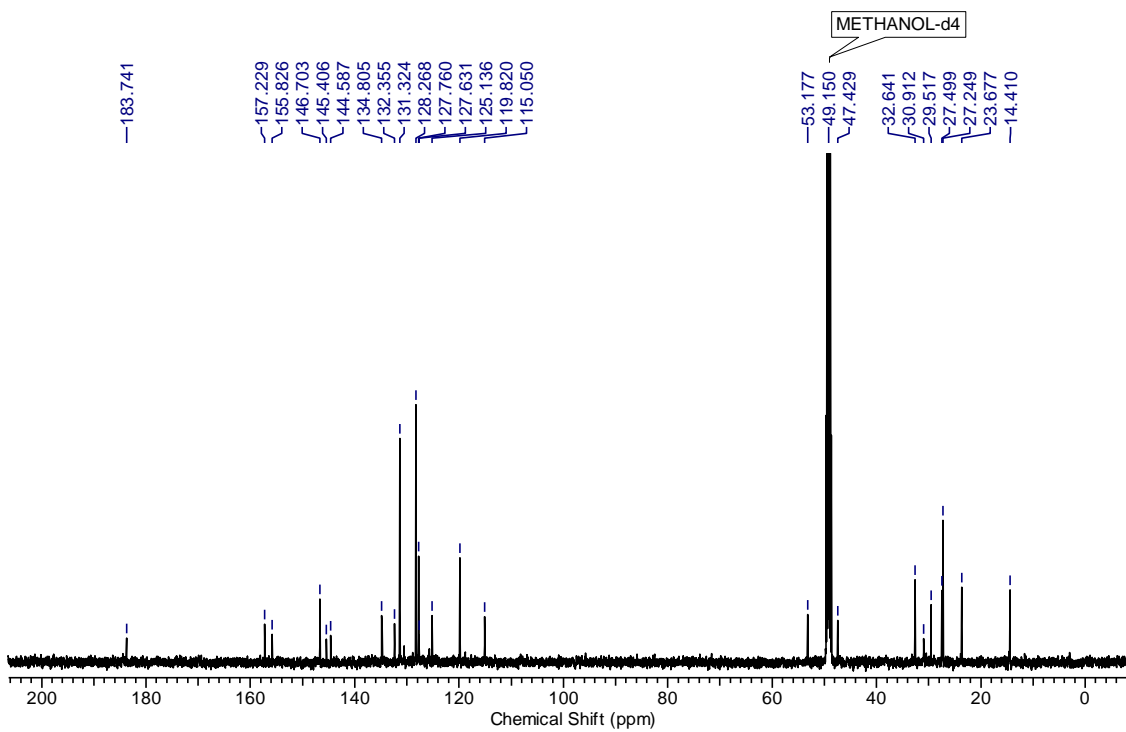


**Figure 28.**  $^{13}\text{C}$  NMR (100 MHz,  $\text{MeOH-}d_4$ ) spectrum of NC5.

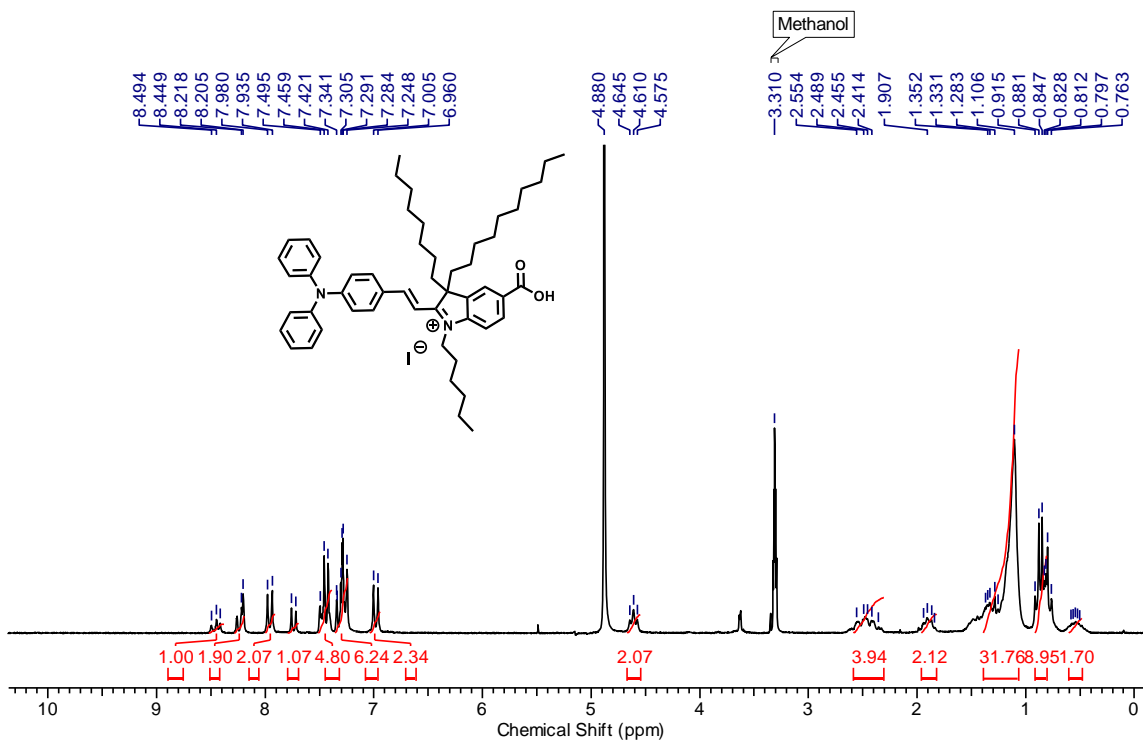


**Figure 29.**  $^1\text{H}$  NMR (200 MHz,  $\text{MeOH-}d_4$ ) spectrum of NC6.

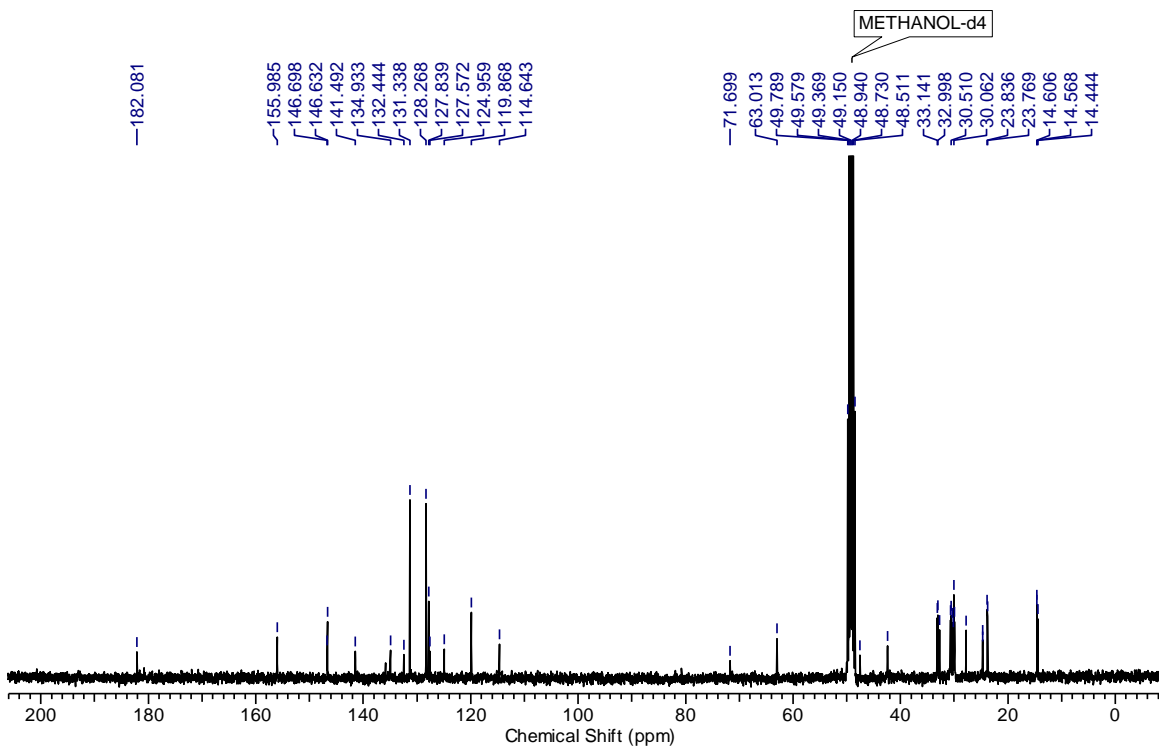


**Figure 30.**  $^{13}\text{C}$  NMR (100 MHz,  $\text{MeOH-}d_4$ ) spectrum of NC6.

**3.6 REFERENCES**

1. Mishra, A.; Fischer, M. K.; Bäuerle, P. *Angew. Chem., Int. Ed.* **2009**, *48*, 2474.
2. Mishra, A.; Behera, R. K.; Behera, P. K.; Mishra, B. K.; Behera, G. B. *Chem. Rev.* **2000**, *100*, 1973.
3. Liang, M.; Chen, J. *Chem. Soc. Rev.* **2013**, *42*, 3453.
4. Meng, F.; Yao, Q.; Shen, J.; Li, F.; Huang, C.; Chen, K.; Tian, H. *Synth. Met.* **2003**, *137*, 1543.
5. Stathatos, E.; Lianos, P.; Laschewsky, A.; Ouari, O.; Van Cleuvenbergen, P. *Chem. Mater.* **2001**, *13*, 3888.
6. Khazraji, A. C.; Hotchandani, S.; Das, S.; Kamat, P. V. *J. Phys. Chem. B* **1999**, *103*, 4693.
7. Sayama, K.; Hara, K.; Mori, N.; Satsuki, M.; Suga, S.; Tsukagoshi, S.; Abe, Y.; Sugihara, H.; Arakawa, H. *Chem. Comm.* **2000**, 1173.
8. Yum, J.-H.; Walter, P.; Huber, S.; Rentsch, D.; Geiger, T.; Nüesch, F.; De Angelis, F.; Grätzel, M.; Nazeeruddin, M. K. *J. Am. Chem. Soc.* **2007**, *129*, 10320.
9. Qin, C.; Wong, W. Y.; Han, L. *Chem. Asian J.* **2013**, *8*, 1706.
10. Ma, X.; Hua, J.; Wu, W.; Jin, Y.; Meng, F.; Zhan, W.; Tian, H. *Tetrahedron* **2008**, *64*, 345.
11. Tang, J.; Wu, W.; Hua, J.; Li, J.; Li, X.; Tian, H. *Energy Environ. Sci.* **2009**, *2*, 982.
12. Wu, W.; Guo, F.; Li, J.; He, J.; Hua, J. *Synth. Met.* **2010**, *160*, 1008.
13. Cheng, M.; Yang, X.; Chen, C.; Zhao, J.; Tan, Q.; Sun, L. *Phys. Chem. Chem. Phys.* **2013**, *15*, 17452.
14. Cheng, M.; Yang, X.; Li, J.; Zhang, F.; Sun, L. *ChemSusChem* **2013**, *6*, 70.
15. Kim, B. G.; Chung, K.; Kim, J. *Chem. Eur. J.* **2013**, *19*, 5220.
16. Liang, Y.; Cheng, F.; Liang, J.; Chen, J. *J. Phys. Chem. C* **2010**, *114*, 15842.
17. Pelet, S.; Moser, J.-E.; Grätzel, M. *J. Phys. Chem. B* **2000**, *104*, 1791.
18. Boschloo, G.; Häggman, L.; Hagfeldt, A. *J. Phys. Chem. B* **2006**, *110*, 13144.
19. Katoh, R.; Kasuya, M.; Kodate, S.; Furube, A.; Fuke, N.; Koide, N. *J. Phys. Chem. C* **2009**, *113*, 20738.
20. Taya, S.; Kuwahara, S.; Shen, Q.; Toyoda, T.; Katayama, K. *RSC Adv.* **2014**, *4*, 21517.
21. Karjule, N.; Mele Kavungathodi, M. F.; Nithyanandhan, J. *J. Phys. Chem. C* **2017**, *121*, 21836.
22. Cai, L.; Tsao, H. N.; Zhang, W.; Wang, L.; Xue, Z.; Grätzel, M.; Liu, B. *Adv. Energy Mater.* **2013**, *3*, 200.
23. Karjule, N.; MK, M. F.; Nithyanandhan, J. *J. Mater. Chem. A* **2016**, *4*, 18910.
24. Field, J. E.; Venkataraman, D. *Chem. Mater.* **2002**, *14*, 962.
25. Do, K.; Kim, D.; Cho, N.; Paek, S.; Song, K.; Ko, J. *Org. Lett.* **2011**, *14*, 222.
26. Hara, K.; Dan-oh, Y.; Kasada, C.; Ohga, Y.; Shinpo, A.; Suga, S.; Sayama, K.; Arakawa, H. *Langmuir* **2004**, *20*, 4205.
27. Yao, Z.; Zhang, M.; Wu, H.; Yang, L.; Li, R.; Wang, P. *J. Am. Chem. Soc.* **2015**, *137*, 3799.



28. Fang, Z.; Chellappan, V.; Webster, R. D.; Ke, L.; Zhang, T. F.; Liu, B.; Lai, Y. H. *J. Mater. Chem.* **2012**, *22*, 15397.
29. Lee, H. J.; Sohn, J.; Hwang, J.; Park, S. Y.; Choi, H.; Cha, M. *Chem. Mater.* **2004**, *16*, 456.
30. Law, K. Y. *J. Phys. Chem.* **1987**, *91*, 5184.
31. Hara, K.; Wang, Z.-S.; Sato, T.; Furube, A.; Katoh, R.; Sugihara, H.; Dan-oh, Y.; Kasada, C.; Shinpo, A.; Suga, S. *J. Phys. Chem. B* **2005**, *109*, 15476.
32. Justin Thomas, K.; Hsu, Y.-C.; Lin, J. T.; Lee, K.-M.; Ho, K.-C.; Lai, C.-H.; Cheng, Y.-M.; Chou, P.-T. *Chem. Mater.* **2008**, *20*, 1830.
33. Peng, X.; Song, F.; Lu, E.; Wang, Y.; Zhou, W.; Fan, J.; Gao, Y. *J. Am. Chem. Soc.* **2005**, *127*, 4170.
34. Ephardt, H.; Fromherz, P. *J. Phys. Chem.* **1993**, *97*, 4540.
35. Tachibana, Y.; Hara, K.; Sayama, K.; Arakawa, H. *Chem. Mater.* **2002**, *14*, 2527.
36. Bisht, R.; Singh, A. K.; Nithyanandhan, J. *J. Org. Chem.* **2017**, *82*, 1920.
37. Bodedla, G. B.; Justin Thomas, K.; Fan, M.-S.; Ho, K.-C. *J. Org. Chem.* **2016**, *81*, 640.
38. Dai, P.; Dong, H.; Liang, M.; Cheng, H.; Sun, Z.; Xue, S. *ACS Sustainable Chem. Eng.* **2016**.
39. Cherepy, N. J.; Smestad, G. P.; Grätzel, M.; Zhang, J. Z. *J. Phys. Chem. B* **1997**, *101*, 9342.
40. Hara, K.; Sato, T.; Katoh, R.; Furube, A.; Ohga, Y.; Shinpo, A.; Suga, S.; Sayama, K.; Sugihara, H.; Arakawa, H. *J. Phys. Chem. B* **2003**, *107*, 597.
41. Daeneke, T.; Mozer, A. J.; Uemura, Y.; Makuta, S.; Fekete, M.; Tachibana, Y.; Koumura, N.; Bach, U.; Spiccia, L. *J. Am. Chem. Soc.* **2012**, *134*, 16925.
42. Wenger, S.; Bouit, P.-A.; Chen, Q.; Teuscher, J.; Di Censo, D.; Humphry-Baker, R.; Moser, J.-E.; Delgado, J. L.; Martin, N.; Zakeeruddin, S. M. *J. Am. Chem. Soc.* **2010**, *132*, 5164.
43. Boschloo, G.; Hagfeldt, A. *Acc. Chem. Res.* **2009**, *42*, 1819.
44. Frisch, M. J.; Pople, J. A.; Binkley, J. S. *J. Chem. Phys.* **1984**, *80*, 3265.
45. Frisch, M. J.; Trucks, G. W.; Schlegel, H. B.; Scuseria, G. E.; Robb, M. A.; Cheeseman, J. R.; Scalmani, G.; Barone, V.; Mennucci, B.; Petersson, G. A.; Nakatsuji, H.; Caricato, M.; Li, X.; Hratchian, H. P.; Izmaylov, A. F.; Bloino, J.; Zheng, G.; Sonnenberg, J. L.; Hada, M.; Ehara, M.; Toyota, K.; Fukuda, R.; Hasegawa, J.; Ishida, M.; Nakajima, T.; Honda, Y.; Kitao, O.; Nakai, H.; Vreven, T.; Montgomery, J. A., Jr.; Peralta, J. E.; Ogliaro, F.; Bearpark, M.; Heyd, J. J.; Brothers, E.; Kudin, K. N.; Staroverov, V. N.; Kobayashi, R.; Normand, J.; Raghavachari, K.; Rendell, A.; Burant, J. C.; Iyengar, S. S.; Tomasi, J.; Cossi, M.; Rega, N.; Millam, J. M.; Klene, M.; Knox, J. E.; Cross, J. B.; Bakken, V.; Adamo, C.; Jaramillo, J.; Gomperts, R.; Stratmann, R. E.; Yazyev, O.; Austin, A. J.; Cammi, R.; Pomelli, C.; Ochterski, J. W.; Martin, R. L.; Morokuma, K.; Zakrzewski, V. G.; Voth, G. A.; Salvador, P.; Dannenberg, J. J.; Dapprich, S.; Daniels, A. D.; Farkas, O.; Foresman, J. B.; Ortiz, J. V.; Cioslowski, J.; Fox, D. J. *Gaussian 09, Revision A.01*; Gaussian, Inc.: Wallingford, CT, **2009**.
46. Feng, S.; Li, Q.-S.; Sun, P.-P.; Niehaus, T. A.; Li, Z.-S. *ACS Appl. Mater. Interfaces* **2015**, *7*, 22504.
47. Chen, Q.; Wu, N.; Liu, Y.; Li, X.; Liu, B. *RSC Adv.* **2016**, *6*, 87969.

48. Zarate, X.; Claveria-Cadiz, F.; Arias-Olivares, D.; Rodriguez-Serrano, A.; Inostroza, N.; Schott, E. *Phys. Chem. Chem. Phys.* **2016**, *18*, 24239.
49. Hagberg, D. P.; Marinado, T.; Karlsson, K. M.; Nonomura, K.; Qin, P.; Boschloo, G.; Brinck, T.; Hagfeldt, A.; Sun, L. *J. Org. Chem.* **2007**, 9550.
50. Wang, H.; Peter, L. M. *J. Phys. Chem. C* **2012**, *116*, 10468.
51. Ziółek, M.; Martín, C.; Sun, L.; Douhal, A. *J. Phys. Chem. C* **2012**, *116*, 26227.
52. Wang, Q.; Moser, J.-E.; Grätzel, M. *J. Phys. Chem. B* **2005**, *109*, 14945.
53. Li, G.; Liang, M.; Wang, H.; Sun, Z.; Wang, L.; Wang, Z.; Xue, S. *Chem. Mater.* **2013**, *25*, 1713.
54. Chai, Q.; Li, W.; Wu, Y.; Pei, K.; Liu, J.; Geng, Z.; Tian, H.; Zhu, W. *ACS Appl. Mater. Interfaces* **2014**, *6*, 14621.
55. Liu, J.; Yang, X.; Zhao, J.; Sun, L. *RSC Adv.* **2013**, *3*, 15734.
56. Ronca, E.; Pastore, M.; Belpassi, L.; Tarantelli, F.; De Angelis, F. *Energy Environ. Sci.* **2013**, *6*, 183.

# CHAPTER IV

---

**Effect of  $\pi$ -spacer and Alkyl Chains on Molecular Orientation, Photophysical and Photovoltaic Properties of Heterotriangulene Based Squaraine Dyes for Dye-Sensitized Solar Cells**

## 4.1 INTRODUCTION

Metal-free near-infrared (NIR) absorbing dyes have been explored mainly to harness longer wavelength photons. The NIR absorbing dye includes squaraine, cyanine and merocyanine dyes exhibits very intense charge transfer bands and high molar extinction coefficient ( $\sim 10^5 \text{ M}^{-1} \text{ cm}^{-1}$ ) at  $\lambda_{\text{max}}$  of 600-800 nm, compared to phthalocyanines and porphyrins.<sup>1</sup> The dye aggregates formed on the  $\text{TiO}_2$  surface are observed to be one of the major issues accounting for the low DSSCs performance.<sup>2</sup> In terms of dye design, a variety of dye configuration have been utilized to harvest the NIR regions of the solar spectrum, to avoid the dye aggregation and for suppressing the charge recombination. In D- $\pi$ -A configuration of metal-free organic dyes, modification and exchange of the donor,  $\pi$ -spacer, and acceptor parts are the main approach to improve the absorption in the visible and near-infrared (NIR) region by modulating their HOMO-LUMO energy levels and also to improve the molar extinction coefficient ( $\epsilon$ ).<sup>3</sup> Moreover, incorporation of additional electron-withdrawing units construct a “D-A- $\pi$ -A” or “D- $\pi$ -A-A” dye configuration, in which a various kind of units such as benzothiadiazole, benzotriazole, phthalimide and diketopyrrolopyrrole are incorporated into the  $\pi$ -bridge to change the molecular structures, enhance their spectral response and optimize energy level.<sup>4</sup> The NIR absorbing dyes such as squaraine consist of D-A-D type configuration; it is having very intense CT bands at far red region with good DSSCs device efficiencies.<sup>5</sup> The anchoring groups has been placed on one of the donors unit (D-A-Danchoring) in the “D-A-D” structure of squaraine dyes. As reported by Yum et al. the squaraine sensitizer showed well optimized photophysical and electrochemical properties with high incident monochromatic photon-to-current conversion (IPCE) and power conversion efficiency ( $\eta$ ) of 4.5 % under irradiance of  $100 \text{ mW/cm}^2$  (simulated AM 1.5G sunlight) at optimized co-adsorbent condition.<sup>6</sup> These squaraine sensitizers make sure a strong electronic coupling to the conduction band (CB) of  $\text{TiO}_2$  and as a result a fast electron transfer, though the driving force for photo-induced electron injection is still very high.<sup>1</sup> So, the future work is focused on the design of squaraine dyes with lower band gap and higher  $\epsilon$ . Apart from dye aggregation on the  $\text{TiO}_2$ , molecular orientation and arrangement of dyes on the also plays an important role for an efficient electron injection from the sensitizer to the CB of  $\text{TiO}_2$ .<sup>7,8</sup> In DSSCs, charge injection and charge recombination process at dye-

TiO<sub>2</sub> interface plays most important role for solar cell performance.<sup>9</sup> It is found that electron transfer usually takes place through the spacer connecting the anchoring group to the semiconductor surface. Imhori and co-workers reported the perpendicular orientation of anchored Zn-porphyrin (ZnP) provides the efficient charge injection of electrons in the CB, which shows increase of photocurrent and solar cell efficiency.<sup>10</sup> Whereas the Zn-porphyrin molecules when anchored to the TiO<sub>2</sub> surface with a tilt angles, then this angle determines the ZnP-TiO<sub>2</sub> electron transfer distance and charge transfer takes place through space, rather than through the spacer linking the porphyrin core and anchoring COOH group.<sup>11</sup> These results specify that the electron transfer between dyes and TiO<sub>2</sub> occurs through-space more readily than through the molecular spacer results in decreased  $\eta$ . This is mainly, because of the decreased efficiency of electron injection. In addition, more severe charge recombination occurs between oxidized sensitizer and injected electrons, because the donor part becomes closer to the TiO<sub>2</sub> surface in tilt position (**Figure 1**).

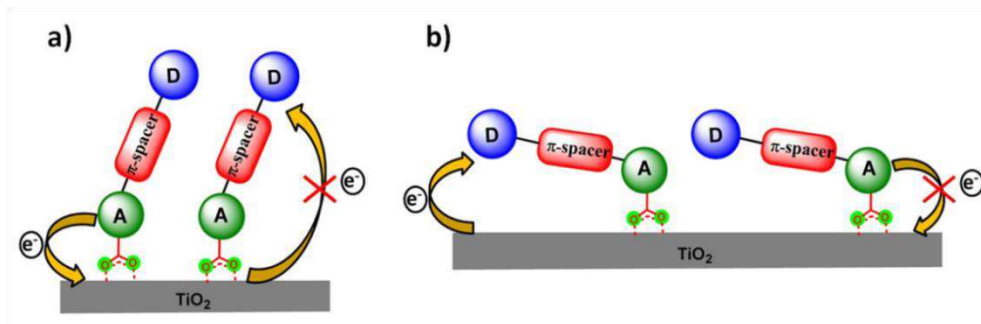


**Figure 1.** D- $\pi$ -A configuration on the TiO<sub>2</sub> surface: a) perpendicular orientation of dyes, b) tilt orientation of dyes.

In D- $\pi$ -A-A systems, planarizing conjugated spacer allows more efficient electronic contact between the donor and the acceptor giving better electron injection efficiency.<sup>12</sup> The  $\pi$ -spacers, such as benzene, pyrrole and thiophene, have a significant influence on the extension of  $\pi$ -conjugation and their absorption spectra, and redox properties.<sup>13,14</sup> So the different dye design have been widely employed in order to keep the planarity of  $\pi$ -spacer, for example, dyes with CPDT spacer confirms better device performance than the bithiophene spacer.<sup>15,16</sup> In BHJ organic solar cells, the dihydroxybenzene moieties forms H-bonding with SQ units and such structures show superior device performance than the

SQ dyes without H-bonding donor sites.<sup>17-19</sup> To our knowledge for the DSSCs such planarizing the donor units with dihydroxybenzene moiety has not been reported yet. In continuation to previous work with Heterotriangulene Based Unsymmetrical Squaraine Dyes (Chapter-II) and Heterotriangulene Based Unsymmetrical Hemicyanine Dyes (Chapter-III), in this chapter, incorporated the hetrotriangulene (HT) donor unit with dihydroxybenzene moiety to maintain the planarity of the dyes. This can help to improve the light harvesting ability and also to widen and intensify the absorption via insertion of  $\pi$ -conjugated spacer. In previous studies, it is found that the HT-based unsymmetrical squaraine sensitizers integrated with planar structures of donor (HT) influence the position of  $\lambda_{\max}$  and shows high  $\epsilon$ . Most significantly, the dye aggregation and charge recombination can be controlled by increasing the steric hindrance of squaraine sensitizers via control of in-plane and out-of-plane alkyl chains on acceptor units.<sup>20</sup>

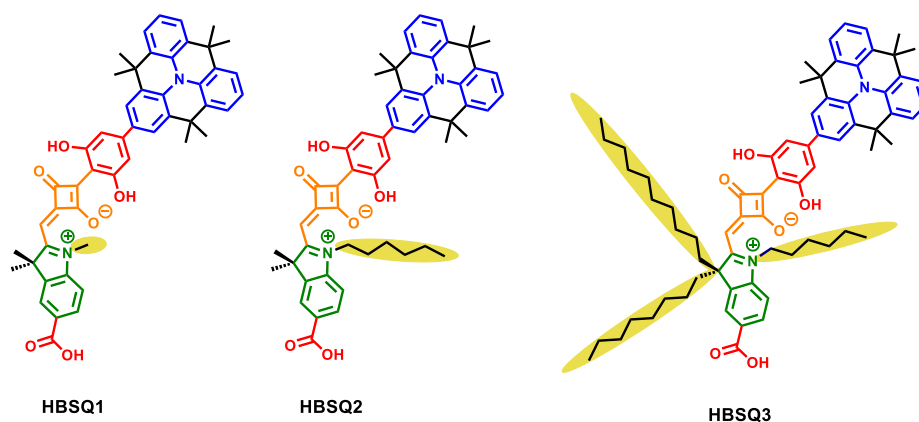


**Figure 2.** Molecular structures of **HBSQ1-3** unsymmetrical squaraine dyes.

For that reason, executed the molecular engineering of the HT-based squaraine sensitizers by introducing dihydroxybenzene units and in-plane, and out-of-plane alkyl chains on indolium unit having a carboxylic acid used as an anchoring group, thus giving target sensitizers of **HBSQ1-3** (**Figure 2**). In this present work, judiciously incorporated the HT donor unit with dihydroxybenzene  $\pi$ -spacer to create D- $\pi$ -A-A configuration. This dihydroxybenzene can make the hydrogen bonding with squaric acid unit (acceptor) to make the planar spacer. Furthermore, the long and branched alkyl groups in the N- and  $sp^3$ -C atoms of indolium unit is to increase the solubility, decrease the undesirable dye aggregation and suppress unfavourable charge recombination on the  $TiO_2$  surface.<sup>21</sup>

## 4.2 EXPERIMENTAL SECTION

### 4.2.1 Materials and Characterization

All reagents were purchased from commercial sources. Solvents were dried and distilled immediately prior to use by standard procedures. All reactions were carried out under an argon atmosphere.  $^1\text{H}$  NMR and  $^{13}\text{C}$  NMRs were recorded in  $\text{CDCl}_3$  and  $\text{DMSO}-d_6$  on 200 MHz, 400 MHz and 500 MHz NMR spectrometers. High-resolution mass spectrometric measurements were carried out using the ESI method and an ion-trap mass analyzer. Absorption spectra were recorded at room temperature in quartz cuvette using Analytik Jena UV-Visible spectrophotometer. Electrochemical measurement was carried out using a Bio-Logic potentiostat (model no: SP300). The cyclic voltammetric analysis (CV) was carried out in dry  $\text{CH}_2\text{Cl}_2$  solvent by using 0.1 M tetrabutylammonium perchlorate as supporting electrolyte and  $\text{Fc}/\text{Fc}^+$  as external reference. The experiments were performed at room temperature in nitrogen atmosphere with a three-electrode cell consisting of a platinum foil as counter electrode, non-aqueous  $\text{Ag}/\text{Ag}^+$  reference electrode, and a platinum wire as working electrode.

### 4.2.2 Device fabrication and characterization

FTO (F-doped  $\text{SnO}_2$  glass; 6 - 8  $\Omega$  /sq; Pilkington TEC 7) was cleaned by mucasol (2 % in water), deionized water, and ethanol, successively. To grow a  $\text{TiO}_2$  under layer, the substrate was immersed in freshly prepared 50 mM  $\text{TiCl}_4$  aqueous solution at 70  $^\circ\text{C}$  for 30 min, and washed with deionized water before drying at 100  $^\circ\text{C}$  for 10 min. A paste of  $\text{TiO}_2$  nanocrystal (< 20 nm, Ti-Nanoxide T/SP, Solaronix) was deposited by the doctor-blade technique on  $\text{TiO}_2$  buffer layer coated FTO substrate, kept in air for 5 min and then annealed at 125  $^\circ\text{C}$  in air for 15 min. The films were about 6 - 8  $\mu\text{m}$  thick. The annealed films were coated with scattering layer  $\text{TiO}_2$  paste (WER2-O, Dyesol) and annealed at 125  $^\circ\text{C}$  in air for 15 min. The annealed films were sintered at 325  $^\circ\text{C}$  for 5 min, 375  $^\circ\text{C}$  for 5 min, 450  $^\circ\text{C}$  for 15 min and 500  $^\circ\text{C}$  for 15 min with heating rate of 5  $^\circ\text{C}$  per min in air. After reaching the furnace temperature of 50  $^\circ\text{C}$ , sintered films were immersed in freshly prepared 50 mM aqueous  $\text{TiCl}_4$  solution at 70  $^\circ\text{C}$  for 30 min. After sintering the

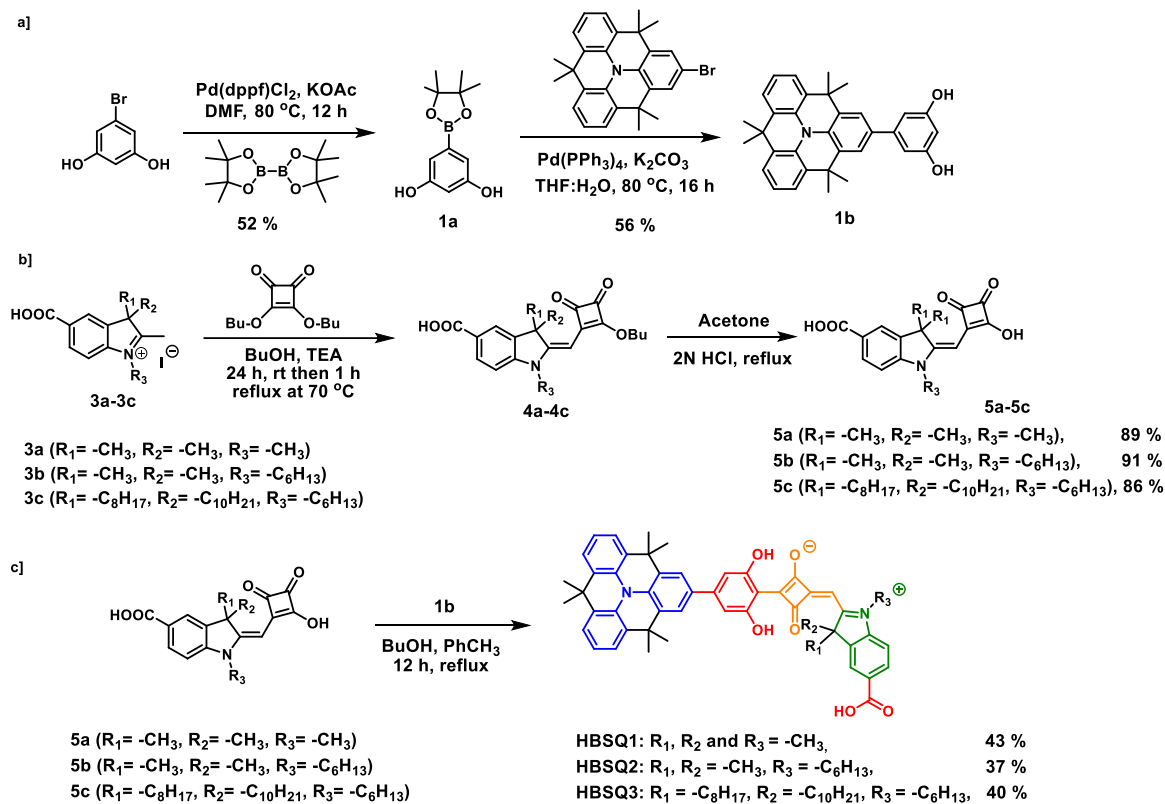
TiCl<sub>4</sub>-treated TiO<sub>2</sub> films at 500 °C for 30 min, they were immediately immersed in 0.1 mM HBSQ dye solution in CH<sub>2</sub>Cl<sub>2</sub> for 12 h, washed and dried. In case of CDCA added experiments, different ratios of CDCA added to 0.1 mM dye solution and photoanode dipped for 12 h. Sandwich type cell configuration was completed using platinum as cathode, 0.5 M LiI, 0.05 M I<sub>2</sub> in CH<sub>3</sub>CN was used as electrolyte and 25 μm spacer. *I-V* characteristics of the cells were measured using Keithley digital source meter (2420, Keithley, USA) controlled by a computer and standard AM 1.5G solar simulator (PET, CT200AAA, USA). To measure the photocurrent and voltage, an external bias of AM 1.5G light was applied using a xenon lamp (450 W, USHIO INC, Philippines) and recorded. IPCE measurements were carried out with a Newport QE measurement kit by focusing a monochromatic beam of light from 300 W Xe lamp onto the devices. The electrochemical impedance spectroscopy (EIS) measurements of the DSSCs were recorded with a Bio-Logic potentiostat (model no: SP300), equipped with an FRA2 module, with different potentials applied in dark. The frequency range explored was 25 mHz to 1 MHz with an ac perturbation of 10 mV. The impedance spectra were analyzed using an equivalent circuit model.

#### 4.2.3 Dye desorption from the photoanode

The TiO<sub>2</sub> coated FTO electrodes (0.24 cm<sup>2</sup>) were dipped in 0.1 mM solution of **HBSQ1-3** dyes in CH<sub>2</sub>Cl<sub>2</sub> for 12 h at room temperature, and then washed with CH<sub>2</sub>Cl<sub>2</sub> to remove the physisorbed dyes. The electrodes were immersed in 2 M ethanolic HCl for 10 min until all the dyes completely desorbed and the amount of adsorbed dye is calculated by UV-Vis absorption study.



## 4.3 SYNTHETIC PROCEDURE AND CHARACTERIZATION DATA



**Scheme 1.** Synthesis of (a) HT donor and  $\pi$ -spacer unit, (b) Semisquaraine units (5a–5c) and (c) **HBSQ1-3** dyes.

## 4.3.1 Synthesis of 1a and 1b

5-(4,4,5,5-Tetramethyl-1,3,2-dioxaborolan-2-yl)benzene-1,3-diol (**1a**)

5-Bromobenzene-1,3-diol<sup>22</sup> (1.5 g, 7.94 mmol), bis(pinacolato)diboron (2.42 g, 9.53 mmol) and potassium acetate (2.34 g, 23.82 mmol) were added into dry DMF (15 mL). The reaction mixture was degassed for 15 min then Pd(dppf)Cl<sub>2</sub>·CH<sub>2</sub>Cl<sub>2</sub> (0.65 g, 0.79 mmol) was added and refluxed for 12 h at 80 °C. The reaction mixture extracted with ethyl acetate, washed with water and dried over Na<sub>2</sub>SO<sub>4</sub>. The organic layer was removed under reduced pressure and the residue was purified by column chromatography on silica with ethyl acetate/pet ether as eluent to afford **1a** (0.98 g, 52 %). <sup>1</sup>H NMR (400 MHz, DMSO-*d*<sub>6</sub>)  $\delta$ : 9.15 (s, 2 H) 6.53 (d,  $J = 1.83$  Hz, 2 H) 6.28 (t, 1 H) 1.26 (s, 12 H). <sup>13</sup>C NMR (100 MHz, DMSO-*d*<sub>6</sub>)

$\delta$ : 158.0, 112.0, 105.6, 83.4, 24.7. HRMS (ESI):  $m/z$  Calcd for  $C_{12}H_{18}O_4B$   $[M + H]^+$ : 237.1293. Found: 237.1285.

**5-(4,4,8,8,12,12-Hexamethyl-8,12-dihydro-4H-benzo[9,1]quinolizino[3,4,5,6,7-defg]acridin-2-yl)benzene-1,3-diol (1b):**

2-Bromo-4,4,8,8,12,12-hexamethyl-8,12-dihydro-4H-benzo[9,1]quinolizino[3,4,5,6,7-defg]acridine-2-carbaldehyde (0.5 g, 1.13 mmol), **1a** (0.4 g, 1.70 mmol), potassium carbonate (6.3 g, 45.2 mmol) and  $Pd(PPh_3)_4$  (67 mg, 0.057 mmol) were added into THF:H<sub>2</sub>O (20:5 mL), and refluxed for 16 h at 80 °C. The reaction mixture extracted with ethyl acetate and dried over Na<sub>2</sub>SO<sub>4</sub>. The organic layer was removed under reduced pressure and the residue was purified by column chromatography on silica with ethyl acetate/pet ether as eluent to afford 5-(4,4,8,8,12,12-Hexamethyl-8,12-dihydro-4H-benzo[9,1]quinolizino[3,4,5,6,7-defg]acridin-2-yl)benzene-1,3-diol, **1b** (300 mg, 56 %). <sup>1</sup>H NMR (400 MHz, CDCl<sub>3</sub>)  $\delta$ : 7.55 (s, 2H), 7.39 (d,  $J = 7.02$  Hz, 4H), 7.14 (t,  $J = 7.02$  Hz, 2H), 6.72 (s, 2H), 6.36 (br. s., 1H), 1.67 (s, 12H), 1.64 (s, 6H). <sup>13</sup>C NMR (100 MHz, CDCl<sub>3</sub>)  $\delta$ : 157.2, 144.1, 131.8, 130.3, 130.0, 129.8, 123.7, 123.7, 123.1, 122.2, 106.5, 101.4, 35.8, 35.6, 33.3. HRMS (ESI):  $m/z$  Calcd for  $C_{33}H_{31}NO_2$   $[M]^+$ : 473.2349. Found: 473.2351.

### 4.3.2 Synthesis of 4a-c

**(E)-2-((2-Butoxy-3,4-dioxocyclobut-1-en-1-yl)methylene)-1,3,3-trimethylindoline -5-carboxylic acid (4a)**

In a 50 mL round bottom flask, Compounds **3a** (1 g, 2.89 mmol) and 3,4-Dibutoxy-3-cyclobutene-1,2-dione (0.79 g, 3.47 mmol, 1.2 equiv) were dissolved in butanol (15 mL). Then dry triethylamine (2 mL) was added and stirred for 24 hrs at room temperature, then refluxed at 70 °C for 1 h. The solvent was removed under reduced pressure and the crude product was purified by column chromatography (silica gel) with ethyl acetate/pet ether as eluent to afford **4a** (0.72 g, 67 %). <sup>1</sup>H NMR (400 MHz, CDCl<sub>3</sub>)  $\delta$ : 8.01 - 8.18 (m, 1H), 7.98 (s, 1H), 6.91 (d,  $J = 8.31$  Hz, 1H), 5.46 (s, 1H), 4.87 (t,  $J = 6.60$  Hz, 2H), 3.40 (s, 3H), 1.78 - 1.94 (m, 2H), 1.65 (s, 6H), 1.47 - 1.55 (m, 2H), 1.01 (t,  $J = 7.46$  Hz, 3H). <sup>13</sup>C NMR

(100 MHz, CDCl<sub>3</sub>)  $\delta$ : 192.4, 189.2, 188.9, 173.5, 171.6, 168.2, 147.9, 140.9, 131.6, 124.0, 123.2, 107.6, 83.6, 74.3, 47.3, 32.2, 30.3, 27.2, 18.8, 13.8. HRMS (ESI):  $m/z$  Calcd for C<sub>21</sub>H<sub>23</sub>NO<sub>5</sub>Na [M + Na]<sup>+</sup>: 392.1468. Found: 392.1465.

**(E)-2-((2-Butoxy-3,4-dioxocyclobut-1-en-1-yl)methylene)-1-hexyl-3,3-dimethylindoline-5-carboxylic acid (4b)**

In a 50 ml round bottom flask, Compounds **3b** (1 g, 2.4 mmol) and 3,4-Dibutoxy-3-cyclobutene-1,2-dione (0.65 g, 2.88 mmol, 1.2 equiv) were dissolved in butanol (15 mL). Then dry triethylamine (2 mL) was added and stirred for 24 hrs at room temperature, then refluxed at 70 °C for 1 h. The solvent was removed under reduced pressure and the crude product was purified by column chromatography (silica gel) with ethyl acetate/pet ether as eluent to afford **4b** (0.85 g, 81 %). <sup>1</sup>H NMR (200 MHz, DMSO-*d*<sub>6</sub>)  $\delta$ : 12.66 (br. s., 1H), 7.82 - 8.01 (m, 2H), 7.23 (d, *J* = 8.34 Hz, 1H), 5.43 (s, 1H), 4.79 (t, *J* = 6.44 Hz, 2H), 3.91 (t, *J* = 6.06 Hz, 2H), 1.68 - 1.87 (m, 2H), 1.55 (s, 6H), 1.18 - 1.46 (m, 10H), 0.78 - 1.00 (m, 6H). <sup>13</sup>C NMR (100 MHz, DMSO-*d*<sub>6</sub>)  $\delta$ : 192.3, 180.7, 173.7, 167.3, 146.8, 145.8, 135.4, 130.2, 124.5, 123.6, 108.4, 108.2, 83.1, 46.5, 43.3, 30.9, 30.8, 26.8, 26.7, 25.7, 24.0, 22.0, 22.0, 13.8. HRMS (ESI):  $m/z$  Calcd for C<sub>26</sub>H<sub>32</sub>NO<sub>5</sub> [M - H]<sup>+</sup>: 438.2275.4936. Found: 438.2295.

**(E)-2-((2-Butoxy-3,4-dioxocyclobut-1-en-1-yl)methylene)-3-decyl-1-hexyl-3-octylindoline-5-carboxylic acid (4c)**

In a 50 mL round bottom flask, Compounds **3c** (1 g, 1.56 mmol) and 3,4-Dibutoxy-3-cyclobutene-1,2-dione (0.42 g, 1.88 mmol, 1.2 equiv) were dissolved in butanol (15 mL). Then dry triethylamine (2 mL) was added and stirred for 24 hrs at room temperature, then refluxed at 70 °C for 1 h. The solvent was removed under reduced pressure and the crude product was purified by column chromatography (silica gel) with ethyl acetate/pet ether as eluent to afford **4c** (0.52 g, 50 %). <sup>1</sup>H NMR (200 MHz, CDCl<sub>3</sub>)  $\delta$ : 8.09 (d, *J* = 7.96 Hz, 1H), 7.89 (s, 1H), 6.87 (d, *J* = 7.96 Hz, 1H), 5.59 (s, 1H), 4.88 (t, *J* = 6.57 Hz, 2H), 4.69 - 4.76 (m, 2H), 3.68 - 3.78 (m, 2H), 3.40 - 3.50 (m, 2H), 1.72 - 1.90 (m, 6H), 1.40 - 1.61 (m, 4H), 1.01 - 1.19 (m, 30H), 0.81 - 0.93 (m, 12H). <sup>13</sup>C NMR (100 MHz, CDCl<sub>3</sub>)  $\delta$ :

192.7, 188.6, 188.3, 173.4, 173.1, 165.5, 149.4, 138.7, 136.9, 128.7, 123.3, 122.3, 120.0, 113.9, 110.0, 107.5, 83.7, 74.2, 73.5, 56.7, 44.2, 44.0, 43.3, 39.8, 32.2, 32.2, 32.1, 32.0, 31.9, 31.6, 31.3, 29.9, 29.8, 29.7, 29.7, 29.6, 29.4, 29.4, 29.4, 29.3, 26.2, 24.2, 24.1, 22.8, 14.2, 13.8. HRMS (ESI):  $m/z$  Calcd for  $C_{42}H_{65}NO_5$   $[M + H]^+$ : 664.4936. Found: 664.4919.

### 4.3.3 General Procedure for the synthesis of 5a-c

In a 50 ml round bottom flask, Compounds **4a-c** and (1 mmol) were dissolved in acetone (15 mL). Then 2N HCl (2 mL) was added and refluxed for 8 h. The solvent was removed under reduced pressure to afford **5a-c** and the product was used without any further purification.

**(E)-2-((2-Hydroxy-3,4-dioxocyclobut-1-en-1-yl)methylene)-1,3,3-trimethylindoline-5-carboxylic acid (5a)**: Yield: 0.28 g (89 %).  $^1H$  NMR (500 MHz,  $DMSO-d_6$ )  $\delta$ : 7.81-7.93 (m, 2H), 7.16 (d,  $J = 8.77$  Hz, 1H), 5.53 (s, 1H), 3.36 (s, 3H), 1.57 (s, 6H).  $^{13}C$  NMR (100 MHz,  $DMSO-d_6$ )  $\delta$ : 192.6, 174.0, 167.3, 165.4, 147.3, 140.1, 130.3, 123.6, 122.8, 107.9, 83.5, 46.3, 29.8, 26.7. HRMS (ESI):  $m/z$  Calcd for  $C_{17}H_{16}NO_5$   $[M + H]^+$ : 314.1023. Found: 314.1012.

**(E)-1-Hexyl-2-((2-hydroxy-3,4-dioxocyclobut-1-en-1-yl)methylene)-3,3-dimethylindoline-5-carboxylic acid (5b)**: Yield: 0.35 g, 91 %.  $^1H$  NMR (400 MHz,  $DMSO-d_6$ )  $\delta$ : 7.88 (s, 1H), 7.86 (d,  $J = 1.47$  Hz, 1H), 7.15 (d,  $J = 8.80$  Hz, 1H), 5.63 (s, 1H), 3.87 (t,  $J = 7.21$  Hz, 2H), 1.59 - 1.66 (m, 2H), 1.56 (s, 7H), 1.29 - 1.38 (m, 6H), 0.80 - 0.86 (m, 4H).  $^{13}C$  NMR (100 MHz,  $DMSO-d_6$ )  $\delta$ : 192.4, 173.9, 167.2, 164.6, 146.8, 140.1, 130.3, 123.7, 122.9, 108.0, 83.3, 46.4, 42.2, 30.9, 26.8, 25.8, 25.8, 22.0, 13.8. HRMS (ESI):  $m/z$  Calcd for  $C_{22}H_{26}NO_5$   $[M + H]^+$ : 384.1805. Found: 384.1798.

**(E)-3-Decyl-1-hexyl-2-((2-hydroxy-3,4-dioxocyclobut-1-en-1-yl)methylene)-3-octylindoline-5-carboxylic acid (5c)**: Yield: 0.52 g, 86 %.  $^1H$  NMR (200 MHz,  $DMSO-d_6$ )  $\delta$ : 12.35 (br. s., 1H), 7.77 (d,  $J = 8.21$  Hz, 1H), 7.57 - 7.65 (m, 1H), 6.86 (d,  $J = 8.46$  Hz, 1H), 5.60 (s, 1H), 3.76 (t,  $J = 6.19$  Hz, 2H), 2.77 (t,  $J = 11.24$  Hz, 2H), 1.53 - 1.73 (m, 4H), 0.96 - 1.23 (m, 32H), 0.76 - 0.85 (m, 9H), 0.43 (br.

s., 2H).  $^{13}\text{C}$  NMR (100 MHz,  $\text{DMSO-}d_6$ )  $\delta$ : 195.4, 178.1, 167.8, 154.0, 150.2, 136.2, 130.4, 122.5, 105.9, 87.0, 54.3, 41.8, 31.4, 31.3, 29.1, 29.0, 28.8, 28.7, 28.6, 28.5, 26.3, 26.2, 23.8, 22.2, 22.2, 22.2, 14.1, 14.0, 14.0. HRMS (ESI):  $m/z$  Calcd for  $\text{C}_{38}\text{H}_{58}\text{NO}_5$   $[\text{M} + \text{H}]^+$ : 608.4310. Found: 608.4291.

#### 4.3.4 General Procedure for the synthesis of HBSQ1-3

5-(4,4,8,8,12,12-Hexamethyl-8,12-dihydro-4H-benzo[9,1]quinolizino[3,4,5,6,7-defg]acridin-2-yl)benzene-1,3-diol, **1b** (100 mg, 0.21 mmol) and compound **5a-5c** (1.1 eq.) were added into toluene (10 mL) and 1-butanol (3 mL) into a 50 mL round bottom flask and refluxed with a Dean–Stark apparatus for 12 h. Then solvent was removed under reduced pressure and the residue was purified by column chromatography on silica with methanol/dichloromethane as eluent to afford **HBSQ1-HBSQ3** as a blue solid.

**HBSQ1**: Yield: 70 mg, 43 %.  $^1\text{H}$  NMR (400 MHz,  $\text{DMSO-}d_6$ )  $\delta$ : 11.89 (br. s., 2H), 8.27 (s, 1H), 8.11 (d,  $J = 7.93$  Hz, 1H), 7.85 (d,  $J = 7.93$  Hz, 1H), 7.72 (s, 2H), 7.41 - 7.48 (m, 4H), 7.12 - 7.21 (m, 2H), 6.75 (s, 2H), 6.24 (s, 1H), 3.96 (s, 3H), 1.76 (br. s., 6H), 1.64 (br. s., 12H), 1.58 (br. s., 6H).  $^{13}\text{C}$  NMR (100 MHz,  $\text{DMSO-}d_6$ )  $\delta$ : 184.0, 180.8, 179.5, 173.2, 166.7, 163.2, 159.9, 147.1, 145.3, 143.2, 130.6, 129.9, 129.6, 123.9, 123.5, 121.9, 113.8, 107.3, 105.8, 92.1, 52.0, 51.2, 35.3, 35.1, 33.3, 33.0, 28.6, 24.7, 23.9. HRMS (ESI):  $m/z$  Calcd for  $\text{C}_{50}\text{H}_{45}\text{N}_2\text{O}_6$   $[\text{M} + \text{H}]^+$ : 769.3272. Found: 769.3252.

**HBSQ2**: Yield: 65 mg, 37 %.  $^1\text{H}$  NMR (500 MHz,  $\text{DMSO-}d_6$ )  $\delta$ : 11.91 (s, 2H), 8.30 (s, 1H), 8.11 (d,  $J = 8.39$  Hz, 1H), 7.87 (d,  $J = 8.39$  Hz, 1H), 7.72 (s, 2H), 7.47 (t,  $J = 6.68$  Hz, 4H), 7.17 (t,  $J = 7.63$  Hz, 2H), 6.76 (s, 2H), 6.27 (s, 1H), 4.36 - 4.52 (m, 2H), 1.78 (s, 6H), 1.64 (s, 12H), 1.58 (s, 6H), 1.38 - 1.44 (m, 2H), 0.99 - 1.06 (m, 6H), 0.83 - 0.87 (m, 3H).  $^{13}\text{C}$  NMR (125 MHz,  $\text{DMSO-}d_6$ )  $\delta$ : 183.7, 180.6, 178.8, 173.7, 166.7, 164.2, 160.0, 147.4, 144.4, 143.4, 131.9, 130.6, 129.9, 129.6, 124.0, 123.9, 123.5, 122.0, 105.9, 91.6, 79.2, 74.6, 69.8, 51.2, 35.3, 35.1, 33.3, 33.0, 30.7, 27.4, 25.7, 25.0, 21.9, 13.8. HRMS (ESI):  $m/z$  Calcd for  $\text{C}_{55}\text{H}_{55}\text{N}_2\text{O}_6$   $[\text{M} + \text{H}]^+$ : 839.4055. Found: 839.4059.

**HBSQ3:** Yield: 90 mg, 40 %.  $^1\text{H}$  NMR (500 MHz, DMSO- $d_6$ )  $\delta$ : 11.92 (s, 2 H), 8.20 (s, 1 H), 8.12 (s, 1 H), 7.87 (d,  $J=8.4$  Hz, 1 H), 7.72 (s, 2 H), 7.44 - 7.51 (m, 4 H), 7.17 (t,  $J=7.6$  Hz, 2 H), 6.76 (s, 2 H), 6.36 (s, 1 H), 4.55 (br. s., 2 H), 2.81 - 2.95 (m, 2 H), 2.16 - 2.27 (m, 2 H), 1.75 - 1.82 (m, 2 H), 1.63 (s, 12 H), 1.58 (s, 6 H), 1.35 - 1.41 (m, 2 H), 1.24 (dd,  $J=13.9, 6.3$  Hz, 4 H), 1.10 (dd,  $J=12.4, 6.7$  Hz, 7 H), 1.03 (br. s., 16 H), 0.82 (t,  $J=7.1$  Hz, 4 H), 0.68 - 0.74 (m, 6 H), 0.62 (br. s., 2 H), 0.38 - 0.44 (m, 2 H).  $^{13}\text{C}$  NMR (125 MHz, DMSO- $d_6$ )  $\delta$ : 183.7, 180.5, 177.5, 173.5, 160.2, 147.6, 139.8, 132.6, 131.9, 130.5, 129.8, 129.6, 124.0, 123.9, 123.6, 123.5, 121.9, 113.3, 107.5, 105.8, 91.9, 60.5, 45.4, 38.0, 35.3, 35.1, 33.3, 33.0, 31.3, 31.3, 30.8, 29.2, 28.8, 28.4, 28.3, 28.1, 27.9, 27.8, 25.9, 22.7, 22.4, 22.0, 21.9, 13.9, 13.8, 13.7. HRMS (ESI):  $m/z$  Calcd for  $\text{C}_{71}\text{H}_{87}\text{N}_2\text{O}_6$   $[\text{M} + \text{H}]^+$ : 1063.6559. Found: 1063.6526.

## 4.4 RESULTS AND DISCUSSION

### 4.4.1 Synthesis and Characterization

The synthetic procedures for **HBSQ1-3** dye are illustrated in **Scheme 1**. The synthesis of unsymmetrical squaraine sensitizers, **HBSQ1-3**, requires 5-(4,4,8,8,12,12-hexamethyl-8,12-dihydro-4H-benzo[9,1]quinolizino[3,4,5,6,7-defg]acridin-2-yl)benzene-1,3-diol (**1b**), semi-squaraine units with either N- or  $sp^3$ -C or both atoms functionalized with alkyl groups (**5a-5c**). The **1a** derivatives were synthesized by borylation of 1-bromo-3,5-dihydroxybenzene. Suzuki coupling of 2-bromo-4,4,8,8,12,12-hexamethyl-8,12-dihydro-4H-benzo[9,1]quinolizino[3,4,5,6,7-defg]acridine<sup>16</sup> with **1a** provided compound **1b**. The corresponding semi-squaric acid (**5a-5c**) were synthesized by reacting indolium salts (**3a-3c**)<sup>20</sup> with 3,4-dibutoxy-3-cyclobutene-1,2-dione followed by acid hydrolysis of **4a-4c** derivatives. The target sensitizers of **HBSQ1-3** were obtained via a condensation reaction between compounds of **1b** and semisquaric acid (**5a-5c**). All the final compounds have good solubility in  $CH_2Cl_2$ ,  $CHCl_3$ , DMSO and limited solubility in  $CH_3CN$  and EtOH. All the intermediates and final dyes were confirmed by  $^1H$ - and  $^{13}C$ -NMR spectroscopy and mass spectrometry (ESI-MS).

**Figure 3** shows the labeled  $^1H$  NMR spectrum of **HBSQ2** as a representative spectrum. This compound shows singlet (**a'**) at 1.58 ppm (6 H) and another singlet (**a**) at 1.64 ppm (12 H) which correspond to 18 protons of bridged methyl groups. The singlet (**b**) at 1.78 ppm corresponds to 2 methyl groups attached to  $sp^3$ -C atom of indolium group. The  $-CH_2$  group which is connected to N-atom of indolium units shows multiplet (**c**) at 4.36-4.52 ppm. The peak at 6.28 ppm corresponds to  $=CH-$  protons shows singlet (**d**). The two aromatic protons of benzene ring shows singlet (**e**) at 6.76 ppm, whereas the two  $-OH$  protons of connected to benzene ring shows singlet (**f**) at 11.91 ppm.

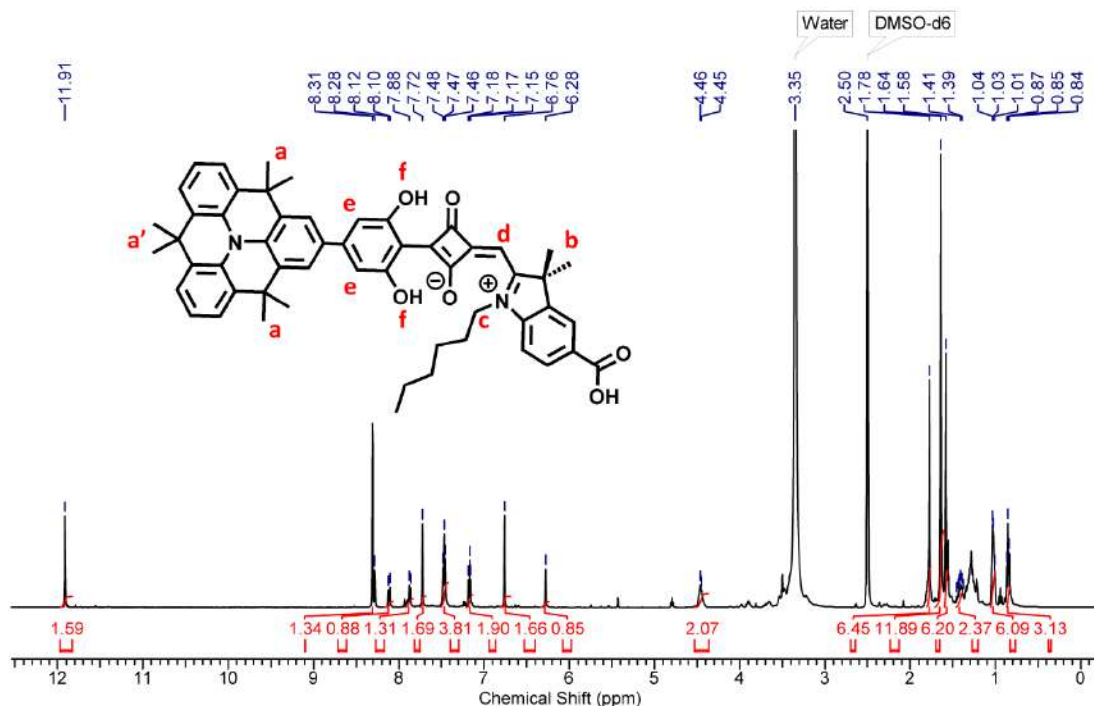


**Figure 3.**  $^1\text{H}$  NMR (500 MHz,  $\text{DMSO}-d_6$ ) spectrum of compound **HBSQ2**.

#### 4.4.2 Photophysical Properties

The UV-Vis absorption spectra of **HBSQ1-3** dyes in  $\text{CH}_2\text{Cl}_2$  solution, on transparent mesoporous  $\text{TiO}_2$  film, and the emission properties are presented in **Figure 4** and the corresponding data are provided in **Table 2**. **HBSQ1-3** showed broad absorption spectra of the sensitizer in the range of 400 to 810 nm. **HBSQ1**, **HBSQ2** and **HBSQ3** were exhibited an intense absorption band centered around 662 nm, 656 nm and 664 nm which is attributed to the ICT transition from the D moiety to the A moiety via  $\pi$ -spacer. The introduction of alkyl groups on the N- and  $\text{sp}^3\text{-C}$  atoms of the indolium unit by long and branched alkyl chains were not having any considerable influence on the position and the width of the UV absorption band. The molar absorption coefficient of the charge transfer transition absorption for **HBSQ1-3** is in the range of  $10^4 \text{ M}^{-1} \text{ cm}^{-1}$  (**Figure 4c**). Other than the ICT transition, **HBSQ1-2** shows  $\pi\text{-}\pi^*$  transition between 400-500 nm, with lower  $\epsilon$  values ( $\sim 10^3 \text{ M}^{-1} \text{ cm}^{-1}$ ).



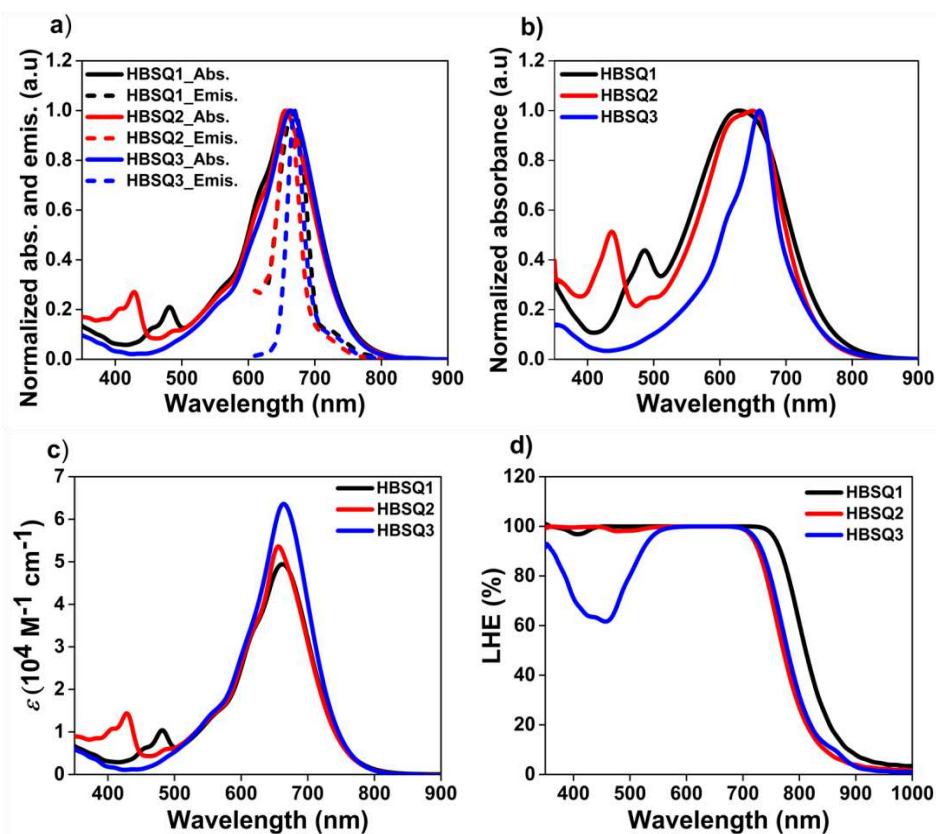


**Figure 4.** (a) Absorption and emission spectra of **HBSQ1-3** in CH<sub>2</sub>Cl<sub>2</sub>, excitation wavelength 600 nm (b) Absorption spectra of **HBSQ1-3** adsorbed on the transparent TiO<sub>2</sub> film (TiO<sub>2</sub> film thickness: 6  $\mu\text{m}$ , [Dye] = 0.1 mM in CH<sub>2</sub>Cl<sub>2</sub> and dipping time 10 min), c)  $\epsilon$  vs wavelength plot, and (d) LHE profile of **HBSQ1-3** sensitizers without co-adsorbent on transparent TiO<sub>2</sub> films of 6  $\mu\text{m}$  thickness (dipping time 12 h).

The absorption spectra of **HBSQ1-2** adsorbed on the TiO<sub>2</sub> films are broadened and slightly blue shifted compared to the solution spectra. The former is ascribed to the interaction between the dyes on the TiO<sub>2</sub> surface and also interaction of carboxylic acid groups with the surface titanium ions.<sup>23</sup> The  $\lambda_{\text{max}}$  of **HBSQ1**, **HBSQ2** and **HBSQ3** is blue shifted by 33 nm, 6 nm and 4 nm respectively, the extent of blue shift shows a more tendency to form H-type aggregation state on TiO<sub>2</sub> (**Figure 4b**).<sup>24</sup> On the other hand, **HBSQ2** and **HBSQ3** showed slightly blue shift towards higher energy compared to **HBSQ1** owing to the presence of in-plane and out-of-plane alkyl segments on indolium sp<sup>3</sup>-C atom, which effectively suppresses extent of dye aggregation on the TiO<sub>2</sub> surface. The emission  $\lambda_{\text{max}}$  are red shifted to some extent to longer wavelength and maximum

stokes shift of  $\sim 5$  nm is obtained for **HBSQ1-3** sensitizers. This result qualitatively validates the small change in dipole moments in excited state for **HBSQ1-3** in solution (**Figure 4a**). **HBSQ1-3** sensitized electrodes showed superior light-harvesting performance and exhibited light harvesting efficiency ( $LHE = 1-10^{-A}$ ) of near unity over a wide spectral region (**Figure 4d**). In the contrast, **HBSQ1-2** sensitized electrode displayed superior spectral broadening of LHE profile than **HBSQ3**. **HBSQ1-2** displayed above 90% LHE from 405 to 800 nm while **HBSQ3** illustrated LHE in the region of 455 to 760 nm. This results indicates that **HBSQ1-3** are beneficial for harvesting the NIR photons along with visible. **HBSQ1-3** dyes also displayed a negative solvatochromic shift, i.e. a hypsochromic shift of maximum wavelength ( $\lambda_{max}$ ), and showed that the ground state is more stabilized than the excited state due to solvation by more polar solvents (**Figure 5, Table 1**).

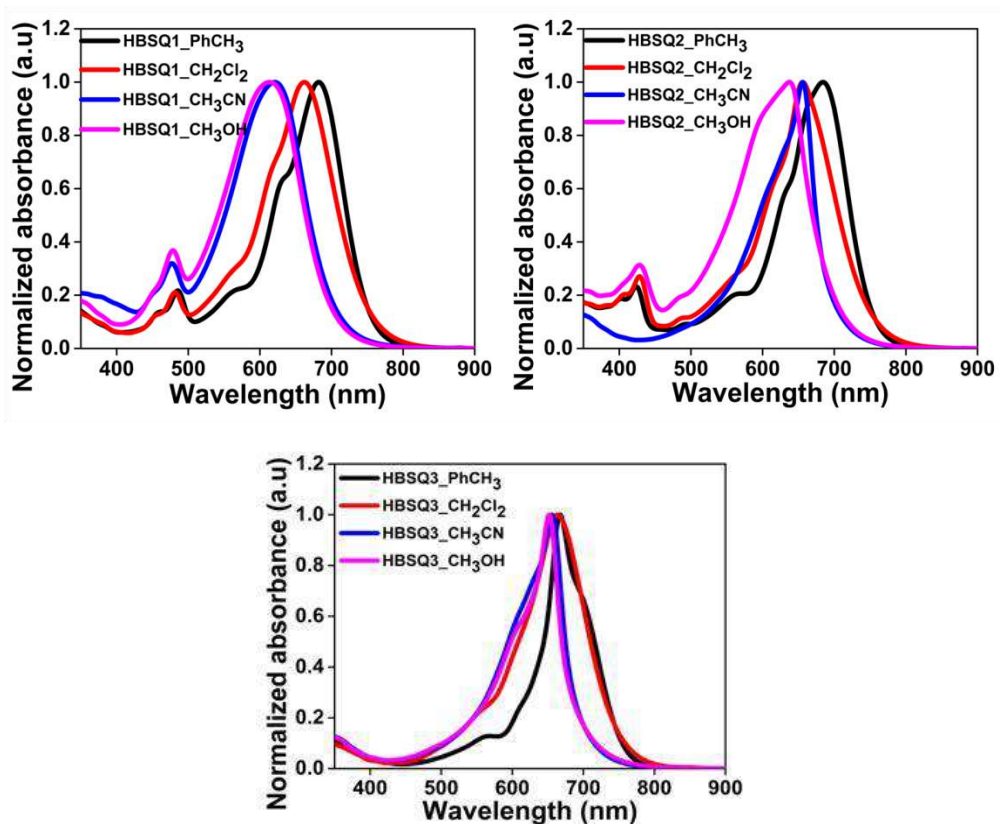


**Figure 5.** Absorption spectra of **HBSQ1-3** dyes in different solvents (PhCH<sub>3</sub>, CH<sub>2</sub>Cl<sub>2</sub>, CH<sub>3</sub>CN and MeOH).

**Table 1.** Maximum absorption wavelength ( $\lambda_{\max}$ ) in different solvents

NC Dyes	$\lambda_{\max}$ / PhCH <sub>3</sub> (nm)	$\lambda_{\max}$ / CH <sub>2</sub> Cl <sub>2</sub> (nm)	$\lambda_{\max}$ / CH <sub>3</sub> CN (nm)	$\lambda_{\max}$ / MeOH (nm)
<b>HBSQ1</b>	486, 682	481, 662	477, 621	479, 614
<b>HBSQ2</b>	424, 684	428, 656	656	429, 637
<b>HBSQ3</b>	667	664	656	662

#### 4.4.3 Electrochemical Properties

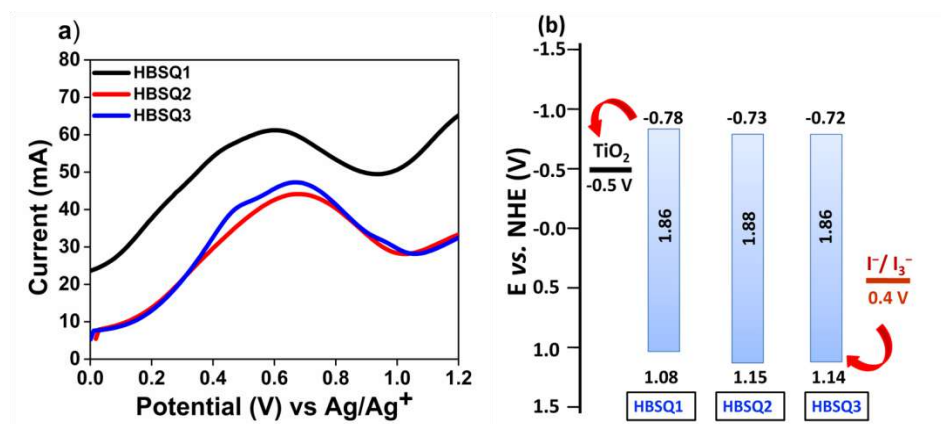


**Figure 6.** (a) Differential pulse voltammograms of **HBSQ1-3** dyes in CH<sub>2</sub>Cl<sub>2</sub> solution with scan rate of 50 mV s<sup>-1</sup> and (b) Energy level diagram for the **HBSQ1-3** dyes vs NHE.

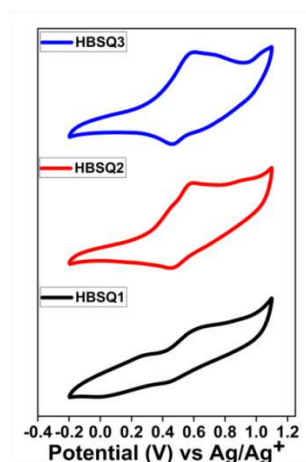


**Figure 7.** Cyclic voltammograms of **HBSQ1-3** dyes in CH<sub>2</sub>Cl<sub>2</sub> solution with scan rate of 50 mV s<sup>-1</sup>.

The electrochemical properties of the **HBSQ1-3** dyes were measured by differential pulse voltammetry (DPV, **Figure 6**) and cyclic voltammetry (CV, **Figure 7**) in CH<sub>2</sub>Cl<sub>2</sub> solution.<sup>25</sup> The redox potentials of these dyes, measured by DPV are presented in **Table 2**. The HOMO levels of three dyes were determined to be 1.08 V, 1.15 V and 1.14 V vs. NHE, respectively. These values are higher than I<sup>-</sup>/I<sub>3</sub><sup>-</sup> redox couple (0.4 V vs. NHE) and gives sufficient energy for dye regeneration. The LUMO levels of these dyes are more negative than conduction band edge ( $E_{CB}$ ) of TiO<sub>2</sub> (-0.5 V vs. NHE). In general, a minimal driving force of 0.2 V is sufficient to guarantee efficient excited-state injection and regeneration of the oxidized dye.<sup>26</sup> As a result; **HBSQ1-3** has a minimal driving force for electron injection from the excited dyes to the  $E_{CB}$  of TiO<sub>2</sub>. The strong interaction between the donor and the acceptor due to  $\pi$ -spacer extends the conjugation which has positive effect on their LUMO energy level. The dihydroxybenzene group shows a significant role in modulating the HOMO-LUMO energy levels and provides sufficient offset for electron injection from LUMO of excited dyes to  $E_{CB}$  of TiO<sub>2</sub>.

**Table 2.** Photophysical and electrochemical properties of the dyes **HBSQ1-3** at room temperature

Dyes	$\lambda_{max}/$ CH <sub>2</sub> Cl <sub>2</sub> (nm) <sup>a</sup>	$\epsilon \times 10^4$ (M <sup>-1</sup> cm <sup>-1</sup> ) <sup>b</sup>	$\lambda_{max}$ /em (nm) <sup>a</sup>	$\lambda_{max}/$ TiO <sub>2</sub> (nm) <sup>c</sup>	$E_{g/DFT}$ (eV)	$E_{HOMO}$ (V vs NHE) <sup>d</sup>	$E_{0-0}$ (eV) <sup>e</sup>	$E_{LUMO}$ (V vs NHE) <sup>f</sup>
<b>HBSQ1</b>	481,662	0.98, 4.9	668	629	2.03	1.08	1.86	-0.78
<b>HBSQ2</b>	428,656	1.5, 5.4	660	650	2.05	1.15	1.88	-0.73
<b>HBSQ3</b>	664	6.2	669	660	2.05	1.14	1.86	-0.72

<sup>a</sup>Absorption and emission spectra were recorded in CH<sub>2</sub>Cl<sub>2</sub>, <sup>b</sup>Molar extinction coefficients ( $\epsilon$ ) were measured in CH<sub>2</sub>Cl<sub>2</sub>. <sup>c</sup>On 6  $\mu$ m transparent TiO<sub>2</sub> film, dye dipping time = 10 min. <sup>d</sup>The oxidation potentials were measured by differential pulse voltammetry (DPV) in CH<sub>2</sub>Cl<sub>2</sub> with tetrabutylammonium perchlorate (TBAClO<sub>4</sub>) as supporting electrolyte, ferrocene/ferrocenium (Fc/Fc<sup>+</sup>) as an external reference and **HBSQ1-3** oxidation peak potential vs Ag/Ag<sup>+</sup> converted to NHE by addition of 0.63 V using the equation  $E_{HOMO}$  (V vs NHE) = ( $E_{p/DPV} - E_{1/2}$  vs Fc/Fc<sup>+</sup>) + 0.63] V vs NHE. <sup>e</sup>Optical energy gaps ( $E_{0-0}$ ) were deduced from the intersection of absorption and

emission spectra,  $E_{0-0}$  (eV) =  $1240/\lambda$ .  $^fE_{\text{LUMO}}$  was calculated from  $E_{\text{LUMO}}$  (V vs NHE) =  $E_{\text{HOMO}} - E_{0-0}$ .

#### 4.4.4 Theoretical Investigations

Density functional theory (DFT) and time-dependent DFT (TD-DFT) calculations at the B3LYP/6-31G (d, p) basis set using Gaussian 09 program were carried out to optimize the molecular geometries of **HBSQ1-3** dyes.<sup>27</sup> In the TDDFT calculations, solvation effects ( $\text{CH}_2\text{Cl}_2$ ) has taken into account with the PCM model implemented in Gaussian 09.<sup>28</sup>

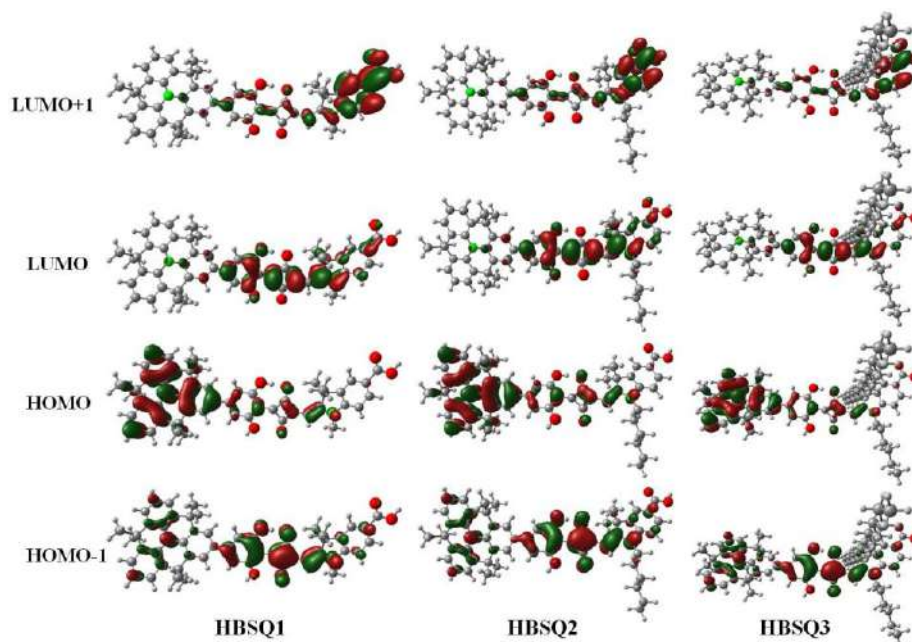


**Figure 8.** HOMO and LUMO isosurface plots for **HBSQ1-3**.

The HOMOs and LUMOs of **HBSQ1-3** were estimated from the optimized ground-state geometries, the isosurface plots for HOMO-1, HOMO, LUMO, and LUMO+1 are presented in **Figure 8**. In the parent squaraine, both HOMO and LUMO are located on SQ units while in **HBSQ** dyes the electron density of HOMO orbital is strongly localized over the donor part while the LUMO orbital is mainly delocalized at the  $\pi$ -spacer, squaraine unit and the indolium unit containing electron withdrawing carboxylic acid. It is found that **HBSQ** dyes are having D- $\pi$ -A-A dye configuration which facilitate efficient directional electron transfer from the HT donor unit to the anchoring group. The calculation also shows that the

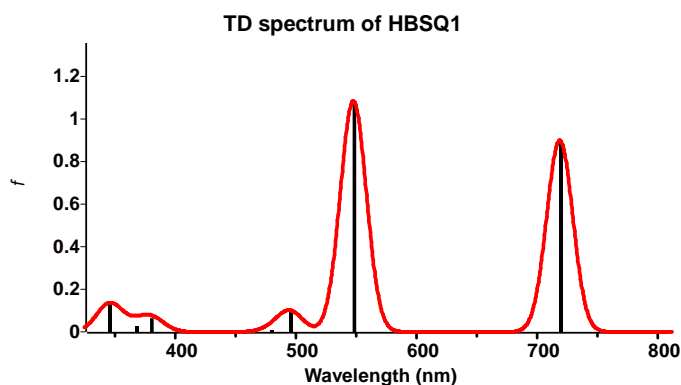
HOMO-1 was more delocalized on the donor part and also well distributed throughout squaric acid. The LUMO+1 of **HBSQ** dyes are mainly localized within the acceptors. The electron density on the anchoring group shows that the efficient excitation from the HOMO to the LUMO or LUMO+1 levels.<sup>29</sup> This can move the electron distribution from the donor unit to the acceptor anchoring moiety which is helpful for the injection of electrons into the CB of TiO<sub>2</sub>.

TD-DFT study showed the lowest transition of charge transfer character from donor to the acceptor, which is beneficial for the charge injection into the CB of TiO<sub>2</sub>. As a result, the transitions from HOMO to LUMO can contribute to an efficient electron injection. TD-DFT excited state calculations provides two transitions with large oscillator strengths (*f*), accordant with the absorption spectrum as shown in **Figure 9** and **Table 3**.

**Table 3.** Calculated maximum absorption wavelengths  $\lambda_{\max}/\text{nm}$ , corresponding vertical excitation energies  $E_{\text{ex}}$  (eV), and oscillator strengths (*f*) by TD-B3LYP/6-311G (d, p)

Dye	$\lambda_{\max}/\text{CH}_2\text{Cl}_2$ (nm) <sup>a</sup>	$\lambda_{\max}/\text{nm}$ (TDDFT)	$E_{\text{ex}}$ (eV)	<i>f</i>
<b>HBSQ1</b>	481, 662	554, 722	2.24, 1.71	1.04, 0.94
<b>HBSQ2</b>	428, 656	554, 720	2.24, 1.72	1.04, 0.95
<b>HBSQ3</b>	664	554, 7.19	2.23, 1.72	0.98, 0.93

<sup>a</sup>Absorption were measured in CH<sub>2</sub>Cl<sub>2</sub>.



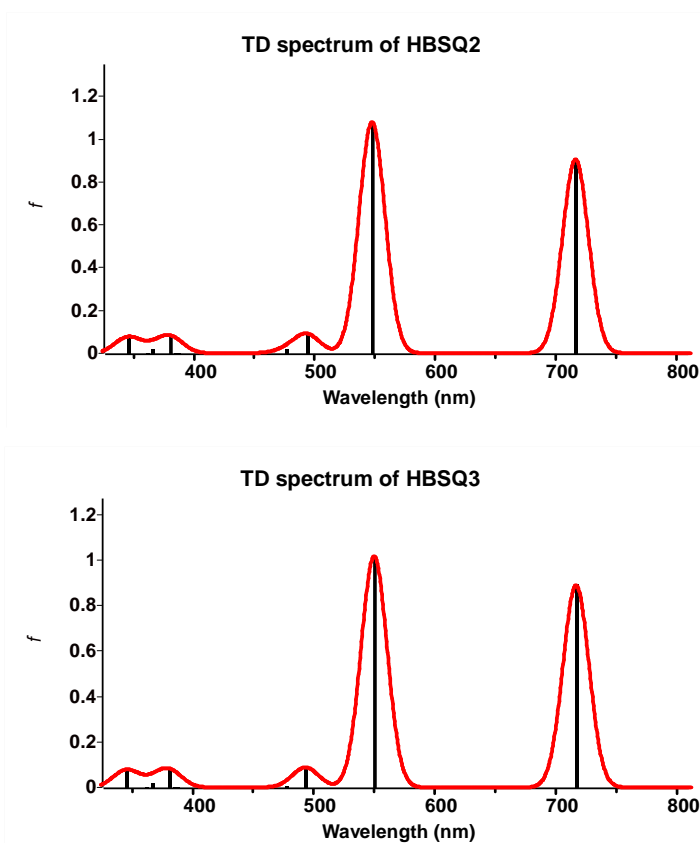


**Figure 9.** Simulated absorption spectrum of **HBSQ1-3** by TD-DFT calculation using B3LYP/6-31G (d, p) basis set.

It is observed that the HOMO-LUMO transition with transition energy 1.71 eV (722 nm) with  $f = 0.94$  and a combined transition: HOMO-1 to LUMO and HOMO to LUMO+1 with 2.24 eV (554 nm) and  $f = 1.04$ .<sup>30</sup> The calculated oscillator strength is large in all the dyes and hence the LHE. The calculated lowest excitation energies ( $E_{ex}$ ) of **HBSQ1-3** dyes are also close to the experimental obtained values.<sup>31</sup> **HBSQ1-3** was giving the smallest HOMO-LUMO energy gaps which featured broaden light absorption window.

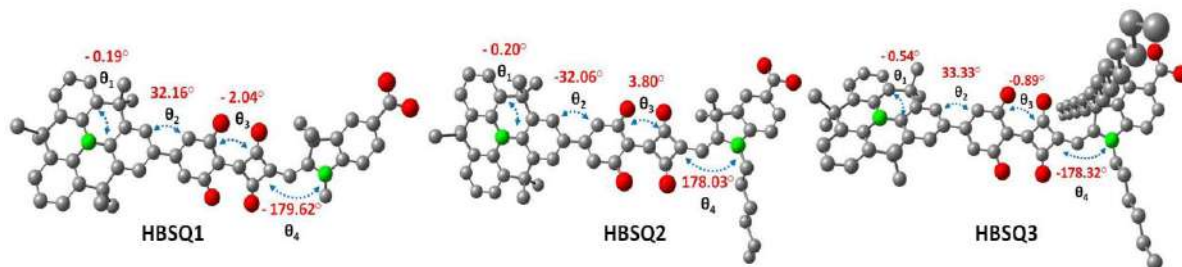




**Figure 10.** Selected dihedral angles of **HBSQ1-3** calculated from the optimized ground state geometry using DFT at the B3LYP/6-31G (d, p) level with the Gaussian 09 program (hydrogen atoms are removed for better clarity).

As extensively known, the ICT process was mostly affected by the planarity of the dyes, whereas large dihedral angle twists the molecular structure and slow down the ICT process.<sup>32</sup> Therefore, the optimized ground-state geometries of three dyes were simulated on the basis of DFT; the calculated dihedral angles were displayed in **Figure 10**. It is observed that HT is strong and planar having dihedral angle almost close to  $0^\circ$  ( $\theta_1$ ) between phenyl ring plane and the plane of N-bonded C atoms. It is showing effective participation of all phenyl groups to the ICT process. The dihedral angle between the HT donor and the spacer was found to be  $\sim 32^\circ$  ( $\theta_2$ ), indicates the twisted confirmation between the donor and  $\pi$ -spacer. Such twisted structure can avoid the charge recombination from  $\text{TiO}_2$  to the oxidized dyes. The dihedral angle between  $\pi$ -spacer and squaraine units is  $2^\circ$  ( $\theta_3$ ). Accordingly, upon incorporation of dihydroxybenzene containing  $-\text{OH}$  groups stabilizes the squaraine unit at the squarylium core via hydrogen bonding and provides a co-planar structure. The dihedral angle between squaric acid and indolium unit ( $\theta_4$ ) was about  $178^\circ$  which helps to improve the photo-physical properties by reducing the aggregation near to the  $\text{TiO}_2$  surface as well as extends the conjugation which is favorable to electron transfer from donor- $\pi$ -spacer to acceptor moiety then injected into the conduction band of  $\text{TiO}_2$ .

#### 4.4.5 Photovoltaic Performance of DSSCs

The performance parameters for devices based on **HBSQ1-3** using the optimized CDCA/dye ratios are listed in **Table 4**, and the corresponding  $J$ - $V$  curves and IPCE plots are presented in **Figure 11** and **Figure 12**. The photovoltaic performance of devices sensitized with **HBSQ1-3** dyes were investigated under standard AM 1.5G ( $100 \text{ mW cm}^{-2}$ ) illumination. The sensitized dye cells were measured using an electrolyte with the composition of 0.5 M DMII, 0.1 M LiI, 0.1 M  $\text{I}_2$  and 10 mM TBP in  $\text{CH}_3\text{CN}$ . **HBSQ1-3** sensitized cells exhibited the moderate performance without any co-absorbents. It is known that the addition of CDCA as co-adsorbent has a positive impact on improving the open-circuit voltage ( $V_{\text{oc}}$ ) and short-circuit photocurrent density



( $J_{SC}$ ) values by avoiding the dye aggregation on the  $TiO_2$  surface. However, with the addition of 10 equivalents of CDCA, the **HBSQ1-3** sensitized cells exhibited an increase in overall  $\eta$ .<sup>33</sup> The  $J_{SC}$  and  $\eta$  of the DSSCs was obtained in the order of **HBSQ1** (14.51  $mA/cm^2$ , 5.39%) > **HBSQ2** (9.68  $mA/cm^2$ , 3.64%) > **HBSQ3** (7.95  $mA/cm^2$ , 3.01%) in presence of co-adsorbents. On the other hand, the dye loading ability decreases in the order of **HBSQ1** > **HBSQ2** > **HBSQ3** which is attributable to progressive increase of alkyl group at N- and  $sp^3$ -C atoms of indolium unit which is close to the  $TiO_2$  surface that significantly reduces the dye anchoring to the penta-coordinated Ti center (**Figure 13, Table 4**).

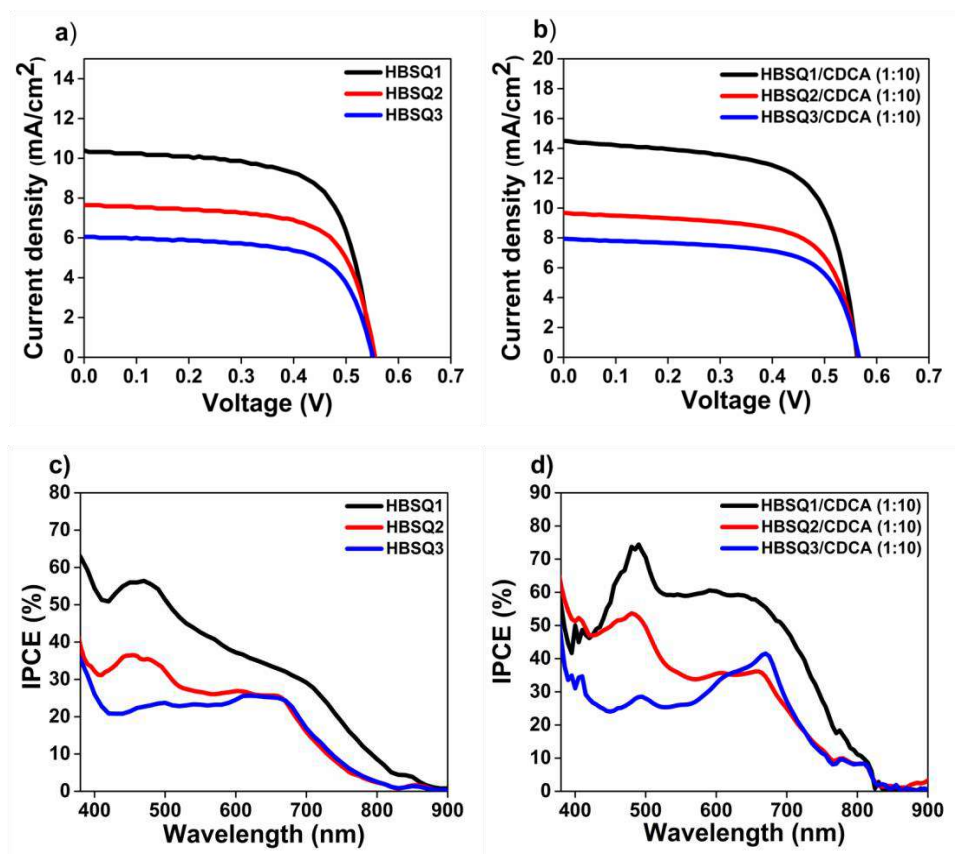


**Figure 11.**  $J$ - $V$  curves of DSSCs sensitized by **HBSQ1-3** dyes a) without CDCA, b) with 10 equivalent CDCA, and IPCE spectra of **HBSQ1-3** dyes c) without CDCA, d) with 10 equivalent CDCA.

**Table 4.** Photovoltaic parameters for **HBSQ1-3** with and without co-adsorbent<sup>a</sup>

Dyes	$J_{sc}$ (mA/cm <sup>2</sup> )	$V_{oc}$ (V)	$ff$ (%)	$\eta$ (%) <sup>a</sup>	Amount of adsorbed dyes ( $\times 10^{-7}$ mol cm <sup>-2</sup> ) <sup>b</sup>
<b>HBSQ1</b>	10.31 $\pm$ 0.07	0.551 $\pm$ 0.001	67.05 $\pm$ 0.15	3.81 $\pm$ 0.03	2.7
<b>HBSQ1/CDCA (1:10)</b>	14.11 $\pm$ 0.39	0.560 $\pm$ 0.002	66.65 $\pm$ 0.45	5.27 $\pm$ 0.12	1.22
<b>HBSQ2</b>	7.53 $\pm$ 0.11	0.545 $\pm$ 0.002	67.82 $\pm$ 0.40	2.80 $\pm$ 0.06	1.25
<b>HBSQ2/CDCA (1:10)</b>	9.59 $\pm$ 0.08	0.567 $\pm$ 0.001	67.35 $\pm$ 0.75	3.66 $\pm$ 0.02	0.64
<b>HBSQ3</b>	5.99 $\pm$ 0.06	0.555 $\pm$ 0.005	66.51 $\pm$ 0.15	2.21 $\pm$ 0.01	0.78
<b>HBSQ3/CDCA (1:10)</b>	7.89 $\pm$ 0.06	0.564 $\pm$ 0.003	67.55 $\pm$ 0.65	3.00 $\pm$ 0.01	0.20

<sup>a</sup>Photovoltaic performance of **HBSQ1-3** with a deviation of 5 cells, thickness of the electrode: 8 + 4 mm (transparent + scattering) layer of TiO<sub>2</sub>, electrolyte: 0.5 M DMII, 0.1 M LiI, 0.1 M I<sub>2</sub> and 10 mM TBP in CH<sub>3</sub>CN. Dipping time was 12 h. Active area of 0.24 cm<sup>2</sup> and measurements were carried out under 1 sun intensity (100 mW/cm<sup>2</sup>). <sup>b</sup>By the dye desorption method, carried out in 2 M ethanolic HCl at rt.

The **HBSQ1** sensitized cell showed a highest  $J_{sc}$  value of 14.51 mA cm<sup>-2</sup>,  $V_{oc}$  of 0.562 V, and  $ff$  of 66.2%, corresponding to highest  $\eta$  of 5.39%. DSSCs fabricated with **HBSQ3** achieved a  $J_{sc}$  of 7.95 mA cm<sup>-2</sup>,  $V_{oc}$  of 0.567 V,  $ff$  of 66.9% and overall  $\eta$  of 3.01% with the addition of CDCA (10 equivalent), and the curves are presented in **Figure 11**. The  $J_{sc}$  and  $V_{oc}$  of **HBSQ1-3** dyes decrease with more addition of CDCA due to competitive binding of CDCA over dyes (**Figure 12 and Table 5**). As a result the addition of a large amount of CDCA is not favorable for **HBSQ1-3** sensitized cells to improve the photovoltaic performance. These results specify that the **HBSQ1-3** showed almost comparable  $V_{oc}$  (~0.56 V) which confirm a negligible effect of co-adsorbents on  $V_{oc}$  and small improvement in the  $J_{sc}$ . It is well known that the integration of a long alkyl chains can efficiently avoid dye aggregation.<sup>34</sup> Still **HBSQ3** sensitized cells showed minor improvement in  $J_{sc}$  even upon co-adsorption and **HBSQ1** achieved the highest device performance.

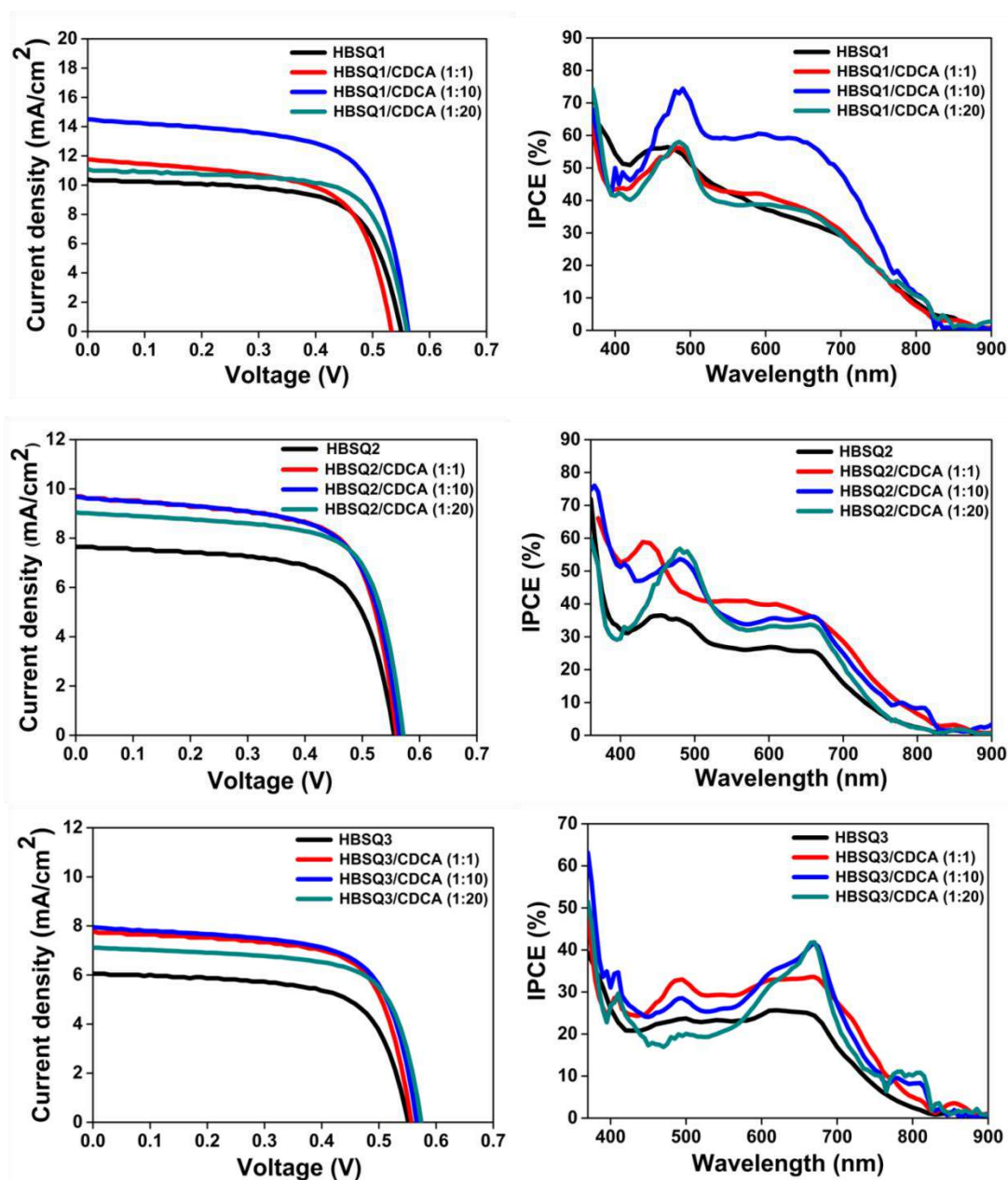


**Figure 12.** a)  $J$ - $V$  curves of DSSCs sensitized by **HBSQ1-3** dyes and b) IPCE spectra of **HBSQ1-3** dyes with different ratios of CDCA.

**Table 5.** Photovoltaic performance of **HBSQ1-3** with different ratios of CDCA

Dyes	$J_{SC}$ (mA/cm <sup>2</sup> )	$V_{OC}$ (V)	$ff$ (%)	$\eta$ (%)
<b>HBSQ1</b>	10.39	0.550	67.2	3.84
<b>HBSQ1/CDCA (1:1)</b>	11.76	0.552	64.1	4.16
<b>HBSQ1/CDCA (1:10)</b>	14.51	0.562	66.2	5.39
<b>HBSQ1/CDCA (1:20)</b>	11.08	0.560	70.0	4.34

<b>HBSQ2</b>	7.65	0.556	67.4	2.86
<b>HBSQ2/CDCA (1:1)</b>	9.70	0.560	67.6	3.67
<b>HBSQ2/CDCA (1:10)</b>	9.68	0.566	66.6	3.64
<b>HBSQ2/CDCA (1:20)</b>	9.04	0.572	69.5	3.59
<b>HBSQ3</b>	6.05	0.551	66.7	2.22
<b>HBSQ3/CDCA (1:1)</b>	7.78	0.559	68.3	2.97
<b>HBSQ3/CDCA (1:10)</b>	7.95	0.567	66.9	3.01
<b>HBSQ3/CDCA (1:20)</b>	7.12	0.575	69.4	2.83

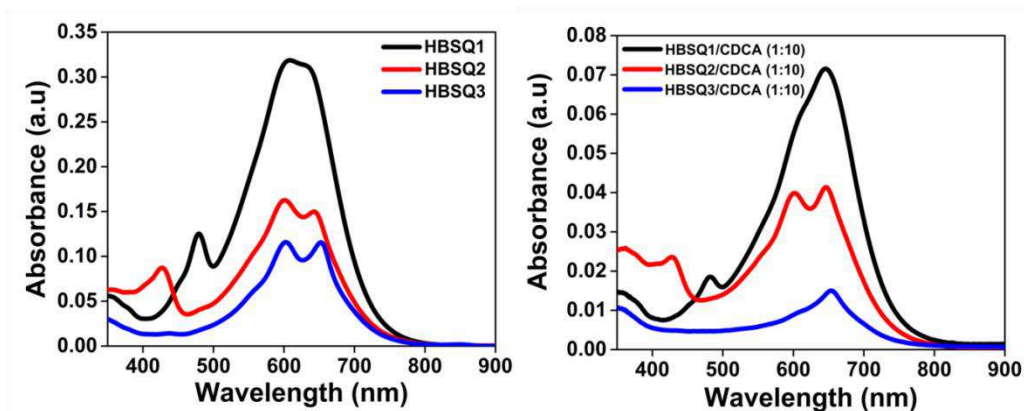


**Figure 13.** UV-Vis absorption spectra of a) desorbed **HBSQ** dyes in 2 M HCl in EtOH and b) desorbed **HBSQ/CDCA (1:10)** dyes in 2 M HCl in EtOH.

To gain insight into the observed  $J_{SC}$  values, the IPCE spectra were recorded for device made with the **HBSQ** dyes, and the results are shown in **Figure 11c, d**. **HBSQ1-3** sensitized cell gives a broad IPCE action spectrum in the range of 400-800 nm. **HBSQ1** demonstrated the highest IPCE value reaching 40% at 580 nm without any co-adsorbents. The IPCE of **HBSQ** series had an onset around 820 nm. The IPCE is interrelated to the LHE, the quantum yield of electron injection from the excited dye to the CB of the  $TiO_2$ , and the efficiency of collection of electrons in the external circuit.<sup>35</sup>

$$IPCE = LHE(\lambda) \Phi_{inj} \eta_{coll} \quad (1)$$

**HBSQ1** displayed more broader IPCE action spectrum than **HBSQ2** and **HBSQ3** due to the higher light harvesting ability and better electron injection efficiency from the excited

dye to the CB of the  $\text{TiO}_2$  (**Figure 11c, d**). Remarkably, the IPCE spectrum of **HBSQ1** exhibited a maximum value of 60%, which is higher than the IPCE values of **HBSQ2** (36%) and **HBSQ3** (32%), in presence of co-adsorbents. The IPCE spectrum of **HBSQ1-3** shows particularly high plateau in the region of 400-530 nm owing to the H-type of dye aggregation on  $\text{TiO}_2$  surface.

#### 4.4.6 Electrochemical Impedance Spectroscopy (EIS)

EIS is generally used to investigate the interfacial charge transfer kinetics of DSSCs by measuring the impedance in the dark with applied potential. The  $V_{OC}$  and  $J_{SC}$  of devices are recognized to be affected by the charge recombination dynamics at the  $\text{TiO}_2$ -dye-electrolyte interface. To elucidate the  $V_{OC}$  and  $J_{SC}$  performance of **HBSQ1-3** dyes, the relative CB positions, charge recombination rate and electron lifetime were investigated.<sup>36</sup>

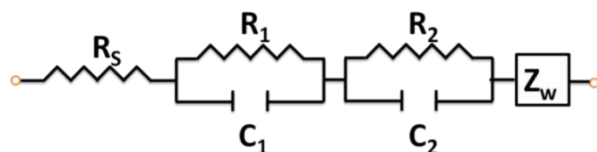


**Figure 14.** Equivalent circuit model ( $R_s+R_1/C_1+R_2/C_2$ ).  $R_1/C_1$  represents Pt/ ( $\text{I}^-/\text{I}_3^-$ ) and  $R_2/C_2$  represents Dye/ $\text{TiO}_2$ / ( $\text{I}^-/\text{I}_3^-$ ) interfaces.

The Nyquist plot of **HBSQ1-3** dye cells with applied potential of  $-0.50$  in the dark as presented in **Figure 15a**. The second semi-circle represents the charge transfer processes at the  $\text{TiO}_2$ -dye-electrolyte interface. This semicircle was bigger for **HBSQ1** than other dyes, it is in the order of **HBSQ1** > **HBSQ2** > **HBSQ3**. **Figure 15b, c** and **d** show observed chemical capacitance ( $C_\mu$ ), charge transfer resistance ( $R_{ct}$ ) and life time ( $\tau$ ) respectively, extracted after fitting the Nyquist plot using an equivalent circuit with different applied potential (**Figure 14**).<sup>37</sup> The  $C_\mu$  is plotted as a function of applied voltage to elucidate the shift of  $\text{TiO}_2$  CB under dark condition. At a given applied potential, the  $C_\mu$  was in the sequence of **HBSQ1** > **HBSQ2** > **HBSQ3**, demonstrating a consecutive upward shift of  $E_{CB}$ . The observed  $R_{ct}$  was in the order of **HBSQ1** ( $17.4 \Omega$ ) > **HBSQ2** ( $10.3 \Omega$ ) > **HBSQ3** ( $4.7 \Omega$ ) at applied bias of  $-0.50$  V (**Table 6**). The  $R_{ct}$  of **HBSQ1** and **HBSQ2** sensitized cells was higher than **HBSQ3**, that means **HBSQ1-2** can suppress charge recombination efficiently than **HBSQ3** and resulting in the better  $J_{SC}$  in

the order of **HBSQ1** > **HBSQ2** > **HBSQ3**.<sup>38</sup> Also, the  $\tau$  of **HBSQ1-2** sensitized cells are 19.14 ms and 9.27 ms times longer than **HBSQ3** (2.82 ms), which illustrate the effect of  $\pi$ -conjugated spacer and long, and branched alkyl chain of acceptor groups on the  $\tau$ . Most importantly, the charge recombination dynamics between the injected electrons in TiO<sub>2</sub> film and I<sub>3</sub><sup>-</sup> in electrolyte is also depends on the molecular structure of the organic dyes and their arrangement on the surface of the oxide electrodes.

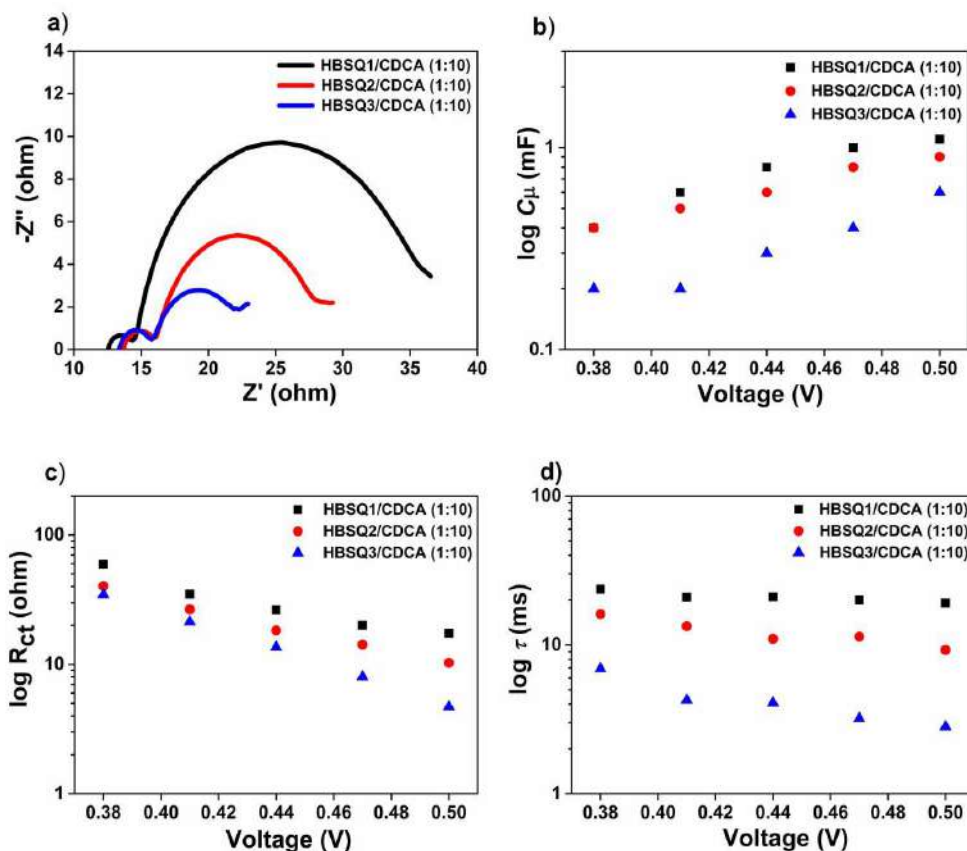


**Figure 15.** Plots of EIS analysis of **HBSQ1-3** dye cells (a) Nyquist plot, (b)  $C_{\mu}$ , (c)  $R_{ct}$ , and d)  $\tau$  as a function of applied voltage, respectively.

**Table 6.** EIS parameters for the DSSCs based on **HBSQ1-3** dyes

NC Dyes	$R_{ct}$ (ohm)	$C_{\mu}$ (mF)	$\tau$ (ms)
<b>HBSQ1/CDCA (1:10)</b>	17.4	1.1	19.14
<b>HBSQ2/CDCA (1:10)</b>	10.3	0.9	9.27
<b>HBSQ3/CDCA (1:10)</b>	4.7	0.6	2.82

EIS data measured at an applied bias of  $-0.50$  V under dark conditions,  $R_{ct}$ : charge transfer resistance;  $C_{\mu}$ : chemical capacitance;  $\tau$ : electron lifetime  $\tau$  (ms) =  $R_{ct} \times C_{\mu}$



#### 4.4.7 Possible orientation of sensitizers on the TiO<sub>2</sub> surface

Between the **HBSQ1-3** dyes, the observed  $J_{SC}$  is decreased in the order of **HBSQ1** > **HBSQ2** > **HBSQ3** at the same time having almost same  $V_{OC}$  and it can be estimated from the information about high dye loading ability of **HBSQ1** than other two dyes. The introduction of N-alkyl and sp<sup>3</sup>-C alkyl groups help to reduce the dye-dye interaction that can be deduced from the UV-Vis absorption properties of dyes on TiO<sub>2</sub>. This broadening and blue shifting of  $\lambda_{max}$  is more for **HBSQ1** and **HBSQ2** than **HBSQ3**. So it is possible that the deprived performance **HBSQ3** is attributable to less amount of dye is anchored than that of **HBSQ1-2**. It is also interesting to take into account that the  $R_{ct}$  is very high for **HBSQ1** which is not even functionalized with any hydrophobic alkyl group for the better surface passivation of TiO<sub>2</sub> than **HBSQ3**. It may be because of either (i) surface passivation due to aggregation of dyes on TiO<sub>2</sub> as compared to the passivation by the in-plane and out-of-plane sp<sup>3</sup>-C alkyl groups present in the dyes or (ii) the molecular orientation of dyes on the TiO<sub>2</sub> surface which can modulate the charge injection and recombination processes.<sup>39</sup> Remarkably, planarity of dyes and molecular orientation on TiO<sub>2</sub> surface is the most critical factor for determining the device performance.<sup>40,41</sup>

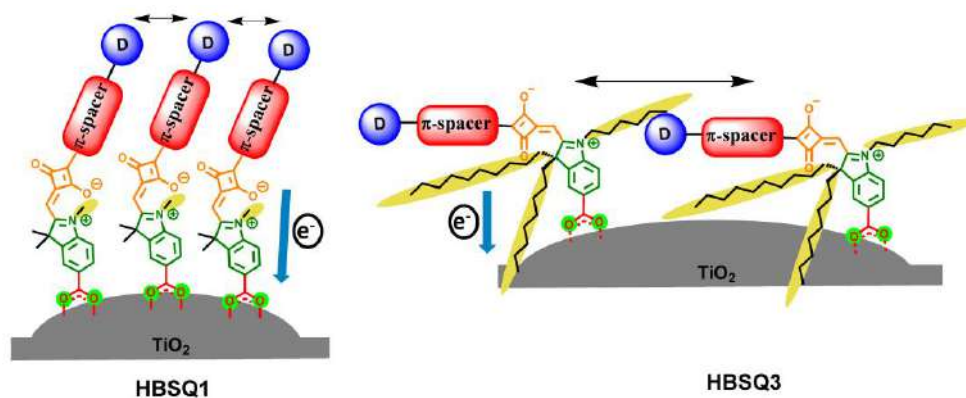


**Figure 16.** Pictorial presentation of possible dye orientation of **HBSQ1-3** dyes on TiO<sub>2</sub> surface.

There two probability of dye orientation on the TiO<sub>2</sub> can be possible, E- and Z-type (**Figure 16**).<sup>42</sup> The emission studies on the TiO<sub>2</sub> and Al<sub>2</sub>O<sub>3</sub> surfaces (6 μm) were carried out to determine the charge injection process.<sup>43</sup> The emission spectra were broadened and red shifted in compared to solution on both the surfaces (**Figure 17a**). In Al<sub>2</sub>O<sub>3</sub> film, emission peak was located around 740 nm and 800 nm while in TiO<sub>2</sub> peak was near

around 800 nm. For **HBSQ1-2**, the extent of fluorescence quenching on TiO<sub>2</sub> film was more than that of **HBSQ3** in comparison to emission intensity in Al<sub>2</sub>O<sub>3</sub>. The incomplete quenching of fluorescence for **HBSQ3** specifies an incompetent charge injection processes compared to **HBSQ1-2**. In addition, the red shifted emission shows the formation of J-type aggregates on the surface. The emission experiments confirm that the spatial dye orientation of **HBSQ1-2** make fast interfacial electron injection from the excited dye molecules to the CB of TiO<sub>2</sub> compared to the **HBSQ3**.<sup>44</sup> **HBSQ3** dyes gave more intense and broad emission on the TiO<sub>2</sub> surface than the **HBSQ1** and **HBSQ2** (**Figure 17a**). So the incompetent charge injection process originated from improper orientation of dyes on the surface.<sup>10</sup> Also from the dye desorption study, it was observed that **HBSQ3** dye loading was less than the other dyes indicating self quenching of excited state is not a main operating mechanism.

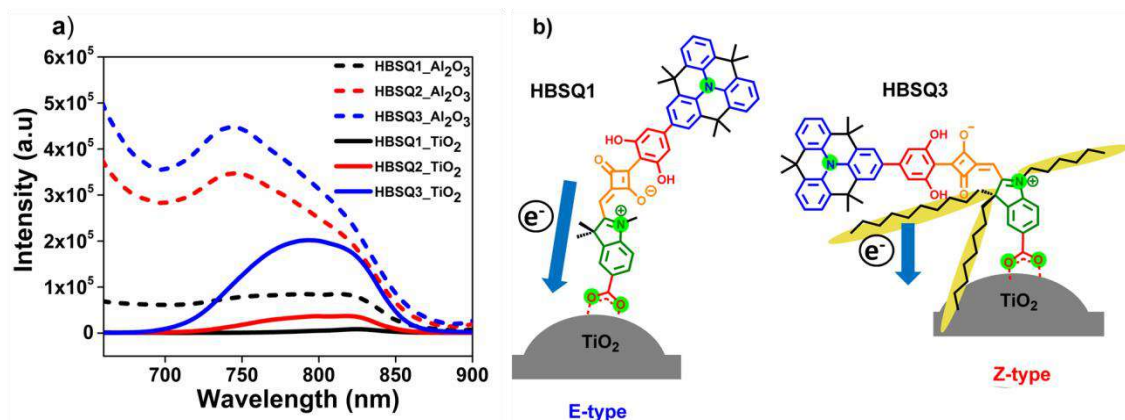


**Figure 17.** a) Emission spectra of **HBSQ1-3** adsorbed on transparent TiO<sub>2</sub> and Al<sub>2</sub>O<sub>3</sub> films of 6 μm thickness, excitation wavelength 600 nm (dipping time 12 h) and b) Possible dye orientation of **HBSQ1** and **HBSQ3** dyes on TiO<sub>2</sub> surface.

Additionally, the  $R_{ct}$  of **HBSQ3** is very low than the **HBSQ1-2** dyes for the recombination process. Therefore, **HBSQ1-2** dyes could bring vertically oriented dye geometry upon binding with TiO<sub>2</sub> surface (E-type), resulting into slightly better  $J_{SC}$  of **HBSQ1** which can be ascribed to the better injection efficiency of the dye for electron transfer from the donor group to the acceptor moiety. On the other hand, **HBSQ3** align with a tilt angle (Z-type) (**Figure 17b**). It can result into a comparatively shorter distance between the donor moiety of dyes and the TiO<sub>2</sub> surfaces.<sup>11</sup> However, the unwanted charge recombination decreases the overall



light-to-electric-energy conversion efficiency.<sup>45</sup> Therefore, as supported by EIS measurements, the orientation of **HBSQ3** may be accountable for less efficient electron injection and fast charge recombination.

#### 4.5 CONCLUSION

In this chapter, unsymmetrical squaraine dyes (**HBSQ1-3**) containing HT donor, dihydroxybenzene as a  $\pi$ -spacer were designed, synthesized and characterized for DSSCs. These dyes utilize the  $\pi$ -conjugated spacer which connects the donor and the acceptor and stabilizes the squaraine core by hydrogen bonding and provides a co-planar structure to dyes. By integrating the  $\pi$ -spacer and branched alkyl chain on the indolium units, the HOMO and LUMO energy levels were modulated and showed a broad absorption spectrum, and high  $\epsilon$  of dyes. The molecular orientation and arrangement of **HBSQ1-3** dyes and their causes on charge recombination between the injected electrons in the CB of TiO<sub>2</sub> and dye cations or I<sub>3</sub><sup>-</sup> were systematically studied. The emission studies demonstrated that the **HBSQ1** and **HBSQ2** dyes have sufficient driving force for the fast injection of excited electrons into the CB of TiO<sub>2</sub> that reflects the higher and broader IPCE response than **HBSQ3**. The **HBSQ1** sensitized cells with co-adsorbents achieved the highest efficiency of 5.39%. The electrochemical impedance measurement was carried out to scrutinize the interfacial charge transfer processes for **HBSQ1-3** dyes. The  $R_{ct}$  and  $\tau$  of **HBSQ1** and **HBSQ2** are higher than **HBSQ3** signifying the slow electron recombination rate at TiO<sub>2</sub>-dye-electrolyte interface which results in high  $\eta$ .

## 4.6 NMR data

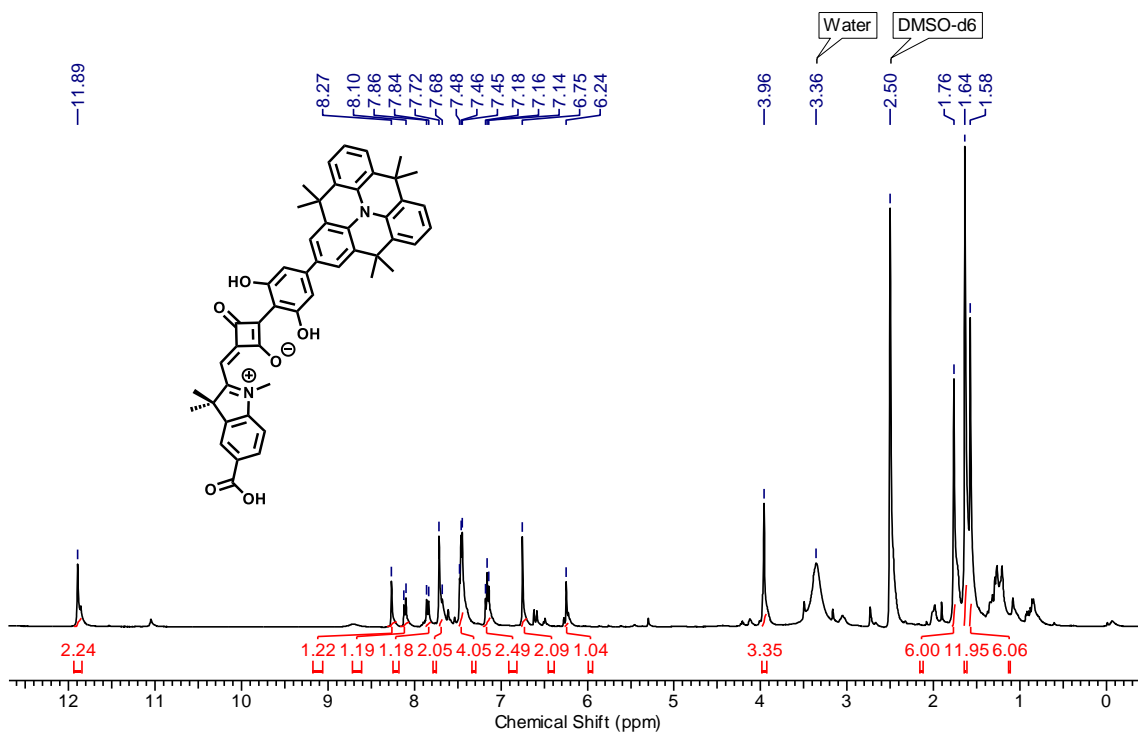


Figure 18.  $^1\text{H}$  NMR (400 MHz,  $\text{DMSO-}d_6$ ) spectrum of compound **HBSQ1**.

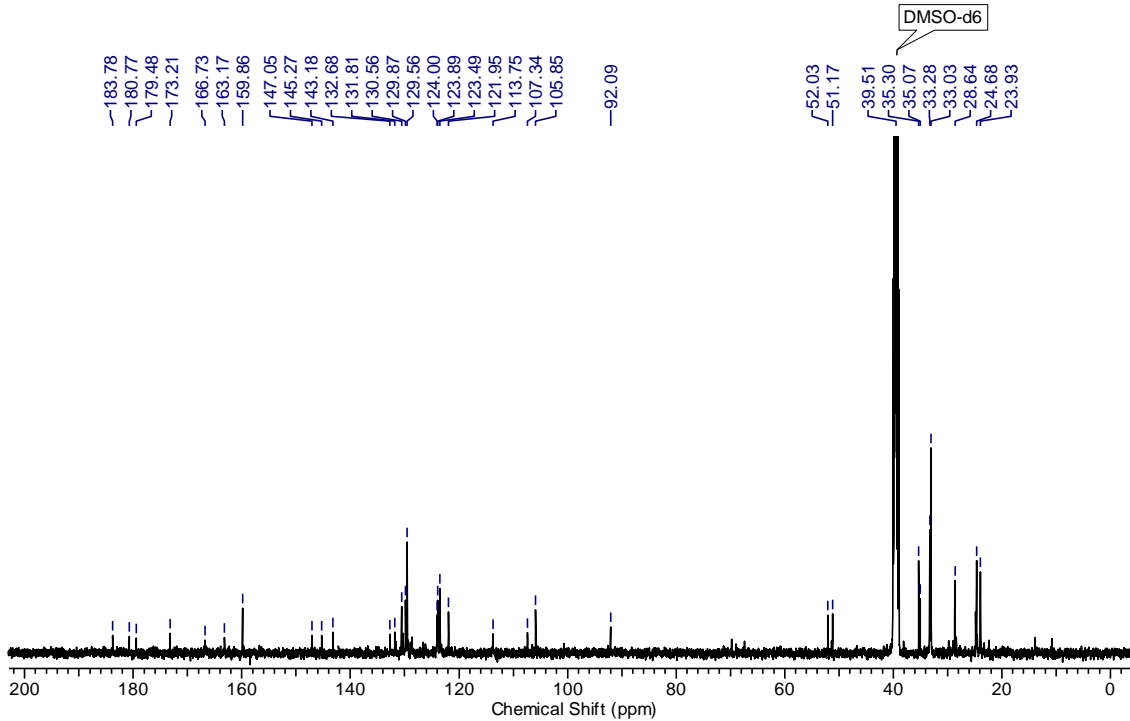


Figure 19.  $^{13}\text{C}$  (100 MHz,  $\text{DMSO-}d_6$ ) spectrum of compound **HBSQ1**.

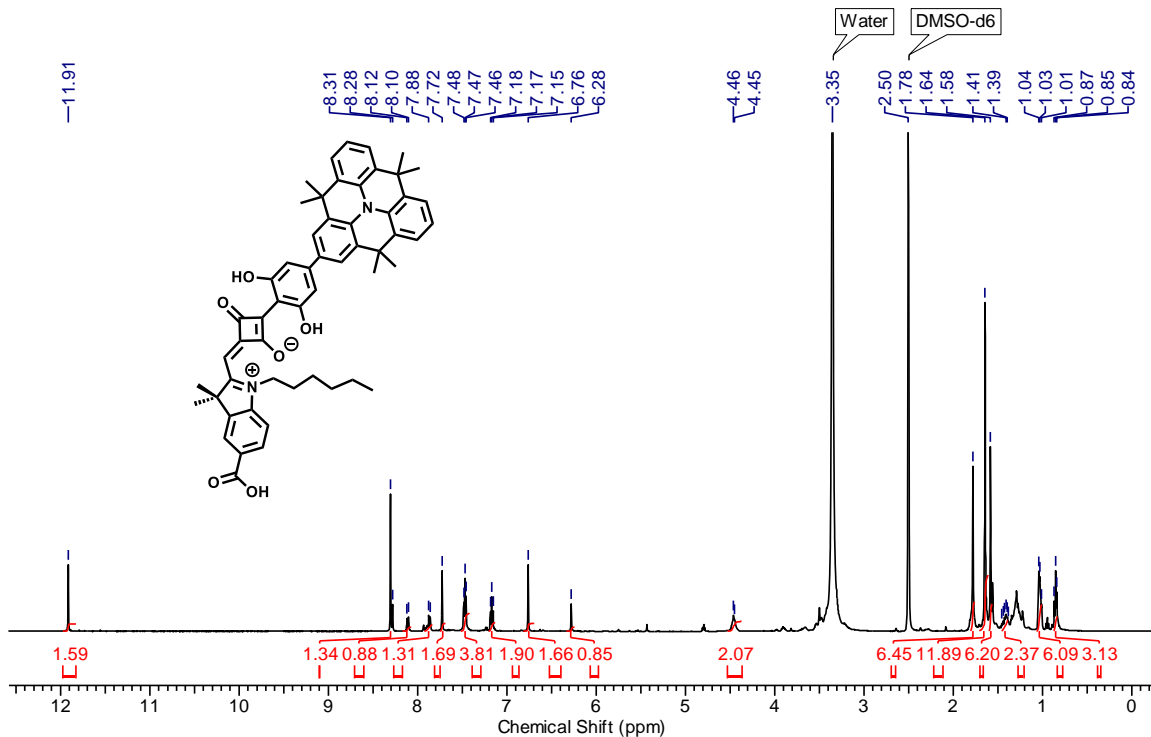


Figure 20.  $^1\text{H}$  NMR (500 MHz,  $\text{DMSO}-d_6$ ) spectrum of compound HBSQ2.

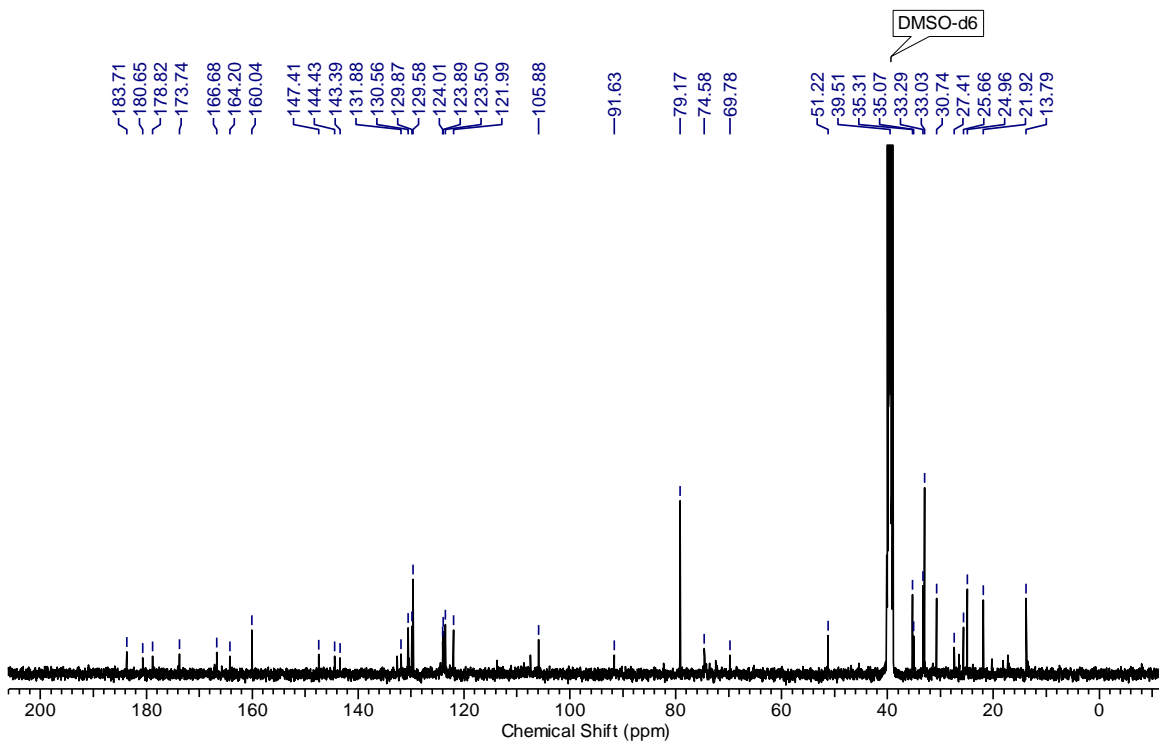


Figure 21.  $^{13}\text{C}$  (125 MHz,  $\text{DMSO}-d_6$ ) spectrum of compound HBSQ2.

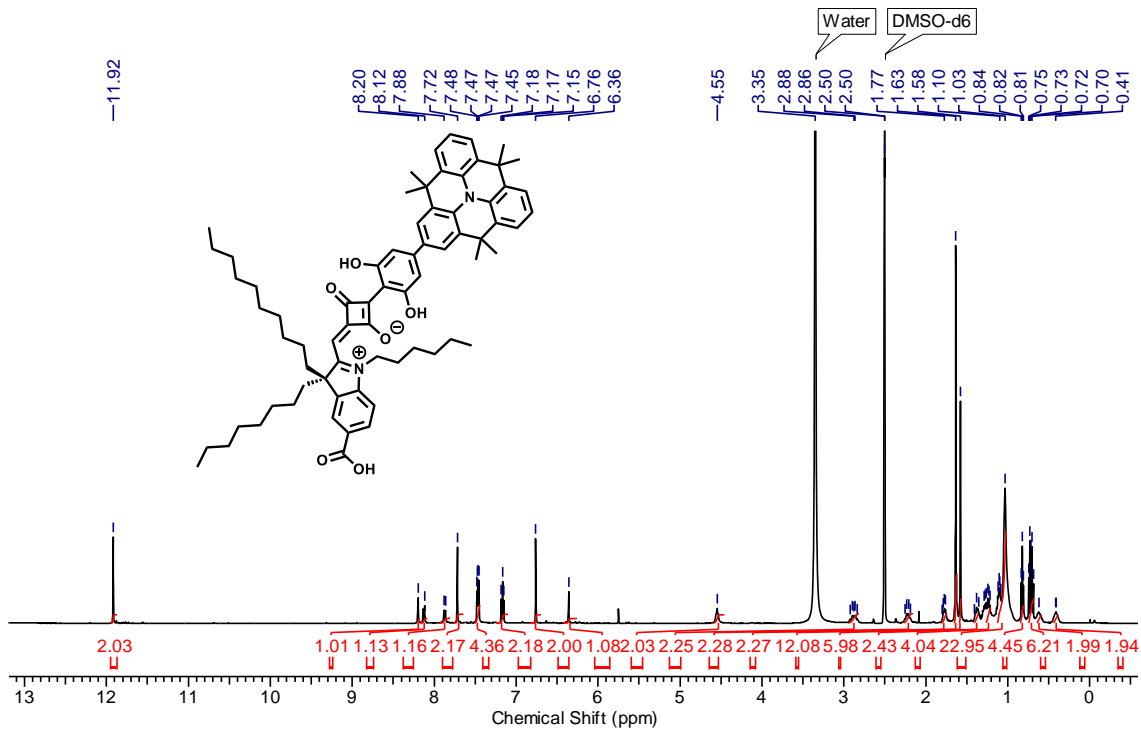


Figure 22.  $^1\text{H}$  NMR (500 MHz,  $\text{DMSO-}d_6$ ) spectrum of compound **HBSQ3**.

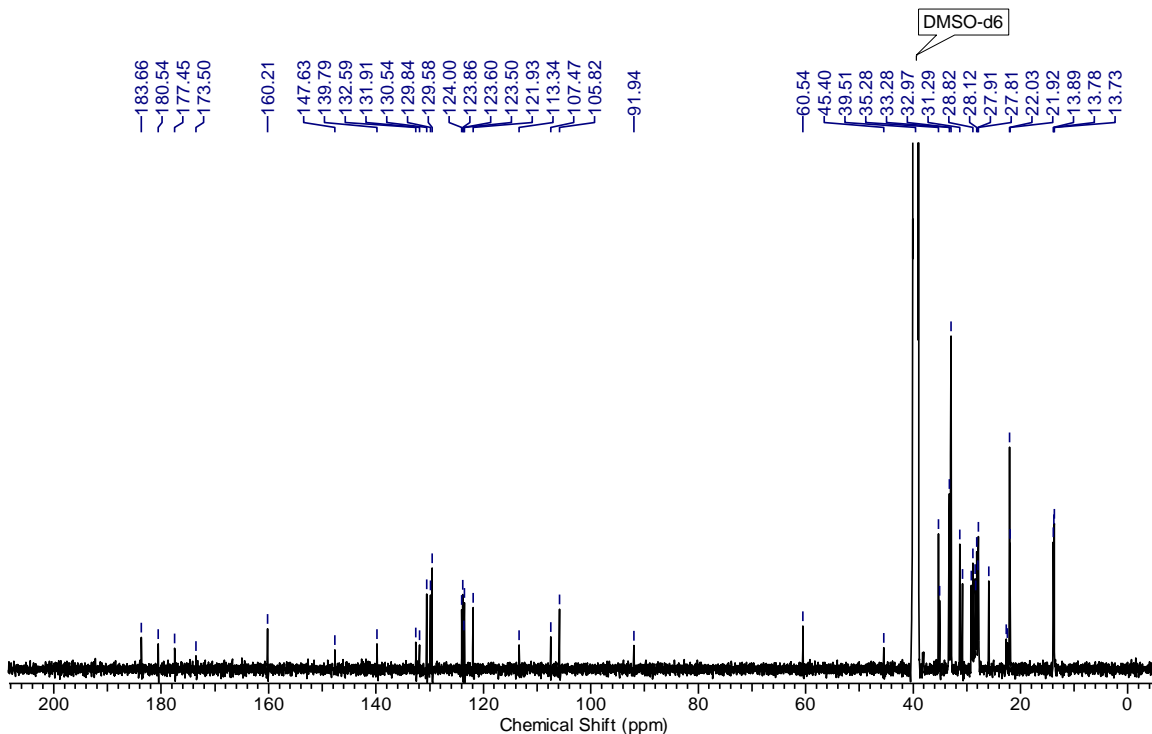


Figure 23.  $^{13}\text{C}$  (125 MHz,  $\text{DMSO-}d_6$ ) spectrum of compound **HBSQ3**.

**4.7. REFERENCES**

1. Qin, C.; Wong, W. Y.; Han, L. *Chem. Asian J.* **2013**, *8*, 1706.
2. Mishra, A.; Fischer, M. K.; Bäuerle, P. *Angew. Chem. Int. Ed.* **2009**, *48*, 2474.
3. Brogdon, P.; Cheema, H.; Delcamp, J. H. *ChemSusChem* **2018**, *11*, 86.
4. Wu, Y.; Zhu, W. *Chem. Soc. Rev.* **2013**, *42*, 2039.
5. Saccone, D.; Galliano, S.; Barbero, N.; Quagliotto, P.; Viscardi, G.; Barolo, C. *Eur. J. Org Chem.* **2016**, *2016*, 2244.
6. Yum, J.-H.; Walter, P.; Huber, S.; Rentsch, D.; Geiger, T.; Nüesch, F.; De Angelis, F.; Grätzel, M.; Nazeeruddin, M. K. *J. Am. Chem. Soc.* **2007**, *129*, 10320.
7. Kim, B. G.; Chung, K.; Kim, J. *Chem. Eur. J.* **2013**, *19*, 5220.
8. Chaurasia, S.; Liang, C.-J.; Yen, Y.-S.; Lin, J. T. *J. Mater. Chem. C* **2015**, *3*, 9765.
9. Yao, Z.; Zhang, M.; Wu, H.; Yang, L.; Li, R.; Wang, P. *J. Am. Chem. Soc.* **2015**, *137*, 3799.
10. Ye, S.; Kathiravan, A.; Hayashi, H.; Tong, Y.; Infahsaeng, Y.; Chabera, P.; Pascher, T. r.; Yartsev, A. P.; Isoda, S.; Imahori, H. *J. Phys. Chem. C* **2013**, *117*, 6066.
11. Imahori, H.; Kang, S.; Hayashi, H.; Haruta, M.; Kurata, H.; Isoda, S.; Canton, S. E.; Infahsaeng, Y.; Kathiravan, A.; Pascher, T. r. *J. Phys. Chem. A* **2010**, *115*, 3679.
12. Zhang, M.; Wang, Y.; Xu, M.; Ma, W.; Li, R.; Wang, P. *Energy Environ. Sci.* **2013**, *6*, 2944.
13. Zarate, X.; Saavedra-Torres, M.; Rodriguez-Serrano, A.; Gomez, T.; Schott, E. *J. Comput. Chem.* **2017**.
14. Qin, P.; Yang, X.; Chen, R.; Sun, L.; Marinado, T.; Edvinsson, T.; Boschloo, G.; Hagfeldt, A. *J. Phys. Chem. C* **2007**, *111*, 1853.
15. Cai, L.; Tsao, H. N.; Zhang, W.; Wang, L.; Xue, Z.; Grätzel, M.; Liu, B. *Adv. Energy Mater.* **2013**, *3*, 200.
16. Do, K.; Kim, D.; Cho, N.; Paek, S.; Song, K.; Ko, J. *Org. Lett.* **2011**, *14*, 222.
17. Della Pelle, A. M.; Homnick, P. J.; Bae, Y.; Lahti, P. M.; Thayumanavan, S. J. *Phys. Chem. C* **2014**, *118*, 1793.
18. Wang, S.; Hall, L.; Diev, V. V.; Haiges, R.; Wei, G.; Xiao, X.; Djurovich, P. I.; Forrest, S. R.; Thompson, M. E. *Chem. Mater.* **2011**, *23*, 4789.
19. Chen, G.; Sasabe, H.; Igarashi, T.; Hong, Z.; Kido, J. *J. Mater. Chem. A* **2015**, *3*, 14517.
20. Karjule, N.; MK, M. F.; Nithyanandhan, J. *J. Mater. Chem. A* **2016**, *4*, 18910.
21. Karjule, N.; Mele Kavungathodi, M. F.; Nithyanandhan, J. *J. Phys. Chem. C* **2017**, *121*, 21836.
22. El-Haggag, R.; Kamikawa, K.; Machi, K.; Ye, Z.; Ishino, Y.; Tsumuraya, T.; Fujii, I. *Bioorganic & medicinal chemistry letters* **2010**, *20*, 1169.
23. Hara, K.; Wang, Z.-S.; Sato, T.; Furube, A.; Katoh, R.; Sugihara, H.; Dan-oh, Y.; Kasada, C.; Shinpo, A.; Suga, S. *J. Phys. Chem. B* **2005**, *109*, 15476.
24. Li, S.-L.; Jiang, K.-J.; Shao, K.-F.; Yang, L.-M. *Chem. Commun.* **2006**, 2792.
25. Ni, J.-S.; Yen, Y.-C.; Lin, J. T. *J. Mater. Chem. A* **2016**, *4*, 6553.

26. Wenger, S.; Bouit, P.-A.; Chen, Q.; Teuscher, J.; Censo, D. D.; Humphry-Baker, R.; Moser, J.-E.; Delgado, J. L.; Martín, N.; Zakeeruddin, S. M. *J. Am. Chem. Soc.* **2010**, *132*, 5164.
27. Frisch, M. J.; Trucks, G. W.; Schlegel, H. B.; Scuseria, G. E.; Robb, M. A.; Cheeseman, J. R.; Scalmani, G.; Barone, V.; Mennucci, B.; Petersson, G. A.; Nakatsuji, H.; Caricato, M.; Li, X.; Hratchian, H. P.; Izmaylov, A. F.; Bloino, J.; Zheng, G.; Sonnenberg, J. L.; Hada, M.; Ehara, M.; Toyota, K.; Fukuda, R.; Hasegawa, J.; Ishida, M.; Nakajima, T.; Honda, Y.; Kitao, O.; Nakai, H.; Vreven, T.; Montgomery, J. A., Jr.; Peralta, J. E.; Ogliaro, F.; Bearpark, M.; Heyd, J. J.; Brothers, E.; Kudin, K. N.; Staroverov, V. N.; Kobayashi, R.; Normand, J.; Raghavachari, K.; Rendell, A.; Burant, J. C.; Iyengar, S. S.; Tomasi, J.; Cossi, M.; Rega, N.; Millam, J. M.; Klene, M.; Knox, J. E.; Cross, J. B.; Bakken, V.; Adamo, C.; Jaramillo, J.; Gomperts, R.; Stratmann, R. E.; Yazyev, O.; Austin, A. J.; Cammi, R.; Pomelli, C.; Ochterski, J. W.; Martin, R. L.; Morokuma, K.; Zakrzewski, V. G.; Voth, G. A.; Salvador, P.; Dannenberg, J. J.; Dapprich, S.; Daniels, A. D.; Farkas, O.; Foresman, J. B.; Ortiz, J. V.; Cioslowski, J.; Fox, D. J. *Gaussian 09, Revision A.01*; Gaussian, Inc.: Wallingford, CT, **2009**.
28. Kaduk, B.; Kowalczyk, T.; Van Voorhis, T. *Chem. Rev.* **2011**, *112*, 321.
29. Choi, H.; Kim, J.-J.; Song, K.; Ko, J.; Nazeeruddin, M. K.; Grätzel, M. *J. Mater. Chem.* **2010**, *20*, 3280.
30. Hagberg, D. P.; Yum, J.-H.; Lee, H.; De Angelis, F.; Marinado, T.; Karlsson, K. M.; Humphry-Baker, R.; Sun, L.; Hagfeldt, A.; Grätzel, M. *J. Am. Chem. Soc.* **2008**, *130*, 6259.
31. Hagfeldt, A.; Ferdowsi, P.; Saygili, Y.; Zhang, W.; Edvinsson, T.; Kavan, L.; Mokhtari, J.; Zakeeruddin, S. M.; Grätzel, M. *ChemSusChem* **2017**.
32. Feng, S.; Li, Q.-S.; Sun, P.-P.; Niehaus, T. A.; Li, Z.-S. *ACS Appl. Mater. & Interfaces* **2015**, *7*, 22504.
33. Joly, D.; Pelleja, L.; Narbey, S.; Oswald, F.; Meyer, T.; Kervella, Y.; Maldivi, P.; Clifford, J.; Palomares, E.; Demadrille, R. *Energy Environ. Sci.* **2015**, *8*, 2010.
34. Otsuka, A.; Funabiki, K.; Sugiyama, N.; Yoshida, T.; Minoura, H.; Matsui, M. *Chem. Lett.* **2006**, *35*, 666.
35. Ooyama, Y.; Harima, Y. *ChemPhysChem* **2012**, *13*, 4032.
36. Adachi, M.; Sakamoto, M.; Jiu, J.; Ogata, Y.; Isoda, S. *J. Phys. Chem. B* **2006**, *110*, 13872.
37. Wang, Q.; Moser, J.-E.; Grätzel, M. *J. Phys. Chem. B* **2005**, *109*, 14945.
38. Li, C.-T.; Wu, F.-L.; Lee, B.-H.; Yeh, M.-C. P.; Lin, J. T. *ACS Appl. Mater. & Interfaces* **2017**, *9*, 43739.
39. Nachimuthu, S.; Chen, W.-C.; Leggesse, E. G.; Jiang, J.-C. *Phys. Chem. Chem. Phys.* **2016**, *18*, 1071.
40. Ning, Z.; Zhang, Q.; Wu, W.; Pei, H.; Liu, B.; Tian, H. *J. Org. Chem.* **2008**, *73*, 3791.
41. Ren, Y.; Li, Y.; Chen, S.; Liu, J.; Zhang, J.; Wang, P. *Energy Environ. Sci.* **2016**, *9*, 1390.
42. Ning, Z.; Fu, Y.; Tian, H. *Energy Environ. Sci.* **2010**, *3*, 1170.
43. Si, L.; He, H. *J. Phys. Chem. A* **2014**, *118*, 3410.

44. Tejerina, L.; Martínez-Díaz, M.; Nazeeruddin, M. K.; Torres, T. *Chem. Eur. J.* **2016**, *22*, 4369.
45. Wiberg, J.; Marinado, T.; Hagberg, D. P.; Sun, L.; Hagfeldt, A.; Albinsson, B. *J. Phys. Chem. C* **2009**, *113*, 3881.

# CHAPTER V

---

**Molecular Engineering of Heterotriangulene Based  
Small Molecules for Organic Field Effect Transistors**



## 5.1 INTRODUCTION

Conjugated small molecules and polymers have been widely utilized in organic electronics due to their easy solution processability, light weight and also potential to explore in flexible devices. As the optical and electronic properties can be modulated systematically, these conjugated small molecules have been explored in organic field effect transistors (OFETs), organic light emitting diode (OLED), organic photovoltaic (OPV) devices. For all the optoelectronic devices, the molecular arrangement or morphology within the active layer dictates the device performance. Among the optoelectronic devices, OFETs are considered as a core component of various digital integrated structures.<sup>1</sup> The molecular design and development of organic molecules for OFET requires excellent  $\pi$ -orbital planarity and small intermolecular distance to facilitate inter-/intra-molecular charge transport in the channel. Conjugated polyaromatic compounds and D-A based low band gap polymers showed high mobility. Small molecules, based on polyaromatic, DPP, isoindigo have been widely used for the high efficient OFETs.<sup>2</sup> Along with  $\pi$ -conjugation, side chain engineering also plays an important role in maintaining the better morphology to enhance co-planarity and inter and intra-molecular interactions.<sup>3</sup> In order to see the synergistic effect of planarization and side chain engineering, a series of HT-based small molecules have been designed for fabricating n-channel or p-channel transistors.

### 5.2A.1 SECTION A

Discotic liquid crystals (disc like) are the most promising class of semiconducting materials for organic electronics due to their self-organization and charge transporting properties for example, hexa-peri-hexabenzocoronone (HBCs), triphenylene, coronene.<sup>4,5</sup> The most remarkable property of discotics is the capability to conduct charges along the stacks of aromatic cores.<sup>6</sup> In 2002, Venkataraman and co-workers reported 4H,8H,12H-benzo[1,9]quinolizino [3,4,5,6,7-defg]acridine-4,8,12-trione (A) as planar core with the high symmetry (**Figure 1**).<sup>7</sup> This molecule is correlated to a class of compounds termed as triangulenes. The planar geometry of heterotriangulene (HT) and 3-fold symmetry make it an ultimate conjugated, electro active building block and also it has discotic liquid-crystalline phases. The three carbonyl groups significantly decrease the electron density of the aromatic core, which makes it attractive as a building block for the

construction of diverse n-type semiconductor. Still there is issue regarding poor solubility of the triangulene core in common organic solvents. This limits the use of this molecule for the organic electronics applications. Because of this reason, the derivatives of heterotriangulene linked with different alkyl chain lengths have been synthesized; these molecules was showing a prominent capability to form one dimensional (1D) nano- and microstructures by self-assembly.<sup>8,9</sup>

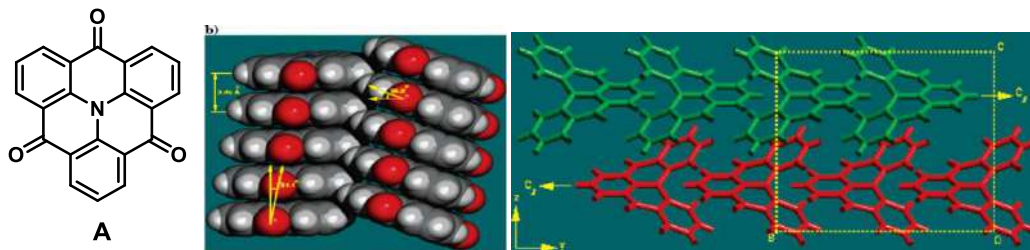


**Figure 1.** Structure of heterotriangulene (A) and the stacking interactions in the single-crystal X-ray structure.

### Molecular engineering for organic semiconductor

Predominantly, the mobility of the organic semiconductor should be as high as possible for the efficient charge transport from one molecule to another. This high mobility can be achieved when molecules will have larger transfer integral and the smaller the reorganization energy. Therefore, there are three major components required in OFETs: conjugated core (backbone), heteroatoms substituents (electron donating or withdrawing), and side chains (i.e., solubilizing groups). The conjugated core determines the electronic properties of semiconductors such as energy level, inter/intramolecular interaction and molecular packing. Also variation in heteroatom is an effective way to change electronic properties and molecular packing.<sup>10</sup> Mostly importantly, core substitution by either electron donating or withdrawing affects electronic properties and molecular arrangements through modifying the dipole. Side chains are usually integrated to impart solubility, and also affect electronic properties in the solid state by changing molecular packing structures.<sup>2</sup>

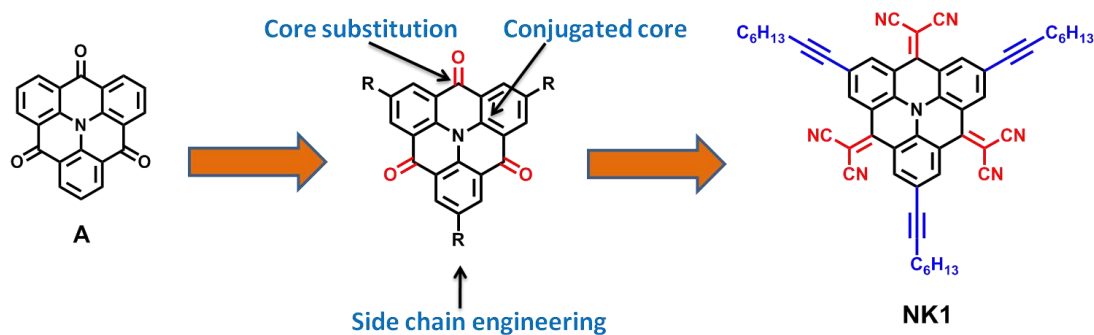


**Figure 2.** Molecular engineering and structure of **NK1** organic semiconductor.

In n-type semiconductor, in order to inject electrons into the LUMO level from gold electrode, the LUMO level must be arranged in a line with the work function of the metal.<sup>11</sup> This can be achieved by using a planar conjugated semiconducting core and adding together strong electron withdrawing groups such as fluorine,<sup>12</sup> cyano,<sup>13</sup> or diimide.<sup>14</sup> Simultaneously, increasing the electron affinity (at least 3 eV) of a semiconductor also improves its environmental stability. In this section A, designed a new discotic shaped n-type organic semiconductor (**NK1**) for the application of OFETs. Here, heterotriangulene (HT) is used as conjugated core followed by their side engineering using alkyl chains helped for better molecular packing of the conjugated backbone and improved their solubility in common organic solvent.<sup>15</sup> Then functionalized this alkyl substituted HT core with an electron withdrawing group, -CN, it can pull electron density away from a  $\pi$ -conjugated system either through a resonance or inductive effect (**Figure 2**). This core substitution lowered the LUMO level considerably in order to align with the work function of the metal and showed high electron affinity of a semiconducting material. Also substitution on a conjugated core with electron withdrawing groups leads to enhanced stability toward oxidation.

## 5.2A.2 EXPERIMENTAL SECTION

### 5.2A.2.1 Materials and Characterization

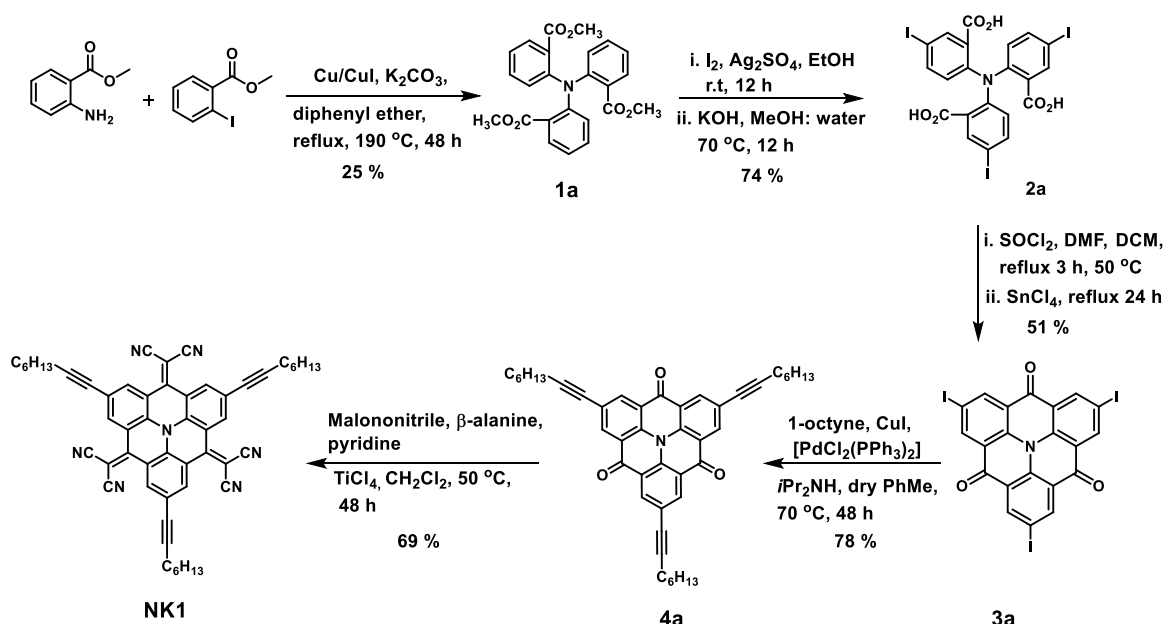
All chemicals were purchased from commercial sources and used without further purification. All reactions were carried out under an inert atmosphere. Procedure for the synthesis of **NK1** is given in **Scheme 1**.  $^1\text{H}$  NMR and  $^{13}\text{C}$  NMRs were recorded in  $\text{CDCl}_3$ ,  $\text{MeOH-}d_4$  or  $\text{DMSO-}d_6$  on 200 MHz NMR, 400 MHz NMR and 500 MHz NMR spectrometers. High-resolution mass spectrometric measurements (HR-MS) were carried out using the ESI method and an ion-trap mass analyzer. Absorption spectra were recorded at room temperature in quartz cuvette using Analytik Jena UV-Visible spectrophotometer. Electrochemical measurement was carried out using a Bio-Logic potentiostat (model no: SP300). The cyclic voltammetric analysis (CV) was carried out in dry  $\text{CH}_2\text{Cl}_2$  solvent by using 0.1 M tetrabutylammonium perchlorate ( $\text{TBAClO}_4$ ) as supporting electrolyte and  $\text{Fc}/\text{Fc}^+$  as external reference. The experiments were performed at room temperature in nitrogen atmosphere with a three-electrode cell consisting of a platinum foil as counter electrode, an  $\text{Ag}/\text{Ag}^+$  reference electrode, and a platinum wire as working electrode. TGA analysis was done using PerkinElmer STA 6000 simultaneous thermal analyzer at a heating rate of  $5\text{ }^\circ\text{C min}^{-1}$  or  $10\text{ }^\circ\text{C min}^{-1}$ . 14. Differential scanning calorimetry (DSC) was conducted on a TA Instruments Q10 DSC, under nitrogen at a heating/cooling rate of  $5\text{ }^\circ\text{C min}^{-1}$ . X-ray diffraction (PXRD) patterns were recorded on a PANalytical X'PERT PRO instrument using iron-filtered  $\text{Cu K}\alpha$  radiation ( $\lambda = 1.5418\text{ \AA}$ ).

### 5.2B.2.2 Device Fabrication

Field effect transistors devices were fabricated using  $\text{SiO}_2$  as a gate dielectric, heavily n-doped Si as a gate electrode and gold as source and drain electrodes. The pre-patterned substrates of bottom-gate-bottom-contact field-effect transistors were purchased from Fraunhofer IPMS (interdigitated S/D electrodes), with channel lengths (L) 2.5, 5, 10 and 20  $\mu\text{m}$  and channel width (W) of 10  $\mu\text{m}$ . All OFET measurements were performed on Agilent 4156C semiconductor probe analyzer and semi probe station. Before making the films of these molecules onto the surface, the substrates were first cleaned with acetone, isopropyl alcohol and dried by heat gun. The OFET substrates were modified with an

OTS (octyltrichlorosilane)/HMDS (Hexamethyldisilazane) by dipping the Si/SiO<sub>2</sub> substrate in 1 mM OTS/ HMDS in chloroform for 1 h at room temperature and annealed at 100 °C for 30 min. These molecules were deposited by spin-coating on the OTS/ HMDS-modified SiO<sub>2</sub> substrate with concentration of 10 mg mL<sup>-1</sup> solution in chloroform at 1500 rpm for 60 sec, and dried. These devices were measured both before and after annealing at 100 °C for 30 min. The charge carrier mobilities of all the molecules were determined from the saturated regime which gave averages and standard deviations.

### 5.2A.2.3 SYNTHETIC PROCEDURE AND CHARACTERIZATION DATA



**Scheme 1.** Synthesis of **NK1**.

#### **Trimethyl 2,2',2''-nitritotribenzoate (1a)**<sup>16</sup>

Methyl anthraliate (1 g, 6.61 mmol), methyl 2-iodobenzoate (4.94 g, 18.86 mmol), potassium carbonate (2.08 g, 15.07 mmol), copper powder (84 mg, 1.32 mmol), copper iodide (0.122 g, 0.64 mmol) and diphenyl ether (10 mL) were added to a 50 mL round bottom flask. This reaction mixture was rapidly heated at 190 °C for 48 h. The reaction mixture was passed through short silica column washed with pet ether to remove diphenyl ether. Then washed with ethyl acetate, collected this reaction mixture, concentrated & purified by column chromatography to afford **1a** (0.7 g, 25 %) as pale yellow powder. <sup>1</sup>H NMR (200 MHz, CDCl<sub>3</sub>) δ: 7.58 (d, J = 6.2 Hz, 3 H), 7.42 - 7.30 (m,

3 H), 7.17 - 6.91 (m, 6 H), 3.36 (br. s., 9 H).  $^{13}\text{C}$  NMR (50 MHz,  $\text{CDCl}_3$ )  $\delta$ : 167.8, 147.0, 132.3, 131.1, 127.5, 126.3, 123.6, 51.7. HRMS (ESI):  $m/z$  calcd for  $\text{C}_{24}\text{H}_{21}\text{O}_6\text{NNa}$  ( $[\text{M} + \text{Na}]^+$ ): 442.1261. Found: 442.1261.

### **6,6',6''-Nitrilotris(3-iodobenzoic acid (2a))<sup>17</sup>**

To a 100 mL round bottom flask were added compound 1 (0.54 g, 1.3 mmol), iodine (0.99 g, 3.9 mmol), silver sulfate (1.22 g, 3.9 mmol) in ethanol (40 mL). This reaction mixture was stirred at room temperature for 12 h. After 12 h, the reaction mixture was filtered through celite and washed with ethanol, this filtrate was concentrated to afford **Trimethyl 6,6',6''-nitrilotris(3-iodobenzoate)** (0.75 g, 72 %) as a pale yellow powder. This compound was used further without purification.  $^1\text{H}$  NMR (200MHz,  $\text{CDCl}_3$ )  $\delta$ : 7.91 (d,  $J = 2.1$  Hz, 3 H), 7.66 (d,  $J = 2.1$  Hz, 1 H), 7.62 (d,  $J = 2.1$  Hz, 2 H), 6.79 (s, 2 H), 6.74 (s, 1 H), 3.43 (s, 9 H).

In a 100 mL round bottom flask, compound **Trimethyl 6,6',6''-nitrilotris(3-iodobenzoate)** (0.54 g, 0.68 mmol) was added in MeOH: water (50 mL, 4:1), stirred this mixture. Then KOH (0.57 g, 10.2 mmol) was added to above reaction mixture and the temperature was raised to 70 °C and stirred for 12 h. Reaction mixture was poured into cold water and then acidified with 1 N HCl (pH 2-3), precipitate was formed, filtered it, washed with water to get pale yellow solid **6,6',6''-nitrilotris(3-iodobenzoic acid, 2a)** (0.38 g, 74 %), dried it and used this compound without purification.

### **2, 6, 10-Triiodo-4H-benzo[9,1]quinolizino[3,4,5,6,7-defg]acridine-4,8,12-trione (3a)**

To a 50 mL round bottom flask, **2a** (0.38 g, 0.50 mmol) was added in dry  $\text{CH}_2\text{Cl}_2$  (30 mL), stirred it. Then  $\text{SOCl}_2$  (1.09 mL, 15 mmol) and DMF (0.1 mL) were added to above reaction mixture and stirred this mixture at 50 °C for 3 h. After 3 h,  $\text{SnCl}_4$  (1.05 mL, 9 mmol) was added to above reaction mixture and reaction was continued for 24 h at 50 °C. After cooling to room temperature, this mixture was filtered, washed with  $\text{CH}_2\text{Cl}_2$  and yellow solid was collected. Then this compound was added to stirred solution of aqueous NaOH and stirred it for 1 h. The precipitate was collected by filtration and washed with water, acetone and the dried to give **3a** (0.18 g, 51 %) as a yellow solid powder. IR: (KBr)  $\nu = 3055, 2328, 1653, 1589, 1442, 1317, 1276, 800$ .

**Synthesis of 2,6,10-Tri(oct-1-yn-1-yl)-4H-benzo[9,1]quinolizino[3,4,5,6,7-defg]acridine-4,8,12-trione (4a)**

To a 50 mL round bottom flask compound **3a** (0.5 g, 0.71 mmol) was added in diisopropylamine (12 mL), toluene (36 mL) (1:3 v/v ratio), then 1-octyne (0.353 g, 3.2 mmol) was added to above reaction mixture, degassed this mixture for 15 min. Then [PdCl<sub>2</sub>(PPh<sub>3</sub>)<sub>2</sub>] (25 mg, 0.0355 mmol) and copper (I) iodide (14 mg, 0.071 mmol) were added and stirred at 70 °C for 48 h. The reaction mixture was filtered through celite and washed with CH<sub>2</sub>Cl<sub>2</sub>, collected this reaction mixture, concentrated & purified by column chromatography to afford **4a** (0.36 g, 78 %) as a yellow solid. <sup>1</sup>H NMR (200 MHz, CDCl<sub>3</sub>) δ: 8.83 (s, 6 H), 2.57 - 2.42 (m, 6 H), 1.76 - 1.63 (m, 6 H), 1.55-1.33 (m, 18 H), 0.98 - 0.89 (m, 9 H).

**2,2',2''-(2,6,10-Tri(oct-1-yn-1-yl)-4H-benzo[9,1]quinolizino[3,4,5,6,7-defg]acridine-4,8,12-triylidene)trimalononitrile (NK1)**

In a 25 mL round bottom flask, compound **4a** (0.3 g, 0.46 mmol), β-alanine (0.41 g, 4.6 mmol), malononitrile (0.91 g, 13.8 mmol) were suspended in CH<sub>2</sub>Cl<sub>2</sub> (20 mL), then Titanium tetrachloride (0.76 mL, 6.9 mmol) was added drop wise keeping the temperature at 0 °C, stirred this mixture. Then pyridine (0.74 mL, 9.2 mmol) was added to above reaction mixture and the temperature was raised to 50 °C and stirred for 48 h. The reaction mixture was extracted with water/ CH<sub>2</sub>Cl<sub>2</sub> and the organic layer was washed with 5 % HCl, dried over Na<sub>2</sub>SO<sub>4</sub>, concentrated & purified by column chromatography to afford **NK1** (0.25 g, 69 %) as a red powder. <sup>1</sup>H NMR (200 MHz, CDCl<sub>3</sub>) δ: 8.70 (s, 6 H), 2.48 (t, J = 7.0 Hz, 6 H), 1.76 - 1.61 (m, 6 H), 1.53- 1.32 (m, 18 H), 0.96 - 0.86 (m, 9 H); <sup>13</sup>C NMR (100 MHz, CDCl<sub>3</sub>) δ: 151.6, 134.4, 129.8, 124.3, 118.1, 113.8, 97.9, 80.2, 31.4, 28.8, 28.3, 22.7, 19.8, 14.2; MALDI-TOF: *m/z* calculated for C<sub>54</sub>H<sub>45</sub>N<sub>7</sub> [M<sup>+</sup>]: 791.37; found 791.7615.

### 5.2A.3 RESULTS AND DISCUSSION

#### 5.2A.3.1 Synthesis

The synthesis of the substituted HT derivative **1a** to **3a** is provided in **Scheme 1**. It was synthesized according to the literature.<sup>16,17</sup> Compound **4a** were obtained in good yields by the Sonogashira cross-coupling of iodinated **3a** with the corresponding 1-octyne. The reactions involving **4a** were carried out in toluene at elevated temperatures to improve the solubility of this HT-core. **NK1** was prepared by reaction of **4a** with malononitrile, afforded a red solid of target molecule. NMR spectra are provided in 5.3 (Section A).

#### 5.2A.3.2 Photophysical Properties

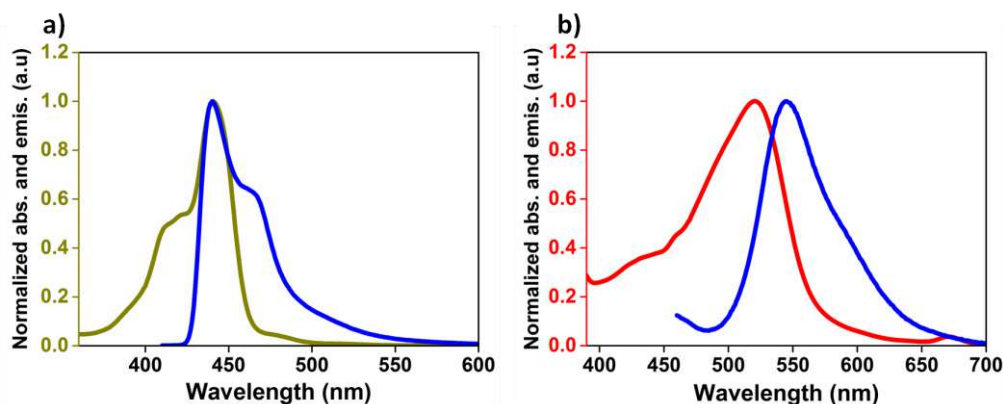


**Figure 3.** a) Absorption and emission spectra of **4a** in CH<sub>2</sub>Cl<sub>2</sub> [excitation wavelength for **4a** 400 nm and **NK1** 450 nm] and b) Absorption and emission spectra of **NK1** in CH<sub>2</sub>Cl<sub>2</sub>.

The UV-Vis absorption and emission spectra of the **4a** and **NK1** in dichloromethane are shown in **Figure 3**. The absorption spectra of **4a** showed intensive transitions in the UV region, with strong absorption bands in the range of 350-500 nm whereas **NK1** showed in the region of 400-650 nm. The absorption spectra of **NK1** exhibited an intense absorption band centered on 520 nm. After substitution with -CN groups, it exhibited red shifted absorption by 80 nm relative to that of **4a**, owing to extended conjugation with electron withdrawing nitrile groups.<sup>18</sup> The emission  $\lambda_{\text{max}}$  are slightly red shifted to longer wavelength and maximum stokes shift of ~25 nm is observed for **NK1**. The band gap ( $E_g$ ) was decreased with the addition of -CN groups, as revealed by the red shift of the long-wavelength absorption peak in the UV-Vis spectra. The optical band gaps ( $E_{0-0}$ )



were determined from the intersection of absorption and emission spectra [ $E_{0-0}$  (eV) =  $1240/\lambda$ ]. The calculated band gap is 2.33 eV for **NK1**.

### 5.2A.3.3 Theoretical Investigations

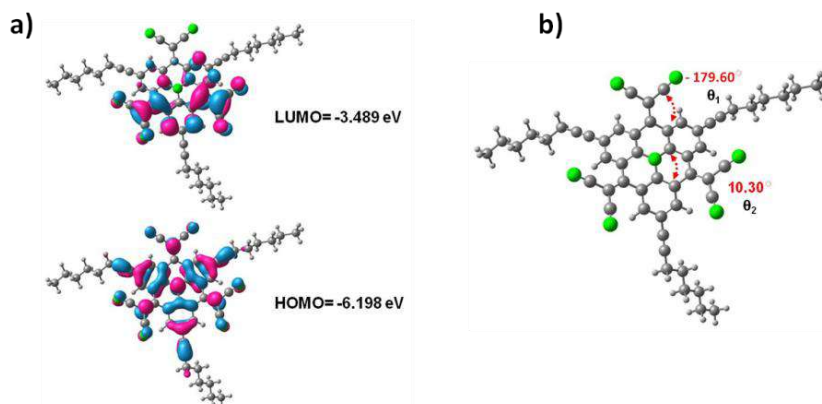


**Figure 4.** DFT calculations for **NK1** using B3LYP/6-31G (d, p) basis set using Gaussian 09 program.

The ground-state geometries of **NK1** was optimized using DFT at B3LYP/6-31G (d, p) basis set using Gaussian 09 program.<sup>19</sup> The electron density in the HOMO is delocalized mostly on the triangulene core and partially on the  $-\text{CN}$  groups while electron density in the LUMO is strongly localized on the electron withdrawing  $-\text{CN}$  groups as shown in **Figure 4**. The calculated band gap by DFT is 2.70 eV. The distortion of the triangulene core (dihedral angles,  $\theta_2 = 10^\circ$ ) is much less after  $-\text{CN}$  addition, which proved relatively easier delocalization of electrons in the **NK1** conjugated core.

### 5.2A.3.4 Electrochemical Properties

Cyclic voltammetry (CV) was carried out to obtain the electronic levels (HOMO and LUMO), which indicate the ability of semiconductor to inject holes and electrons in the material. These compounds showed irreversible reduction peaks as shown in **Figure 5**. A LUMO level of -3.63 eV was determined from the onset value of the reduction peak ( $E_{\text{onset red}} = -0.982$  V vs  $\text{Fc}/\text{Fc}^+$ ). The addition of cyano groups in the core region progressively lowered the LUMO levels of the **NK1** derivatives.<sup>20</sup> Using the optical band gap of 2.33 eV, the HOMO level of -5.96 eV has been calculated.

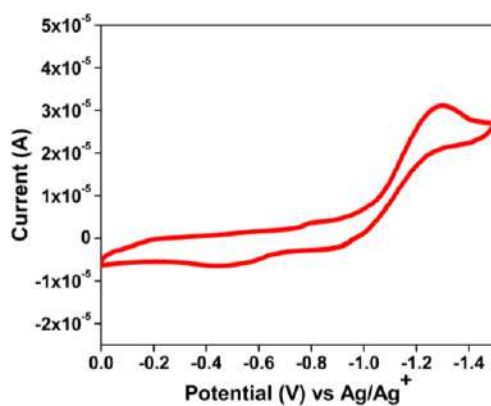


**Figure 5.** Cyclic voltammograms of **NK1** in  $\text{CH}_2\text{Cl}_2$  with  $\text{TBAClO}_4$  (0.1 M) at the scan rate of  $50 \text{ mV s}^{-1}$ .

### 5.2A.3.5 Thermal analysis

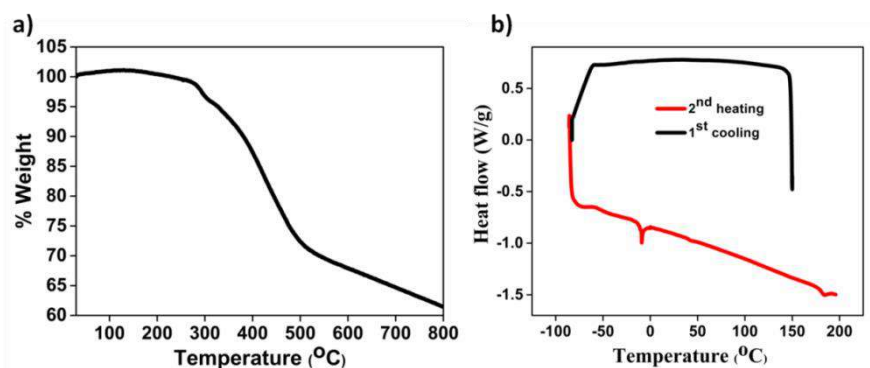


**Figure 6.** a) Thermogravimetric plots for **NK1** (heating rate at  $5 \text{ }^\circ\text{C min}^{-1}$  under  $\text{N}_2$  atmosphere) and b) differential scanning calorimetry plots for **NK1** (The data were recorded at heating and cooling rate of  $5 \text{ }^\circ\text{C min}^{-1}$ ).

Thermal stability of **NK1** was investigated with thermogravimetric analysis (TGA), as shown in **Figure 6a**. This molecule was thermally stable up to  $230 \text{ }^\circ\text{C}$  though there was only 2 wt% loss at  $284 \text{ }^\circ\text{C}$ . **NK1** is thermally well stable and can be used for a number of high-temperature processes in the construction of electronic devices. By using differential scanning calorimetry (DSC), different degree of  $\pi$ - $\pi$  stacking was supported as shown in **Figure 6b**. The DSC patterns showed only one phase transition on heating at  $185 \text{ }^\circ\text{C}$  which corresponds to their melt points.<sup>9,21</sup>

### 5.2A.3.6 Thin film morphology

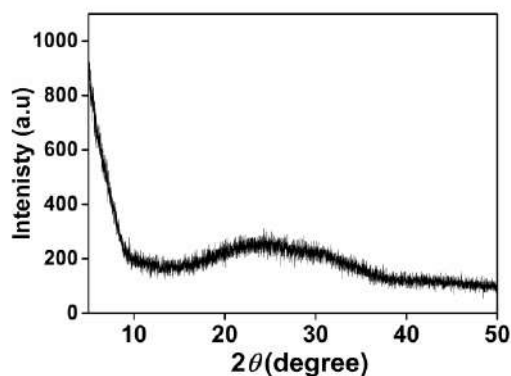


**Figure 7.** Thin film XRD pattern for **NK1**.

To find information on the molecular order and orientations in relation to the substrate surfaces, XRD experiments of **NK1** were carried out on thin films prepared by drop casting on glass substrate. In the wide-angle region of XRD spectra, broad and diffuse scattering features have been observed (**Figure 7**). This corresponds to the short-range correlations of the alkyl side chains of **NK1**. This broadened peak suggests that either the stacking might be less regular or the triangulene cores are tilted to some extent with respect to the columnar axis due to the intermolecular  $\pi$ - $\pi$  interactions of cores.<sup>9</sup>

### 5.2A.3.7 Charge-Transport Properties

The prefabricated substrate has a bottom gate-bottom contact configuration.<sup>22</sup> **NK1** contains long branched alkyl chains, hence hydrophilic  $\text{SiO}_2$  surface was modified using OTS (octyltrichlorosilane) for favorable contact between molecules and channels.<sup>23</sup> **NK1** molecule was spin coated on top of the substrates with concentration of  $10 \text{ mg mL}^{-1}$  in  $\text{CHCl}_3$ , 1500 rpm for 60 seconds. Output and transfer characteristic curves for device fabricated with as cast film of **NK1** are given in **Figure 8**. Output characteristic curves were recorded by sweeping the drain voltage ( $V_D$ ) between 0 and 100 V while keeping the gate voltage ( $V_G$ ) constant. The output characteristic curves showed standard linear and saturation regimes with a good gate modulation as a function of applied gate voltage ( $V_G$ ) (**Figure 8**). Electron carrier mobilities are calculated using the standard saturation regime quadratic model equation. The field-effect mobility ( $\mu_{\text{FET}}$ ) was calculated in the

saturation regime using the equation,  $I_{D,sat} = (WC_i/2L) \mu_{FET} (V_G - V_{Th})^2$  where  $C_i$  is the capacitance of the  $\text{SiO}_2$  insulator,  $V_G$  and  $V_{Th}$  are the gate and threshold voltages, respectively. Current on/off ratio ( $I_{on}/I_{off}$ ) was determined from the  $I_D$  at  $V_G = 0$ .<sup>24-26</sup> From the transfer characteristic curves, the threshold voltages for **NK1** calculated. OFET devices were thermally annealed at 100 °C, as annealing helps for better intermolecular connectivity and that in turn would improve charge carrier mobility values.<sup>27</sup> Device data are given in **Table 1**.

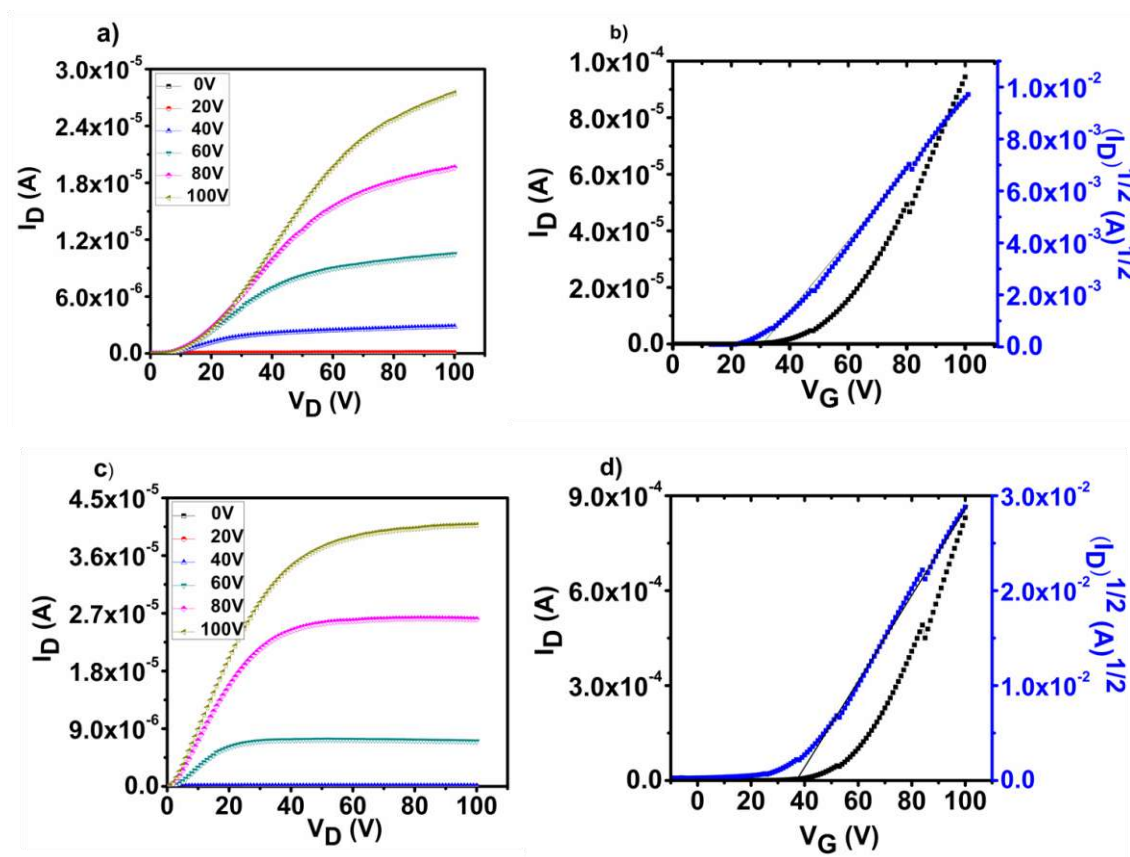


**Figure 8.** (a) Output characteristic curves and (b) transfer characteristic curves of OFET devices of **NK1** without modified substrate, and c) Output characteristic curves and d) transfer characteristic curves of OFET devices of **NK1** with OTS modified substrate for measuring electron transport.

The **NK1** films on an untreated  $\text{SiO}_2/\text{Si}$  substrates surface showed electron highest mobility of  $1.34 \times 10^{-3}$  after annealing at 100 °C, with a  $10^3$  on–off current ratio ( $I_{on}/I_{off}$ ). **NK1** on the OTS-treated  $\text{SiO}_2/\text{Si}$  substrate annealed at 100 °C showed the highest mobilities of  $1.00 \times 10^{-2} \text{ cm}^2 \text{ V}^{-1} \text{ s}^{-1}$  with an  $I_{on}/I_{off}$  ratio as high as  $10^6$ , and a threshold

voltage ( $V_{Th}$ ) of about 38 V. However, the triangulene core-functionalized with electron withdrawing -CN groups showed an excellent planarity of the  $\pi$ -conjugated core, which is beneficial for electron charge transport. These solution processable semiconductors could be of interest as electron acceptors in the application of organic photovoltaic (OPV) cells.<sup>28</sup>

**Table 1.** Summary of the OFET Characteristics of the **NK1**

Substrate <sup>a</sup>	Electron mobility ( $\text{cm}^2 \text{V}^{-1} \text{s}^{-1}$ )	$V_{Th}$ (V)	$I_{on}/I_{off}$
<b>Unmodified</b>	$8.05 \times 10^{-4}$ ( $1.34 \times 10^{-3}$ ) <sup>b</sup>	+31	$10^3$
<b>OTS</b>	$5.52 \times 10^{-3}$ ( $1.00 \times 10^{-2}$ ) <sup>b</sup>	+38	$10^6$

<sup>a</sup>Annealed at 100°C for 30 min, <sup>b</sup>Average mobilities.

#### 5.2A.4 Conclusion

This section A described the synthesis and structural analyses of heterotriangulene core-functionalized with electron withdrawing groups and characterized their electrical properties as n-channel semiconductors. The LUMO level molecules decreased due to –CN groups and matched well with work function of electrode for charge injection. **NK1** showed an excellent planarity of the  $\pi$ -conjugated core, which is favourable to charge transport. **NK1** exhibited the best field-effect mobility up to  $1.00 \times 10^{-2} \text{ cm}^2 \text{ V}^{-1} \text{ s}^{-1}$ . **NK1** are found to be highly promising n-channel candidates for practical applications in low-cost, large-area, flexible electronics, because of their straight forward synthesis, processing versatility and high performance.

### 5.2B.1 SECTION B

Squaraine dyes (SQ) belongs to a donor-acceptor-donor (D-A-D') configuration in which a  $\pi$ -conjugated resonance structure helps to stabilize the molecule. SQ dyes have shown significant importance because of their intense light absorption and less pronounced fluorescence emission for potential applications in various fields. They have been used as donor materials in organic photovoltaic (OPV) cells and received growing interest because of their simple synthetic routes, high molar extinction coefficient ( $\epsilon$ ) with tunable band gaps in the visible-NIR region, as well as high photochemical and thermal stabilities.<sup>29</sup> Due to their high  $\epsilon$ , thinner films of SQ dyes can be obtained which may facilitate the better charge transport. Moreover, because of the intermolecular interaction and aggregation of SQ molecules in solid-state films is found to play a main role in improving their light harvesting and charge transport properties.<sup>30</sup> SQ dyes showed distinct aggregation character that affects the absorption bands both in solution and at the solid-liquid interface, which is an often encountered trend in dye chemistry due to strong intermolecular interactions between the molecules.<sup>31</sup> This trait along with suitable synthetic accessibility makes these SQ molecules suitable targets for small-molecule based photovoltaic an area that has caught substantial attention in recent times.<sup>32</sup> Symmetric squaraines bearing a N, N-diisobutylamino used as a donor material, it displayed a relatively low band gap and good solubility on account of the presence of an electron-rich N, N-diisobutylamino group.<sup>33</sup> But the poor device performance might be attributed to the relatively high HOMO energy level and also the electron-insulating nature of isobutyls. However, it has poor solubility unless substituted with large alkyl groups, absorption bands primarily in the red and less hole carrier mobility.<sup>34</sup> So, the incorporation of N-aryl groups replacing the N-alkyl groups of anilinosquaraines has shown to maximize the charge transport properties in films because of enhanced intermolecular  $\pi$ - $\pi$  overlap. It also improved both charge transport, absorption bands in the NIR region to reach broadband response, and tuned the molecular frontier orbital energy levels.<sup>35</sup>

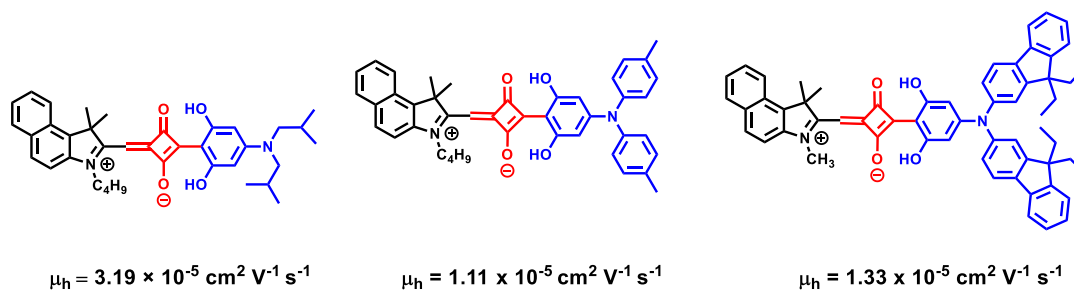


**Figure 9.** The molecular structure of the squaraine derivatives.<sup>36</sup>

Recent research results have shown that asymmetrical SQs have displayed promising properties owing to their fine-tuning optoelectronic properties and good solubility in common organic solvents.<sup>36</sup> The –OH groups on the arylamine play an important role in the squaraine dye; the –OH groups are hydrogen bonded with the enolate-type oxygen in the central ring, giving planarization to the molecule. As compared with a diisobutylamino end capper, aryl amine end capper exhibits a much broader absorption band and a deeper HOMO energy level.<sup>37</sup> Yang et al. designed and synthesized asymmetric SQ dyes having N-(3,5-dihydroxyphenyl) indoline which showed planar geometry was an ultimate segment for creating high performance SQs with relatively low band gaps. However, it is found that the asymmetrical squaraines (D-A-D') are more advantageous with regard to the fine-tuning of optoelectronic properties and showed better solubility in common organic solvents than SQs (**Figure 9**).<sup>38</sup>

Based on previous findings, heterotriangulene (HT) is an important planar unit,<sup>39,40</sup> after further synthetic modifications that can provide scientifically relevant n-type or p-type organic materials and able to compete with the well-known classes of semiconductors.<sup>7,8</sup> Inspired by these discoveries, here, designed a series of heterotriangulene-based squaraine molecules (**NSQ2** and **KSQ1-3**) containing strong donor-strong acceptor-strong donor structure (D-A-D'). These molecules are bearing strong HT donor, SQ acceptor units and other side indolium group. The well organized columnar superstructures of HT derivatives would give better charge-carrier pathways for organic molecular devices.<sup>41</sup> The introduction of HT donor instead of N,N-diarylamino substituents in photovoltaic materials possibly lead to increase intermolecular  $\pi$ - $\pi$  overlap that broaden the absorption spectra, systematically tune the frontier orbital energy levels and also enhances the charge-transporting properties (**Figure 10**).



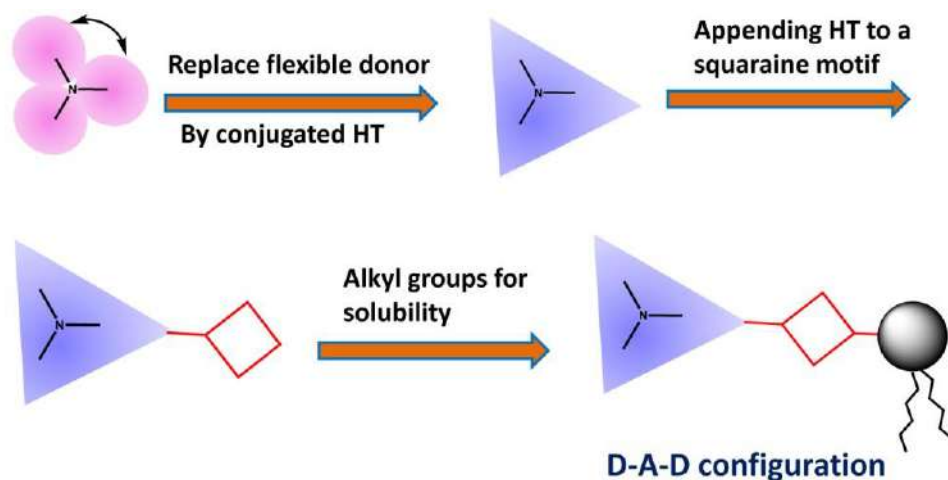


**Figure 10.** Pictorial presentation of molecular design form HT-SQ based semiconductors.

These HT derivatives of unsymmetrical squaraine have been designed to obtain highly efficient molecule possessing proper HOMO levels, high  $\epsilon$ , and broad NIR absorption in order to get high mobility. Herein, the indolium unit with different alkyl side chains represent a promising strategy for controlling the aggregation of squaraine molecules. The **NSQ2** molecules were functionalized with strong electron-withdrawing carboxylic acid group whereas **KSQ1-2** is functionalized with in-plane and out-of-plane alkyl chains. **KSQ3** are introduced with hydroxyl groups, these hydroxyl groups forms the coplanarity between the aryl ring and the four-membered SQ unit (**Figure 11**).

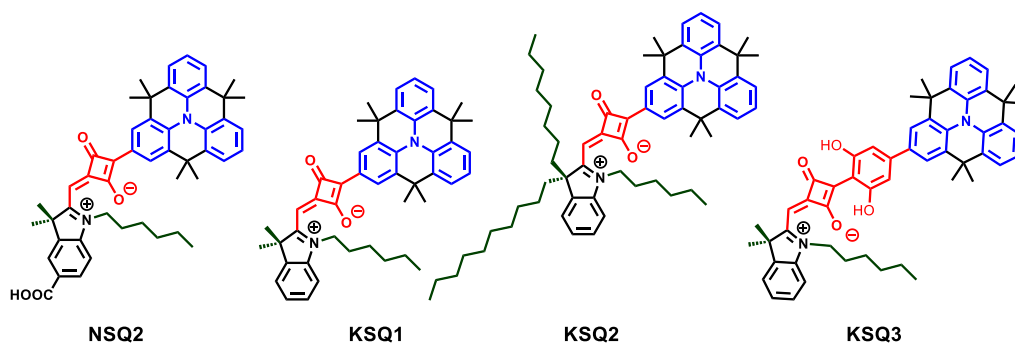


**Figure 11.** Molecular structures of **NSQ2** and **KSQ1-3** molecules.

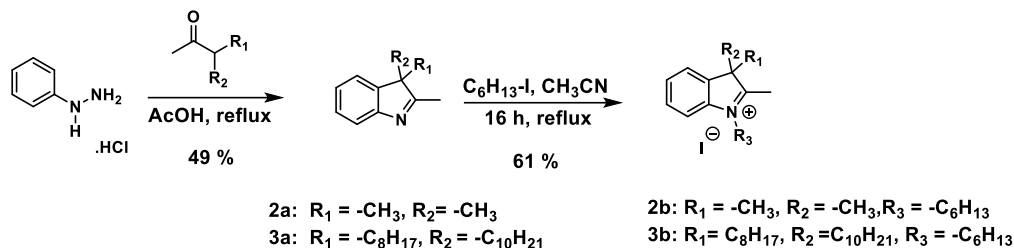
## 5.2B.2.1 EXPERIMENTAL SECTION

Characterization and Device Fabrication is similar as mentioned in 5.2A.2.1 and 5.2A.2.2 (Section A).

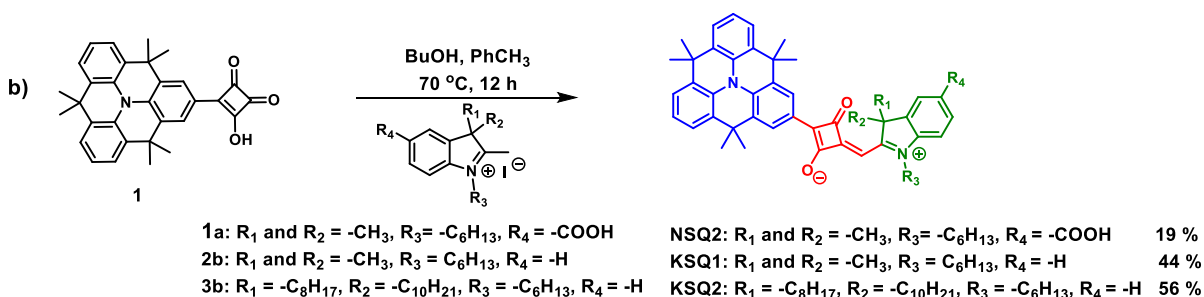
## 5.2B.2.2 SYNTHETIC PROCEDURE AND CHARACTERIZATION DATA

Synthesis of NSQ2, KSQ1 and KSQ2

a)



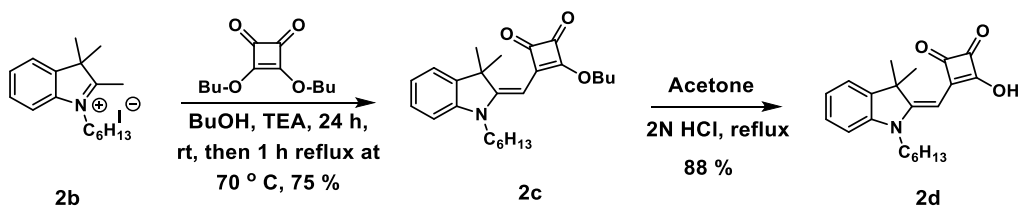
b)



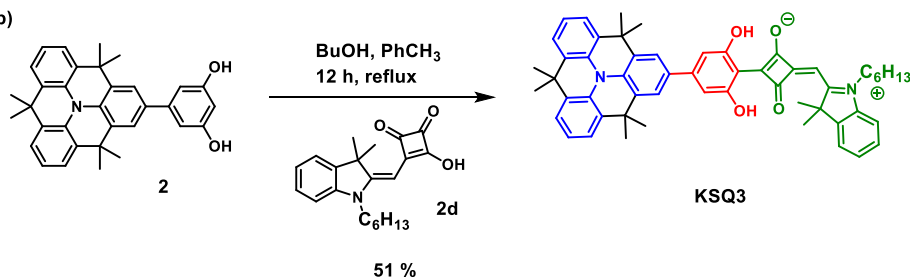
**Scheme 2.** Syntheses of (a) indolium units and (b) NSQ2, KSQ1-2 dyes.

## Synthesis of KSQ3

a)



b)



**Scheme 3.** Syntheses of (a) Semisquaraine units (2b–2d) and (b) KSQ3 dyes.

**Synthesis of 1-Hexyl-2,3,3-trimethyl-3H-indolium iodide (2b)**

2,3,3-Trimethyl-3H-indole, **2a** (1g, 6.28 mmol) and 1-iodohexane (1.6 g, 7.54 mmol) were dissolved in CH<sub>3</sub>CN (100 mL) and refluxed under nitrogen for 16 h. The solvent was evaporated and the crude product was washed with diethyl ether three times to afford **2b** (1.5 g, 78 %). <sup>1</sup>H NMR (400 MHz, CDCl<sub>3</sub>) δ: 7.67 - 7.61 (d, 1H), 7.60- 7.52 (m, 3H), 4.65 (t, J = 7.93 Hz, 2H), 3.10 (s, 3H), 1.98 - 1.86 (m, 2H), 1.64 (s, 6H), 1.50 - 1.39 (m, 2H), 1.37-1.26 (m, 4H), 0.86 (t, J = 7.02 Hz, 3H). <sup>13</sup>C NMR (100 MHz, MeOH-*d*<sub>4</sub>) δ: 195.6, 141.7, 141.0, 130.2, 129.6, 123.5, 115.4, 54.8, 50.2, 31.2, 28.0, 26.5, 23.3, 22.4, 17.2, 13.9. HRMS (ESI): m/z Calcd for C<sub>17</sub>H<sub>26</sub>N [M]<sup>+</sup>, 244.2060; found, 244.2059.

**Synthesis of (E)-3-((1-Hexyl-3, 3-dimethylindolin-2-ylidene)methyl)-4-hydroxycyclobut-3-ene-1,2-dione (2c)**

In a 50 mL round bottom flask, 1-Hexyl-2,3,3-trimethyl-3H-indol-1-ium iodide (**2b**, 1 g, 2.69 mmol) and 3,4-Dibutoxy-3-cyclobutene-1,2-dione (0.73 g, 3.23 mmol, 1.2 equiv) were dissolved in butanol (10 mL). Then dry triethylamine (2 mL) was added and stirred for 24 hrs at room temperature, then refluxed at 70 °C for 1 h. The solvent was removed under reduced pressure and the crude product was purified by column chromatography (silica gel) with ethyl acetate/pet ether as eluent to afford **2c** (0.8 g, 75 %). <sup>1</sup>H NMR (500 MHz, CDCl<sub>3</sub>) δ: 7.28 (d, J = 7.25 Hz, 2H), 7.08 (t, J = 7.25 Hz, 1H), 6.88 (d, J = 8.01 Hz, 1H), 5.42 (s, 1H), 4.86 (t, 2H), 3.81 (t, 2H), 1.87 (quin, J = 7.15 Hz, 2H), 1.77 - 1.72 (m, 2H), 1.56 - 1.49 (m, 2H), 1.45 - 1.39 (m, 2H), 1.38 - 1.31 (m, 4H), 1.01 (t, J = 7.44 Hz, 3H), 0.90 (t, J = 6.87 Hz, 3H). <sup>13</sup>C NMR (125 MHz, CDCl<sub>3</sub>) δ: 192.8, 187.7, 187.6, 173.7, 168.4, 142.8, 141.0, 127.9, 122.8, 122.1, 108.5, 81.3, 73.8, 48.0, 43.1, 32.3, 31.5, 27.1, 26.8, 26.4, 22.6, 18.8, 14.1, 13.8. HRMS (ESI): m/z Calcd for C<sub>25</sub>H<sub>34</sub>NO<sub>3</sub> [M + H]<sup>+</sup>, 396.2533; found, 396.2526.

**Synthesis of (E)-3-((1-Hexyl-3, 3-dimethylindolin-2-ylidene)methyl)-4-hydroxycyclobut-3-ene-1,2-dione (2d)**

In a 50 mL round bottom flask, Compounds **2c** and (1 g, 2.53 mmol) were dissolved in acetone (15 mL). Then 2 N HCl (2 mL) was added and refluxed for 8 h. The solvent was removed under reduced pressure to afford **2d** (0.75 g, 88 %) and the product was used without any further purification. <sup>1</sup>H NMR (500 MHz, CDCl<sub>3</sub>) δ: 7.34 - 7.27 (m, 2H), 7.18

- 7.11 (m, 1H), 6.95 (d,  $J = 7.63$  Hz, 1H), 5.66 (br. s., 1H), 3.90 (br. s., 2H), 1.77 (m, 2H), 1.66 (s, 6H), 1.45 - 1.39 (m, 2H), 1.28 - 1.37 (m, 4H), 0.90 (t, 3H).  $^{13}\text{C}$  NMR (100 MHz,  $\text{CDCl}_3$ )  $\delta$ : 187.7, 170.6, 158.1, 142.6, 141.5, 128.0, 123.6, 122.3, 109.2, 82.4, 48.7, 43.6, 31.6, 27.0, 26.8, 26.7, 22.6, 14.1. HRMS (ESI):  $m/z$  Calcd for  $\text{C}_{21}\text{H}_{25}\text{NO}_3$   $[\text{M}]^+$ , 339.1829; found, 339.1823.

### Synthesis of 3-Decyl-2-methyl-3-octyl-3H-indole (3a)

Phenylhydrazine hydrochloride (2 g, 13.83 mmol) and 3-Octyltridecan-2-one (5.2 g, 16.60 mmol) were dissolved into glacial acetic acid (15 mL) and refluxed under nitrogen for 12 h. The mixture was cooled and the solvent was removed under reduced pressure. The crude product was extracted with  $\text{CH}_2\text{Cl}_2$ , washed with saturated solution of  $\text{NaHCO}_3$ , dried over  $\text{Na}_2\text{SO}_4$  and solvent was evaporated. The reaction mixture was purified by column chromatography (silica gel) with ethyl acetate/pet ether as eluent to afford **3a** (2.6 g, 49 %) as a light red liquid.  $^1\text{H}$  NMR (500 MHz,  $\text{CDCl}_3$ )  $\delta$ : 7.50 (d,  $J = 7.63$  Hz, 1H), 7.30 - 7.27 (m, 1H), 7.17 (d,  $J = 7.63$  Hz, 2H), 2.19 (s, 3H), 1.85 (m, 2H), 1.70 (m, 2H), 1.15 - 1.27 (m, 10H), 1.15 - 1.04 (m, 14H), 0.87 - 0.79 (m, 6H), 0.75 - 0.63 (m, 2H), 0.59 - 0.51 (m, 2H).  $^{13}\text{C}$  NMR (125 MHz,  $\text{CDCl}_3$ )  $\delta$ : 186.6, 155.4, 142.4, 127.5, 125.0, 121.7, 119.7, 62.8, 37.1, 32.0, 31.9, 29.9, 29.6, 29.6, 29.4, 29.3, 29.3, 23.7, 22.8, 22.7, 16.2, 14.2, 14.2. HRMS (ESI):  $m/z$  Calcd for  $\text{C}_{27}\text{H}_{46}\text{N}$   $[\text{M} + \text{H}]^+$ , 384.3625; found, 384.3618.

### 3-Decyl-1-hexyl-2-methyl-3-octyl-3H-indol-1-ium iodide (3b)

3-Decyl-2-methyl-3-octyl-3H-indole **3a** (1.5 g, 3.9 mmol) and 1-Iodo-hexane (1.7 g, 7.8 mmol) were dissolved in MeCN (15 mL) in a 25 mL round bottom flask and refluxed at 100 °C under nitrogen for 16 h. The solvent was evaporated and the crude product was purified by silica gel chromatography to afford **3b** (1.4 g, 61 %) as a light red liquid.  $^1\text{H}$  NMR (500 MHz,  $\text{CDCl}_3$ )  $\delta$ : 7.76 (d,  $J = 7.25$  Hz, 1H), 7.64 - 7.57 (m, 2H), 7.50 (d,  $J = 7.25$  Hz, 1H), 4.84 (t, 2H), 3.10 (s, 3H), 2.15 (m, 2H), 2.06 (m, 2H), 1.89 (m, 2H), 1.48 (m, 2H), 1.36 - 1.22 (m, 6H), 1.19 (m, 4H), 1.15 (br. s., 9H), 1.08 (br. s., 11H), 0.87 - 0.77 (m, 9H), 0.61 - 0.52 (m, 2H).  $^{13}\text{C}$  NMR (125 MHz,  $\text{CDCl}_3$ )  $\delta$ : 195.7, 142.3, 138.9, 130.2, 129.8, 123.7, 115.5, 63.8, 50.5, 37.4, 31.8, 31.7, 31.3, 29.4, 29.2, 29.0, 29.0, 28.6,

26.6, 24.0, 22.6, 22.6, 22.4, 17.4, 14.1, 14.1, 14.0. HRMS (ESI):  $m/z$  Calcd for  $C_{33}H_{58}N$   $[M]^+$ , 468.4564; found, 468.4516.

### General synthesis of KSQ1 and KSQ2

3-(4,4,8,8,12,12-Hexamethyl-8,12-dihydro-4H-benzo[9,1]quinolizino[3,4,5,6,7-defg]acridin-2-yl)-4-hydroxycyclobut-3-ene-1,2-dione (**1**) (0.2 g, 0.43 mmol) and compound **2b** or **3b** (1.1 eq.) were added into toluene (6 mL) and 1-butanol (6 mL) was added into a 25 mL round bottom flask and refluxed with a Dean–Stark apparatus for 12 h. Then solvent was removed under reduced pressure and the residue was purified by column chromatography on silica with methanol/dichloromethane as eluent to afford **KSQ1** or **KSQ2** as a blue solid.

**KSQ1**: 0.13g (44 %).  $^1H$  NMR (500 MHz,  $CDCl_3$ )  $\delta$ : 8.41 (s, 2H), 7.47 (d,  $J = 7.25$  Hz, 1H), 7.42 (m, 5H), 7.30 - 7.36 (m, 1H), 7.15 - 7.22 (m, 3H), 6.30 (s, 1H), 4.21 (t, 2H), 1.88 (s, 6H), 1.76 (m, 2H), 1.68 (s, 12H), 1.66 (s, 6H), 1.49- 1.44 (m, 2H), 1.39 - 1.30 (m, 4H), 0.89 (t, 3H).  $^{13}C$  NMR (125 MHz,  $CDCl_3$ )  $\delta$ : 192.1, 184.9, 180.8, 177.0, 172.6, 143.3, 141.5, 135.2, 131.1, 131.0, 130.8, 130.3, 128.4, 126.6, 124.3, 124.0, 123.8, 123.7, 122.9, 111.5, 90.2, 51.3, 45.1, 35.8, 35.6, 34.1, 32.8, 31.5, 27.7, 26.7, 26.4, 22.6, 14.1. HRMS (ESI):  $m/z$  Calcd for  $C_{48}H_{50}N_2O_2$   $[M]^+$ , 686.3867; found, 686.3854.

**KSQ2**: 0.22g (56 %).  $^1H$  NMR (400 MHz,  $CDCl_3$ )  $\delta$ : 8.41 (s, 2 H), 7.47 - 7.38 (m, 6 H), 7.36 (d,  $J = 7.3$  Hz, 1 H), 7.23 - 7.14 (m, 3 H), 6.34 (s, 1 H), 4.26 (br. s., 2 H), 3.09 (br. s., 2 H), 2.14 - 2.01 (m, 2 H), 1.85 (m, 2 H), 1.69 (s, 12 H), 1.66 (s, 6 H), 1.50 - 1.41 (m, 2 H), 1.37 - 1.29 (m, 4 H), 1.11 (br. s., 14 H), 1.03 (br. s., 12 H), 0.89 (t, 3 H), 0.80 - 0.71 (m, 6 H), 0.43 (br. s., 2 H).  $^{13}C$  NMR (100 MHz,  $CDCl_3$ )  $\delta$ : 185.1, 180.5, 175.9, 143.5, 140.2, 135.0, 131.1, 131.0, 130.8, 130.3, 128.4, 126.7, 126.5, 124.2, 123.9, 123.8, 123.7, 122.9, 111.2, 90.8, 60.8, 45.3, 40.0, 35.8, 35.6, 34.0, 33.0, 32.0, 31.9, 31.6, 29.6, 29.6, 29.5, 29.4, 29.3, 29.3, 29.2, 28.0, 27.0, 24.1, 22.7, 22.7, 22.6, 14.2, 14.1. HRMS (ESI):  $m/z$  Calcd for  $C_{64}H_{82}N_2O_2$   $[M]^+$ , 910.6371; found, 910.6366.

### Synthesis of KSQ3

5-(4,4,8,8,12,12-Hexamethyl-8,12-dihydro-4H-benzo[9,1]quinolizino[3,4,5,6,7-defg]acridin-2-yl)benzene-1,3-diol **2** (150 mg, 0.32 mmol) and compound **2d** (1.1 eq.) were added into toluene (5 mL) and 1-butanol (5 mL) was added into a 25 mL round

bottom flask and refluxed with a Dean–Stark apparatus for 12 h. Then solvent was removed under reduced pressure and the residue was purified by column chromatography on silica with methanol/dichloromethane as eluent to afford **KSQ3** as a blue solid.

**KSQ3**: 0.130 g, (51 %).  $^1\text{H}$  NMR (500 MHz,  $\text{CDCl}_3$ )  $\delta$ : 12.04 (s, 1 H), 12.02 (s, 1 H), 7.70 (s, 2 H), 7.49 (d,  $J = 7.2$  Hz, 1 H), 7.45 - 7.35 (m, 6 H), 7.24 (d,  $J = 7.6$  Hz, 1 H), 7.15 (t,  $J = 7.6$  Hz, 2 H), 6.78 (d,  $J = 2.7$  Hz, 2 H), 6.14 (s, 1 H), 4.20 (t, 2 H), 1.87 (m, 2 H), 1.82 (s, 6 H), 1.68 (s, 12 H), 1.65 (s, 6 H), 1.49 - 1.43 (m, 2 H), 1.38 - 1.33 (m, 4 H), 0.90 (t, 3 H).  $^{13}\text{C}$  NMR (125 MHz,  $\text{CDCl}_3$ )  $\delta$ : 184.3, 181.0, 177.2, 175.3, 169.0, 161.6, 161.0, 149.5, 143.4, 141.2, 133.3, 132.8, 131.6, 130.3, 130.2, 130.1, 128.8, 127.3, 123.8, 123.7, 123.3, 122.9, 122.3, 112.0, 108.5, 106.6, 106.5, 89.9, 51.5, 45.4, 35.9, 35.6, 33.5, 33.4, 31.5, 27.9, 26.7, 26.3, 22.6, 14.1. HRMS (ESI):  $m/z$  Calcd for  $\text{C}_{54}\text{H}_{55}\text{N}_2\text{O}_4$   $[\text{M}]^+$ , 795.4156; found, 795.4136.

### 5.2B.3 RESULTS AND DISCUSSION

#### 5.2B.3.1 Synthesis and Characterization

The synthetic route for **NSQ2**, **KSQ1-2** and **KSQ3** dyes are illustrated in **Scheme 2** and **3**. The synthetic procedure for **1** and **NSQ2** are provided in section 2.2.4. The synthesis of **KSQ1** and **KSQ2** requires 3-(4,4,8,8,12,12-hexamethyl-8,12-dihydro-4H-benzo[9,1]quinolizino[3,4,5,6,7-defg]acridin-2-yl)-4-hydroxycyclobut-3-ene-1,2 dione (**2**) which is synthesized according to section 2.2.4. 3-octyltridecan-2-one<sup>39</sup> (Section 2.2.4) reacted with phenylhydrazine hydrochloride to give the intermediate **3a**. Then, the corresponding indolium salts (**2b** or **3b**) were prepared by reacting 2,3,3-trimethyl-3H-indole (**2a**) or **3a** with alkyl halide to get with either N- or sp<sup>3</sup>-C or both atoms functionalized with alkyl groups. A condensation reaction between semi-squaraine derivatives **1** and indolium salts (**2b** or **3b**) provided the targeted **KSQ1** or **KSQ2** molecules. The corresponding semisquaric acid (**2d**) were synthesized by reacting indolium salts (**2b**) with 3,4-Dibutoxy-3-cyclobutene-1,2-dione followed by acid hydrolysis of **2c** derivatives. The target molecules of **KSQ3** were obtained via a condensation reaction between compounds of **2** (section 4.3.1) and **2d**. All the final molecules have good solubility in CH<sub>2</sub>Cl<sub>2</sub>, CHCl<sub>3</sub>, CH<sub>3</sub>CN and THF. All the intermediates and final molecules were confirmed by <sup>1</sup>H- and <sup>13</sup>C-NMR spectroscopy and mass spectrometry (ESI-MS). NMR spectra are provided in 5.3 NMR data (Section B).

#### 5.2B.3.2 Photophysical properties

The absorption and emission properties of all the molecules in CH<sub>2</sub>Cl<sub>2</sub> solution are listed in **Table 2**, and spectra are given in **Figure 12**. In solution, **NSQ1** displayed an intense band with  $\lambda_{\text{max}}$  of 681 nm whereas **KSQ1-3** showed peak maxima of 652 nm, which are ascribed to an ICT absorption process.<sup>35</sup> **NSQ2** and **KSQ1-3** showed fluoresce in the wavelength range of 720-780 nm. **KSQ3** displayed larger Stokes shifts of 123 nm whereas other squaraine molecules showed around 70 nm. The large Stokes shifts obtained for **KSQ3** suggested that excited state formation in the **KSQ3** is accompanied by a larger degree of intramolecular distortion than in **NSQ2** and **KSQ1-2**. In addition, absorbance spectra of all squaraine dyes were also recorded in THF and CH<sub>3</sub>CN (**Figure**

**12b** and **12c**). The  $\lambda_{\max}$  is blue shifted with increasing solvent polarity (negative solvatochromism). The solvatochromic response showed that the ground states of all squaraine molecules are more polarizable and also strongly stabilized by polar media.<sup>42</sup>

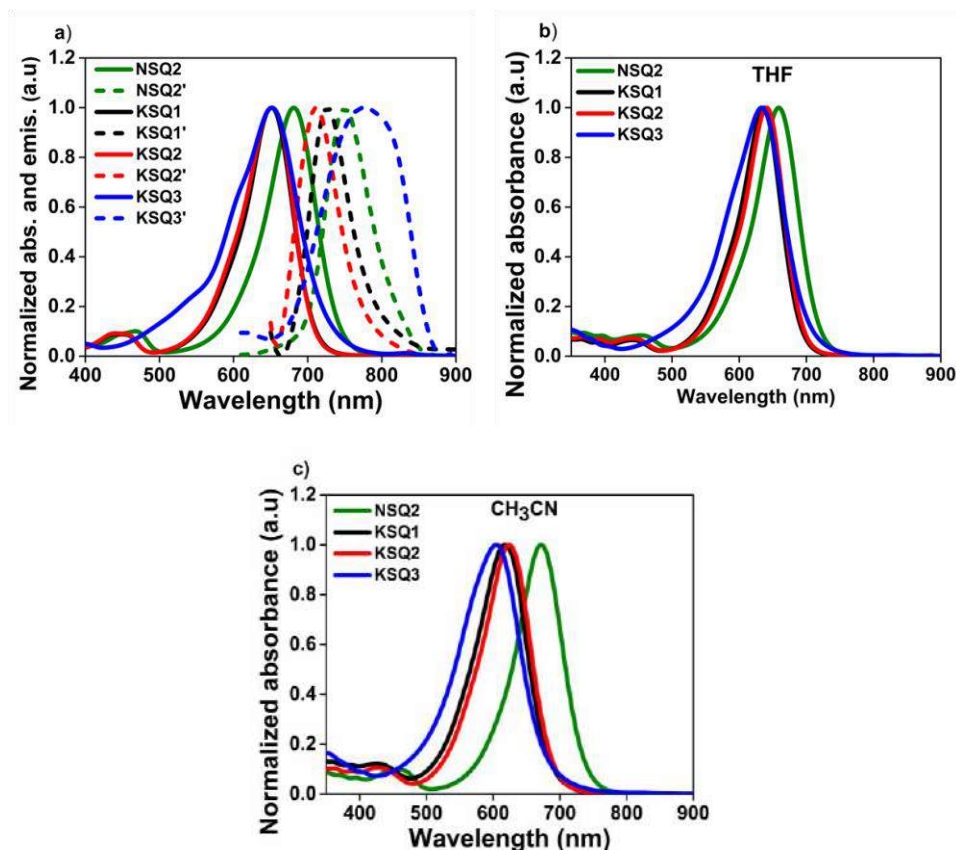


**Figure 12.** (a) Absorption (solid lines) and emission (dotted lines) spectra for **NSQ2** and **KSQ1-3** in  $\text{CH}_2\text{Cl}_2$  solution [excitation wavelength for **NSQ2** and **KSQ3** 600 nm and **KSQ1-2** 640 nm], b) and c) Absorbance spectra of the squaraine dyes in THF and  $\text{CH}_3\text{CN}$  solution.

SQ dyes usually show well-defined aggregation properties that are known to affect absorption bands both in solution and in the solid films. Aggregates with narrow absorption bands that shifts to longer (red-shift) or short wavelengths (blue-shift) with respect to the monomer band are denoted as J- or H-aggregates. Therefore, owing to strong inter-molecular coupling aggregation gives an opportunity to tune the energy levels and improve charge carrier mobilities of thin films. Herein, the absorption spectra for all squaraine molecules showed red-shift and undergo noteworthy broadening in thin



films (**Figure 13**) compared to the solution signifying considerable aggregation in the film.<sup>43</sup> As a result, broadened absorption spectrum of active layer and controlled aggregation states of SQ dyes modify the film morphologies of materials for enhancing the charge transport. Thermal annealing is the process to know different aggregation states of SQ dyes in solid films. The film annealing at 100 °C showed the small change in absorption spectra. This elucidates a degree of ordering in the film upon annealing, mainly expected due to the reorientation of the alkyl groups allowing for better packing.<sup>26</sup>

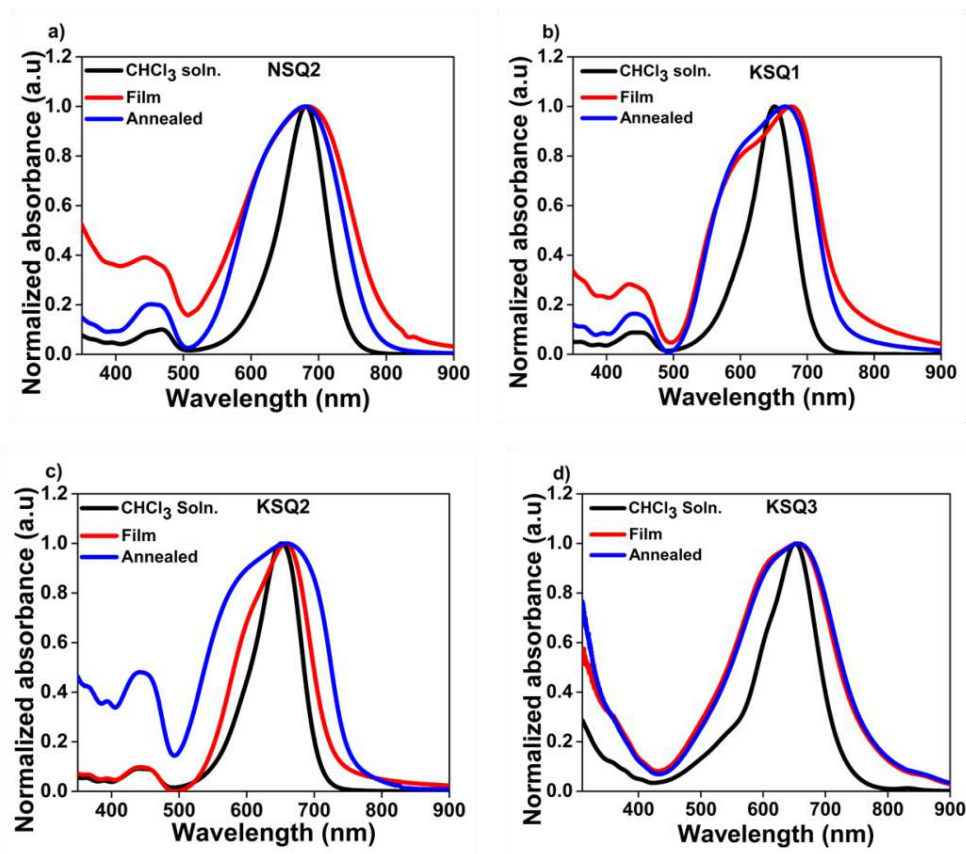


**Figure 13.** Absorbance spectra of the squaraine dyes in thin film a) NSQ2, b) KSQ1, c) KSQ2 and d) KSQ3.

**Table 2.** Photophysical and electrochemical Properties of the **NSQ2** and **KSQ1-3**

Dyes	$\lambda_{\max}$ / CHCl <sub>3</sub> (nm) <sup>a</sup>	$\varepsilon \times 10^4$ (M <sup>-1</sup> cm <sup>-1</sup> ) <sup>b</sup>	$\lambda_{\max}$ /em (nm) <sup>a</sup>	$E_{g/DFT}$ (eV)	$E_{0-0}$ (eV) <sup>c</sup>	$E_{HOMO}$ (eV vs Fc/Fc <sup>+</sup> ) <sup>d</sup>	$E_{LUMO}$ (eV vs Fc/Fc <sup>+</sup> ) <sup>e</sup>
<b>NSQ2</b>	681, 468	15.5, 1.6	751	2.01	1.73	-4.98	-3.25
<b>KSQ1</b>	651, 442	12, 1.1	727	2.09	1.79	-4.90	-3.11
<b>KSQ2</b>	652, 443	11.2, 1.07	711	2.07	1.82	-4.91	-3.09
<b>KSQ3</b>	652	6.74	775	2.14	1.77	-5.0	-3.23

<sup>a</sup>Absorption and emission spectra were recorded in CHCl<sub>3</sub>, <sup>b</sup>Molar extinction coefficients ( $\varepsilon$ ) were measured in CHCl<sub>3</sub>, <sup>c</sup>Optical energy gaps ( $E_{0-0}$ ) were deduced from the intersection of absorption and emission spectra,  $E_{0-0}$  (eV) = 1240/ $\lambda$ , <sup>d</sup>HOMO were calculated following the equation  $E_{HOMO} = -(E_{ox} + 4.8)$  eV and <sup>e</sup> $E_{LUMO}$  was calculated from  $E_{LUMO}$  (V vs NHE) =  $E_{HOMO} - E_{0-0}$  and calibrated with respect to the external standard Fc/Fc<sup>+</sup> couple.

### 5.2B.3.3 Electrochemical Properties

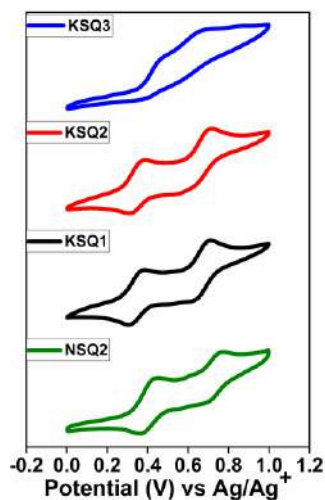


**Figure 14.** Cyclic voltammograms of **NSQ2** and **KSQ1-3** in CH<sub>2</sub>Cl<sub>2</sub> with TBAClO<sub>4</sub> (0.1 M) at the scan rate of 50 mV s<sup>-1</sup>.

The HOMO and LUMO energy levels as well as the electrochemical band gap,  $E_g$  elec, were determined by cyclic voltammetry (CV) as shown in **Figure 14**.<sup>38</sup> Electrochemical

analysis of **NSQ2** and **KSQ1-3** were performed in  $\text{CH}_2\text{Cl}_2$  and referenced to  $\text{Fc}/\text{Fc}^+$  as an external standard and the results are summarized in **Table 2**. **NSQ2** and **KSQ1-3** showed reversible or quasi-reversible oxidation peak of **NSQ2** at 0.31 V and for **KSQ1-3** at 0.26 (**KSQ1**), 0.27 (**KSQ2**) and 0.36 (**KSQ3**) V vs.  $\text{Fc}/\text{Fc}^+$ . The holes injection into the HOMO level was easily achieved using gold electrodes for p-channel transistors because the HOMO level of all the squaraine molecules is in the range of -4.9 to -5.0 eV, which aligned better with the work function of gold (-4.8 eV).

#### 5.2B.3.4 Theoretical Investigations

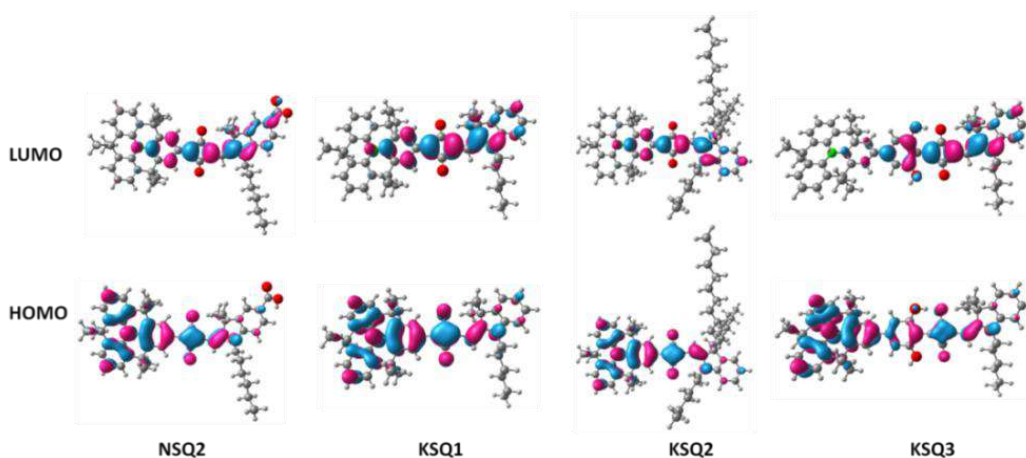


**Figure 15.** HOMO and LUMO isosurface plots for **NSQ2** and **KSQ1-3**.

DFT calculations were performed using Gaussian 09 at the B3LYP/6-31G (d, p) basis set in order to get additional insight into the change in charge carrier polarity (**Figure 15**).<sup>19</sup> In all the squaraine molecules the electron density of HOMO orbital is strongly delocalized over the donor part and SQ unit whereas the LUMO orbital is mainly distributed over the  $\pi$ -spacer, squaraine unit and the indolium unit.<sup>38</sup> There are no considerable differences in the surfaces of the HOMO and LUMO energy levels of all these molecules.

#### 5.2B.3.5 Thin film morphology

To understand the substituent effects on solid-state packing, thin film XRD of all squaraine molecules was recorded (**Figure 16**). XRD pattern of this drop casted film of all molecules showed broadened peak owing to their amorphous nature. These results

indicated broad and diffuse scattering pattern, it confirmed the alkyl substituent afforded a more compact packing owing to strong intermolecular  $\pi$ - $\pi$  stacking in the solid films.<sup>9</sup>

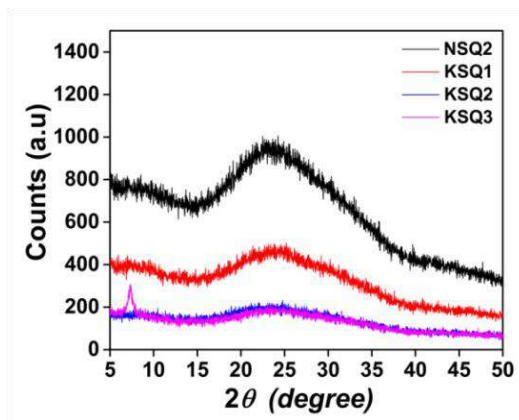


**Figure 16.** XRD patterns of self-assemblies of NSQ2 and KSQ1-3.

### 5.2B.3.6 Thermal gravimetric analysis

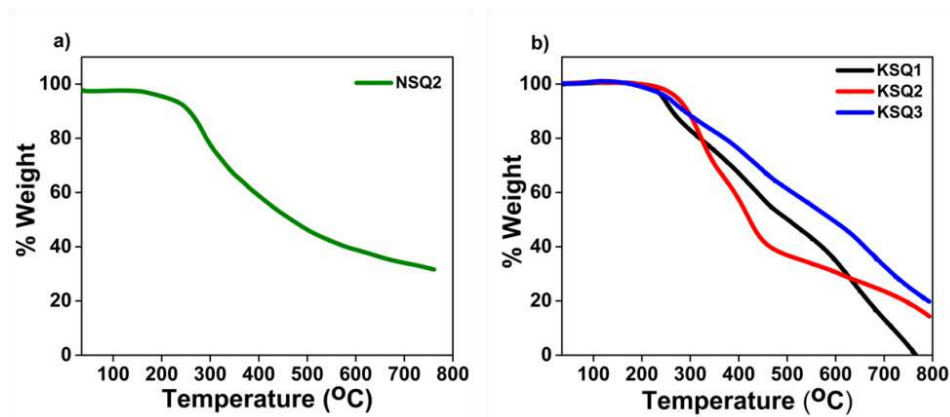


**Figure 17.** TGA plots of NSQ2 and KSQ1-3 with a heating rate of 10 °C min<sup>-1</sup> under N<sub>2</sub> atmosphere.

TGA was performed to evaluate the thermal stability of all squaraine molecules (**Figure 17**).<sup>34</sup> These molecules were found stable up to 200 °C and undergo 5% weight loss at 240 °C. All molecules are moderately thermally stable and can be used for making high-temperatures devices in the construction of OFETs.<sup>9</sup>

### 5.2B.3.7 Charge-Transport Properties

These squaraine molecules were investigated for their charge-transport properties using bottom-contact field effect transistors.<sup>1,22</sup> Herein, two types of devices were fabricated (i) bare SiO<sub>2</sub> substrates ii) with silane (HMDS) modification.<sup>44</sup> HMDS modification helps to change of morphology of semiconductor film, increase the number of trap states, and create dipoles at the surface. Output characteristic curves of **NSQ2**, **KSQ1**, **KSQ2** and **KSQ3** were measured by sweeping the drain voltage ( $V_D$ ) between 0 and -100 V while keeping the gate voltage ( $V_G$ ) constant. Output and transfer characteristic curves for device fabricated with as spin coated film of **NSQ2**, **KSQ1** and **KSQ3** are given in **Figure 18**, **19**, and **20**, respectively. Output characteristic curves for **KSQ2** recorded but it did not show any standard linear and saturation regimes. One probable reason could be the irregular film formation due to hydrophobic longer alkyl chains giving improper contact between the channel and the spin coated material. Hole carrier mobilities ( $\mu_h$ ) are calculated using the standard saturation regime quadratic model equation  $I_{D,sat} = (WC_i/2L) \mu_{FET} (V_G - V_{Th})^2$ .<sup>24,26</sup> From the transfer characteristic curves, the threshold voltages for **NSQ2**, **KSQ1** and **KSQ3** calculated and the device data are given in **Table 3**, **4**.

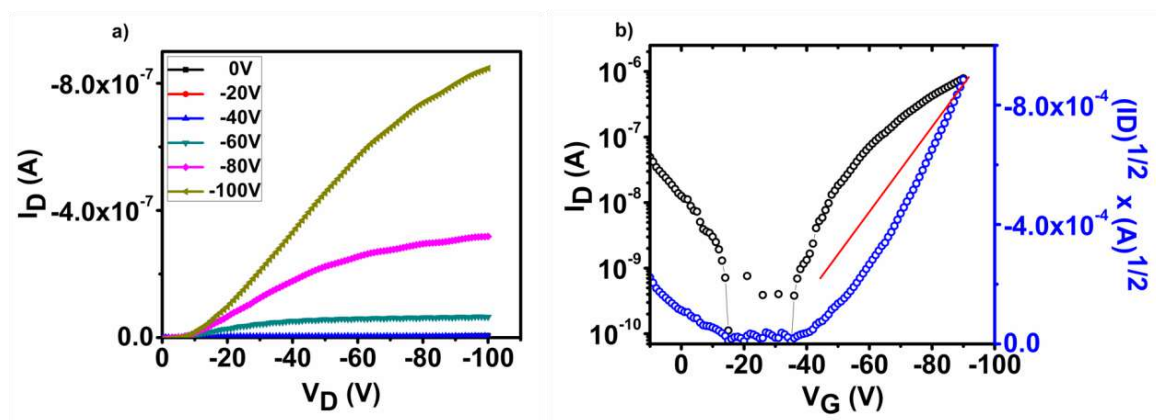


**Figure 18.** Output (a), transfer (b) characteristic curves for **NSQ2** at after annealing at 100 °C.

**Table 3.** Summary of OFET properties of **NSQ2** and **KSQ1-3** molecules with bare SiO<sub>2</sub> substrates after annealing

Compound <sup>a</sup>	$\mu_h$ (cm <sup>2</sup> V <sup>-1</sup> s <sup>-1</sup> )		$V_{Th}$ (V)	$I_{on}/I_{off}$
	Linear	Saturation		
<b>NSQ2</b>	$3.37 \times 10^{-5}$ ( $2.80 \times 10^{-5}$ ) <sup>b</sup>	$4.04 \times 10^{-5}$ ( $1.85 \times 10^{-5}$ ) <sup>b</sup>	-35	$10^4$
<b>KSQ1</b>	$2.85 \times 10^{-5}$ ( $1.29 \times 10^{-5}$ ) <sup>b</sup>	$2.74 \times 10^{-5}$ ( $1.36 \times 10^{-5}$ ) <sup>b</sup>	-45	$10^4$
<b>KSQ3</b>	$1.06 \times 10^{-5}$ ( $8.68 \times 10^{-6}$ ) <sup>b</sup>	$1.55 \times 10^{-5}$ ( $9.46 \times 10^{-6}$ ) <sup>b</sup>	-50	$10^3$

<sup>a</sup>Annealed at 100°C for 30 min, <sup>b</sup>Average mobilities.

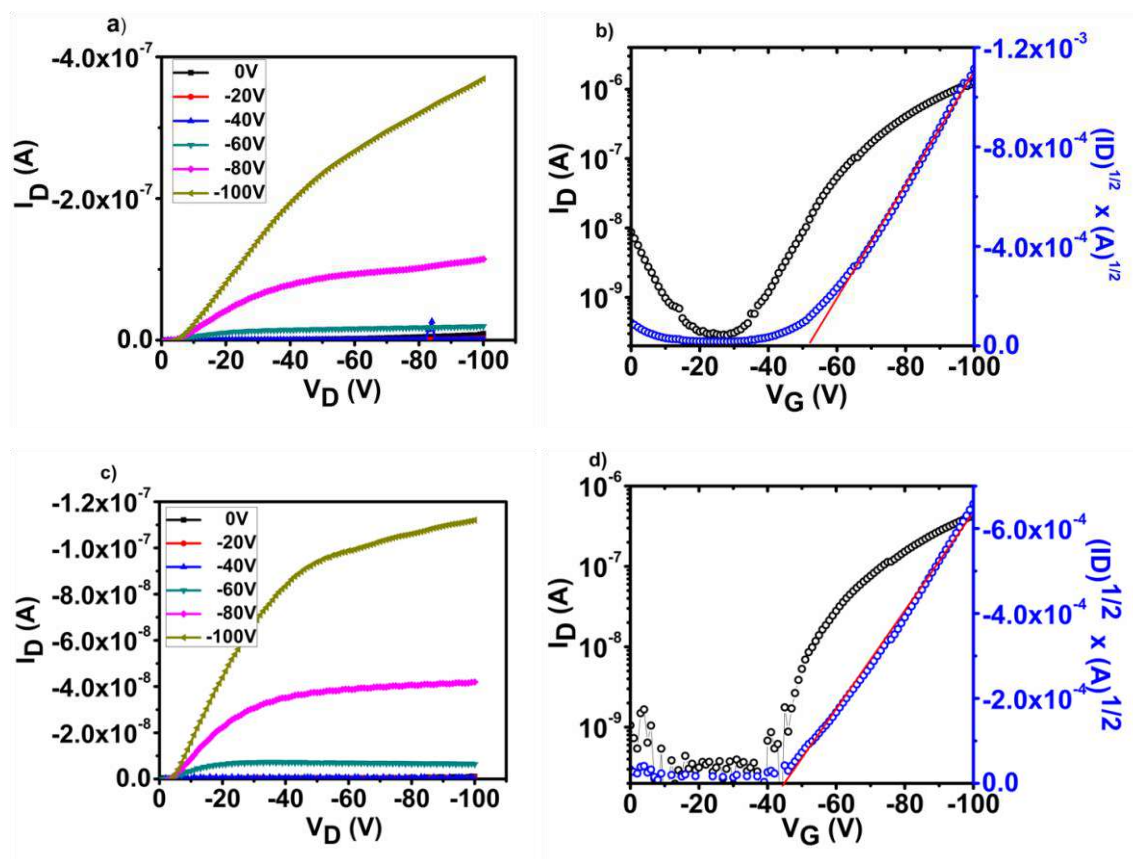


**Figure 19.** Output (a), transfer (b) for **KSQ1** ( $W = 10$  mm,  $L = 2.5$   $\mu\text{m}$ ) and output (c), transfer (d) characteristic curves for **KSQ1** ( $W = 10$  mm,  $L = 5$   $\mu\text{m}$ ) after annealing at 100 °C.

The hole carrier mobility calculated for **NSQ2** was found to be  $1.85 \times 10^{-5}$  cm<sup>2</sup> V<sup>-1</sup> s<sup>-1</sup> on bare SiO<sub>2</sub> substrate whereas on HMDS modified substrate the hole mobility was  $2.58 \times 10^{-5}$  cm<sup>2</sup> V<sup>-1</sup> s<sup>-1</sup> in saturation regime. Also, the threshold voltage is -30 V for **NSQ2** with



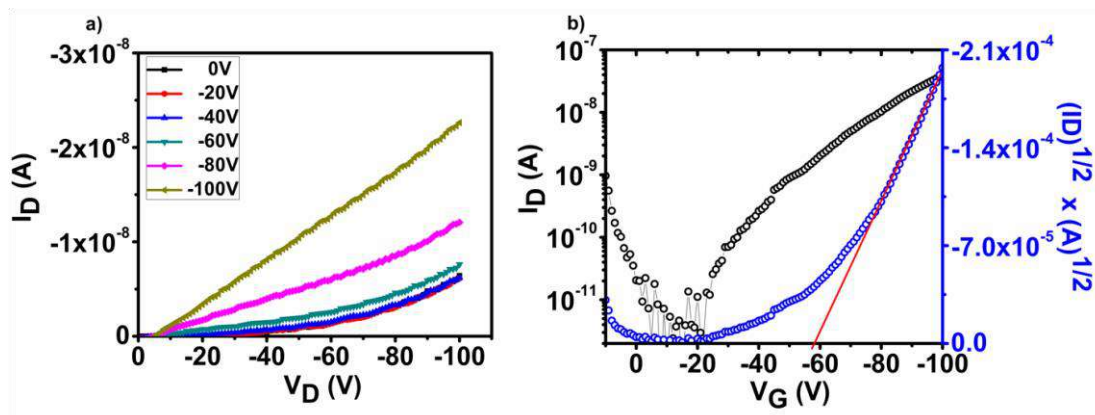
$I_{\text{on}}/I_{\text{off}}$  ratio of  $10^4$ . Average hole mobilities for **KSQ1** and **KSQ3** with HMDS modified substrate are  $4.74 \times 10^{-5} \text{ cm}^2 \text{ V}^{-1} \text{ s}^{-1}$  and  $1.68 \times 10^{-5} \text{ cm}^2 \text{ V}^{-1} \text{ s}^{-1}$ .

**Table 4.** Summary of OFET properties of **NSQ2** and **KSQ1-3** with HMDS modified substrates after annealing

Compound	$\mu_{\text{h}} (\text{cm}^2 \text{ V}^{-1} \text{ s}^{-1})$		$V_{\text{Th}}$ (V)	$I_{\text{on}}/I_{\text{off}}$
	Linear	Saturation		
<b>NSQ2</b>	$3.41 \times 10^{-5} \text{ }^{\text{a}}$	$2.58 \times 10^{-5} \text{ }^{\text{a}}$	-30	$10^4$
<b>KSQ1</b>	$4.22 \times 10^{-5} (2.740 \times 10^{-5})^{\text{a}}$	$6.08 \times 10^{-5} (4.74 \times 10^{-5})^{\text{a}}$	-41	$10^4$
<b>KSQ3</b>	$8.44 \times 10^{-6} (5.3 \times 10^{-6})^{\text{a}}$	$3.04 \times 10^{-5} (1.68 \times 10^{-5})^{\text{a}}$	-45	$10^3$

<sup>a</sup>Annealed at 100 °C for 30 min, <sup>b</sup>Average mobilities.

Molecular design modification and thermal annealing is the most efficient way to recognize different aggregation states in solid films. Optical properties of these dyes in solid film showed J- and H-type aggregates while thermal annealing showed very small improvement in broadening of their spectra as compared to without annealed film. So that means thermal annealing did not much impact to the charge transport, due to the relatively planar structure of heterotriangulene owing to strong intermolecular interactions of molecules. It is found that the heterotriangulene core and the alkyl groups are favourable for the self-assembly both in solution and in the film due to their improved the  $\pi$ - $\pi$  stacking. These HT-squaraine molecules were found to exhibit p-type charge-carrier characteristics.



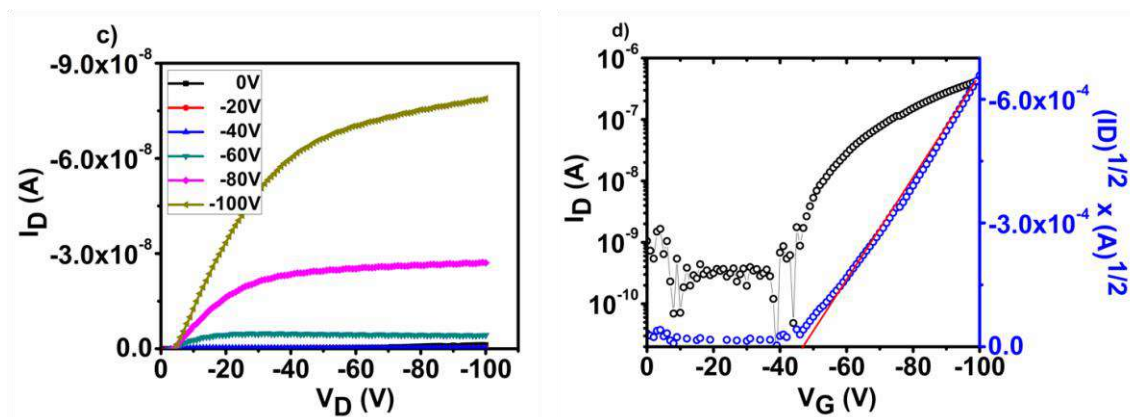


**Figure 20.** Output (a), transfer (b) for **KSQ3** ( $W = 10$  mm,  $L = 2.5$   $\mu\text{m}$ ) and output (c), transfer (d) characteristic curves for **KSQ3** ( $W = 10$  mm,  $L = 5$   $\mu\text{m}$ ) after annealing at  $100$   $^{\circ}\text{C}$ .

### 5.2B.4 Conclusion

In summary, a solution processable of HT-based unsymmetrical squaraine molecule was synthesized and characterized. All of these molecules exhibit an ICT absorption band centered on 650-680 nm with high  $\epsilon$  in the far-red and NIR region. The presence of alkyl chains robustly affects the solubility of the squaraine and accordingly the morphology of solution cast thin films. The absorption band is significantly broadened in thin film which has been credited to the expected improvement in  $\pi$ - $\pi$  interactions in the solid state. These molecules showed suitable HOMO energy levels relative to the gold electrode; thus showed a significant improved charge carrier transport. HT-squaraine molecules were investigated for hole mobility in both before and after annealing at various channel lengths, and all molecules were entirely hole-transporting materials. This study demonstrated careful combination of HT units and SQ units with variation of substituent results in new p-type semiconducting molecules.



### 5.3 NMR data (Section A)

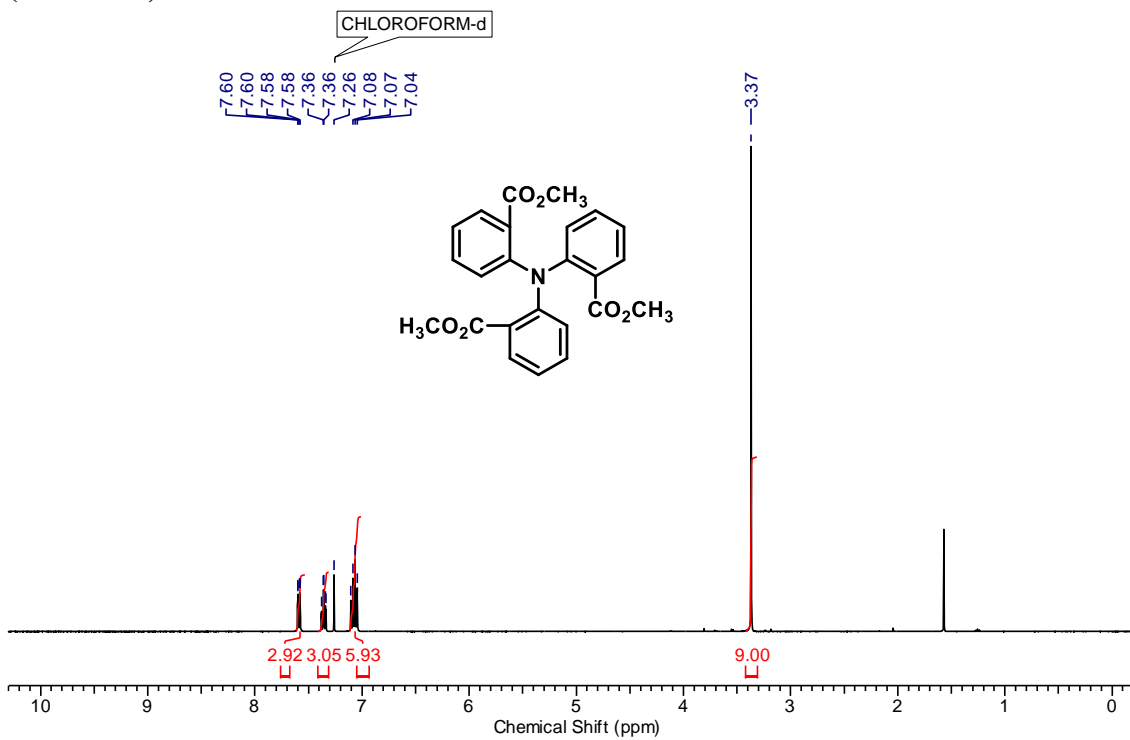


**Figure 21.** <sup>1</sup>H NMR (200 MHz, CDCl<sub>3</sub>) spectrum of compound **1a**.

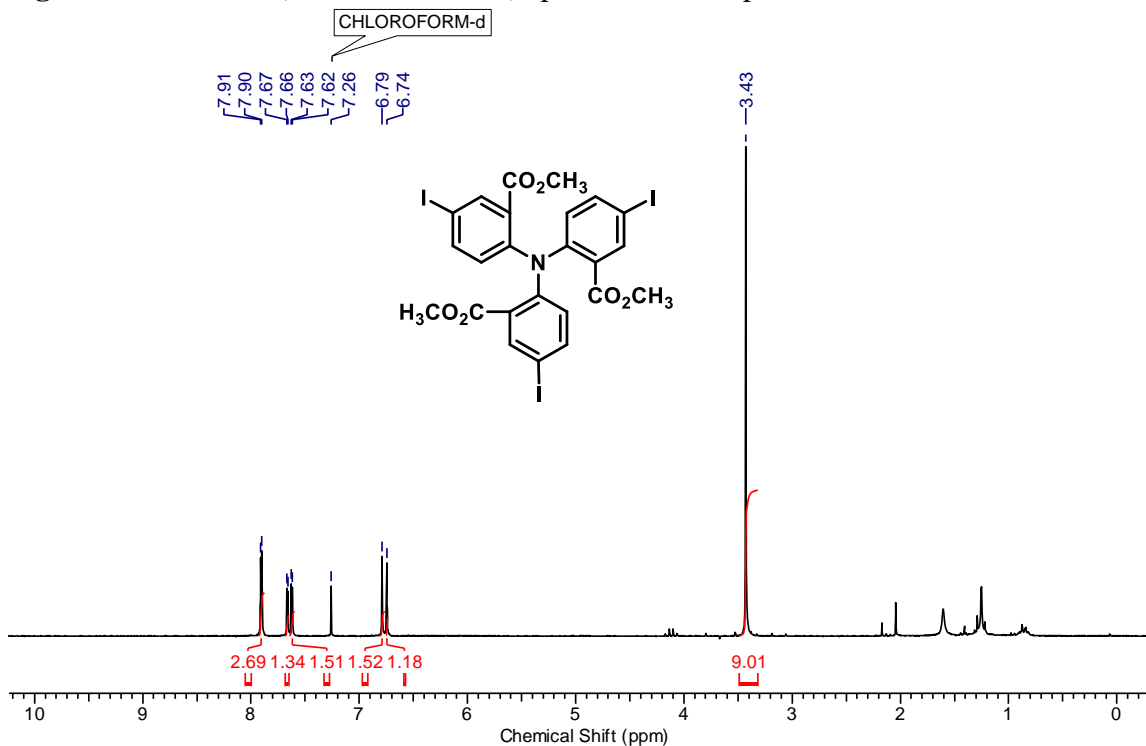


**Figure 22.** <sup>1</sup>H NMR (200 MHz, CDCl<sub>3</sub>) spectrum of compound **Trimethyl 6, 6', 6''-nitrotris(3-iodobenzoate)**.

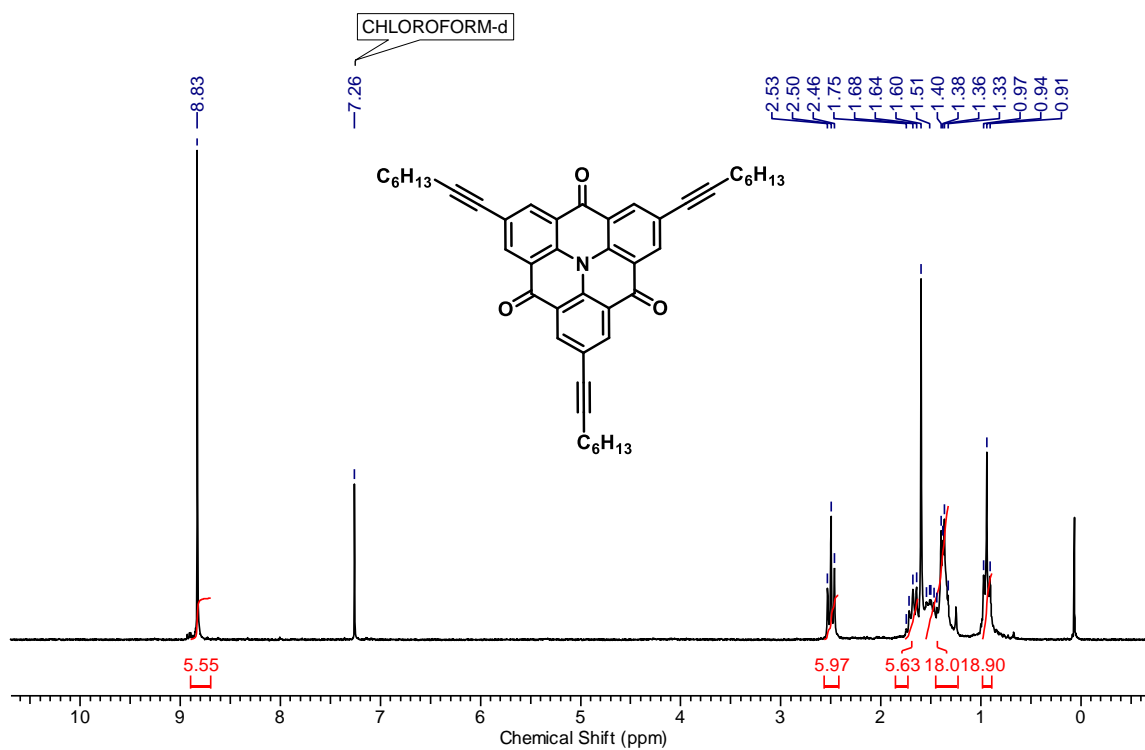


Figure 23.  $^1\text{H}$  NMR (200 MHz,  $\text{CDCl}_3$ ) spectrum of compound **4a**.

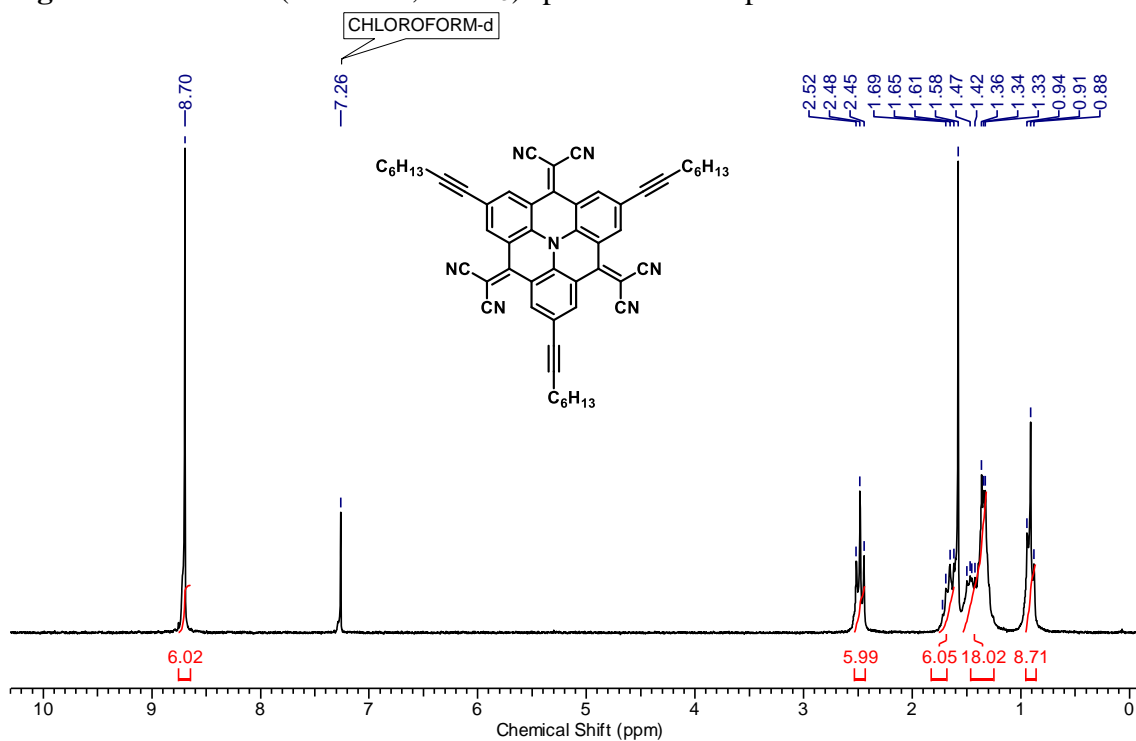


Figure 24.  $^1\text{H}$  NMR (200 MHz,  $\text{CDCl}_3$ ) spectrum of compound **NK1**.

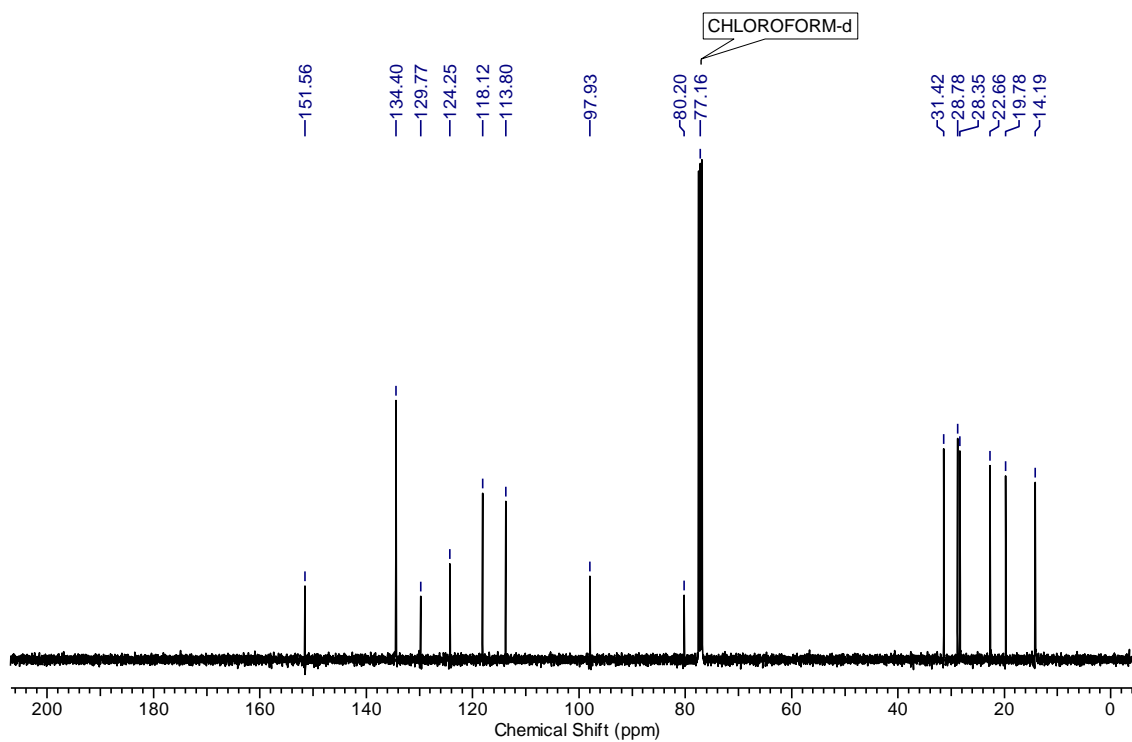


Figure 25. <sup>13</sup>C NMR (100 MHz, CDCl<sub>3</sub>) spectrum of compound NK1.

### Section B

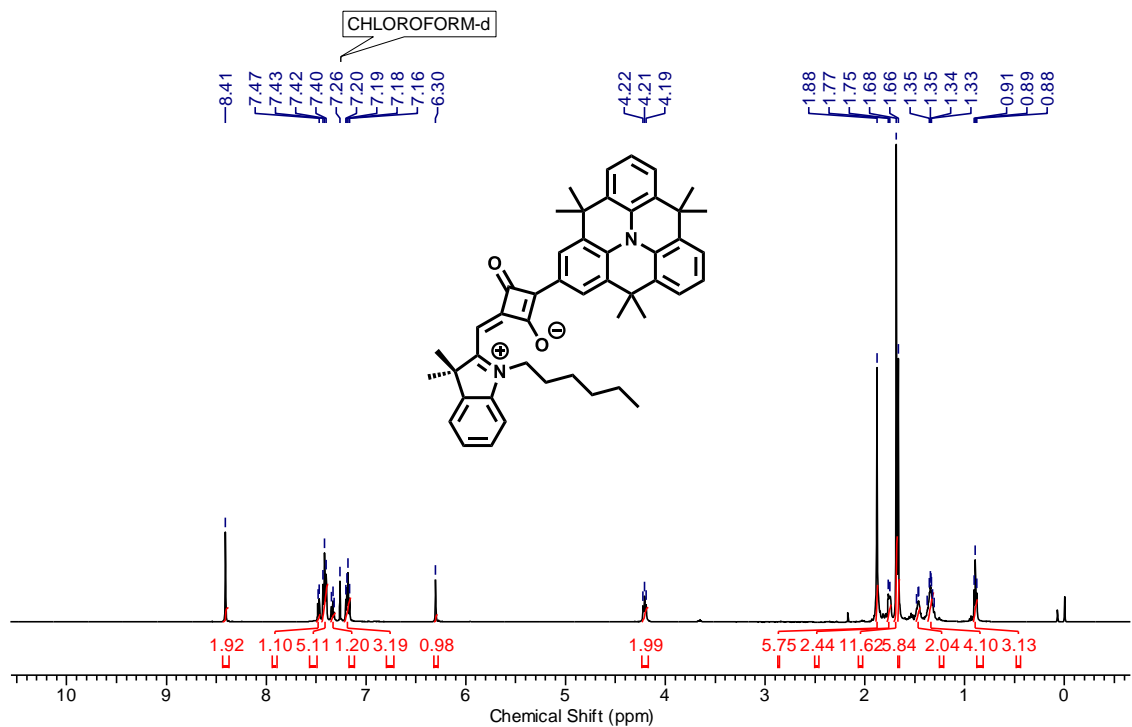


Figure 26. <sup>1</sup>H NMR (500 MHz, CDCl<sub>3</sub>) spectrum of compound KSQ1.

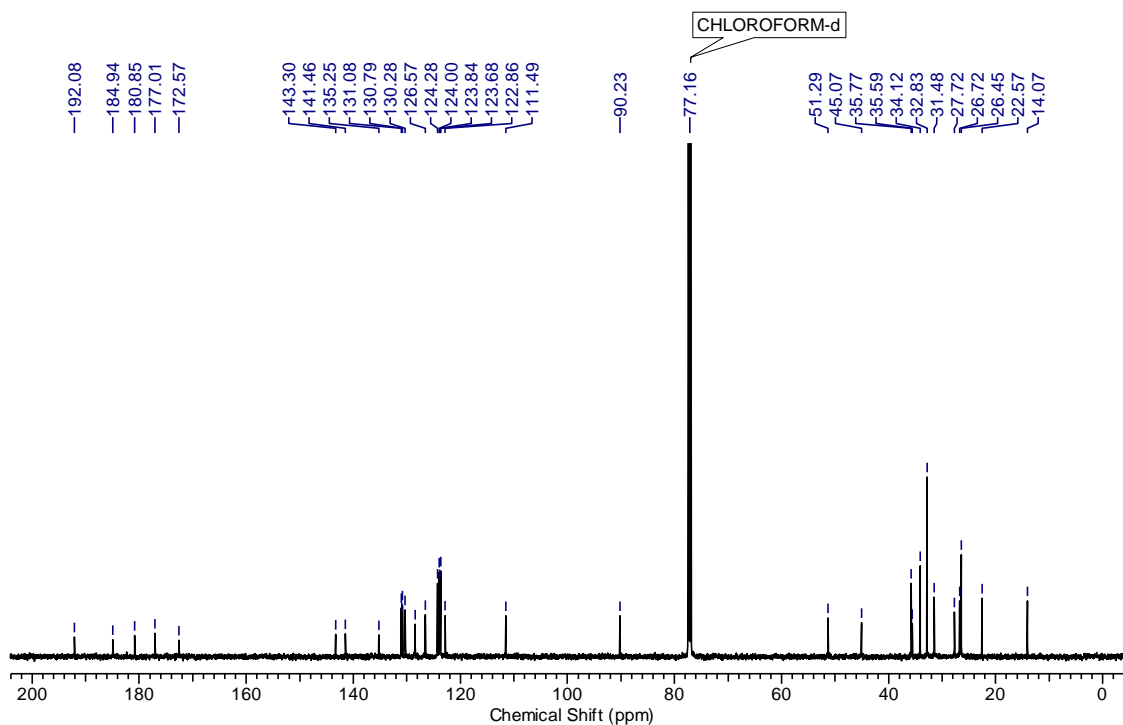


Figure 27.  $^{13}\text{C}$  NMR (125 MHz,  $\text{CDCl}_3$ ) spectrum of compound **KSQ1**.

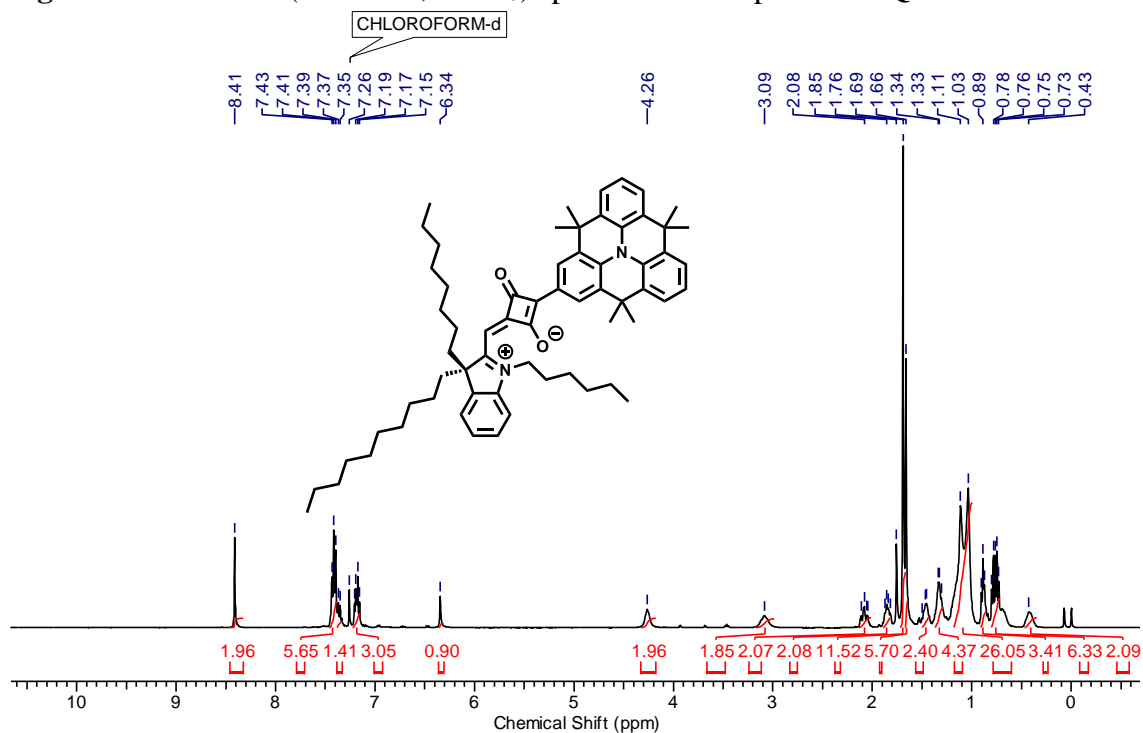


Figure 28.  $^1\text{H}$  NMR (400 MHz,  $\text{CDCl}_3$ ) spectrum of compound **KSQ2**.

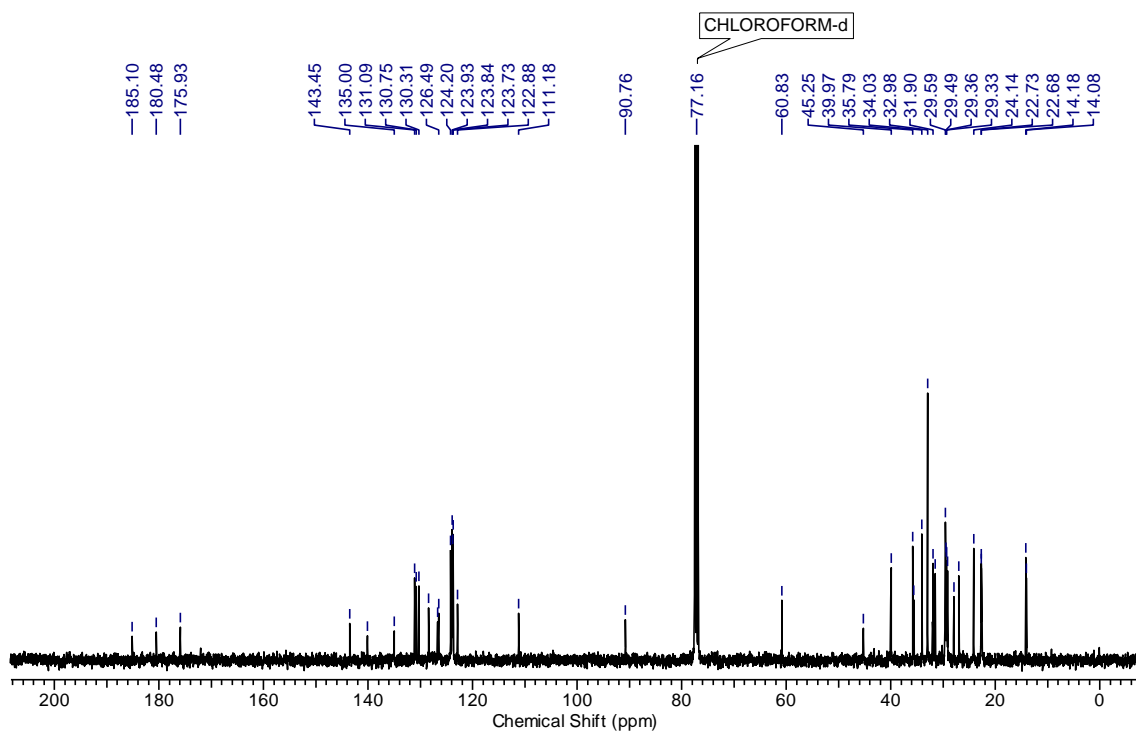


Figure 29.  $^{13}\text{C}$  NMR (100 MHz,  $\text{CDCl}_3$ ) spectrum of compound **KSQ2**.

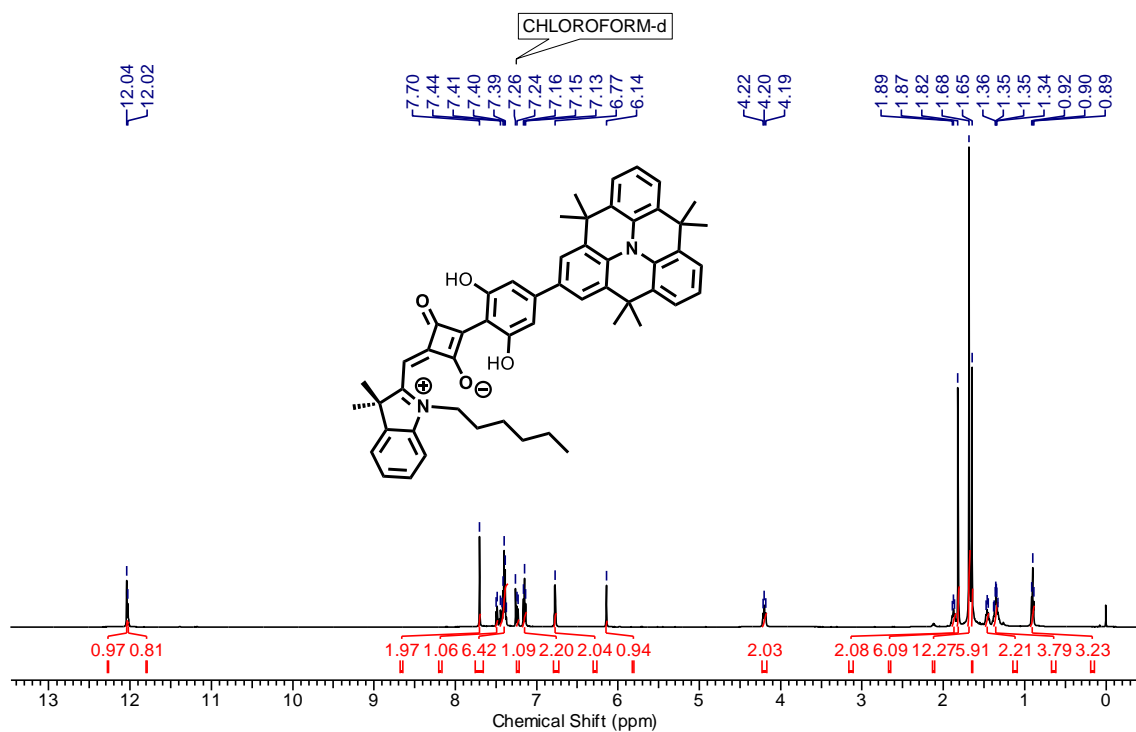
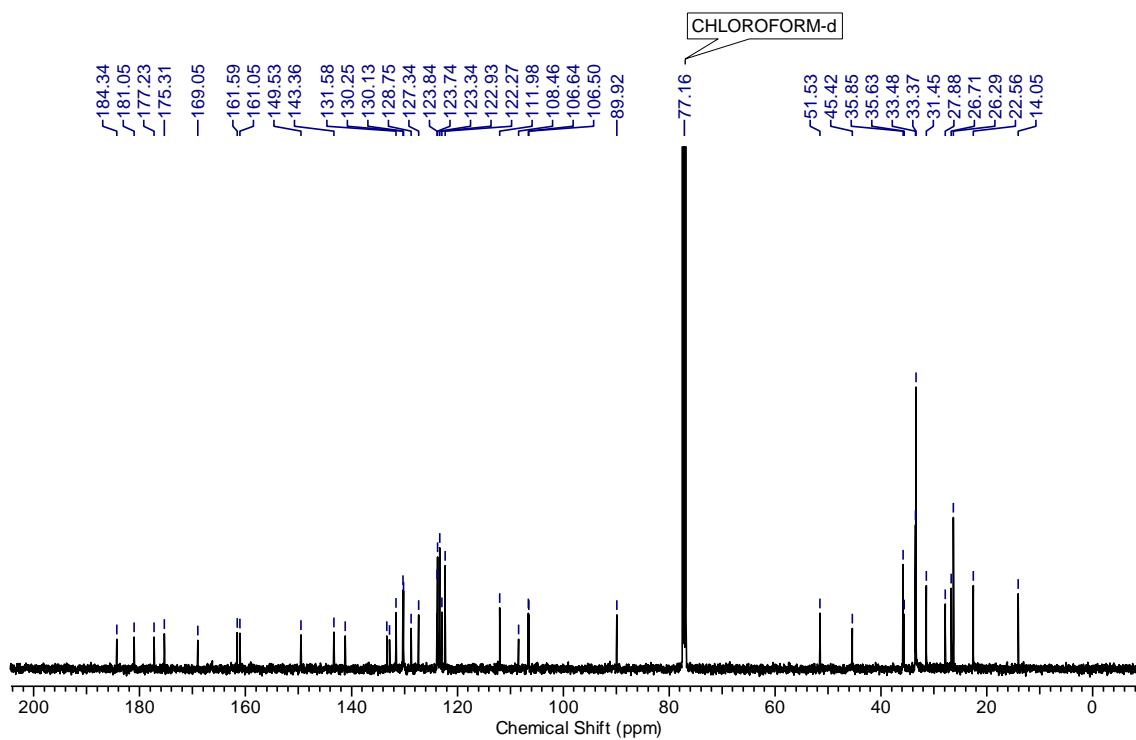


Figure 30.  $^1\text{H}$  NMR (500 MHz,  $\text{CDCl}_3$ ) spectrum of compound **KSQ3**.



**Figure 31.**  $^{13}\text{C}$  NMR (125 MHz,  $\text{CDCl}_3$ ) spectrum of compound **KSQ3**.

**5.4 REFERENCES**

1. Zaumseil, J.; Sirringhaus, H. *Chem. Rev.* **2007**, *107*, 1296.
2. Mei, J.; Diao, Y.; Appleton, A. L.; Fang, L.; Bao, Z. *J. Am. Chem. Soc.* **2013**, *135*, 6724.
3. Jurchescu, O. D.; Popinciuc, M.; Van Wees, B. J.; Palstra, T. T. *Adv. Mater.* **2007**, *19*, 688.
4. Feng, X.; Marcon, V.; Pisula, W.; Hansen, M. R.; Kirkpatrick, J.; Grozema, F.; Andrienko, D.; Kremer, K.; Müllen, K. *Nat. Mater.* **2009**, *8*, 421.
5. Senthilkumar, K.; Grozema, F.; Bickelhaupt, F.; Siebbeles, L. *J. Chem. Phys.* **2003**, *119*, 9809.
6. Debije, M. G.; Piris, J.; de Haas, M. P.; Warman, J. M.; Tomović, Ž.; Simpson, C. D.; Watson, M. D.; Müllen, K. *J. Am. Chem. Soc.* **2004**, *126*, 4641.
7. Field, J. E.; Venkataraman, D. *Chem. Mater.* **2002**, *14*, 962.
8. Kivala, M.; Pisula, W.; Wang, S.; Mavrinskiy, A.; Gisselbrecht, J. P.; Feng, X.; Müllen, K. *Chem. Eur. J.* **2013**, *19*, 8117.
9. Wan, X.; Zhang, H.; Li, Y.; Chen, Y. *New J. Chem.* **2010**, *34*, 661.
10. Dong, H.; Wang, C.; Hu, W. *Chem. Commun.* **2010**, *46*, 5211.
11. Quinn, J. T.; Zhu, J.; Li, X.; Wang, J.; Li, Y. *J. Mater. Chem. C* **2017**, *5*, 8654.
12. Katz, H.; Lovinger, A.; Johnson, J.; Kloc, C.; Siegrist, T.; Li, W.; Lin, Y.-Y.; Dodabalapur, A. *Nature* **2000**, *404*, 478.
13. Wu, Q.; Li, R.; Hong, W.; Li, H.; Gao, X.; Zhu, D. *Chem. Mater.* **2011**, *23*, 3138.
14. Jones, B. A.; Facchetti, A.; Wasielewski, M. R.; Marks, T. J. *J. Am. Chem. Soc.* **2007**, *129*, 15259.
15. Wang, C.; Dong, H.; Hu, W.; Liu, Y.; Zhu, D. *Chem. Rev.* **2011**, *112*, 2208.
16. Fang, Z.; Chellappan, V.; Webster, R. D.; Ke, L.; Zhang, T.; Liu, B.; Lai, Y.-H. *J. Mater. Chem.* **2012**, *22*, 15397.
17. Zhang, H.; Wang, S.; Li, Y.; Zhang, B.; Du, C.; Wan, X.; Chen, Y. *Tetrahedron* **2009**, *65*, 4455.
18. Zhang, Y.; Hanifi, D.; Alvarez, S.; Antonio, F.; Pun, A.; Klivansky, L. M.; Hexemer, A.; Ma, B.; Liu, Y. *Org. Lett.* **2011**, *13*, 6528.
19. Frisch, M. J.; Trucks, G. W.; Schlegel, H. B.; Scuseria, G. E.; Robb, M. A.; Cheeseman, J. R.; Scalmani, G.; Barone, V.; Mennucci, B.; Petersson, G. A.; Nakatsuji, H.; Caricato, M.; Li, X.; Hratchian, H. P.; Izmaylov, A. F.; Bloino, J.; Zheng, G.; Sonnenberg, J. L.; Hada, M.; Ehara, M.; Toyota, K.; Fukuda, R.; Hasegawa, J.; Ishida, M.; Nakajima, T.; Honda, Y.; Kitao, O.; Nakai, H.; Vreven, T.; Montgomery, J. A., Jr.; Peralta, J. E.; Ogliaro, F.; Bearpark, M.; Heyd, J. J.; Brothers, E.; Kudin, K. N.; Staroverov, V. N.; Kobayashi, R.; Normand, J.; Raghavachari, K.; Rendell, A.; Burant, J. C.; Iyengar, S. S.; Tomasi, J.; Cossi, M.; Rega, N.; Millam, J. M.; Klene, M.; Knox, J. E.; Cross, J. B.; Bakken, V.; Adamo, C.; Jaramillo, J.; Gomperts, R.; Stratmann, R. E.; Yazyev, O.; Austin, A. J.; Cammi, R.; Pomelli, C.; Ochterski, J. W.; Martin, R. L.; Morokuma, K.; Zakrzewski, V. G.; Voth, G. A.; Salvador, P.; Dannenberg, J. J.; Dapprich, S.; Daniels, A. D.; Farkas, O.; Foresman, J. B.; Ortiz, J. V.; Cioslowski, J.; Fox, D. J. *Gaussian 09, Revision A.01*; Gaussian, Inc.: Wallingford, CT, **2009**.

20. Oh, J. H.; Suraru, S. L.; Lee, W. Y.; Könemann, M.; Höffken, H. W.; Röger, C.; Schmidt, R.; Chung, Y.; Chen, W. C.; Würthner, F. *Adv. Funct. Mater.* **2010**, *20*, 2148.
21. Tonzola, C. J.; Alam, M. M.; Kaminsky, W.; Jenekhe, S. A. *J. Am. Chem. Soc.* **2003**, *125*, 13548.
22. Allard, S.; Forster, M.; Souharce, B.; Thiem, H.; Scherf, U. *Angew. Chem. Int. Ed.* **2008**, *47*, 4070.
23. Virkar, A. A.; Mannsfeld, S.; Bao, Z.; Stingelin, N. *Adv. Mater.* **2010**, *22*, 3857.
24. Horowitz, G. *Adv. Mater.* **1998**, *10*, 365.
25. Sirringhaus, H. *Adv. Mater.* **2014**, *26*, 1319.
26. Bao, Z.; Lovinger, A. J.; Dodabalapur, A. *Adv. Mater.* **1997**, *9*, 42.
27. Murphy, A. R.; Chang, P. C.; VanDyke, P.; Liu, J.; Fréchet, J. M.; Subramanian, V.; DeLongchamp, D. M.; Sambasivan, S.; Fischer, D. A.; Lin, E. K. *Chem. Mater.* **2005**, *17*, 6033.
28. Chochos, C. L.; Tagmatarchis, N.; Gregoriou, V. G. *RSC Adv.* **2013**, *3*, 7160.
29. Chen, G.; Sasabe, H.; Igarashi, T.; Hong, Z.; Kido, J. *J. Mater. Chem. A* **2015**, *3*, 14517.
30. Ajayaghosh, A.; Chithra, P.; Varghese, R.; Divya, K. P. *Chem. Commun.* **2008**, 969.
31. Würthner, F.; Kaiser, T. E.; Saha-Möller, C. R. *Angew. Chem. Int. Ed.* **2011**, *50*, 3376.
32. Bagnis, D.; Beverina, L.; Huang, H.; Silvestri, F.; Yao, Y.; Yan, H.; Pagani, G. A.; Marks, T. J.; Facchetti, A. *J. Am. Chem. Soc.* **2010**, *132*, 4074.
33. Wang, S.; Hall, L.; Diev, V. V.; Haiges, R.; Wei, G.; Xiao, X.; Djurovich, P. I.; Forrest, S. R.; Thompson, M. E. *Chem. Mater.* **2011**, *23*, 4789.
34. Chen, G.; Sasabe, H.; Sasaki, Y.; Katagiri, H.; Wang, X.-F.; Sano, T.; Hong, Z.; Yang, Y.; Kido, J. *Chem. Mater.* **2014**, *26*, 1356.
35. Della Pelle, A. M.; Homnick, P. J.; Bae, Y.; Lahti, P. M.; Thayumanavan, S. *J. Phys. Chem. C* **2014**, *118*, 1793.
36. Yang, D.; Zhu, Y.; Jiao, Y.; Yang, L.; Yang, Q.; Luo, Q.; Pu, X.; Huang, Y.; Zhao, S.; Lu, Z. *RSC Adv.* **2015**, *5*, 20724.
37. Yang, D.; Yang, Q.; Yang, L.; Luo, Q.; Huang, Y.; Lu, Z.; Zhao, S. *Chem. Commun.* **2013**, *49*, 10465.
38. Yang, L.; Yang, Q.; Yang, D.; Luo, Q.; Zhu, Y.; Huang, Y.; Zhao, S.; Lu, Z. *J. Mater. Chem. A* **2014**, *2*, 18313.
39. Karjule, N.; MK, M. F.; Nithyanandhan, J. *J. Mater. Chem. A* **2016**, *4*, 18910.
40. Karjule, N.; Mele Kavungathodi, M. F.; Nithyanandhan, J. *J. Phys. Chem. C* **2017**, *121*, 21836.
41. Sergeev, S.; Pisula, W.; Geerts, Y. H. *Chem. Soc. Rev.* **2007**, *36*, 1902.
42. Liptay, W. *Angew. Chem. Int. Ed.* **1969**, *8*, 177.
43. Chen, Y.; Zhu, Y.; Yang, D.; Luo, Q.; Yang, L.; Huang, Y.; Zhao, S.; Lu, Z. *Chem. Commun.* **2015**, *51*, 6133.
44. Park, Y. D.; Lim, J. A.; Lee, H. S.; Cho, K. *Mater. Today* **2007**, *10*, 46.



**List of Publications**

1. **Neeta Karjule**, Mrityunjay K. Sharma, Jayaraj Nithyanandhan\*, Amol A. Kulkarni\*  
“Modulation of Reactivity of Singlet Radical Pair in Continuous Flow: Photo-Fries Rearrangement” (2018, *Accepted to publish in J. Photochem. Photobiol. A*)
2. **Neeta Karjule**, Munavvar Fairoos M. K. and Jayaraj Nithyanandhan\*  
“Molecular Control of the Band Edge Movement and the Recombination Process in Donor–Acceptor Hemicyanine-Sensitized Solar Cells” *J. Phys. Chem. C*, **2017**, *121*, 21836–21847.
3. **Neeta Karjule**, Munavvar Fairoos M. K. and Jayaraj Nithyanandhan\*  
“Heterotriangulene-based unsymmetrical squaraine dyes: synergistic effects of donor moieties and outof- plane branched alkyl chains on dye cell performance”. *J. Mater. Chem. A*, **2016**, *4*, 18910–18921. (Selected for themed collection of **2016 Journal of Materials Chemistry A HOT Papers**)
4. Sreekuttan M. Unni, Saikrishna Devulapally, **Neeta Karjule** and Sreekumar Kurungot\* “Graphene enriched with pyrrolic coordination of the doped nitrogen as an efficient metal-free electro catalyst for oxygen reduction”. *J. Mater. Chem.* **2012**, *22*, 23506-23513.
5. **Neeta Karjule**, Munavvar Fairoos M. K. and Jayaraj Nithyanandhan\*  
“Effect of  $\pi$ -spacer and Alkyl Chains on Molecular Orientation, Optoelectronic and Photovoltaic Properties of Heterotriangulene Based Squaraine Dyes for Dye-Sensitized Solar Cells”. (2018, *Manuscript under review*)
6. Rajesh Bisht, Munavvar Fairoos MK, **Neeta Karjule** and Jayaraj Nithyanandhan\*  
“Controlling the Steric and Electronic Factors in Unsymmetrical Squaraine Dyes: Fused Fluorenylindolenine Donor based Unsymmetrical Squaraine Dyes for Dye-sensitized Solar Cells”. (2018, *Manuscript under review*)
7. **Neeta Karjule**, S. Chithiravel and Jayaraj Nithyanandhan\*  
“Molecular Engineering of Heterotriangulene-based Small Molecules for Organic Field Effect Transistors”. (2018, *Manuscript under preparation*)



